Numerical simulation of ductile-brittle behaviour of cracks in aluminium and bcc iron

Marios Zacharopoulos

THÈSE

Présentée par

Marios ZACHAROPOULOS

Pour obtenir le grade de

DOCTEUR de L'UNIVERSITE PIERRE ET MARIE CURIE

Spécialité

Physique et Chimie des Matériaux

SIMULATION NUMERIQUE DES FISSURES ET DU COMPORTEMENT DUCTILE-FRAGILE DE L'ALUMINIUM ET DU FER

Soutenance prévue le 16 mai 2017,

devant le jury composé de:

Jérôme CREPIN	Professeur	Lab. Ecoles des Mines ParisTech	Rapporteur
Georgios EVANGELAKIS	Professeur	Université d'Ioannina (Grèce)	Rapporteur
Bernard MARINI	Doctorat 3-ème cycle	CEA - DEN	Tuteur
Constantin MEIS	Professeur	CEA - INSTN	Examinateur
Laurent PONSON	Doctorat d'état	UPMC - MISES	Examinateur
Vassilis PONTIKIS	Doctorat d'état	CEA - IRAMIS	Directeur de thèse
Philippe SINDZINGRE	Doctorat d'état	UPMC - LPTMC	Examinateur

À Milto, ma femme.

Acknowledgement

The present dissertation has been funded by the Research Center Commissariat à l'Energie Atomique (CEA) of Saclay. The project has been conducted at the Laboratoire d'Etude du Comportement Mécanique des Matériaux (LC2M) of the Service de Recherches Métallurgiques Appliquées (SRMA).

Foremost, I would like to express my sincere gratitude and deepest regards to my supervisor Dr. Vassilis Pontikis and to my tutor Dr. Bernard Marini for their mentoring and their willingness, patience and support during these years of the project. I have benefitted greatly from their expertise, experience, motivation and immense knowledge. They contributed significantly to the progress I have made during this period.

Besides my advisor and my tutor, I would like to thank the rest of my thesis committee members who have honoured me with assessing my thesis defence. In particular, Prof. Jérôme Crépin and Prof. Georgios Evangelakis, for agreeing to report on this thesis, as well as Prof. Constantin Meis, Dr. Laurent Ponson and Dr. Philippe Sindzingre for agreeing to participate in the examination of this work.

I would also like to express my gratitude and appreciation to the director of my doctoral school, Christian Bonhomme, and to the former head of the SRMA, Philippe Chapelot, for giving me the opportunity to accomplish my goal to become a Doctor of Philosophy. My sincere thanks also go to the former head of the LC2M Ms. Laetitia Nicolas for the warm welcome during my contract and for giving me access to the laboratory and research facilities. Furthermore, I would like to thank Mr. David Simeone and Mr. Gianguido Baldinozzi for assisting me in the acquisition of a 3 month contract in Centrale Supélec. I also like to thank the head of the laboratory SPMS, Guilhem Dezanneau.

I thank all my fellow colleagues in LC2M for the very pleasant and friendly atmosphere that I have been able to benefit while working. In particular, I would like to thank Louis Ziolek and Jean-Philippe Bonthonneau, who have often helped me with computer hardware issues, as well as Nathalie Palayan, Muriel Fine and Cathy Vidal for their patience in handling my administrative requests during my thesis. A big thank you to all my friends: Raphaël Ilhat, Camille Liard, Liang Huang, Ali Charbal, Karl Buchanan, Zhengxuan Fan, Mohamed Ould

Moussa, Xiangjun Shi, Yiting Cui, Jérôme Hazan, Youcef Youcef, Hubert Salmon-Legagneur and Lu Ding for their support and encouragement during the difficult moments of this thesis.

A big thanks to Stefano Pastoris, my flatmate, with whom we shared the apartment for the most part of our studies. No matter how fast time goes by, I will never forget all your help, support and the moments spent together. I wish you a life full of happiness and prosperity with your family. I thank all my friends: Stelios Polydorou, Nicolas Hiras, Pavlos Schizas, Yiannis Koromias, Olga Patsia, Yiorgos Stathopoulos and Sarra Gkanem, for helping and supporting me throughout my thesis.

Finally, I would like to thank my family. Words cannot express how grateful I am to my mother and father for all of the sacrifices that you have made on my behalf. Your prayers for me have sustained me this far. I would also like to thank my beloved wife, Milto, for her support in everything. Thanking you is not enough for encouraging me throughout this experience. Thank you to my beloved brothers, Giorgos and Christoforos, for being always by my side and showing me their love.

Titre: Simulation numérique des fissures et du comportement ductile-fragile de l'aluminium et du fer

Résumé:

Ce manuscrit présente les résultats d'une étude à l'échelle atomique des fissures et du comportement mécanique résultant de cristaux métalliques sous charge. Il porte en particulier sur les mécanismes de déformation d'un cristal parfait en présence d'une fissure unique. Les deux métaux utilisés, pour l'aluminium (Al) et le fer (Fe), ont été choisis pour leur différence de comportement mécanique, ductile à toute température pour le premier et fragile à basse température (T<77K) pour le second. Dans les deux cas la cohésion a été représentée par des potentiels phénoménologiques à n-corps, bien adaptés aux simulations numériques de systèmes de grande taille, le premier développé pour cette étude (Al) et le deuxième (Fe) sélectionné dans la littérature.

Les modèles géométriques ont été obtenus à partir de configurations monocristallines dont les atomes ont été déplacés selon la prescription de la théorie élastique anisotrope pour une fissure de mode-I (010)[001] en équilibre instable sous contrainte appliquée. Ce choix est conforme aux observations de clivage primaire du fer et théoriquement justifié pour le clivage hypothétique de l'aluminium. Des conditions périodiques aux limites le long de la direction cristallographique [001] confèrent à la fissure une extension pseudo-infinie, alors que dans les deux autres directions cubiques, les atomes proches des limites du système simulé sont maintenus fixes aux positions dictées par l'élasticité. Avec ces conditions initiales, un schéma quasi dynamique de minimisation d'énergie, a permis de générer des configurations relaxée set de vérifier la compatibilité des déplacements atomiques entre régions statique et dynamique. Dès lors que les dimensions linéaires des systèmes étudiés sont suffisamment grandes, les déplacements atomiques anélastiques sont contenus dans une région centrale des modèles étudiés tandis que loin de ce noyau anélastique, les déplacements entre atomes statiques et dynamiques deviennent compatibles.

Alors que l'équilibre mécanique des fissures dans un milieu continu est instable, une plage de stabilité existe dans les cristaux dans un intervalle de valeurs de la contrainte appliquée, dont l'origine est le phénomène de piégeage de la fissure par le réseau cristallin. C'est cette propriété des milieux discrets contenant des fissures qui permet l'étude des propriétés thermodynamiques des systèmes étudiés dans ce travail. Nous avons trouvé que l'intervalle de stabilité d'une fissure dans le fer est plus important que dans l'aluminium et que les limites de contrainte délimitant le

domaine de stabilité sont indépendantes de sa longueur, suggérant ainsi que la résistance à sa propagation est une propriété intrinsèque. Ces limites sont reliées à la longueur de la fissure par une relation linéaire, $a = f\left(1/C\sigma_i^2\right)$, ($a$: demi-longueur de fissure, σ_i : valeurs de contrainte aux limites de piégeage inférieure/supérieure) et conduisent à une énergie efficace de surface dans les deux métaux, γ, de valeur comparable à l'énergie d'excès de la surface libre à T=0K. Cette constatation montre que le la théorie élastique des fissures (critère de Griffith) s'applique avec succès à l'échelle atomique, établissant ainsi que les propriétés obtenues par simulation atomistique peuvent être extrapolées en toute sécurité à l'échelle macroscopique.

En comparant les valeurs calculées des limites supérieures de piégeage avec les limites élastiques des deux métaux, nous constatons que la déformation par glissement de dislocations est toujours favorisée dans Al qui est trouvé ductile, alors que le contraire est vrai dans le Fe qui est donc fragile à T=0K, conformément à l'expérience. Dans Al, lorsque la contrainte appliquée dépasse la limite de stabilité la fissure se propage par clivage (010) alors que dans le Fe des dislocations sont émises en pointe de fissure. Dans ce dernier, des petits incréments de contrainte provoquent le clivage alors que l'augmentation de leur amplitude conduit à la propagation de la fissure associée simultanément à la germination aux pointes de dislocations et de défauts d'empilement. On en conclut que dans les métaux étudiés, le caractère de la propagation en régime dynamique des fissures, ductile ou fragile, dépend également des conditions de charge modifiant le cas échéant la réponse intrinsèque observée en régime quasi-statique.

Enfin, quelques calculs de Dynamique Moléculaire ont montré que dans Al le domaine de contrainte dans lequel la fissure est stable ne dépend pas de la température ce qui implique que le modèle représentant l'aluminium reproduit le comportement ductile de ce métal à toute température en accord avec les observations. En revanche, des résultats préliminaires obtenus dans le Fe suggèrent la disparition de la zone de stabilité à température croissante. Consolider ces résultats préliminaires est une tâche à entreprendre en perspective.

Mots-clés:

Simulations atomiques, minimisation d'énergie, simulations de Dynamique Moléculaire, fissures à l'équilibre, fer cubique centré, aluminium cubique à faces centrées, réponse ductile-fragile, piégeage de réseau, barrière contrainte/déformation

Title: Numerical simulation of ductile-brittle behaviour of cracks in aluminium and bcc iron

Abstract:

The present dissertation reports results of an atomic scale study of the role of sharp cracks on the mechanical behaviour of crystals under load. The question is about the deformation mechanisms in presence of a single crack in an otherwise perfect crystal at the mechanical equilibrium. Two models of metallic crystals have been considered as case studies in this work, namely aluminium (Al), ductile at any temperature, and iron (Fe), brittle at low temperatures (T<77K). In both, cohesive forces are modelled via phenomenological n-body potentials well adapted to large scale atomistic simulations among which the former has been developed on purpose (Al) whereas the latter has been selected from the literature.

The geometrical models have been obtained by imposing to the atomic configurations of initially perfect crystals the displacements obtained by the anisotropic elasticity theory for a (010)[001] mode-I crack at unstable equilibrium in presence of applied stress, which is consistent with the primary cleavage planes in Fe and good candidate for the crystallographic orientation of hypothetic cleavage in Al. Periodic boundary conditions are applied along the [001] axis whereas atoms in thin slabs at the limits of the computational box are held fixed, thus yielding an initial configuration of a crystal containing a crack of infinite extension along the [001] axis. By using such initial conditions and a quasi-dynamic numerical scheme, minimum energy configurations have been obtained that allow for compatibility testing of atomic displacements between the static and dynamic regions of the models. With linear dimensions of the studied systems chosen such as to minimize the mismatch the anelastic atom displacements are localized within the dynamic, central region of the models whereas far from this anelastic core, static and dynamic atoms comply with the displacements predicted by the elastic theory.

Although, the mechanical equilibrium of elastic cracks is unstable, cracks in crystals are submitted to the lattice trapping effect that is the barrier opposed by the lattice to the crack propagation, so that cracked crystals can reach stable mechanical equilibrium states over a finite range of applied stress/strain values. This is of fundamental importance for it allows the meaningful determination of thermodynamic properties of such defective systems. The crack stability strain range has been found significantly larger in Fe than in Al, whereas upper and lower trapping limits resulted crack-length independent, thus suggesting resistance to cleavage is an intrinsic property.

Testing for validity Griffith's criterion, shows that lattice trapping limits obey a linear relationship, $a = f\left(1/C\sigma_i^2\right)$, ($a$: crack half-length, σ_i : stress values at the lower/upper trapping limits) thus leading to an effective surface energy, γ, associated with the crack (010) faces, which values reveal close to the free surface excess energy at T=0 K in both metals. This finding shows the domain of the elastic theory of cracks extending far down the atomic scale thus establishing that properties of cracks obtained via atomistic simulations could be safely extrapolated at the macroscopic scale (scale coupling).

By comparing the calculated values of upper trapping limits with the elastic limits in the two metals we modelled, we found that dislocation glide is always favoured in Al, thus deforming ductile, whereas the opposite is true in Fe, which therefore behaves brittle at T=0K. Moreover, increasing the external load triggers dynamic, brittle (010) cleavage in Al unlike the dynamic response of the crack in Fe transforming from brittle to ductile. In the last, low stress increments induce cleavage whereas larger stress increments induce propagation of the crack associated with nucleation of dislocations and of stacking faults at the crack tips. Accordingly, the conclusion is reached that the dynamic propagation of cracks ductile or brittle does also depend on the loading conditions adding to the intrinsic, quasi-static mechanical response of cracks in the studied metals.

Finally, few Molecular Dynamics calculations have shown that lattice trapping in aluminium is almost temperature independent thus implying that the model representing aluminium behaves ductile at any temperature as is experimentally observed. On the other hand, preliminary results suggest the vanishing of the stability region in Fe with increasing temperature. Consolidating these preliminary results is a task left for work in perspective.

Keywords:

Atomistic simulations, energy minimization, molecular dynamics simulations, equilibrium crack configurations, body-centered cubic iron, face-centered cubic aluminium, ductile versus brittle mechanical response, lattice trapping effect, lattice trapping stress-strain barrier

Table of contents

CHAPTER I: Introduction

1.1. The context

It is well established experimentally that the mechanical failure mode of iron and several of its alloys, as well as many other metallic systems with the body-centered cubic (bcc) crystal structure, changes on decreasing the temperature from ductile to brittle [FRA2002, ARG2001, HAH1984]. This phenomenon stems from the increase of the fracture toughness on increasing the temperature and indicates that competing underlying mechanisms of strain-stress accommodation exist that control the change of the mechanical response from brittle to ductile. The crossover between plastic and brittle failure modes is commonly referred to as the ''ductile-brittle transition'' (DBT). The transition can be either gradual (Ge[SER1994], Mo[ROB1993, GUM1998], W[GIA2007], γ-TiAl[BOO1997], NiAl[SER1995] and MgO[ROB1993]) or sharp (Si[JOH1975, SAM1989, GEO1979, BRE1988], Al_2O_3[KIM1994], Fe-3%Si[HA1994], and bcc single crystalline α-iron [TAN2008]). Despite the fact that even single-crystals undergo DBT, the transition is not thermodynamic since the transition temperature (DBTT) is shown to relate closely to the microstructure and the external loading conditions. In addition, the DBTT increases under specific conditions including, irradiation [BOU2005], deformation, long exposures to operating temperatures, and, in some cases, with the chemical environment.

Experimental studies of material crack propagation (e.g. Charpy and Compact Tension test), have provided insight into the mode of fracture which directly relates to the fracture toughness of the material, i.e. its ability to resist failure in the presence of a crack. Crack extension in ductile materials is always associated with plastic deformation not opposing the fact that in some cases the propagation of the crack is prevented or slowed down. Therefore, ductile fracture formation is a slow process absorbing relatively high amounts of elastic energy. Conversely, cracks spread rapidly in a brittle material with low absorption of energy, whereas, once initiated, these keep growing to lead to the catastrophic failure of the material. Despite its practical importance in a number of industrial applications (Nuclear, Chemical, Construction, etc.) the physical understanding of the DBT remains limited, thus forcing engineers to resort to empirical approaches with poor predictive power. Since cracks are at the origin of fracture and their propagation mode is representative of the ductile or

brittle failure, the ingredients explaining the DBT are inferred identical to those controlling the crack propagation mechanisms. This is the exact reason that the present thesis focuses on the cracks mechanical response.

1.2. Fracture at atomic scale

Although material fracture is observed at the macro-scale, it is widely recognized that the crack propagation mode is determined by the atomic structure evolution at the crack-tip resulting from the atomic-scale mechanisms in its neighbourhood of stress-strain accommodation [GUM1995, GUM1998, CAO2006, GUO2006]. This is most clear in brittle fracture where the propagating crack-tip remains atomically sharp in order to break atomic bonds along a specific crystallographic plane. Alternatively, in a ductile fracture, the crack-tip region induces plastic deformation by means of dislocation nucleation and/or motion. Since it is essential for the interpretation of brittle versus ductile behaviour of metals, significant attention has been devoted to the study of the crack-tip mechanical response at the atomic level under different loading and temperature conditions.

DBT models divide principally into two categories labelled respectively as the nucleation-controlled [KEL1967, RIC1974, RIC1992, RIC1994, KHA1994] and the mobility-controlled models [HIR1989, HIR1996, ROB1996, HAR1997, GUM1998]. The former model accounts for the competition between crack propagation and thermally activated generation of a single dislocation at the crack-tip, thereby, establishing criteria of dislocation nucleation, whereas the latter describes the thermally activated generation of a single dislocation at the crack-tip as a dynamic mechanism controlled by the mobility of generated and/or pre-existing dislocations in the crack-tip region. However, the experimental evidence concerning the controlling factors on DBT is still inconclusive: On the one hand, the strong dependence of the DBTT on the strain rate allows the empirical calculation of an activation energy characterizing the transition, which is revealed to be equal to the activation energy for the dislocation glide in bcc metals, a result that implies DBT is dislocation mobility-controlled [BRE1988, HIR1989, ROB1996]. On the other hand, the fracture toughness is greatly influenced by the size of the specimen and the availability of dislocation sources in such a manner that the mechanical response of the material has been observed to switch from brittle to ductile on increasing the sample's experimental dimensions [MIC1994].

Moreover, experimental observations revealed that plastic deformation occurs in conjunction with the crack propagation [OHR1985, ZIE1992]; a result suggesting that the bond rupture, dislocation generation and dislocation activity can be coexisting phenomena at the crack-tip and its region. Since cracks and dislocations both accommodate stress and/or strain preferring the easiest deformation atomic mechanism, ductile versus brittle behaviour of metals could correspond to a combination of both nucleation-controlled and mobility-controlled models. However, since single-crystalline systems with very low density of dislocations [BRE1988, SAM1989, KIM1994] still exhibit sharp DBT, fundamental understanding should be first gained from systems without microstructure, such as dislocation free pure and perfect crystals. This is the customary path followed in most atomistic studies and is also the choice made in the present work. Accordingly, the present study aims at investigating atomistic cracks in the absence of any other kind of micro-structural element at this scale with principal target the interpretation of the brittle versus ductile mechanical behaviour.

1.3. Scope of the thesis

The majority of the studies on cracks at the atomic scale focus on the dynamic response of the crack under different loading and temperature conditions. This procedure constitutes a logical approach for investigating the DBT, since fracture is a dynamic phenomenon. However, the dynamic evolution of cracks in such studies depends on the applied dynamic loading conditions and the results are likely affected by model size limitations (Chapter III). In addition, the time evolution of such systems does not correspond to thermodynamic states, which precludes estimating the thermodynamic properties of the evolving defected systems (Chapter III). Therefore, it is difficult to relate the thermodynamic properties of the system to the mechanical response of a pre-existing crack.

In the present study, a different approach is adopted as we study the properties of quasi-static cracks, i.e. crack configurations at the mechanical equilibrium. The stability of quasi-static cracks inside materials is governed by the criterion of Griffith [GRI1920], which is further described in Chapter II, stating that a crack of a certain length is stabilized in an unstable mechanical equilibrium condition by an external stress. In an ideal brittle material, the Griffith's stability limit corresponds to the brittle fracture threshold. However, as

explained in Chapter II, this criterion is the condition for the crack ''mechanical stabilization'' inside a material, yet it does not represent the activation stress barrier for the brittle propagation of a pre-existing crack. This barrier is related to the discrete crystal lattice effect on the crack mechanical response which provides an additional factor of the configuration stabilization, the ''lattice trapping effect'' [THO1971, SIN1972, SIN1975, CUR1990]. Lattice trapping is the resistance opposed by the discrete crystal lattice to the extension of a pre-existing crack initially in mechanical equilibrium. This barrier should be compared to the corresponding barrier for the motion of pre-existing dislocations inside the crystal lattice, a comparison that will determine the most favourable mechanism of stress-strain accommodation. This is how in this work the test is made if the mechanical response of the crystal containing a crack is brittle or ductile upon increasing the load (Chapter V). Additional effort has been devoted to identify the mechanisms of crack propagation in the absence of pre-existing dislocations. Finally, the effect of temperature on the barrier opposing the propagation of quasi-static cracks has been investigated.

1.4. Approach

Two cohesion models are used in this work representing respectively aluminium, a metal known as ductile at any temperature below melting point, and α-iron which transforms from ductile to brittle upon decreasing the temperature below 77 Kelvin [TAM2002]. Other differences in physical properties of these metals are the elastic anisotropy and the crystal structure; aluminium is an almost elastically isotropic face-centered cubic (fcc) crystal whereas iron is anisotropic with body-centered cubic (bcc) structure [HIR1982]. The first step in studying crystalline systems at the atomic level is to model their cohesive energy through the description of the inter-atomic interactions. As presented in Chapter III, the atomic interactions can be described via analytic functions or inter-atomic potentials, which can replicate the physical properties. As part of this project, a phenomenological n-body potential describing cohesion in fcc aluminium has been optimized [ZAC2017] to yield results with good agreement to the experimental properties (Chapter III). Additionally, the inter-atomic potential developed by V. Pontikis et al. [PON2007] is used for the study in bcc α-iron, as it provides satisfactory results (Chapter III).

The second step in studying crack-containing systems at the atomic scale involves choosing a reasonable initial crack configuration embedded in an otherwise perfect crystal lattice. To this end, the present study follows the approach that is applied in previous atomistic studies of cracks [DEC1983, CHE1990, MAC1998, BEL2004, CAO2006, GUO2006], i.e. the analytical determination of the crack displacement field by using the linear continuum theory. In particular, as presented in Chapter III, the construction of the atomistic crack models was achieved by utilization of the complex variable method [SIH1968]. It is worth mentioning that the FORTRAN codes developed for this process are provided in the appendix F. The complex variable approach offers two major advantages: (i) it accounts for the crystal elastic anisotropy, and (ii) allows the easy implementation of the loading conditions. The investigation is focused on the $(010)[001]$ (crack plane/crack front) nano-crack, an orientation that is chosen in consistency with both the primary cleavage planes in bcc iron and the hypothetically favourable cleavage planes of fcc aluminium (Chapter III).

Continuum mechanics constitutes an analytic methodology capable of determining the mechanical properties of materials, at the macro-scale. However, it is widely recognized that the crack displacement field thereby provided is not applicable in the vicinity of the crack-tip as the analytic solution of the stress field nearby the crack-tip singularity diverges. Moreover, since continuum mechanics considers the materials as continuous and homogeneous, no prediction of phenomena that relate to the discrete nature of the crystalline lattice is possible. In short, continuum mechanics cannot adequately describe the non-linear and discrete character of the crack-tip region at the atomic level. Nevertheless, the far-displacement field of a crack configuration can be appropriately described by continuum mechanics. Since the spatial range of non-linearity close to the crack-tip region is atomistic [GUO2006], crack-tip description is ideally suited for atomistic methods (Molecular Statics and Dynamics, Monte-Carlo). Indeed, atomistic simulation is used to compute the individual motion of atoms (Appendix I), and hence it is appropriate to study the non-linear properties at the crack-tip region both in equilibrium and non-equilibrium configurations. At the same time, atomistic simulations account for the discrete nature of the crystal system and thus are widely used to investigate the mechanical properties of crack-containing systems at the atomic scale in complement to continuum mechanics.

Despite the significant increase in computational power during the last decades, even the largest atomistic simulation systems that can run on modern computers are too small compared to the laboratory scale. To circumvent this inevitable limitation, atomistic simulation models are usually divided into two main regions: (i) the atomistic region and (ii) the boundary conditions. The former is the region of interest at the atomic scale, while the latter is the part of the system that surrounds the region of interest and aims to simulate the effect of the macroscopic system on it. Within this framework, atomistic models of cracks use as boundary conditions the elastic field of cracks described by continuum mechanics and vice-versa. Indeed, the combined atomistic-continuum technique couples material properties from macro-scale to the discrete atomistic scale [GUM1995, ABR1997, RAF1998, BRO1999] and is the method that is used in the present work (Chapter III). As is further explained in Chapter III, the boundary conditions integrate the loading conditions on the atomistic crack model. For this reason, special attention has been given to their implementation. Atomistic studies on cracks focus in general only on the crack-tip region [DEC1983, CHE1990, MAC1998, MAC2004, BEL2004, BEL2007]. This approach causes the boundary conditions to generate non-physical constraints in the model, since they do not allow the physical relaxation and/or motion of the crack surfaces; thus possibly affecting the crack response to the external load. In this study, a different approach is followed as the atomistic model contains the entire crack configuration (Chapter III). Thus, the crack faces are able to relax and/or move physically during the simulation and to shape the crack under different conditions of loading and temperature. Additional advantage of this choice is that it allows investigation of the effect of the crack-size on the mechanical response.

For the first time, the present thesis highlights an important issue concerning the study of nano-sized cracks. As described in Chapter IV, according to the criterion of Griffith [GRI1920], the applied load stabilizing a crack configuration of atomistic length is of order of magnitude of giga-Pascals. This load exceeds the elastic limit of both the studied metals, causing large displacements into the system which does not comply with the usual elastic behaviour [HIR1982]. Based on the above, the elastic properties of the crack-containing crystal can be affected considerably; hence their evaluation is required critically in order to appropriately interpret the mechanical response of the crystal. This

issue, which concerns all atomistic studies on nano-sized cracks, as well as the present work, is discussed and treated in Chapter IV.

1.5. Presentation

The manuscript contains five additional chapters:

- The second chapter presents the experimental and computational results of the brittle versus ductile behaviour of materials from the literature. Additionally, the necessary mathematical formulation for describing a crack-containing system in mechanical equilibrium is given in the framework of linear continuum mechanics.

- In the third chapter, the technical and computational details of the simulation process are presented in detail together with the description of the project's approach.

- The fourth chapter is devoted to highlight the need of evaluating the elastic properties of systems that contain nano-sized cracks in mechanical equilibrium. This issue is addressed within the framework of linear elasticity.

- The fifth chapter presents the atomistic simulations concerning equilibrium, non-equilibrium and dynamic cracks in fcc aluminium and bcc iron. Simulation findings are accompanied with the corresponding analysis, interpretation and discussion.

- Finally, the last chapter summarizes results and conclusions of this work and draws perspectives for future work.

CHAPTER II: Literature Review

2.1. Ductile-Brittle Transition: Experimental information

The experimental study of the ductile-to-brittle transition has been conducted within a very large range of scales; from the macroscopic scale, an area where mechanical tests and measurements are performed, up to the microscopic scale, an area of experimental observations and measurements [ROS1996, REN1996, MÄN1999, OBR2005, CHA2010]. At the macroscopic scale, the ductile-brittle transition can be experimentally studied by performing the Charpy impact test [ROS1996, TAN2005a, TAN2005b], which determines the amount of energy absorbed by a material during fracture. From the experimental results, as it is shown in figure II.1, it can be observed, that at low temperatures fracturing a material requires a low amount of energy (lower-shelf), relating to the brittle-cleavage failure mode. On the contrary, at high temperatures, the material requires a much higher amount of energy (upper-shelf) to fracture in a ductile-plastic manner. This experimental finding can be interpreted in two different ways: (i) the ability of a crack to propagate may be affected by the temperature and/or (ii) the temperature increase can possibly give rise to another mechanism of stress-strain accommodation, which is energetically more favourable than the brittle propagation of the crack.

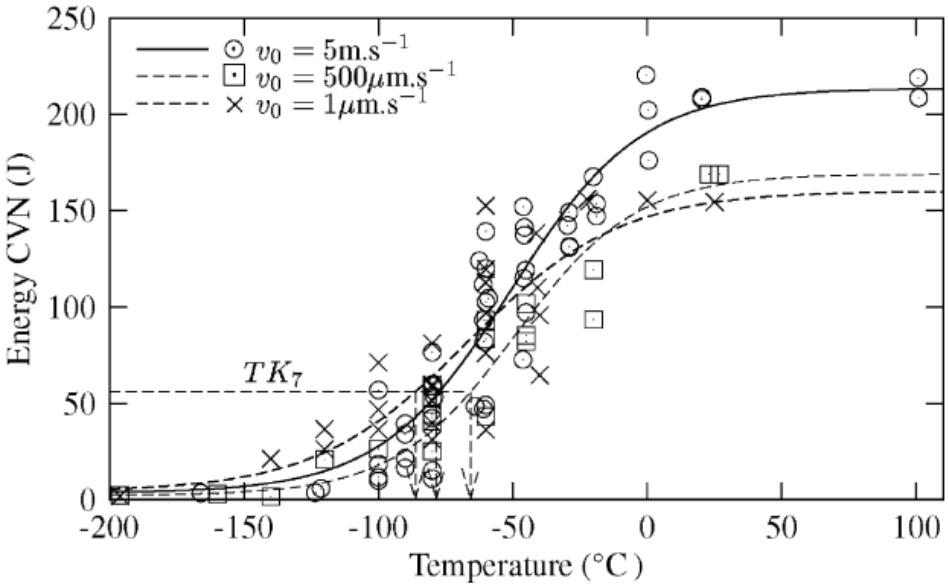

Figure II.1: Charpy V-notch test curves of A508 steel [TAN2005a].

It is common, for practical reasons, that the engineers determine a specific temperature, T_{DBT}, which describes the ductile-brittle transition of an industrial material. This T_{DBT} is

usually defined by the use of several empirical criteria on Charpy experimental data [MOU2009], including the average between the lower and the upper shelf, a specific absorbed energy etc. These criteria are not based on the physical interpretation of the transition; hence, the T_{DBT} will not be employed in the current thesis. Another category of mechanical tests that use to study the transition are the Compact Tension (CT) tests [IWA1985, REN1996], which are extensively used in the field of fracture mechanics, in order to establish the fracture toughness values of a material system; hence they can provide a direct description of the DBT transition (figure II.2).

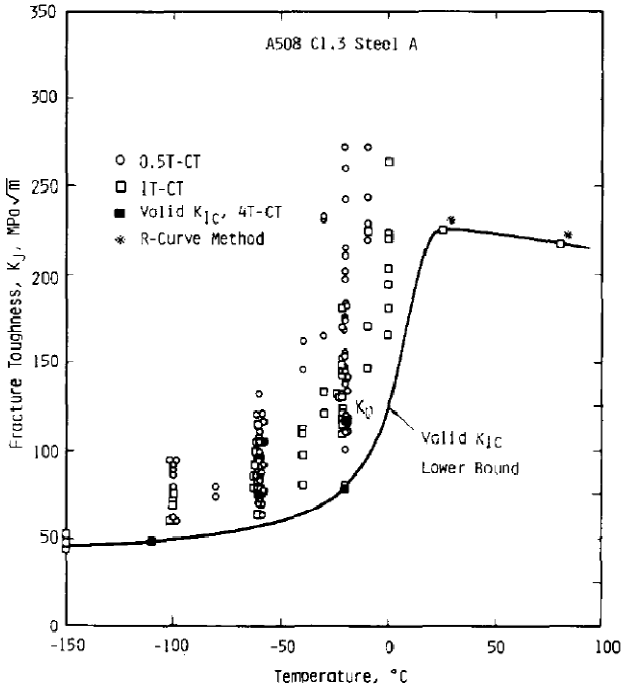

Figure II.2: Fracture toughness versus temperature for the A508 steel in the transition region [IWA1985].

The transition can also be observed from the fracture surfaces [MÄN1999, QIA2003, SPI2007] of mechanical tests samples. These are appearing as shiny for a complete brittle fracture, while are dull and fibrous for a totally ductile failure. However, it is worth mentioning that at the microscopic level the ductile features are always present on the fracture surfaces of industrial metals. This experimental finding implies the existence of a competition between micro-scale mechanisms of stress accommodation which are related with structural defects. Experiments on single-crystal systems reveal the existence of two different forms of the DBT phenomenon, the ''sharp'' and the ''soft'' transition. The ''soft'' transitions (Ge[SER1994], Mo[ROB1993, GUM1998], W[GIA2007], γ-TiAl[BOO1997],

NiAl[SER1995] and MgO[ROB1993]) are characterized by a gradual increase of the stress intensity to fracture in relation with the temperature below the transition temperature, T_{DBT}. In addition, within this temperature range the activity of dislocations at the crack-tip region increases with the temperature increase. On the other hand, ''sharp'' transitions (Si[JOH1975, SAM1989, GEO1979, BRE1988], Al_2O_3[KIM1994], Fe-3%Si[HA1994], and single crystalline α-iron [TAN2008]) are characterized by the sharp increase of the stress intensity at the transition temperature, T_{DBT}. In such a transition, dislocations in the vicinity of the crack-tip become active, only, at and above T_{DBT}. It is also worth to mention that the type of transition of a single-crystal system can be changed due to its pre-testing preparation. In particular, the sharp transition in silicon can be transformed to a soft one by the introduction of dislocations and dislocation sources before testing [WAR1989]. Such an observation indicates the significant role of the micro-structure and the pre-existing structural defects with this phenomenon. Another experimental result is that T_{DBT} for both types of transitions increases in respect with increasing the strain rate. Such a result suggests that the T_{DBT} is not a thermodynamic or intrinsic property of a material system since it is affected by external conditions. Observations on microscopic scale reveal that dislocation activity occurs during the loading of specimens, prior to system failure, if the stress level of a material at fracture is larger than the brittle critical threshold of Griffith (§2.3) [BRE1988, JOH1975, WAR1989]. On the contrary, dislocation activity is absent, not even for a few degrees below T_{DBT}, for systems exhibiting sharp form transition [JOH1975, SAM1989]. In addition, for single-crystalline systems that exhibit soft transitions, dislocation activity increases with increasing the temperature [WAR1989]. Now, since every real system contains pre-existing dislocations, the following question inevitably arises: why dislocations remain inactive and the system prefers the brittle breakage at low temperatures?

2.2. Plastic deformation in metals

As it is known from the solid state theory [HIR1982], the plastic deformation of metals occurs primarily via the motion of dislocations. It is widely established that dislocation motion in crystals is mainly performed through glide on specific crystallographic planes and along specific crystallographic directions, which compose the glide slip systems [HIR1982], depending on the type of the crystalline lattice (Table II.1). The slip systems usually consist of crystallographic planes of the highest planar density and the crystallographic directions of

the highest linear density, where the energetic barrier for the dislocation to glide is lower [HIR1982]. In fcc crystals, like aluminium, dislocation glide occurs on the close-packed $\{111\}$ planes and along the close-packed $\langle 110\rangle$ directions, hence resulting in total 12 available slip systems [HIR1982]. The corresponding magnitude of the Burgers vector, i.e. the magnitude of the lattice distortion, is equal to:

$$\left|\vec{b}\right| = \frac{a_0}{2}\langle 110\rangle = \frac{a_0}{\sqrt{2}}$$

where a_0 is the lattice parameter of the unit cell (Appendix H). In bcc crystals, like α-iron, dislocation glide can occur on $\{110\}$, $\{123\}$ and $\{112\}$ crystallographic planes and along the $\langle 111\rangle$ directions, resulting totally 48 available slip systems [HIR1982]. The norm of the Burgers vector in this case is given by:

$$\left|\vec{b}\right| = \frac{a_0}{2}\langle 111\rangle = \frac{\sqrt{3}a_0}{2}$$

According to the solid state theory [HIR1982], a static dislocation existing within a crystal can potentially glide on an available slip system, if it is subjected to a force which has a component along the respective slip plane and slip direction. This force can be the result of applied load on the crystal and is known as the resolved shear stress, τ_{RSS}. In the case of uni-axial loading, the τ_{RSS} of a given slip system is given by Schmid's law [HIR1982]:

$$\tau_{RSS} = \sigma \cdot cos\varphi \cdot cos\lambda = \sigma \cdot m \qquad (II.1)$$

where σ is the tensile stress, φ is the angle between tensile direction and slip plane normal and λ is the angle between tensile direction and slip direction (figure II.3). The coefficient m in equation II.1 is called the Schmid-factor and takes the values $0 < |m| < 0.5$ depending on the relative orientation between the slip system and the tensile axis. According to the theory of dislocations [HIR1982], dislocation glide on a specific slip system can be triggered only under the condition where the τ_{RSS} has surpassed a stress threshold; the critical resolved shear stress, τ_{CRSS}. For a pure crystal, the τ_{CRSS} expresses the intrinsic resistance of the crystalline lattice against to the dislocation glide on a specific slip system, due to the existing atomic potential barriers. In this case, the τ_{CRSS} depends on the crystal structure, the family of the slip system, the type of the gliding dislocation (edge or screw [HIR1982]), the type of the atomic bonds and the temperature.

Table II.1: Slip systems of the fcc and bcc crystal lattice

fcc lattice Slip system $\{111\}\langle 110\rangle$			**bcc lattice Slip system $\{110\}\langle 111\rangle$**			**bcc lattice Slip system $\{211\}\langle 111\rangle$**		
Slip system	Slip plane	Slip direction	Slip system	Slip Plane	Slip direction	Slip system	Slip plane	Slip direction
1	$(11\bar{1})$	$[011]$	1	(011)	$[11\bar{1}]$	1	$(2\bar{1}1)$	$[11\bar{1}]$
2	$(11\bar{1})$	$[101]$	2	(101)	$[11\bar{1}]$	2	$(1\bar{2}\bar{1})$	$[11\bar{1}]$
3	$(11\bar{1})$	$[1\bar{1}0]$	3	$(1\bar{1}0)$	$[11\bar{1}]$	3	(112)	$[11\bar{1}]$
4	$(1\bar{1}\bar{1})$	$[01\bar{1}]$	4	$(01\bar{1})$	$[1\bar{1}\bar{1}]$	4	(211)	$[1\bar{1}\bar{1}]$
5	$(1\bar{1}\bar{1})$	$[101]$	5	(101)	$[1\bar{1}\bar{1}]$	5	$(12\bar{1})$	$[1\bar{1}\bar{1}]$
6	$(1\bar{1}\bar{1})$	$[110]$	6	(110)	$[1\bar{1}\bar{1}]$	6	$(1\bar{1}2)$	$[1\bar{1}\bar{1}]$
7	$(1\bar{1}1)$	$[011]$	7	(011)	$[1\bar{1}1]$	7	$(21\bar{1})$	$[1\bar{1}1]$
8	$(1\bar{1}1)$	$[10\bar{1}]$	8	$(10\bar{1})$	$[1\bar{1}1]$	8	(121)	$[1\bar{1}1]$
9	$(1\bar{1}1)$	$[110]$	9	(110)	$[1\bar{1}1]$	9	$(1\bar{1}\bar{2})$	$[1\bar{1}1]$
10	(111)	$[01\bar{1}]$	10	$(01\bar{1})$	$[111]$	10	$(2\bar{1}\bar{1})$	$[111]$
11	(111)	$[10\bar{1}]$	11	$(10\bar{1})$	$[111]$	11	$(1\bar{2}1)$	$[111]$
12	(111)	$[1\bar{1}0]$	12	$(1\bar{1}0)$	$[111]$	12	$(11\bar{2})$	$[111]$
bcc lattice Slip system $\{123\}\langle 111\rangle$								
Slip system	Slip Plane	Slip direction	Slip system	Slip Plane	Slip direction	Slip system	Slip plane	Slip direction
1	(123)	$[11\bar{1}]$	9	(213)	$[11\bar{1}]$	17	(312)	$[111]$
2	(123)	$[\bar{1}11]$	10	(213)	$[1\bar{1}1]$	18	$(3\bar{1}2)$	$[11\bar{1}]$
3	(132)	$[1\bar{1}1]$	11	(231)	$[1\bar{1}1]$	19	(321)	$[111]$
4	(132)	$[\bar{1}11]$	12	(231)	$[11\bar{1}]$	20	$(32\bar{1})$	$[1\bar{1}1]$
5	(312)	$[\bar{1}11]$	13	(123)	$[111]$	21	(213)	$[111]$
6	(312)	$[1\bar{1}1]$	14	$(\bar{1}23)$	$[1\bar{1}1]$	22	$(2\bar{1}3)$	$[\bar{1}11]$
7	(321)	$[\bar{1}11]$	15	(132)	$[111]$	23	(231)	$[111]$
8	(321)	$[11\bar{1}]$	16	$(\bar{1}32)$	$[11\bar{1}]$	24	$(23\bar{1})$	$[\bar{1}11]$

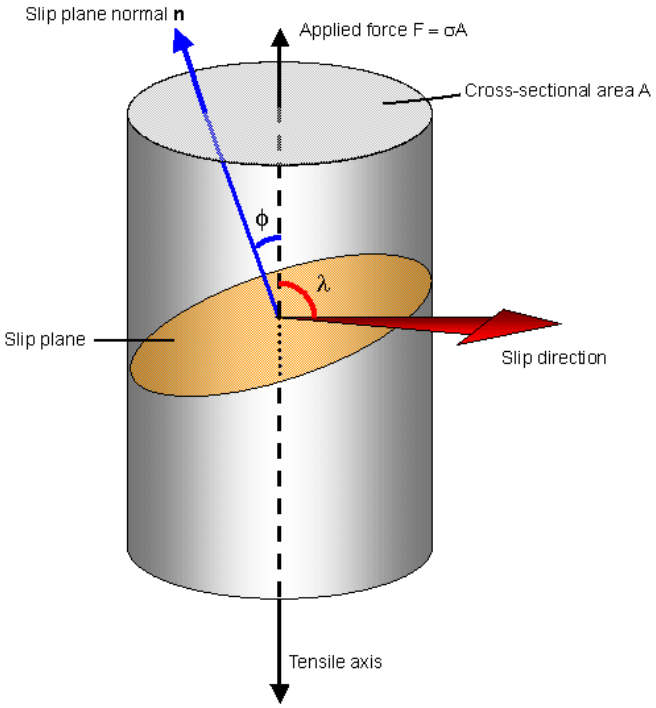

Figure II.3: Schmid's law: the critical resolved shear stress [INT5].

Experimental data from mechanical tests and atomistic results from computational simulations shown that materials, which are of the same crystalline structure family, present similar plastic behaviour. Starting from the fcc crystals, the τ_{CRSS} at $T = 0K$ amounts to values which are proportional to the $10^{-5}G$ [HOW1961, SUZ1988, WAN1996, KOI2000, SHI2013], where G is the shear modulus. On the other hand, the τ_{CRSS} at $T = 0K$ in bcc crystals is significantly higher and proportional to $10^{-3}G$ [KUR1979, WAN1996, SUZ1999]. The difference in the magnitude of τ_{CRSS} at $T = 0K$ between the two crystalline structures can be attributed to two reasons:

(i) The first reason is that the bcc crystals do not contain closed-packed planes, while the fcc crystals do contain [HIR1982]. As already mentioned, the higher the planar density of the slip plane the lower the energy barriers for a dislocation to glide.

(ii) The second reason is the fact that the plastic deformation in bcc metals is controlled by the glide of screw dislocations [HIR1982]. Atomistic calculations demonstrate that a screw $1/2\,[111]$ dislocation can splits into three $1/6\,[111]$ fractional dislocations extending its core within the crystal on the $\{110\}$ and $\{112\}$ crystallographic planes [SEE1976, PUL1981]. The glide of this equilibrium configuration [VIT1974, HIR1982] upon applied loading is accompanied by the structural change of the extended dislocation core; a mechanism that absorbs significant amount of elastic energy.

Furthermore, experiments in bcc crystals [SUZ1999, TAM2002] show that the increase of temperature significantly decreases the τ_{CRSS} (figure II.4). This behaviour demonstrates that the dislocation glide is a thermally-activated mechanism in bcc metals. Additionally, Suzuki et al. [SUZ1999] has studied the temperature dependence of the τ_{CRSS} using a scaling relation and proved that the plastic behaviour of several bcc metals (α-Fe, Nb, Mo, Ta, K) can be described by a ''master curve''. Hence, his study demonstrates the existence of a plastic homology for the bcc metals. On the other hand, in fcc crystals, the τ_{CRSS} is not affected significantly from the temperature, suggesting that the glide of a dislocation is an athermal process [TAM2002]. Based on the above information, it can be concluded that:

(i) at low temperatures, the $\tau_{CRSS}^{bcc} > \tau_{CRSS}^{fcc}$, while

(ii) at high temperatures, the τ_{CRSS}^{bcc} and the τ_{CRSS}^{fcc} are converging.

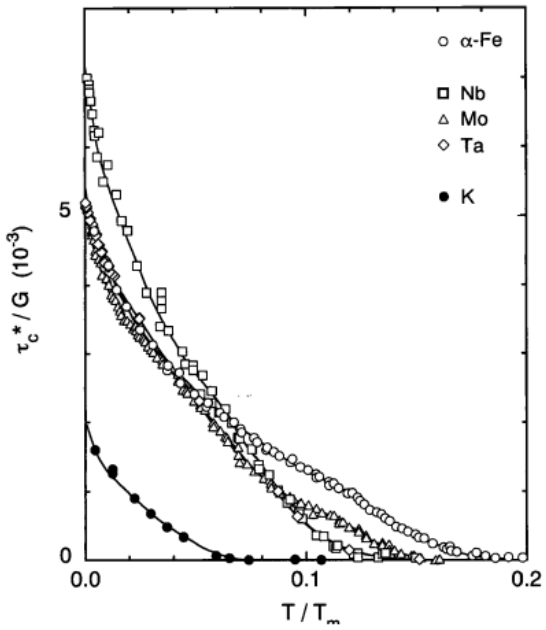

Figure II.4: Temperature dependence of the effective critical shear stress of bcc metals [SUZ1999].

Apart from the temperature, the τ_{CRSS} can be also affected from the microstructure, including solute atoms, precipitates, interfaces, grain boundaries and other obstacles for the dislocation glide. If under specific conditions (e.g. temperature or microstructure) the τ_{CRSS} becomes too high, a loaded crystal can use alternative mechanisms of stress accommodation. Such a mechanism is the cracks' propagation which results to brittle fracture of the crystal. Jaoul [JAO1965] has stated that the mechanical response of a material upon loading can be interpreted phenomenologically by the coexistence of these two competing mechanisms. Hence, depending on which of the mechanisms requires the smallest activation stress, either plastic flow (ductile response) or crack propagation (brittle response) will take place. Jaoul's simple model can qualitative describe the temperature effect on the ductile versus brittle behaviour in bcc metals. According to his model (figure II.5), the yield stress, which is the experimental quantity representing the τ_{CRSS}^{bcc}, decreases significantly with increasing the temperature. On the other hand, the fracture stress, i.e. the stress that causes brittle fracture on cleavage planes, remains relatively independent from temperature due to the very small change in surface energy to temperature. Based on these considerations, there is a possibility that for a specific temperature (T_{DBT}) the yield stress and fracture stress can be equal. According to this scenario, for $T < T_{DBT}$, the yield stress is larger than the fracture stress, which means that the propagation of cracks is the preferable mechanism of stress accommodation. On the contrary, for $T > T_{DBT}$, the yield stress is lower

compared to the fracture stress and hence the dislocation glide is triggered easier that the crack propagation. Thus, failure mode changes from plastic flow to brittle fracture by decreasing temperature. Finally, in contrast to the bcc metals, a ductile-to-brittle transition in the fcc metals such as aluminium does not exist [SMI2014]. Hence, it is apparent that there is a relation between the type of crystalline structure and the mechanical behaviour of materials. Based on Jaoul's phenomenological approach, this behaviour is caused due to the very low values of τ_{CRSS}^{fcc}, which promote dislocation glide at all temperatures. Having presented the aspects of dislocations behaviour in both crystalline structures, the attention now should shift on cracks.

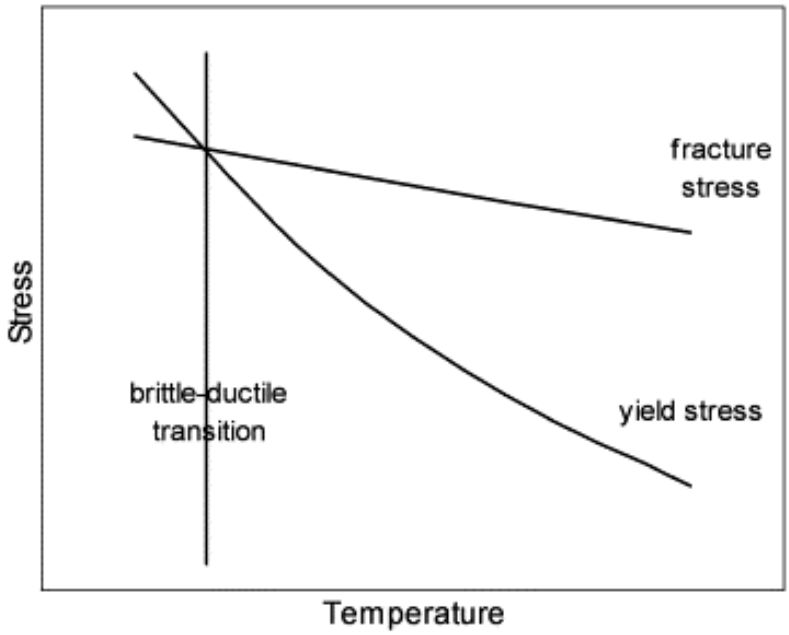

Figure II.5: Temperature dependence of the yield stress and fracture stress.

2.3. Griffith's theory of cracks

The fundamental starting point for studying fracture in cracked material systems is the Griffith's energy balance concept [GRI1920]. The idea of Griffith is based on a system containing a crack, which mechanical response upon loading is described via a reversible thermo-dynamical process. He considered an elastic body containing a narrow elliptical crack, with length equal to $2a$ and width $b \to 0$ (Griffith's crack). The body is subjected to a constant uniform tensile load, as illustrated in figure II.6, and is considered being ideally linear elastic up to the fracture.

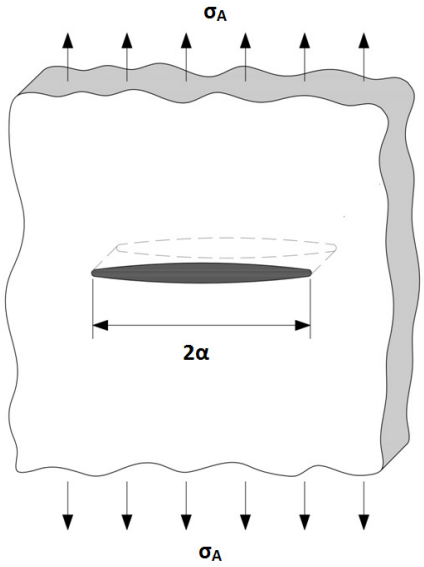

Figure II.6: Griffith's crack problem

Under this concept, Griffith studied the relation of the change of the energy of the system in respect to the crack length. According to his analysis, the total energy for a quasi-static crack system consists of three terms:

$$U = U_L - U_E + U_S \qquad (II.2)$$

where U_L is the elastic energy stored in elastic body in the absence of the crack due to the constant applied load, U_E is the elastic energy released from regions of the medium close to the crack during its formation, and U_S is the excessive energy of the two newly created surfaces enclosing the crack. Thus, the total energy of the crack configuration itself is given by:

$$U^{crack} = U - U_L = -U_E + U_S \qquad (II.3)$$

The thermodynamic equilibrium state of the crack system can be determined by:

$$\frac{dU^{crack}}{da} = 0 \qquad (II.4)$$

Griffith used the Inglis solution of the stress and strain field around a sharp crack [ING1913] in order to calculate the strain energy release due to the crack formation. Considering the case of an isotropic medium, the strain energy release per unit thickness of the model, over the domain close to the formed crack, is given by:

$$U_E = \frac{\pi a^2 \sigma_A^2}{E} \qquad (II.5a)$$

where σ_A is the tensional applied stress and E is the Young's modulus. Equation II.5a refers to the case of a plane state of stress, which can be achieved inside a thin plate (§D.2). A similar expression is obtained for the case of plane state of strain (§D.2), for a thick plate system:

$$U_E = \frac{\pi a^2 \sigma_A^2}{E}(1 - \nu^2) \qquad (II.5b)$$

with ν being the Poisson's ratio. In addition, Griffith considered that the crack faces are approximately flat and do not interact. Under these assumptions, the surface energy of the system per unit thickness is simply expressed by:

$$U_S = 4a\gamma \qquad (II.6)$$

where γ is the free surface energy per unit area. Thusly, the total energy of an Griffith-Inglis crack in the case of plane state of stress becomes:

$$U^{crack} = -U_E + U_S = -\frac{\pi a^2 \sigma_A^2}{E} + 4a\gamma \qquad (II.7a)$$

Similarly, for the case of the plane state of strain:

$$U^{crack} = -U_E + U_S = -\frac{\pi a^2 \sigma_A^2}{E}(1 - \nu^2) + 4a\gamma \qquad (II.7b)$$

By using the equilibrium condition (equation II.4), Griffith was able to calculate the critical stress for the onset of fracture of a crack configuration with a specific crack length, a_0:

$$\sigma_{A,c} = \sqrt{\frac{2E\gamma}{\pi a_0}} \qquad (II.8a)$$

$$\sigma_{A,c} = \sqrt{\frac{2E\gamma}{(1 - \nu^2)\pi a_0}} \qquad (II.8b)$$

for plane stress and plane strain conditions, respectively. At the same time, the equilibrium condition provides the critical half-length, α_c, corresponding to an equilibrium crack configuration inside a system under a specific constant applied load, $\sigma_{A,0}$:

$$\alpha_c = \frac{2E\gamma}{\pi\sigma_{A,0}^2} \qquad (II.9a)$$

$$\alpha_c = \frac{2E\gamma}{(1-\nu^2)\pi\sigma_{A,0}^2} \qquad (II.9b)$$

for plane stress and plane stress conditions, respectively. Figure II.7 illustrates the energy release, the surface energy and the total crack energy in respect to the crack length.

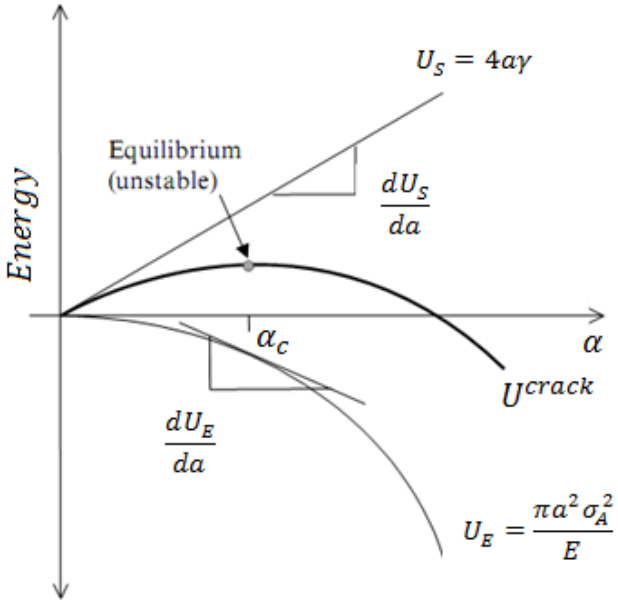

Figure II.7: Energetics of the Griffith-Inglis crack in uniform tension and under plane stress conditions.

As it can be seen, a cracked system under a constant applied load reaches a maximum energy at α_c, hence the quasi-static crack configuration is in an **unstable equilibrium**. As a result, if the applied stress exceeds the critical level defined by equation II.8, an initially equilibrium crack configuration is free to propagate spontaneously without limit. On the other hand, if the applied stress reduces below the critical level, an unstable equilibrium crack is going to close through a reverse propagation-like process. Equations II.8 and II.9 are known in literature as the criterion of Griffith [GRI1920], which is presented graphically in figure II.8. Griffith's criterion implies that every crack configuration, with a specific length, is stabilized upon applying a specific load. This constitutes the foundation in dealing with the

''mechanical stabilization'' of any sized crack inside a material system. In addition, the fact that the equilibrium condition of a crack is represented by a zero-dimensional point on the crack's energetics diagram (figure II.7) it proves that the Griffith's critical stress (equation II.8) is not related to the activation stress barrier of brittle propagation for a pre-existing equilibrium crack in the system.

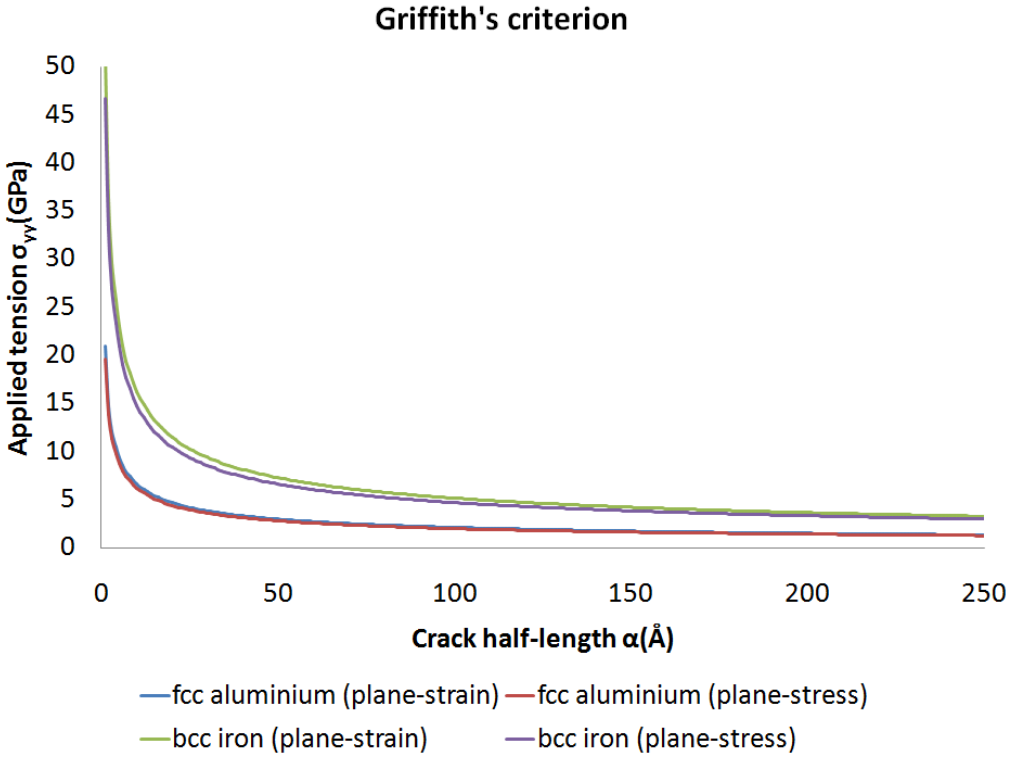

Figure II.8: Griffith's criterion applied on fcc aluminium [ZAC2017] and bcc iron [PON2007].

More importantly, Griffith's analysis provides the mathematical framework for the ''mechanical homology'' of cracks inside elastic systems. Considering the case of the plane strain deformation mode, the total energy of the crack configuration at equilibrium is equal to:

$$U^{crack,e} = U^{crack}|_{a=a_c} = 2a_c\gamma \qquad (II.10)$$

Expression II.10 provides us with the possibility to express the total energy of a crack in normalized units:

$$U^{crack,*} = \frac{U^{crack}}{U^{crack,e}} = 2\left(\frac{a}{a_c}\right) - \left(\frac{a}{a_c}\right)^2 \qquad (II.11)$$

By setting $\alpha^* = a/a_c$ the normalized total energy of a Griffith-Inglis crack can be expressed in normalized units of crack length as:

$$U^{crack,*} = 2\alpha^* - \alpha^{*2} \qquad (II.12)$$

Equation II.12 constitutes a ''master curve'' (figure II.9) which describes every crack configuration independent from its crack-length. This master curve demonstrates that inside an ideally brittle medium, where Griffith's criterion is valid, every-sized crack configuration presents similar mechanical response upon loading. This ''mechanical homology'' of cracks inside elastic systems offer us the basis to study nano-sized cracks at atomistic scale using Griffith's mathematical formulation (Chapter V).

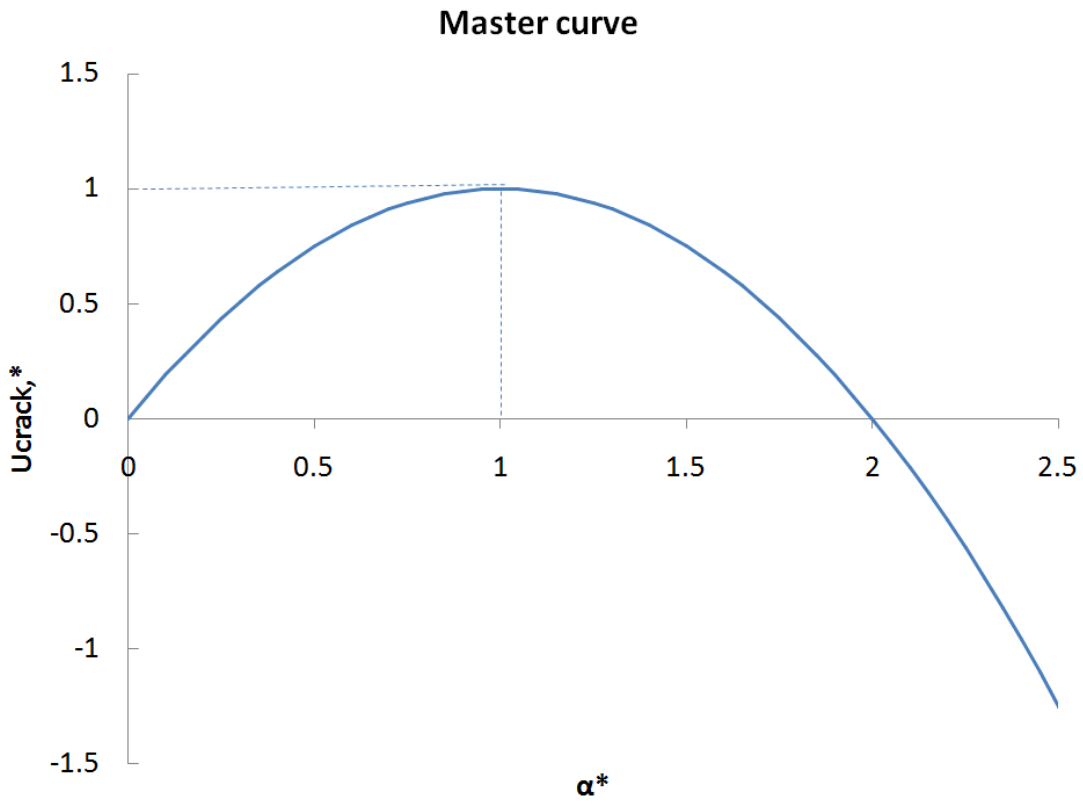

Figure II.9: The mechanical homology of cracks inside ideally elastic system.

2.4. Ductile-Brittle Transition: Models [ROB1996, HIR1997]

2.4.1. Nucleation-based models

Among the first efforts in understanding the ductile-brittle transition, Kelly [KEL1967, CHE1990] proposed that a crack-containing material can be classified as intrinsically brittle or ductile, depending on its mechanical response upon applied loading. In particular, if a

pre-existing crack is able to propagate upon loading along a crystallographic plane via brittle cleavage, the material is characterized as ''intrinsically brittle''. On the contrary, if a pre-existing crack prefers to accommodate the applied stress field through plastic deformation, including the formation and emission of dislocations or other shear-like processes, the material is classified as ''intrinsically ductile''. Based on this approach, Rice and Thomson [RIC1974] attempted to distinguish the intrinsic behaviour of materials by comparing the necessary load to propagate a crack with the load required for a dislocation emission from the crack-tip (figure II.10). Their idea gave rise to the construction of similar models focusing on the conditions for dislocation nucleation at the tip of a crack. These models are focusing on the ''nucleation-based'' interpretation of the ductile-brittle transition. This type of physical modelling has been further refined over the last decades by means of complex analytical treatments [RIC1992, SCH1996, XU1997] and atomistic simulations [RIC1994, PAN1998].

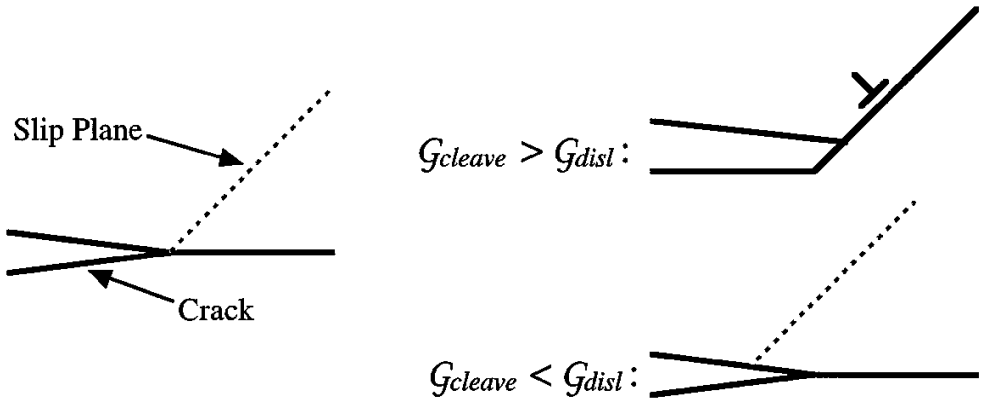

Figure II.10: A sharp crack with intersecting slip plane (left), showing the competition between dislocation emission (upper right) and cleavage de-cohesion (lower right). The G is the rate of decrease of the stored elastic energy in the system, due to the respective mechanism, and is proportional to the load required for its activation. [BEL1999].

The main limitation to achieve the complete description of the ductile-brittle transition through the use of the nucleation-based models, relies on the fact that they focus only on the conditions required for the emission of the first dislocation from the crack-tip. Such models hold a common implicit hypothesis, which states that once a dislocation is formed for the crack-tip, then, many others will nucleate. In this case, the crack will become either blunted or shielded thus cleavage will not occur. However, experimental observations have shown that brittle cleavage propagation of the crack can be performed in coexistence with the activity of dislocations [OHR1985, ZIE1992]. This is particularly clear in the case of the soft transitions, where below the T_{DBT} dislocation activity increases with the temperature.

2.4.2. **Mobility-based models** [HIR1989, HIR1996, ROB1996, HAR1997, GUM1998]

Another category of models developed to reproduce the ductile-brittle transition in materials is based on the nucleation of a dislocation at the crack-tip, as a dynamic mechanism controlled by the mobility of pre-existing dislocations at the crack-tip region. In general, dislocations have two different effects on the tip of a crack. The first (''blunting effect'') is the transformation of the crack-tip due to the nucleation mechanism, becoming blunt and thus reducing the stress concentration. The second (''shielding effect'') is that in presence of dislocations in the vicinity of the crack, the state of stress at the tip is altered thus the conditions for dislocation emission. The effective stress intensity at the crack tip is lowered, by both effects, for dislocations emitted from near-the-crack-tip sources. This process accelerates as the number of emitted dislocations increases due to its linear relation with temperature. To move on to the next step for the prediction of the ductile-brittle transition, a fracture criterion must be used, which is usually the fracture toughness provided by Griffith, corresponding to pure cleavage.

2.5. Ductile - Brittle transition: Atomistic simulations

Despite their physical significance, the existing analytic models of continuum mechanics lack of a convincing treatment of thermal and nonlinear stress effects in the vicinity of the crack tip. On the other hand, such local information is not available experimentally and therefore, the mechanical response of crack systems is difficult to be predicted. Moreover, existing continuum models do not take into consideration the discrete nature of the crystalline systems and hence, they are unable to reproduce experimentally observed phenomena (e.g. anisotropic cleavage [RIE1996]). Atomistic simulations, based on molecular statics and molecular dynamics, provide an opportunity to study the ductile-brittle behaviour of crystals by overcoming limitations of continuum mechanics. For example, unlike continuum elastic models, atomistic simulations avoid stress singularities that are associated with crack-tips [WES1939, SIH1968] and dislocation cores [HIR1982], since stress and strain fields are government by the lows of the inter-atomic interactions. Additionally, atomistic simulations allow the monitoring of dynamic processes that taking place close to the crack-tip and its neighbourhood. Characteristic examples are the formation of structural defects (e.g, dislocations, twins and stacking faults) and the crack-tip structural

evolution (e.g. blunting, atomic bonds de-cohesion) which constitute mechanisms of the accommodation of the applied stress. Moreover, atomistic simulations enable the validation and further development of failure criteria used in continuum models [BEL2004].

In the following paragraphs, the most salient contributions of atomistic studies on the attempt to understand the ductile-brittle behaviour of crystals are listed. Atomistic simulations (e.g. [KOH1991, SHA1996]) have shown that the ductile versus brittle response of cracks in single-crystal systems depends on the relative orientation of the crack plane and available slip systems. Specifically, for the active slip system in bcc iron $\langle 111 \rangle \{112\}$, three different shear processes may be observed at a crack tip under plane strain conditions [BEL2004, MAC2004]: (i) generation of extrinsic stacking faults, (ii) twinning formation, or (iii) emission of edge dislocations. In addition, molecular dynamic simulations in bcc iron [MAC1999] have shown that, for the crack orientation $(001)[110]$ (crack plane/crack front), the generation of unstable stacking faults and twinning at the crack tip are preferred to the $\langle 111 \rangle \{112\}$ slip systems, whereas, for the $(\underline{1}10)[110]$ crack orientation, emission of complete edge dislocations is observed on the same type of slip system [LAN2002]. This is explained by the orientation of the active shear systems $\langle 111 \rangle \{112\}$ ahead of the crack-tip along the easy twinning direction for the crack $(001)[110]$ [MAC2004] and along the hard (or ''anti-twinning'') direction for the crack $(\underline{1}10)[110]$ [BEL2004]. Atomistic results indicate that these different shear processes have different consequences for the stability of nano-cracks in bcc iron, in possible connection with the embrittlement of ferritic steels. For that reason, the topic has been studied in bcc iron both via continuum [CHA2002, WEE1997] and atomistic methods [MAC1999, LAN2002, BEL2004]. Dislocation emission on the $\langle 111 \rangle \{112\}$ type slip systems and stability of $(110)[110]$ cracks were studied by Beltz et al. [BEL2004]. Generation of unstable stacking faults and twinning on the same type of slip system and crystal orientation have been studied for $(001)[110]$ cracks by Machová et al. [MAC1999]. Therefore, it has been concluded that the crystallographic orientation of the crack within the crystal lattice is a significant parameter in understanding the brittle versus ductile behaviour of crystals.

Another important parameter for understanding the ductile-brittle behaviour of crystals is the crack blunting. Crack blunting influence on dislocation emission has dragged limited

attention [WEE1997, SCH1997, GUM1995]. Weertman described a mechanism of crack blunting by dislocation emission exhaustion [WEE1997]. Atomistic studies [SCH1997, GUM1995] agree on one major point: the ratio of crack advance versus dislocation emission changes as the crack tip blunts. G.E. Beltz et al. [BEL1999] showed that a crystal should not be classified as intrinsically ductile or brittle based on the emission of the first dislocation, but rather on the ongoing competition between crack propagation and subsequent dislocation nucleation as the crack-tip curvature evolves toward a steady state. Therefore, it has been concluded that the morphology of the crack-tip affects the mechanical response of the material system.

Finally, atomistic simulations reveal the existence of effects that are related with the discrete nature of the crystal systems at the atomic scale. The most important amongst all is the ''lattice trapping effect'' [THO1971, SIN1972, SIN1975, CUR1990]. This phenomenon describes the resistance of the crystalline lattice against both the healing and propagation of a pre-existing crack, which is initially in mechanical equilibrium. The lattice trapping effect transforms the unique and unstable equilibrium state of a crack configuration (§2.3) to a finite stability region, which is defined by the upper (crack propagation) and lower (crack healing) trapping stress-strain limits. Therefore, the mechanical stability of a crack is characterized by a range of stresses or strains which represents the barrier for triggering the propagation of a pre-existing crack.

Chapter III: Computational Methods and Details

3.1. Atomic crack models

3.1.1. Crystallographic orientation of the crack

The first step in the study of cracks at the atomic scale is the construction of the atomic model. Focusing on the intrinsic mechanical behaviour of pure aluminium and α-iron, we choose to simplify the investigation by not taking into account other micro-structural ingredients (i.e. dislocations, interfaces, grain boundaries, precipitates, etc.). This is also the approach found in the literature, i.e. the study of the mechanical response of a crystalline system which contains only a single crack [DEC1983, CHE1990, MAC1998, MAC2004, BEL2004, BEL2007]. Unlike continuum approaches, at the atomic scale matter is discrete and the arrangement of atoms in crystals is dictated by the symmetry and geometry of the lattice (Appendix H). Crystalline materials present directional dependence for both their structural and elastic properties, resulting to the anisotropic mechanical response under applied load. Hence, for a single-crystal containing a crack, the crystallographic orientation of the applied external load is decisive for its mechanical response, and the operated choice in aluminium and α-iron should be justified.

The fundamental process in the final failure of most engineering materials is the cleavage propagation of cracks. Hence, the resistance of the crystalline lattice to cleavage activation is crucial for evaluating the intrinsic mechanical behaviour of a solid. It is well established that crystals of different classes prefer to be cleaved along specific crystallographic planes [BEA1968]; hence, in order to appropriately simulate the resistance of aluminium and α-iron to fracture, the crack orientation of the respective atomic models should be chosen in consistency to these metals' primary cleavage planes. Experimental data demonstrate that the primary cleavage planes in bcc iron are of the type $\{100\}$ [ALL1956, HUL1958, HUL1963]. On the other hand, it is experimentally known that the pure fcc metals, like aluminium, are ductile systems and they do not have cleavage planes [BEA1968, MAS1980]. Hence, experimental data can only propose the appropriate crack plane for the models of α-iron, but not for aluminium. To select the appropriate crack plane for aluminium models we resort to the physical description of the cleavage phenomenon. Several criteria have been proposed in order to interpret the experimentally observed cleavage planes of crystal

systems [HUG1923, WOO1932, SHA1936, STE1949, GIL1959]. Among them, superior predictability is exhibited by the criterion developed by Gilman [GIL1959], which is able to correctly determine the primary cleavage planes in α-iron. For the case of the fcc crystals, Gilman's criterion predicts that if the cleavage phenomenon was possible it would be performed also along the $\{100\}$ planes. Hence, resistance to crack propagation for both fcc aluminium and bcc iron should be investigated through the construction of crack models with the crack plane being the $\{100\}$ crystallographic planes.

The ''intrinsic'' resistance of the crystalline lattice to the propagation of a crack is described by a phenomenon, known as the ''lattice trapping effect'' [THO1971, SIN1972, SIN1975, CUR1990]. According to this, a crack configuration can be stabilized in mechanical equilibrium within a finite range of applied deformation or load, the lattice trapping stress-strain barrier. In order to determine this barrier, the equilibrium crack configurations corresponding to the lattice trapping limits should be determined. The most convenient way to analytically describe [GRI1920] as well as to simulate an equilibrium crack inside a system is by using mode I deformation or load. In practice, this means that a tensile stress is applied on the system normal to the plane of the crack [WEE2008], as illustrated in figure III.1.

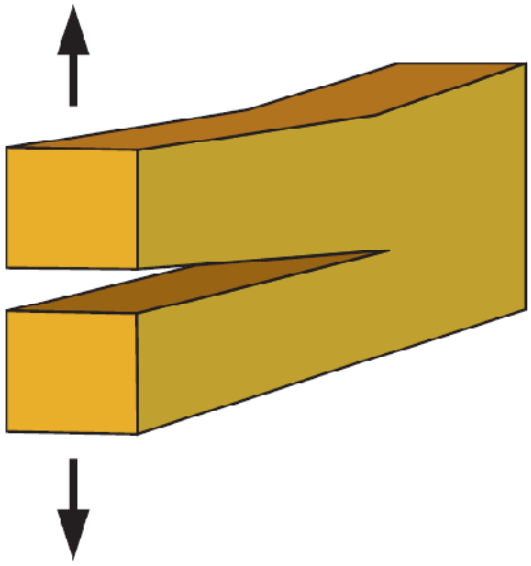

Figure III.1: Model I uni-axial loading.

Hence, mode I geometry of applied loading was selected for the crack models. For the above reasons, the present thesis focuses on the mechanical response of $(010)[001]$ mode I cracks (figure III.2), in both fcc aluminium and bcc iron, where:

(i) the crack surfaces coincide with (010) planes,

(ii) the crack front is oriented along the $[001]$ direction, and

(iii) the potential cleavage propagation (§3.5.3) of the crack is performed along the $[100]$ direction.

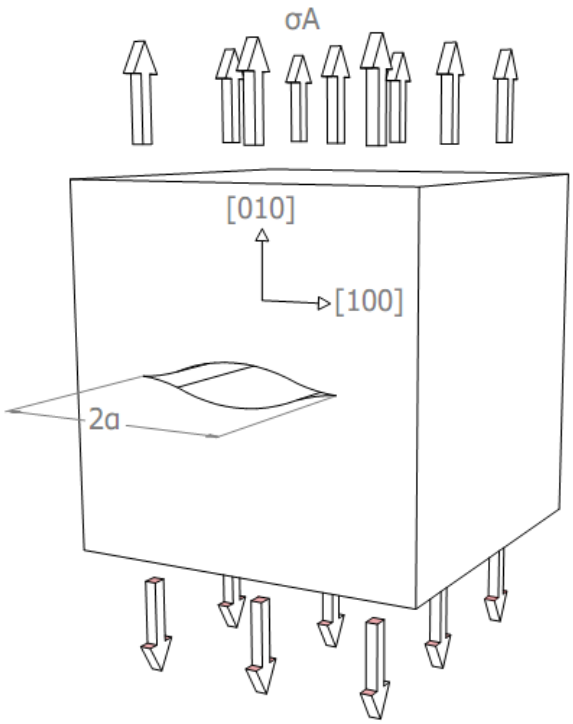

Figure III.2: Central Griffith's $(010)[001]$ crack configuration under mode I uni-axial plane strain loading condition. The Cartesian coordinate system of the system's representation coincides with the cubic crystallographic system, i.e. x is the $[100]$, y is the $[010]$ and z is the $[001]$ crystallographic direction.

3.1.2. Numerical models

Having defined the crack's crystallographic orientation and the direction of applied loading geometry, the setup of the atomic initial configuration proceeds in two steps. The first, is defining the atomic positions in the perfect crystalline lattice (Appendix H). Perfect crystal structures are oriented along the cubic axes (i.e. x is the $[100]$, y is the $[010]$ and z is the $[001]$ crystallographic direction) so that to comply with the crack crystallographic orientation. The second step is introducing the crack in the crystal by appropriately displacing atoms. The crack displacement field is determined as a function of the material's elastic properties and the external loading conditions. The present thesis follows the approach used in the majority of studies in the literature, which is the analytic determination of the crack displacement field by the use of the complex variable approach (CVA). The CVA, which is based on continuum linear elasticity (Appendix D), has two major advantages:

(1) it accounts for the elastic anisotropy of the studied system, and

(2) it allows the control of the main parameters defining the crack displacement field, i.e. the crack length and the applied loading conditions of the system.

The method allows for determining explicitly the crack displacement field with respect to its crystallographic orientation. The CVA is restricted to two-dimensional anisotropic elastic problems [SIH1968]; hence, the present thesis is focused on the $(010)[001]$ crack configurations under plane strain uni-axial loading conditions (figure III.2). According to the CVA (appendix D), the numerical solution of the crack displacement field requires calculating first the complex parameters, of this two-dimensional mechanical problem, which depend on both the material system and the crack orientation. To this end, the following procedure has been applied:

(1) Calculation of the elastic constants of stiffness, C_{11}, C_{12} and C_{44} referring to the cubic axes orientation and using the inter-atomic potentials (appendix B),

(2) Calculation of the elastic compliances, S_{11}, S_{12} and S_{44} of the same crystallographic orientation. These material parameters are determined by the following relations derived from anisotropic elasticity [KIT2004]:

$$S_{11} = \frac{C_{11} + C_{12}}{C_{11}^2 + C_{11}C_{12} - 2C_{12}^2} \qquad (III.1)$$

$$S_{12} = \frac{-C_{12}}{C_{11}^2 + C_{11}C_{12} - 2C_{12}^2} \qquad (III.2)$$

$$S_{44} = \frac{1}{C_{44}} \qquad (III.3)$$

(3) Calculation of the compliance coefficients, a_{ij}, corresponding to the applied deformation mode, according to the equations D.28.

(4) Solution of the governing differential equation (D.39) of the plane crack problem to determine the corresponding complex roots, μ_i.

The different quantities of this mathematical procedure are summarized in Table III.1.

Table III.1: Complex variable approach parameters for the $(010)[001]$ crack configuration under mode I plane-strain conditions in fcc aluminium and bcc iron.

Properties	**Aluminium**	**Iron**
$C_{11}[GPa]$	116.63	243.1
$C_{12}[GPa]$	61.028	137.5
$C_{44}[GPa]$	29.618	121.8
$S_{11}[GPa^{-1}]$	1.33895×10^{-2}	6.9565×10^{-3}
$S_{12}[GPa^{-1}]$	-4.59845×10^{-3}	-2.5132×10^{-3}
$S_{44}[GPa^{-1}]$	3.376325×10^{-2}	8.2102×10^{-3}
$a_{11}[GPa^{-1}]$	1.181×10^{-2}	6.04856×10^{-3}
$a_{12}[GPa^{-1}]$	-6.178×10^{-3}	-3.42113×10^{-3}
$a_{16}[GPa^{-1}]$	0	0
$a_{22}[GPa^{-1}]$	1.181×10^{-2}	6.04856×10^{-3}
$a_{26}[GPa^{-1}]$	0	0
$a_{66}[GPa^{-1}]$	3.376325×10^{-2}	8.2102×10^{-3}
Complex roots	$\mu_1 = 0.216 + i0.976$ $\mu_2 = -0.216 + i0.976$	$\mu_1 = 0.666 + i0.746$ $\mu_2 = -0.666 + i0.746$

The analysis reveals that the $(010)[001]$ crack geometry leads to complex parameters that belong to the case III orthotropic solution (Table D.1) for both material systems. As a result, the crack displacement field is given by the expressions D.53, where u_x and v_y are the displacements components along the $x = [100]$ and $y = [010]$ crystallographic direction, respectively. However, as presented in Appendix D, the displacement field (u_x and v_y) provided by the CVA contain rigid body terms that should be eliminated in order to obtain the correct form of the crack. The rigid body terms can be determined by the general expressions of displacements provided by Savin [SAV1961]. According to his analysis the rigid body terms of u_x and v_y components are equal to:

$$u_x^{RBT} = a_0 - \gamma_0 y \qquad (III.4a)$$

$$v_y^{RBT} = \beta_0 + \gamma_0 x \qquad (III.4b)$$

where a_0, β_0, γ_0 are arbitrary real constants and x, y are the atomic position coordinates of the perfect system. In particular, the constants a_0 and β_0 correspond to rigid body translation terms and can be calculated through the translation of the system's mass center, when the displacement field formulas (Eqs. D.53) are applied on the perfect crystal system. Hence,

$$a_0 = \frac{1}{N}\left(\sum_{i=1}^{N} x_i^{'} - \sum_{i=1}^{N} x_i\right) = \frac{1}{N}\left(\sum_{i=1}^{N}(x_i + u_{xi}) - \sum_{i=1}^{N} x_i\right) = \frac{1}{N}\sum_{i=1}^{N} u_{xi} \qquad (III.5a)$$

$$\beta_0 = \frac{1}{N}\left(\sum_{i=1}^{N} y_i^{'} - \sum_{i=1}^{N} y_i\right) = \frac{1}{N}\left(\sum_{i=1}^{N}(y_i + v_{yi}) - \sum_{i=1}^{N} y_i\right) = \frac{1}{N}\sum_{i=1}^{N} v_{yi} \qquad (III.5b)$$

where x_i, y_i and $x_i^{'}$, $y_i^{'}$ are the atomic position coordinates before and after applying the displacement components u_{xi} and v_{yi} into the perfect N-atom crystalline systems. In addition, the constant γ_0 corresponds to a rigid body rotation around the z-axis (i.e. the $[001]$ crystallographic direction), and can be determined by the equation:

$$\gamma_0 = \omega_z = \frac{1}{2}\left(\frac{\partial u}{\partial y} - \frac{\partial v}{\partial x}\right) \qquad (III.6)$$

The partial derivatives of the displacement components can be calculated from the x_i, y_i and $x_i^{'}$, $y_i^{'}$ atomic coordinates of representative positions in the system ($i = P$, $R1$ and $R2$), which are based on the schematic representation of figure III.3, through the following set of equations,

$$\Delta x = |x_P - x_{R1}| \qquad (III.7a)$$

$$\Delta y = |x_P - x_{R2}| \qquad (III.7b)$$

$$u = x_{P'} - x_P \qquad (III.7c)$$

$$v = y_{P'} - y_P \qquad (III.7d)$$

$$u + \frac{\partial u}{\partial x}\Delta x = x_{R1'} - x_{R1} \qquad (III.7e)$$

$$u + \frac{\partial u}{\partial y}\Delta y = x_{R2'} - x_{R2} \qquad (III.7f)$$

$$v + \frac{\partial v}{\partial x}\Delta x = y_{R1'} - y_{R1} \qquad (III.7g)$$

$$v + \frac{\partial v}{\partial y}\Delta y = y_{R2'} - y_{R2} \qquad (III.7h)$$

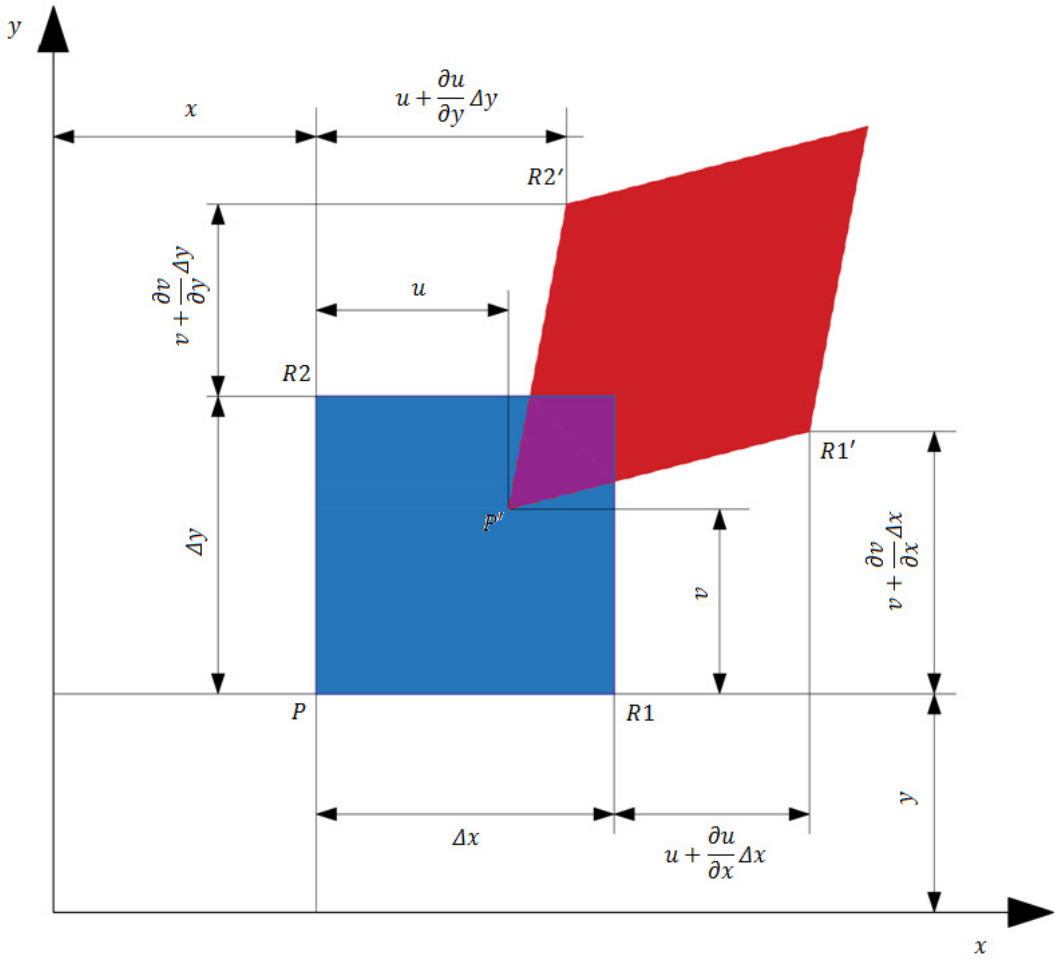

Figure III.3: Rigid body rotation calculation of an initially perfect system (blue rectangular) after its homogeneous deformation (red parallelogram).

The mathematical points P, $R1$ and $R2$, being under study, were chosen to be located far from the centre of the crack (Appendix F). The stress functions (Eqs. D.73) used for determining the crack displacement field can describe the entire contour of the crack configuration, an approach known as the ''central crack'' or ''entire crack'' field. This approach is different compared to the ''crack-tip field' followed in the majority of atomistic studies [DEC1983, CHE1990, MAC1998, MAC2004, BEL2004, BEL2007], which can provide only a part of the contour of the crack. The reason for this decision is explained in the §3.3.2. Moreover, the stress functions (Eqs. D.73) allow the determination of the crack displacement field by controlling the **crack length** magnitude, a, along the $[100]$ direction as well as the **applied mode I tension**, σ_A, along the $[010]$ direction. Part of this work focused on the development of the appropriate codes, capable of creating the numerical models of $(010)[001]$ crack configurations under mode I plane strain conditions, in both fcc aluminum and bcc iron. These programs, are given in Appendix F, and allow setting the a

and the σ_A for obtaining the atomic model of the crack as output. Examples of such atomic models for the two material systems are illustrated in figures III.4.

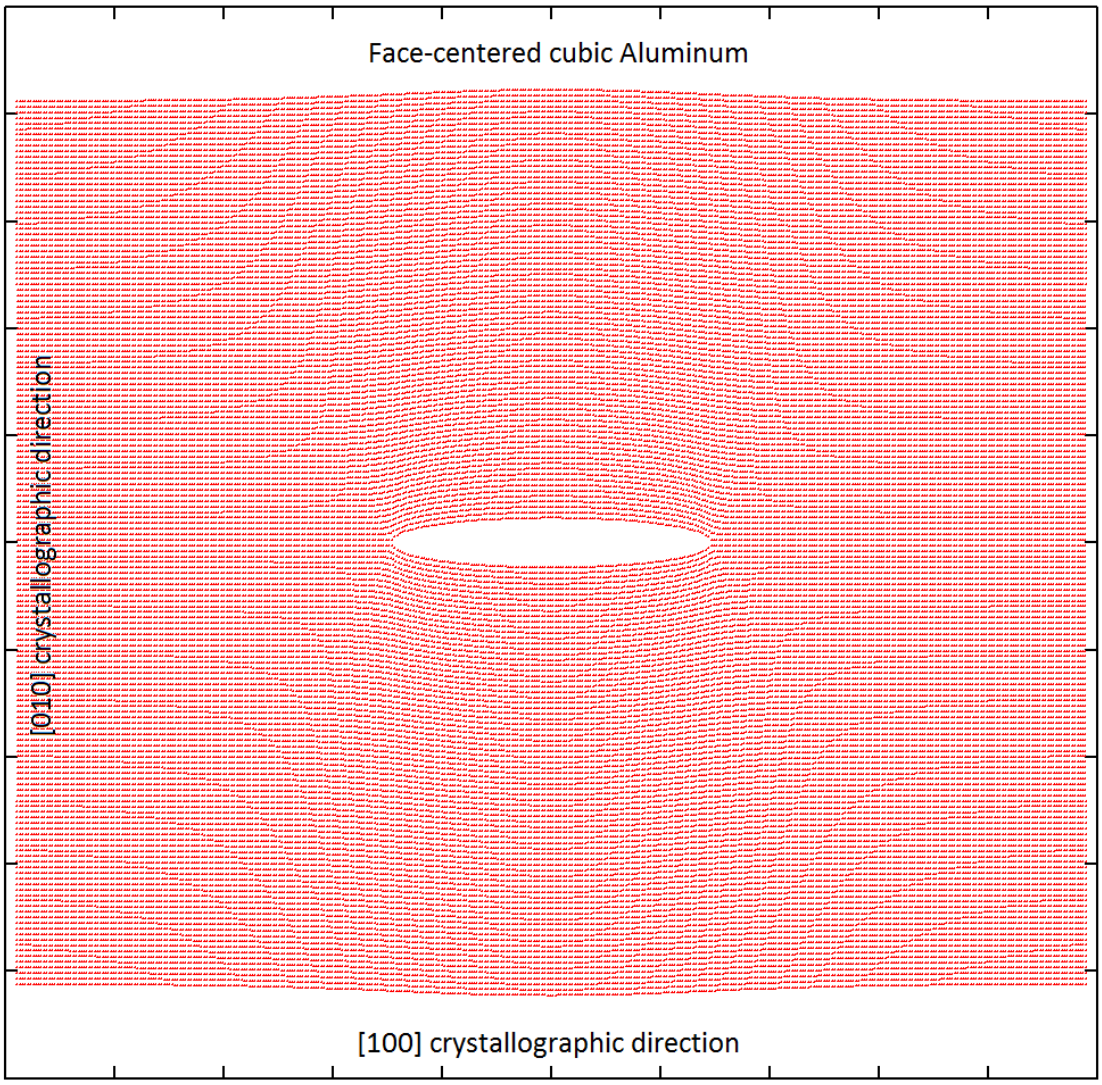

Figure III.4a: Model of a $(010)[001]$ central crack under mode I loading conditions in fcc lattice of aluminum. The system is subjected to a 3GPa tension along the $[010]$ direction and the crack length is equal to 60 lattice parameters.

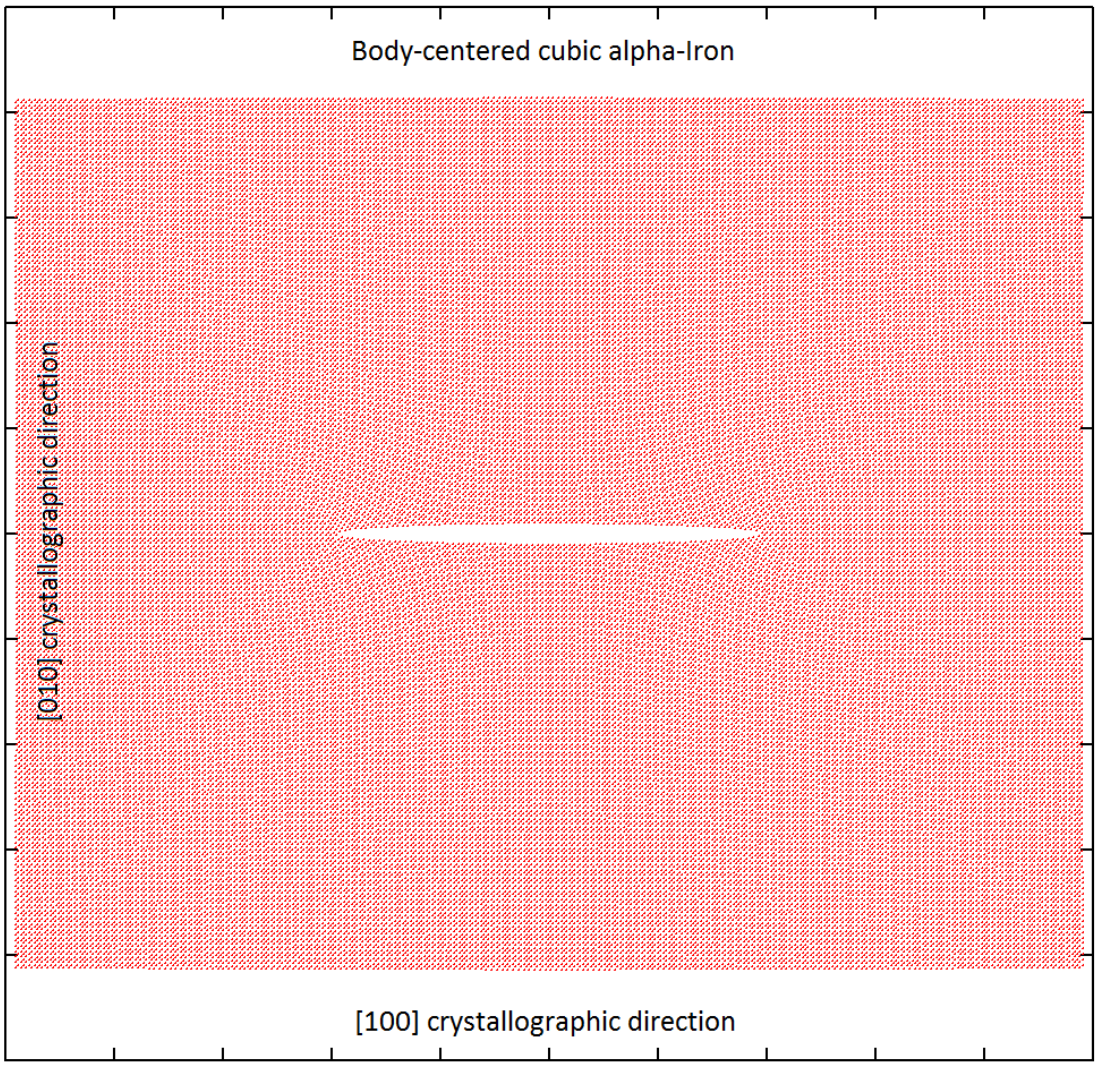

Figure III.4b: Model of a $(010)[001]$ central crack under mode I loading conditions in bcc lattice of alpha iron. The system is subjected to a 5GPa tension along the $[010]$ direction and the crack length is equal to 80 lattice parameters.

3.2. Inter-atomic potentials

The second step in our atomistic study is the appropriate description of the cohesion of the metals under study; the fcc aluminium and bcc iron crystalline systems at the atomic scale. In classical atomistic simulations (Molecular Statics and Dynamics, Monte-Carlo), the rules that govern the interaction of atoms in an atomic system are determined through the use of analytic functions, the inter-atomic potentials. A potential function, U, described how the potential energy of an N-body classical system depends on the atomic coordinates $\vec{r}_1, \vec{r}_2, \dots, \vec{r}_N$:

$$U = U(\vec{r}_1, \vec{r}_2, \dots, \vec{r}_N), (i = 1, \dots, N) \qquad (III.8)$$

This expression is based on the Born-Oppenheimer approximation [BOR1927], which states that the motion of atomic nuclei and electrons in an atom can be separated and allows the incorporation of all electronic effects in U. Based on equation III.8, the atomic system is conservative [YOU1999], thus the force acting on each atom is given by the relation:

$$\vec{F}_i(\vec{r}_1, \dots, \vec{r}_N) = -\vec{\nabla}_i U(\vec{r}_1, \dots, \vec{r}_N), (i = 1, \dots, N) \qquad (III.9)$$

where ∇_i is the derivative operation for each atom i:

$$\vec{\nabla}_i \equiv \frac{\partial}{\partial \vec{r}_i} = \frac{\partial}{\partial x_i}\vec{\imath} + \frac{\partial}{\partial y_i}\vec{\jmath} + \frac{\partial}{\partial z_i}\vec{k} \qquad (III.10)$$

The potential model expresses the different types of interactions between atoms in the system which are mainly based on the number of participant atoms in each type of interaction. As a result, the total potential energy is determined by a linear superposition of terms that depend on individual atoms, two atoms, three atoms or more atoms. To obtain the inter-atomic potential of a particular material atomic system, several mathematical functions and/or functionals can be developed using phenomenological approaches. The unknown parameters of these functionals are fit to various fundamental state properties, experimentally determined and/or calculated from first-principle methods. This constitutes a developing process aiming the construction of analytic schemes that are capable to model the energetics, static states and dynamic properties of the system of interest. In general, the effectiveness of an inter-atomic potential is indicated by the following properties [BRE2000]:

(a) Flexibility: The potential function should be flexible in terms of accommodating a wide range of fitting database in order to incorporate as many physical properties and characteristics of the system as possible.

(b) Accuracy: The potential function must be able to calculate an appropriate set of fitting data with sufficient accuracy in order to correctly reproduce the corresponding properties of the system of interest.

(c) Transferability: It is also crucial for the potential model to reproduce properties of the system that are not included in its fitting set of data. The reproduction of such properties should be at least qualitative, if not with quantitative accuracy, leading to a more comprehensive description of the system.

(d) Computational efficiency: Computational cost is another important factor for the efficiency of the potential models. The analytic functions should be developed in such a way that optimize the simulation time in respect to the system sizes, the time scale of interest and the available computing resources.

In the following paragraphs, the atomic interaction models for the pure single-crystalline fcc aluminium [ZAC2017] and the bcc alpha iron [PON2007] used in our work are presented in detail.

3.2.1. Face-centered cubic aluminium

An analytic N-body inter-atomic potential for face-centered cubic (fcc) aluminium, which was phenomenologically developed on earlier studies [ASL1998a, ASL1998b, ASL2000], has been recently optimized [ZAC2017]. The potential energy of this semi-empirical model is made of three contributions:

(i) a repulsive Born-Mayer pair-wise functional (U^r),

(ii) an attractive N-body cohesive functional, like those derived from within the second-moment approximation in tight-binding theory for transition metals, (U^a), and,

(iii) a long-ranged oscillatory pair-wise functional accounting for the screened ion-ion Friedel interactions in simple metals (U^o).

More specifically, the total energy of a solid crystalline aluminium system of N interacting atoms can be obtained by summing all the atomic contributions:

$$U_{Al}^{total} = \sum_{i=1}^{N} U_i \qquad (III.11)$$

where, U_i, the potential energy of an atom i is given by the expression:

$$U_i = U_i^r + U_i^a + U_i^o \qquad (III.12a)$$

or

$$U_i = \sum_{j \neq i}^{N} \Phi_r(r_{ij}) - \sqrt{\sum_{j \neq i}^{N} \Phi_a(r_{ij})} + \sum_{j \neq i}^{N} \Phi_o(r_{ij})$$

$$U_i = \sum_{j \neq i}^{N} A\, exp\left[-p\left(\frac{r_{ij}}{r_0} - 1\right)\right] - \left\{\sum_{j \neq i}^{N} \xi^2\, exp\left[-2q\left(\frac{r_{ij}}{r_0} - 1\right)\right]\right\}^{1/2} + \sum_{j \neq i}^{N} \left(\frac{C_1 cos(2k_F r_{ij})}{(r_{ij}/r_0)^3} + \frac{S_1 sin(2k_F r_{ij})}{(r_{ij}/r_0)^4} + \frac{C_2 cos(2k_F r_{ij})}{(r_{ij}/r_0)^5}\right) \qquad (III.12b)$$

This scheme is central since the potential energy depends solely on the Euclidean distance $r_{ij} = |\vec{r}_i - \vec{r}_j|$ between the atom i and each j-neighbouring atom. Moreover, inside the equation III.12, the $r_0 = a_0/\sqrt{2}$ is the first-neighbour distance, with a_0 the lattice parameter of the Bravais fcc aluminium lattice, and k_F is the modulus of the Fermi wave-vector of aluminium at $T = 0K$,

$$k_F = \left(\frac{3\pi^2 N}{V}\right)^{\frac{1}{3}} = (3\pi^2 n_e)^{\frac{1}{3}} \approx 1.127[2\pi/a_0] \qquad (III.13)$$

where $n_e = 12/a_0^3$, is the number of free electrons per unit cell volume. The N-body character of the potential can be revealed through the resulting analytic expression of the force (Appendix G). The adjustable parameters of the model A, p, ξ, q, C_1, S_1 and C_2 have been determined by a least-squares fit to experimental properties extrapolated at $T = 0K$ using MERLIN [EVA1987], a multi-dimensional minimization package. The restricted set of these bulk quantities includes:

- the lattice parameter a_0 [SIM1971],
- the shear elastic constants $C' = (C_{11} - C_{12})/2$ and C_{44} [SIM1971],
- the bulk modulus B [SIM1971],
- the cohesive energy E_c [KIT1976],
- the vacancy formation energy E_v^f [POP1974, GIL1989, SIM1960, TRI1975, FLU1978], and

- the intrinsic stacking-fault energy γ_I [HAM1992, SMA1970, MUR1975, PÉS1979, MIL1989].

Table III.2 presents the optimal values of the potential's adjustable parameters resulting from the fitting procedure. The experimental physical properties used to fit the potential's analytic function along with their calculated values are listed in Table III.3. Table III.3 also presents additional experimental and calculated fundamental state properties in order to evaluate the transferability of the atomic model. The potential predicts satisfactory structural, energetic and defect properties of the solid crystal fcc aluminium. Concerning the crack problem, since the elastic constants are adjusted to the experimental values (calculations in appendices B and C), the model is capable to correctly evaluate the elastic energy of the strain crack field. Moreover, the surface excess energies, $\gamma_{(hkl)}$, derived by the atomic model, are in agreement with the experimental data; hence, the effects of the crack surface energy can be reliably simulated in both static and dynamic conditions. Therefore, the present inter-atomic potential is reasonably well adapted to study the mechanical response of nano-sized crack configurations in single-crystalline fcc aluminium at the atomic scale.

Table III.2: Parameters of the inter-atomic potential of fcc aluminium. The cut-off radius of inter-atomic interactions, r_c, is expressed in units of the equilibrium lattice constants used in the fitting procedure, $a_0 = 4.02\text{Å}$.

Adjustable parameters (units)	**Values**
$A\ (eV \cdot atom^{-1})$	0.178
$\xi\ (eV \cdot atom^{-1})$	1.3831
$C_1\ (eV \cdot atom^{-1})$	9.473×10^{-3}
$S_1\ (eV \cdot atom^{-1})$	5.149×10^{-3}
$C_2\ (eV \cdot atom^{-1})$	1.664×10^{-2}
$p\ (-)$	6.50
$q\ (-)$	2.07
$r_c/a_0\ (-)$ (10^{th}-neighbour distance)	2.291
$m\ (u)$	26.982

Table III.3: Comparison between the potential calculations and experimental fcc aluminium properties at $T = 0K$. Shaded part of the table summarizes the data entered in the fitting procedure. Values between parentheses are results of previous calculations found in the literature.

Quantity (units)	Potential Calculations	Experimental Data
a_0 (Å)	4.02	4.03[SIM1971]
C' $(10^2 GPa)$	0.278	0.23-0.26 [SIM1971]
C_{44} $(10^2 GPa)$	0.296	0.28-0.32 [SIM1971]
B $(10^2 GPa)$	0.796	0.79-0.82 [SIM1971]
E_c (eV)	3.336	3.339 [KIT1976]
E_v^f $(eV\ at\ cm^{-1})$	0.73 (unrelaxed) 0.69 (relaxed) (0.6-0.86 [POP1974]/ 0.56 [GIL1989])	- 0.76 [SIM1960]/ 0.66±0.01[TRI1975, FLU1978]
γ_I	136(156[HAM1992])	135-166 [SMA1970, MUR1975, PÉS1979, MIL1989]
$E_{bcc} - E_{fcc}(eV)$	-0.112	-
$E_{hcp} - E_{fcc}(eV)$	0.0034(0.037[HAM1992])	-
$\gamma_{(100)}$ (mJ/m^2)	790(1081[BOH1988])	1169[WAW1975] – 1180 [TYS1977a]
$\gamma_{(110)}$ (mJ/m^2)	857(913[NEE1987],1090[HO1985])	
$\gamma_{(111)}$ (mJ/m^2)	766(704[NEE1987],939[SCH1995])	

3.2.2. Body-centered cubic iron

An analytic N-body phenomenological potential developed by V. Pontikis [PON2007] is used to describe the inter-atomic interactions in body-centered cubic (bcc) iron. In this model, the description of the repulsive and attractive contribution to energy is made of by two electron-density functionals. In particular, the repulsive part (U^r) is represented by a Thomas-Fermi free-electron gas functional of the electronic density of $4s$ valence electrons. In addition, the attractive part (U^a) is described by a square root functional, similar to the second-moment approximation of the tight-binding scheme, applying to the electronic density of $3d$ valence electrons in iron. The total energy of a N-atom crystalline system is derived by summing the atomic energy contributions:

$$U_{\alpha-Fe}^{total} = \sum_{i}^{N} U_i \qquad (III.14)$$

where the potential energy of each atom i , U_i, is expressed as:

$$U_i = U_i^r + U_i^a \qquad (III.15a)$$

or

$$U_i = A\left(\sum_{j\neq i}^{N}\rho_{4s}(r_{ij})\right)^{5/3} - \xi\left(\sum_{j\neq i}^{N}\rho_{3d}(r_{ij})\right)^{1/2} \qquad (III.15b)$$

Alike the potential for aluminium [ZAC2017], this potential is also central. The electronic-densities corresponding to the $4s$ and $3d$ valance electrons are given by:

$$\rho_{4s}(r_{ij}) = \left[\Psi_{4s}(r_{ij})\right]^2 \qquad (III.16a)$$

$$\rho_{3d}(r_{ij}) = \left[\Psi_{3d}(r_{ij})\right]^2 \qquad (III.16b)$$

where $\Psi(r)$ are hydrogen-like radial wave functions expressed by:

$$\Psi_{4s}(r) = \frac{1}{96}\left(24 - 18Z_{4s}^{*}r + 3(Z_{4s}^{*}r)^2 - \left(\frac{Z_{4s}^{*}r}{2}\right)^3\right)exp\left(-\frac{Z_{4s}^{*}r}{4}\right) \qquad (III.17a)$$

$$\Psi_{3d}(r) = \frac{1}{9\sqrt{30}}\left(\frac{2Z_{3d}^{*}r}{3}\right)^2 exp\left(-\frac{Z_{3d}^{*}r}{3}\right) \qquad (III.17b)$$

with r the inter-atomic distances expressed in atomic parameters and A, ξ and the effective charges Z_{4s}^{*} and Z_{3d}^{*} being adjustable parameters of the model. Moreover, in order for the model to appropriately describe the short-range interactions exhibiting in transition metals, the range of the electronic densities, ρ_{4s} and ρ_{3d}, is modified by the use of a Fermi-Dirac step function:

$$f(r, r_c, \varepsilon) = \frac{1}{1 + exp\left[\varepsilon\left(\frac{r}{r_c} - 1\right)\right]} \qquad (III.18)$$

acting as a multiplicative factor. Consequently, the analytic model has totally six adjustable parameters, which are fitted to a selected set of experimental properties extrapolated at $T = 0K$, such as:

- the lattice constant a_0 [SIM1971, BAS1955],
- the shear elastic constants $C' = (C_{11} - C_{12})/2$ and C_{44} [SIM1971],
- the bulk modulus B [SIM1971],
- the cohesive energy E_c [KIT1976], and

- the vacancy formation energy E_v^f [SCH1983]

Table III.4 lists the optimal numerical values of the potential parameters resulting from the adjustment made by the use of MERLIN minimization code [EVA1987]. Additionally, the Table III.5 presents the calculated properties in comparison with their experimental counterparts, which are used to the fitting procedure, along with Ab-Initio data from the literature. Despite the restricted set of the model's adjustable parameters, the Table III.5 validates a remarkable good agreement between calculated and experimental values for all ground state properties at $T = 0K$. According to V. Pontikis [PON2007], the model has been additionally tested by computing the temperature dependence of both the lattice constant (figure III.5) and the mean square displacements (figure III.6). The results indicate that the potential is capable to describe the temperature effects on the crystal structure; hence, the model is well adapted to study the mechanical response of cracks under different temperature conditions. Moreover, the correct prediction of both elastic constants and surface excess energies provide the necessary factors to appropriately simulate the crack configuration energetics and mechanical state.

Table III.4: Parameters of the inter-atomic potential of bcc iron. The cut-off radius of inter-atomic interactions, r_c, is expressed in units of the equilibrium lattice constant at $T = 0K$, $a_0 = 2.86\text{Å}$, whereas the effective charges , Z_{4s}^* and Z_{3d}^* are in elementary charge units.

Adjustable parameters (units)	**Values**
$A\ (eV \cdot atom^{-1})$	1011
$\xi\ (eV \cdot atom^{-1})$	147.9
Z_{4s}^*	3.15
Z_{3d}^*	0.507
ε	15.4712
$r_c/a_0\ (-)$	1.0351
$m\ (u)$	55.847

Table III.5: Ground state properties of the bcc iron at $T = 0K$, calculated by the inter-atomic potential function. The comparison is made with experimental values extrapolated at $T = 0K$ and data of Ab-Initio calculations found in the literature. The shaded part of the table summarizes data enter in the fitting procedure.

Quantity (units)	Potential Calculations	Experimental Data	Ab-Initio Calculations
$\alpha_0(nm)$	0.286	0.286[SIM1971, BAS1955]	0.283[WAL2005]
$B(GPa)$	172.7	173.1[SIM1971]	-
$C'(GPa)$	52.8	52.5[SIM1971]	-
$C_{44}(GPa)$	121.8	121.8[SIM1971]	-
$E_{coh}(eV)$	4.289	4.28[KIT1976]	-
$E_f^v(eV)$	1.78 (relaxed value)	2±0.2[SCH1983]	2.12 [WAL2005]
$E_{fcc} - E_{bcc}(eV)$	0.03	0.05[BEN1982]	0.09 [WAL2005]
$E^f_{\langle 110\rangle}$	5.83 (relaxed value)	3.0-12.0[MOS1966, BIL1968]	3.4 – 4.0 [WAL2005, FU2004, DOM2001]
$E^f_{\langle 110\rangle} - E^f_{\langle 111\rangle}$	-0.11	-	-0.7, -0.67 [WAL2005, FU2004, DOM2001]
$\gamma_{(100)}\ (mJ/m^2)$	1868	2410[TYS1977a]	-

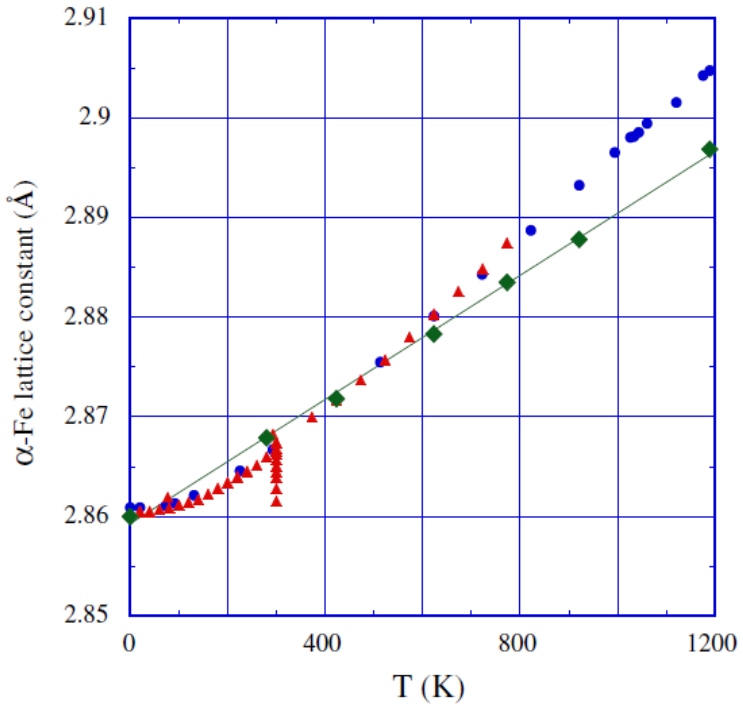

Figure III.5: Equilibrium lattice parameter in respect to the temperature. Experimental data are denoted with full blue circles and red triangles [SIM1971,BAS1955] whereas atomistic results presented with full green diamonds (from [PON2007]).

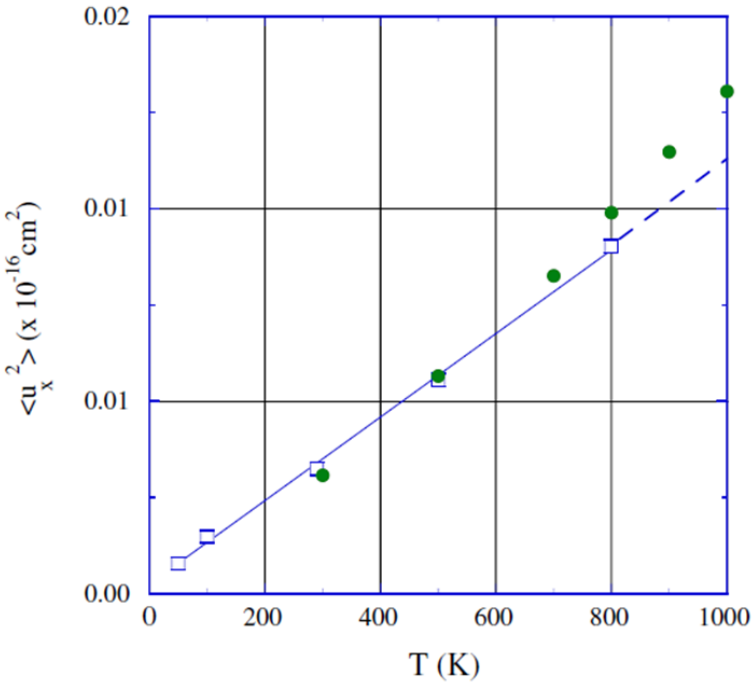

Figure III.6: Atomic mean square displacements as a function of temperature. Experimental data are denoted with open blue squares and red triangles whereas atomistic results correspond to the full green circles (from [PON2007]).

3.3. Boundary conditions

Most atomistic studies [DEC1983, CHE1990, MAC1998, MAC2004, BEL2004, BEL2007] are applied to systems with several thousand up to few hundred thousand of atoms (our models $N = 384000$ atoms, Appendix H). These numbers of atoms are not large enough to form bulk systems ($N \sim 10^{23}$ atoms) but only atomic clusters. The atomic systems are enclosed in a simulation box of which the form and shape are strongly related to their characteristics (e.g. crystallography, geometry, etc). The most common form of the simulation box is the rectangular parallelepiped with sides lengths of L_x, L_y, and L_z along the three perpendicular directions and a total volume equal to $V = L_x L_y L_z$. In such small-sized systems, a non-negligible number of atoms is located at or near the surfaces of the atomic model or the simulation box [HAI1997, RAP2004]. Such atoms are subjected to force fields different from those of atoms in the bulk state, a fact that affects significantly the properties of the atomic model. In order to simulate an atomic model as a part of a bulk system, appropriate boundary conditions are implemented on its edges or at the limits of the simulation box, aiming at eliminating surface effects. At the same time, the boundary conditions are set such that it mimic the way the surrounding bulk system affects the atomic model, including the

application of mechanical loading, pressure, etc. This is of great importance for investigating the mechanical response of cracks, since both their stabilization and propagation requires the implementation of external applied stress-strain fields (Appendix D). For these reasons, the proper selection of the boundary conditions of the atomic crack models is the third basic technical step of the present study.

3.3.1. Loading approach

In order to select the appropriate set of boundary conditions, it is first necessary to determine the type of the desired loading conditions to be applied on the atomic crack configurations. It is experimentally known that the fracture of real materials is a dynamic phenomenon tightly associated with the propagation of cracks. For this reason, the vast majority of atomistic studies on crack-containing systems focuses on the dynamic propagation of the crack configurations under applied loading [DEC1983, CHE1990, MAC1998, MAC2004, BEL2004, CAO2006, BEL2007]. According to this approach, the mechanical behaviour of the systems at the atomic scale can be determined through the evaluation of the mechanisms of dynamic structural evolution of the crack-tip. Despite its popularity, this ''dynamic propagation approach'' (DPA) is characterized by the following fundamental weaknesses:

(1) The dynamic response of a crack configuration in these studies is investigated through the implementation of dynamic or quasi-static loading conditions and aims to model the experimental mechanical conditions [GUO2003, NIS2004]. However, the dynamic structural evolution of the crack-tip during simulation significantly affects the stress field within the atomic model. Hence, the crack configuration inevitably experiences dynamic loading, which cannot be realistic due to time and space scale limitations.

(2) Since dynamic cracks push the system outside the thermodynamic regime they do not allow the calculation of thermodynamic properties. This inability prevents to quantitatively study the phenomenon of crack propagation, thus limiting it only to a qualitative description.

The aim of the present thesis is to calculate, quantitatively, the stress-strain barrier required to trigger the propagation of a pre-existing equilibrium crack. Based on the aforementioned, the DPA is undoubtedly incapable to provide this result. To achieve this objective, we propose a novel method in studying the mechanical response of cracks, called the ''quasi-static propagation approach'' (QPA). According to the QPA, the triggering process for the propagation of a crack inside a crystal is described as a series of successive states of all the possible equilibrium configurations of the crack under static load, which corresponds to a gradual increase of the applied load. This sequence of equilibrium states approximates the loading process of the crack-containing system until the mechanic instability limit (propagation or healing). Hence, the equilibrium configurations corresponding to the lowest and highest static loading conditions define the limits of the stability region of the crack under increasing load, that is the stress-strain barrier below/above which the dynamic response occurs. The QPA allows the quantitative determination of the stress-strain limits of this barrier, since the corresponding equilibrium crack configurations belong to a constrained thermodynamic regime. In conclusion, by following QPA in the present thesis, the application of constant-static loading conditions on the atomic crack models is required.

3.3.2. Modelling approach

Having decided the loading approach to be followed, the next step is to achieve its technical-wise implementation. As demonstrated in Appendix D, the analytic solution of the crack displacement field, provided by CVA, corresponds to the application of static mode I loading conditions on the system. Hence, the atomic model incorporates *a priori* the effect of a specific macroscopically applied stress field on the nano-sized crack configuration. Based on this, the technical implementation of a constant-static load on the atomic configuration of the crack can be achieved by the use of a mixed type of boundary conditions (MTBC):

(1) Here we set the atomic positions fixed at the $x = [100]$, $\bar{x} = [\bar{1}00]$, $y = [010]$ and $\bar{y} = [0\bar{1}0]$ limits of the atomic model, according to the analytic solution of the crack displacement field [SAV1961, LIM2001].

(2) In addition, its two-dimensional form allows the implementation of periodic boundary conditions [ALL1987] along the direction of the plane-strain

mode ($\varepsilon_{zz} = \varepsilon_{zx} = \varepsilon_{zy} = 0$). As a result, the crack model is of pseudo-infinite length along the direction of the crack front, i.e. the $z = [001]$ crystallographic direction.

This approach of boundaries is commonly used [GUO2006, GUO2007a, GUO2007b] because it is capable of reproducing the 2D heterogeneous stress fields characterizing structural defects at the atomic scale. Projecting the atomic system along the $xy = (001)$ crystallographic plane (figure III.7), it can be observed that the model is divided into two regions: the ''inner atomic region'' of interest and its ''outer-shell fixed atomic region'' with rectangular-like form.

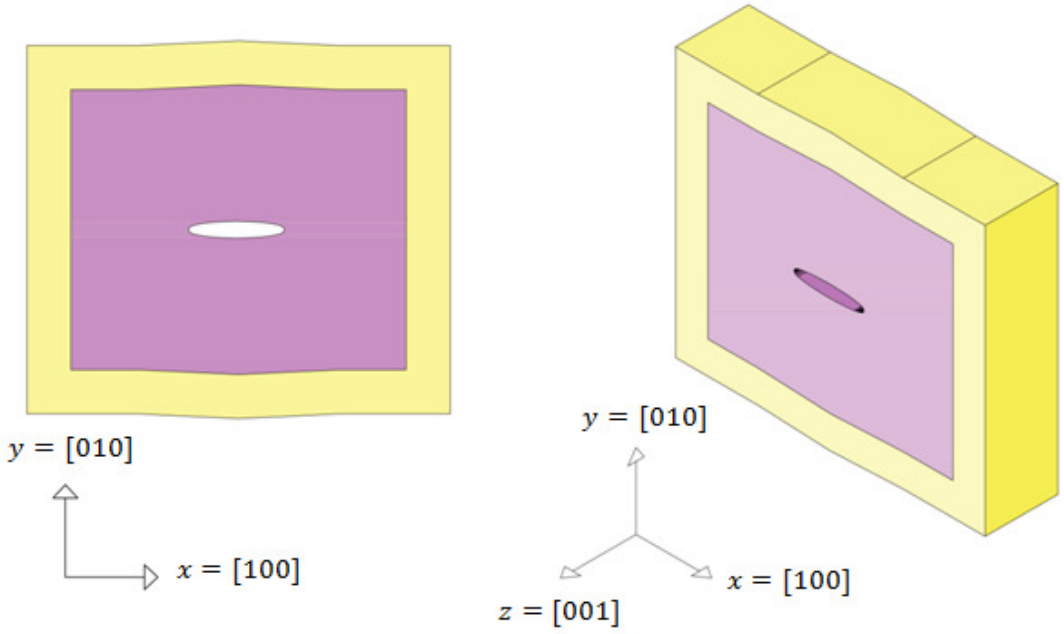

Figure III.7: Mixed type of boundary conditions of the atomic crack model. The fixed-displacement region is presented with yellow while the free region with pink color. In addition, the periodic boundary conditions are applied along the $z = [001]$ crystallographic direction.

Now, according to the CVA, the crack displacement field is additionally depended on the crack length size, a. Hence, MTBC approach is valid only for equilibrium cracks (a=constant), given that any change of a requires the change of the elastic field at the boundary conditions of the model in order to maintain a constant applied load on the system. This proves the need for employing a simulation technique capable to examine if the atomic models constructed with the CVA are mechanically stable. Such investigation can be achieved via structural relaxation of the atomic model according to both the MTBC effect and the laws govern the inter-atomic interactions. In this process, a crucial parameter is the position of

the ''fixed atomic region'' in respect to the crack configuration. It is well established [GUO2006] that the crack displacement field, determined by the CVA, cannot appropriately describe the crack-tip region since the associated analytic solution of the stress field at the crack-tip singularity diverges [SIH1968]. In addition, the derived displacement field is based on the continuum description of the system and hence it is lacking to integrate the effect of the discrete nature of the crystalline lattice. Thus, in order to obtain the correct atomic configuration of the crack-tip region and close to the crack faces (i.e. the near-crack displacement field), structural relaxation of the crystal model is, again, required. Nonetheless, it has been proven that the range of atomic relaxations from the crack-tip position for equilibrium configurations is atomistic [GUO2006], hence the far-crack displacement field can be appropriately described by the CVA. Therefore, in order to achieve a reliable structural relaxation of the crack atomic configuration, the ''fixed atomic region'' should be located at a sufficient distance from the crack-tips and the crack faces. A significant difference of the present work, compared to most studies in literature [DEC1983, CHE1990, MAC1998, MAC2004, BEL2004, CAO2006, BEL2007], is the fact that the atomic model contains the entire contour of the crack and not only a part of it (e.g. the half crack configuration or the crack-tip region). With this ''central crack'' approach, the ''fixed atomic region'' does not intersect with the crack faces and hence allowing them to move and evolve during structural relaxation process (figure III.8a). On the contrary, in the ''crack-tip field'' models, the ''fixed atomic region'' keeps a part of crack faces fixed and thus are causing un-physical constrains on the near crack strain-stress fields during structural relaxation (figure III.8b). Hence, this simple modification in crack modelling improves the reliability of results regarding the mechanical stability of cracks under load. However, throughout the entire bibliography examined in this thesis, no study was found that follows the ''central crack'' approach. In practice, the ''central crack'' model has anisotropic shape along the crack plane and thus it cannot be adjusted perfectly into the rectangular parallelepiped simulation box. As a result, the simulation box is chosen to be larger than the atomic model along the $x = [100]$ and $y = [010]$ directions leading to the formation of free surfaces. In order to isolate the ''inner atomic region'' from the surface effects, the thickness of the ''fixed atomic region'' has to be larger compared to the range of the forces calculation (Appendix G). Hence, the outer-shell of fixed boundary conditions

must have a thickness larger than double the cut-off distance of the inter-atomic interactions, $R > 2r_c$ (figure III.9).

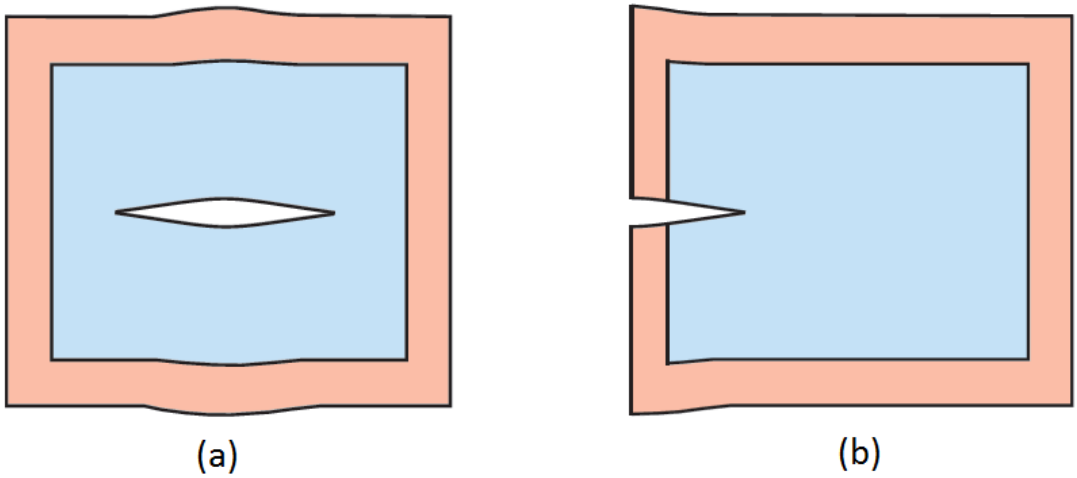

Figure III.8: (a) Central crack and (b) crack-tip field models. The pink outer-shell of both models denotes the fixed atomic region while the blue represents the inner atomic region of interest where the simulation is performed.

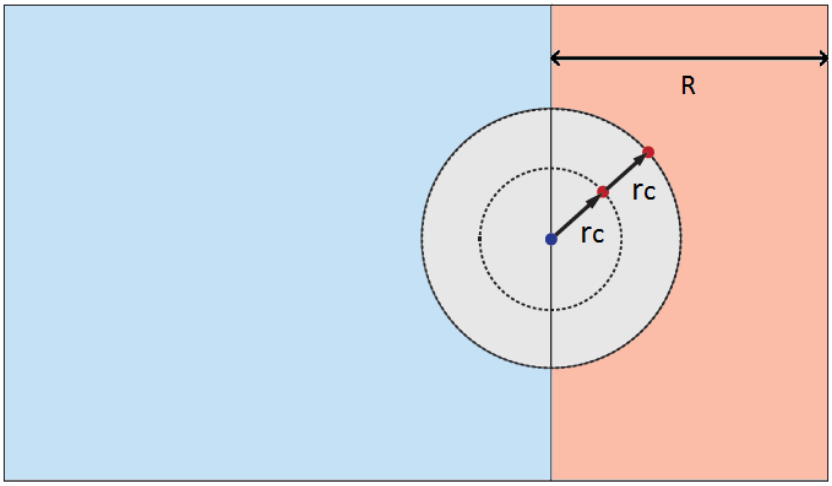

Figure III.9: The thickness of the outer-shelf of fixed boundary conditions (pink) is larger compared to the range of the forces calculation ($R > 2r_c$). In this way, the inner atomic region of interest (blue) is isolated from surface effects.

3.4. Simulation Techniques

3.4.1. Energy Minimization

The fourth step in our atomistic study is the selection of an appropriate simulation technique capable to examine the mechanical stability of nano-sized cracks under loading at the atomic scale. According to the §3.3, the crack models constructed using continuum mechanics (§3.1) contain atoms that are placed in energetically unfavourable positions.

Hence, in order to evaluate the crack model's mechanical response under specific load, their atomic conformations should be optimized according to the laws governing the inter-atomic interactions (§3.2). The energy minimization (EM) is the simulation technique for computationally finding the optimal atomic placements of an atomic conformation. The optimum configuration is obtained through an iterative relaxation process which progressively subtracts energy out of the system until it reaches at the closest local (or global) minimum of energy. This is due to the fact that the atoms are approaching step-by-step their energetically favourable positions. The resulting atomic conformation corresponds to a static equilibrium state of the system, which is uniquely defined by the total potential energy, U. Based on this, the mechanical stability of a crack model can be determined by comparing its initial and relaxed atomistic configuration (§3.5.1). The EM technique can be achieved by the use of several algorithms. In the present study, the ''localized damping'' (LD) method [BEE1972, GEH1972, EVA1974, BEN1975, BEE1983] has been used, which is presented in Appendix I. Its simple algorithm allows a fast relaxation process. Hence, it can be applied to the study of large atomic systems ($\sim 10^5$ atoms) through the use of reasonable computer resources. It is important, however, to emphasize that the EM technique is limited due to the lack of taking into account the temperature effect. Particularly, the static relaxation neglects the atomic vibrations induced by the thermal activation, and therefore the optimum configuration obtained characterize the system at zero Kelvin, only. Therefore, in order to examine the mechanical stability of nano-sized cracks at finite temperature, a different simulation technique is required. A technique that is capable to take into account temperature effects is the Molecular Dynamics.

3.4.2. Molecular Dynamics

Molecular dynamics (MD) is a computational technique capable of simulating the atomic motion in many-body systems, based on the principles of Classical Mechanics [ALL1987]. The physical movement of the atoms is determined by solving the Newton's equations of motion via numerical integration. The integration procedure relies on the force fields between the atoms of the system, derived by the inter-atomic potential function (§3.2). In the MD case, the aim is not to reduce energy (like the EM), but to conserve energy while allowing the atoms to move due to their thermal oscillations. In this way, the MD technique follows the time evolution of the system and generates information regarding atomic positions,

velocities and forces necessary to quantify the equilibrium and transport properties of the system of interest according to the prescriptions of Statistical Mechanics [GUN1990, WIL1997]. Particularly, the MD simulations enable the calculation of the time-average of a property when the system reaches a thermodynamic equilibrium state. However, a thermodynamic property of the system is defined as the average of the property over all the possible equilibrium microscopic states, also called the ensemble-average. Based on the ergodic hypothesis [BON2007], Statistical Mechanics establishes equality between the time-average and ensemble-average quantities of a property, enabling the MD method to quantify macroscopic properties of the system under study. Such properties include the temperature of the system as well as the applied stress state. The molecular dynamics technique is described further in Appendix I.

3.5. Simulation procedure

3.5.1. Cracks stabilization under load at $T = 0K$

The first part of the thesis focuses on the study of $(010)[001]$ cracks at $T = 0K$, aiming at determining equilibrium configurations under quasi-static mode I load. This investigation has been performed by examining the mechanical response of cracks with specific length, a, under different applied stress-strain conditions (ε_{ii} or σ_{ii}, with $i = x, y, z$). The crack containing models of fcc aluminium and bcc iron were constructed according to §3.1.2. The mechanical response of the cracks under load has been determined though structural relaxation by using the localized damping method (Appendix I.4) with the mixed set of boundary conditions described in §3.3.2. Initial atomic configurations have been relaxed for more than 10^5 simulation time steps, with $\delta t = 10^{-14}$ seconds. The relaxation process is considered completed when the two ''relaxation'' criteria, which are presented in Appendix I.4, are satisfied. The mechanical stability of each strained system has been examined, upon relaxation, by using two different ''stabilization'' criteria:

(1) First criterion, is the change in the number of atoms at the internal surface area of the crack, ΔN, obtained by comparison of N between the initial and relaxed configuration. An atom i is considered belonging to the crack faces if its potential energy, U_i, is larger than the potential energy of the second surface layer of the crack surfaces. Whenever N remains constant (or $\Delta N = 0$) during the relaxation process

then the crack is in mechanical equilibrium. If N is decreasing ($\Delta N < 0$) or increasing ($\Delta N > 0$), the crack is closing or opening, respectively.

(2) Second criterion, is the change of the crack half-length, Δa, determined by comparison of a between the initial and relaxed conformation. The value of a is simply determined from the coordinates of surface atoms in the $[100]$ and $[\bar{1}00]$ directions. It happens that the crack length determinations via atomistic model or continuum mechanics solution (Appendix D) are slightly different for the initial configurations due to the discreteness of the former. A crack is considered to be in mechanical equilibrium if $|\Delta a| < d_{100}$, where d_{100} is the distance between the $\{100\}$ planes. On the other hand, if $\Delta a < -d_{100}$ or $\Delta a > +d_{100}$ the crack is healing or propagating, respectively.

Additionally, the mechanical response of the crack has been monitored by examining the potential energy at the near crack region, U_{nc}, i.e. close to the crack-tip and the crack faces. This quantity is capable to capture the structural evolution of the crack-tip during relaxation process. For example, in the case of crack propagation, the increase of the area of the crack surfaces leads to an increase of the U_{nc}. On the contrary, in the case of crack healing, the reborn of new bonds causes reduction of the U_{nc}. Finally, every mechanism of plasticity at the crack-tip and/or its region (e.g. dislocation emission) causes release of the system's stored elastic energy and hence can also be detected through the associated reduction of U_{nc}.

3.5.2. Cracks stabilization under load at $T \neq 0K$

The second part of the thesis focuses on the determination of $(010)[001]$ cracks in mechanical equilibrium under quasi-static mode I load, at finite temperature conditions, $T \neq 0K$. The investigation of the cracks' mechanical response has been performed by employing the molecular dynamics technique (Appendix I) in the following three-step simulation process:

- Step 1: The perfect crystalline models of the two metals (Appendix H) have undergo NVT molecular dynamics simulation in order to reach a thermodynamic equilibrium state at a specific temperature, $\langle T \rangle_{NVT}$. The lattice parameters of the models (a_{fcc-Al} and a_{bcc-Fe}) are defined *a priori* from the $a = f(T)$ relations (figures III.10),

resulting from the corresponding inter-atomic potentials [ZAC2017, PON2007]. The implementation of temperature into the system is performed by the initiation of the atomic velocities ($\vec{v}_i(0)$), with values chosen randomly from a Maxwell-Boltzmann distribution corresponding to the desirable value of $\langle T \rangle_{NVT}$. Periodic boundary conditions were considered along the three orthogonal directions of the perfect crystalline model (i.e. the cubic crystallographic axes), and every atom in the system is free to move without constraints. Different perfect samples were equilibrated at different values of $\langle T \rangle_{NVT}$ for 2×10^5 simulation time steps, with $\delta t = 10^{-15}$ seconds. The simulation process has been monitored by recording the instantaneous and the average values of the systems' temperature in respect to the simulation time-steps (figures III.11). Eventually, when each system reaches the thermodynamic equilibrium, the simulation is stopped and the atomic coordinates of positions and velocities are stored.

- Step 2: Having the atomic coordinates of a snapshot of the perfect systems, which corresponds to a specific $\langle T \rangle_{NVT}$, the displacement field of the central $(010)[001]$ mode I crack is introduced by the use of the complex variable approach (§3.1.2). It is important to mention that the displacement field calculation is made under the approximation that the elastic constants are not affected from the temperature, i.e. $C_{ij}(T > 0K) = C_{ij}(T = 0K)$.
- Step 3: The models constructed in step 2 constitute the initial configurations for the simulation of crack-containing crystals at finite temperature. The mechanical response of these models was investigated by the use of NVT molecular dynamics simulation which was performed at the same $\langle T \rangle_{NVT}$ as in step 1. However, this time, the initial velocities of the atoms, $\vec{v}_i(0)$, are not determined by a Maxwell-Boltzmann distribution. Instead, the $\vec{v}_i(0)$ values of the MD models were determined from the velocity values that were saved in the step 1. In this way, the crystalline models do not experience ''thermal shock'' due to the initialization of atomic velocities (figures III.11), like in step 1, which can affect the mechanical stability of the crack. Simulations were performed with the mixed set of boundary conditions described in §3.3.2 and with time step equal to $\delta t = 10^{-15}$ seconds. In order to determine the equilibrium configurations at each $\langle T \rangle_{NVT}$, the mechanical response of several models corresponding to different values of static applied strain mode I conditions

were examined for a specific crack-length ($22a_{Al}$ for aluminium and $40a_{Fe}$ for iron). Finally, the mechanical stability of the cracks was determined by the use of the two criteria defined in §3.5.1.

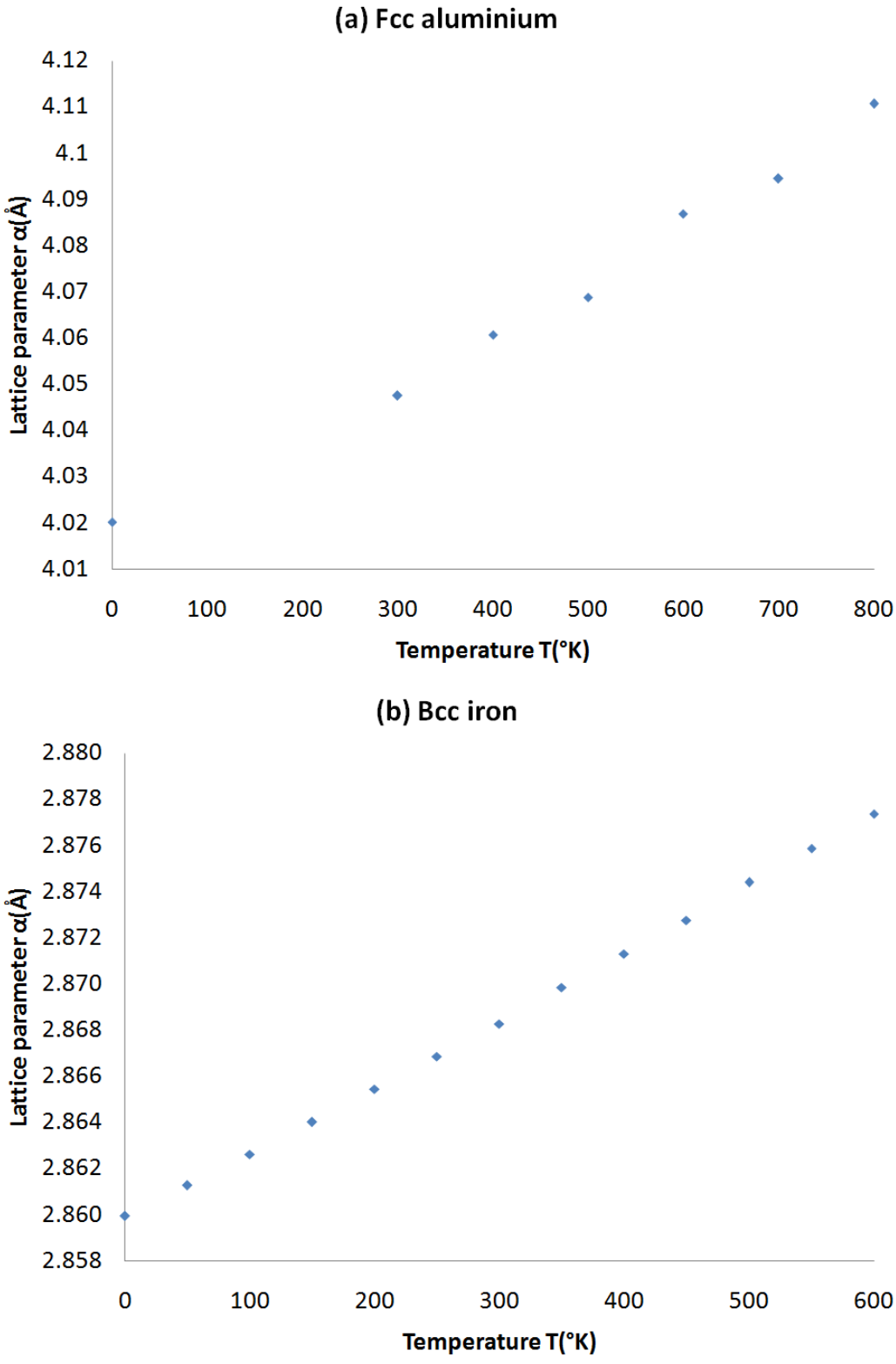

Figures III.10: The change of the lattice parameter in relation to the temperature, calculated for (a) aluminium and (b) iron from the respective inter-atomic potentials [ZAC2017, PON2007].

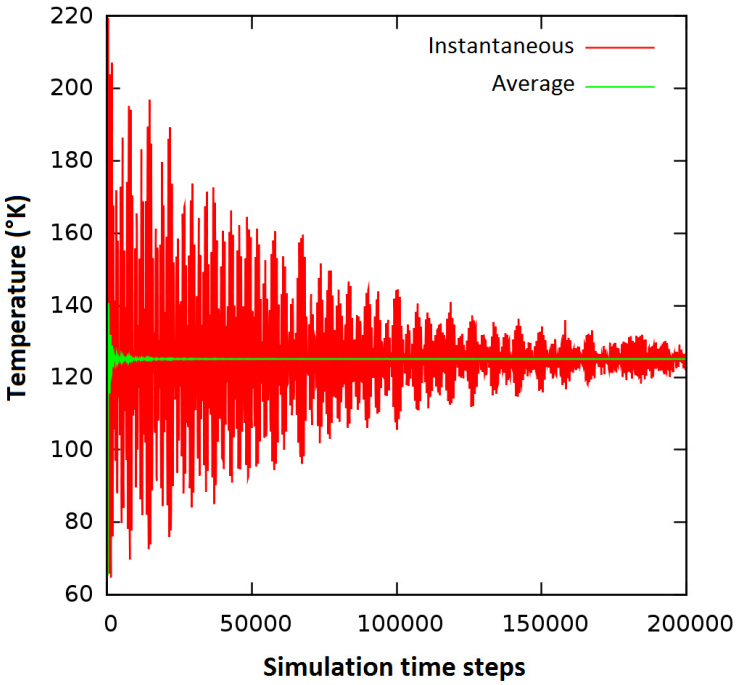

Figures III.11: The evolution of the instantaneous and the average temperature of a defect-free aluminium system during a NVT molecular dynamic simulation at $T_{NVT} = 125K$. The initialization of the atomic velocities, using a Maxwell-Boltzmann distribution, causes a temporary thermal shock into the system.

3.5.3. Ductile and Brittle propagation of a crack at the atomic scale

The final part of the thesis focuses on the investigation of the dynamic response of cracks, aiming at identifying the type of mechanical behaviour the system follows upon loading, in the absence of pre-existing dislocations. To this end, it is first necessary to consolidate the characteristics of both the ductile and brittle crack propagations at the atomic scale.

It is established that the ''inherently'' brittle propagation of a crack is performed by the cleavage mechanism [GRI1920, TYS1973, TYS1977b, DEC1983, CHE1990, FIS2001, GUO2006]. According to this mechanism, an atomically sharp crack propagates through atomic bonds rupture at the crack-tip, along a specific crystallographic plane and a specific crystallographic direction, where for the mode I geometry they coincide to the crack plane and the crack-tip direction, respectively. According to Griffith [GRI1920, TYS1973, DEC1983], the ''perfect'' brittle cleavage is characterized by the absence of plastic deformation, hence no nucleation and/or motion of dislocations in the crack tip region occurs during the crack propagation. Since cleavage cracks can propagate without absorbing plastic energy, the brittle fracture is generally characterized by low absorption of elastic energy; a behaviour which can be

experimentally observed from Charpy diagrams [TAN2005a, TAN2005b]. One of the fundamental features of the cleavage mechanism at the atomic scale is the fact that the crack maintains the initial, atomically sharp, shape of its tip during the crack extension [BEL1999]. This behaviour ensures that the applied stress will be continuously concentrated sufficiently at the crack-tip in order to break the inter-atomic bonds and hence, the cleavage mechanism will be persistent.

On the other hand, according to the two predominantly DBT models, the nucleation-controlled [KEL1967, RIC1974, RIC1992, RIC1994, KHA1994] and the mobility-controlled models [HIR1989, HIR1996, ROB1996, HAR1997, GUM1998], the ''inherently'' ductile propagation of a crack corresponds to the onset of dislocation nucleation and/or emission at the crack-tip. This mechanism increases the dislocation density of the crystal; hence it is accompanied by high absorption of elastic energy, as it can be experimentally observed from Charpy diagrams [TAN2005a, TAN2005b]. Dislocation nucleation and/or emission mechanisms cause the crack-tip to become blunt and hence to lose its initial atomically sharp shape [TYS1977b, DEC1983]. This process can ''shield'' the stress singularity at the crack tip and hence prevent the possibility for cleavage propagation [DEC1983, FIS2001]. In addition, the plastic atomic mechanisms at the vicinity of the crack-tip can alter the crack propagation's direction.

Based on the aforementioned, the dynamic response of a crack under load is classified to the following categories, for the purpose of the present thesis:

(1) **''brittle''**, in the case which the crack propagates via perfect cleavage,

(2) ''**ductile**'', in the case which the crack accommodates the applied stress via plastic deformation by means of dislocation nucleation and/or emission at the crack-tip and/or its vicinity, and

(3) **''mixed''**, for every other atomistic mechanism of stress accommodation, which has characteristics form both the first two categories.

Based on the above, the first criterion to distinguish the type of dynamic response of our initially dislocation-free crack models upon load is by investigating the existence of generated dislocations. Particularly, the existence or absence of dislocations within the

dynamic crack models suggests their potentially ''ductile'' or ''brittle'' character respectively. The detection, as well as the characterization, of dislocations inside the atomic models, has been performed with the use of the Dislocation Extraction Algorithm (DXA) [STU2010, STU2012], which is provided by the OVITO2.6.1 visualization tool. The second criterion to distinguish the type of the dynamic response of our, initial, atomically sharp cracks is by studying the structural evolution of the shape of their crack-tips. As already presented, an atomically sharp shape of the crack-tip suggests the potential ''brittle'' character of a propagating crack, while a blunted crack-tip shape implies its potential ''ductile'' character. The topological analysis of the models of dynamic cracks in order to determine the morphology of their crack-tips and crack faces has been performed by the use of visualization tools (OVITO2.6.1, VMD, GNUPLOT). Finally, the structural evolution of the shape of the crack configurations has been monitored by a simple scheme. This scheme describes the change of the crack length, compared to the initial state, in respect to the corresponding change of the number of the crack surface atoms, i.e.:

$$\Delta\alpha = f(\Delta N) \Rightarrow \left(a^i - a^0\right) = f\left(N^i - N^0\right) \qquad (III.19)$$

where i denotes the simulation time steps and 0 denotes to the initial configuration.

Chapter IV: Validity of linear elasticity at large strains

4.1. Nano-sized equilibrium cracks: the effect of the loading conditions

According to the Griffith's energy balance criterion, a crack with a given half-length, a, can be stabilized by an applied uni-axial mode I load in an unstable equilibrium configuration [GRI1920]. For an ideally brittle material, this mechanical state also corresponds to the threshold for crack propagation. Most atomic crack models in the literature [DEC1983, CHE1990, MAC1998, BEL2004, CAO2006, BEL2007] do not exceed about 250 Å (where $1\text{Å} = 10^{-10}\ m$) in a. Within this length range, the Griffith's criterion [GRI1920, TAD2000] with physical properties of aluminium and α-iron (Table IV.1) predicts the stress and strain magnitudes required for stabilizing a central $(010)[001]$ mode I crack. Figure IV.1a shows that the critical stress (Griffith's stress), determined analytically with the elastic constants of the perfect single crystals and the free surface energy of the $\{100\}$ planes, is higher for α-iron compared to aluminium; $+145.8\%$ for the plane strain and $+138.4\%$ for the plane stress deformation mode. More importantly, the configurations of the equilibrium nano-sized cracks amount very large applied strains (figure IV.1b, $\varepsilon_{yy} > 1.5\%$) which can potentially affect the elastic properties of the strained crystalline systems (Appendix A). Another reason that can cause the chance of the elastic properties is the fact that the uni-axial mode I applied deformation gives rise to hydrostatic pressure, $p \neq 0$ (Appendix A) [BAR1965, WAL1967, CAG1988]. Based on these considerations, the present work raises for the first time the need for evaluating the elastic properties of crystalline systems containing equilibrium nano-sized cracks and aims to examine the validity of the fundamental law of the linear elasticity (Appendix D). This is crucial for allowing the use of continuum mechanics formulation [GRI1920, HIR1982, LIM2001, KIT2004], which derives from the linear approximation, in order to study the mechanical state and properties of equilibrium cracks at the atomic scale and under these applied strain conditions.

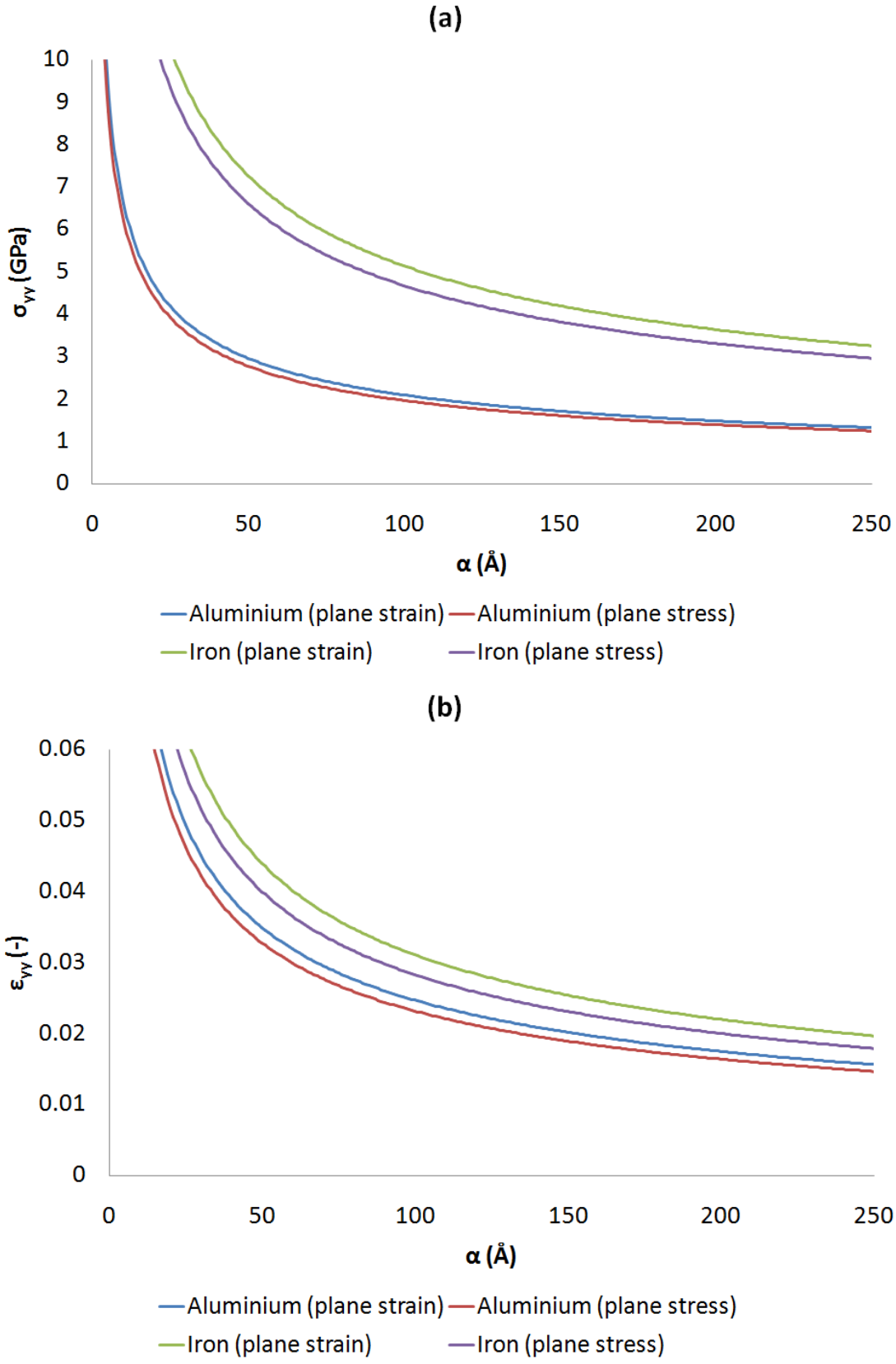

Figure IV.1: Griffith's criterion in terms of (a) stress and (b) strain in aluminium and iron under mode I loading.

Table IV.1: Properties of the perfect single crystalline fcc aluminium and bcc iron

Properties	**aluminium**[ZAC2017]	**α-iron**[PON2007]
Lattice	Face-centered cubic	Body-centered cubic
$\alpha(\text{Å})$	4.02	2.86
$C_{11}(GPa)$	116.63	243.1
$C_{12}(GPa)$	61.028	137.5
$C_{44}(GPa)$	29.618	121.8
$S_{11}(GPa^{-1})$	1.3387×10^{-2}	6.9565×10^{-3}
$S_{12}(GPa^{-1})$	-4.5985×10^{-3}	-2.5132×10^{-3}
$S_{44}(GPa^{-1})$	3.3763×10^{-2}	8.2102×10^{-3}
$\gamma_{\{100\}}(mJ/m^2)$	789.77	1867.79

4.2. The elastic constants under large strains

As presented in Appendix D, the linear elasticity is a mathematical theory capable to describe the deformation and the internal stress state of a solid elastic body under prescribed loading conditions. Linear elasticity relies on the Hooke's law, linearly relating strain to the applied stress, which is an operational approximation at the limit of small stresses, strains and displacements [HIR1982, KIT2004]:

$$\begin{bmatrix}\sigma_1\\ \sigma_2\\ \sigma_3\\ \sigma_4\\ \sigma_5\\ \sigma_6\end{bmatrix} = \begin{bmatrix}C_{11} & C_{12} & C_{13} & C_{14} & C_{15} & C_{16}\\ C_{21} & C_{22} & C_{23} & C_{24} & C_{25} & C_{26}\\ C_{31} & C_{23} & C_{33} & C_{34} & C_{35} & C_{36}\\ C_{41} & C_{14} & C_{34} & C_{44} & C_{45} & C_{46}\\ C_{51} & C_{25} & C_{35} & C_{54} & C_{55} & C_{56}\\ C_{61} & C_{26} & C_{36} & C_{64} & C_{65} & C_{66}\end{bmatrix}\begin{bmatrix}\varepsilon_1\\ \varepsilon_2\\ \varepsilon_3\\ 2\varepsilon_4\\ 2\varepsilon_5\\ 2\varepsilon_6\end{bmatrix} \qquad (IV.1)$$

The correlation coefficients between the stress (σ_i) and strain (ε_j) components are the **elastic constants** (C_{ij}); hence, their determination is required for examining the validity of the stress-strain linear approximation demonstrated in equation IV.1. In equation IV.1 the two indexed elements of both the stress and strain tensors (σ_{ij} and ε_{ij}, with $i,j = 1,2,3$) are converted to single indexed elements (σ_i and ε_i, with $i = 1,\ldots,6$) by means of the Voigt notation (Appendix D). Elastic constants can be determined by the use of the **energy approach** [HIR1982, STA1996, JAM2014]. The potential energy of a solid elastic body in its unstrained or perfect state, U_0, can be increased via the application of distortional (change in shape but not in volume) and/or dilatation (change in volume but not in shape) strain. Within the regime of Hooke's law, i.e. for small strains ($\varepsilon_i \ll 1$), the potential energy of a strained elastic body can be expanded in a Taylor series about its unstrained state:

$$U = U_{\{\varepsilon_k\}} = U_0 + \sum_{i=1}^{6} \varepsilon_i \left[\frac{\partial U}{\partial \varepsilon_i}\right]_{\{\varepsilon_k\}=0} + \frac{1}{2}\sum_{i,j=1}^{6} \varepsilon_i \varepsilon_j \left[\frac{\partial^2 U}{\partial \varepsilon_i \partial \varepsilon_j}\right]_{\{\varepsilon_k\}=0} + \cdots, (k = 1, \ldots, 6)$$

$$U(V, \{\varepsilon_k\}) = U_0(V_0) + V\left(\sum_{i=1}^{6} \sigma_i\, \varepsilon_i + \frac{1}{2}\sum_{i,j=1}^{6} C_{ij}\varepsilon_i \varepsilon_j\right) + \cdots \qquad (IV.2)$$

In this expression, the $\{\varepsilon_k\}$ denotes the different strain components (i.e. the ε_1, ε_2,…, ε_6) and $V_0(V)$ is the volume of the unstrained (strained) elastic body in question. Based on equation IV.2, the elastic constants are approximately determined by the second-order partial derivatives of the $U_{\{\varepsilon_k\}}$ with respect to applied strains, for both distortional and/or dilatation deformations, at the limit of zero strains:

$$C_{ij}(0) = C_{ij}{}_{\{\varepsilon_k\}=0} = \frac{1}{V}\left[\frac{\partial^2 U}{\partial \varepsilon_i \partial \varepsilon_j}\right]_{\{\varepsilon_k\}=0}, \quad (i, j, k = 1, \ldots, 6) \qquad (IV.3)$$

Equation IV.3 signifies that the calculated values of the $C_{ij}(0)$ correspond to the unstrained state of the elastic system or equivalently to the minimum of the potential energy, $U_0(V_0)$, as illustrated in figure IV.2 (point 0). For this reason, the $C_{ij}(0)$ are so-called ''**equilibrium**'' elastic constants.

The present work follows a similar approach in order to determine the elastic constants of the elastic body at a prescribed strain state, i.e. $\{\varepsilon_k\} \neq 0$ $(k = 1, \ldots, 6)$. The potential energy corresponding in a strained state of the system, $U_{\{\varepsilon_k\}} = f(V, \{\varepsilon_k\})$, can be changed by altering the applied deformations or strains. This can be achieved through the implementation of strain increments or decrements, $\{\delta\varepsilon_k\}$ $(k = 1, \ldots, 6)$, in respect to the initial strain state, as presented in figure IV.2 (point P). If these $\{\delta\varepsilon_k\}$ are elastic, i.e. $\{\delta\varepsilon_k\} \ll 1$, the resulting potential energy of the elastic system can be expressed as a Taylor expansion about the initial mechanical operating point, i.e. $\{\delta\varepsilon_k\} = 0$:

$$U = U_{\{\delta\varepsilon_k\}=0} + \sum_{i=1}^{6} \delta\varepsilon_i \left[\frac{\partial U}{\partial \delta\varepsilon_i}\right]_{\{\delta\varepsilon_k\}=0} + \frac{1}{2}\sum_{i,j=1}^{6} \delta\varepsilon_i \delta\varepsilon_j \left[\frac{\partial^2 U}{\partial \delta\varepsilon_i \partial \delta\varepsilon_j}\right]_{\{\delta\varepsilon_k\}=0} + \cdots, (k = 1, \ldots, 6)$$

$$U(V, \{\varepsilon_k\}, \{\delta\varepsilon_k\}) = U_{\{\varepsilon_k + \delta\varepsilon_k\}} = U_{\{\varepsilon_k\}} + V\left(\sum_{i=1}^{6} \delta\sigma_i\, \delta\varepsilon_i + \frac{1}{2}\sum_{i,j=1}^{6} C_{ij}\delta\varepsilon_i \delta\varepsilon_j\right) + \cdots \quad (IV.4)$$

In this relation the $\delta\sigma_i$ denote the stress increments (or decrements) in respect to the initial stress state, $\{\sigma_k\}$, caused by the application of the $\{\delta\varepsilon_k\}$. Based on equation IV.4, the elastic constants of the system corresponding to a prescribed deformation state, $\{\varepsilon_k\}$, can be approximated by the second-order partial derivatives of $U_{\{\varepsilon_k+\delta\varepsilon_k\}}$ in respect to $\{\delta\varepsilon_k\}$, at the limit of zero $\{\delta\varepsilon_k\}$:

$$C_{ij}(\{\varepsilon_k\}) = C_{ij}{}_{\{\delta\varepsilon_k\}=0} = \frac{1}{V}\left[\frac{\partial^2 U}{\partial\delta\varepsilon_i\partial\delta\varepsilon_j}\right]_{\{\delta\varepsilon_k\}=0}, \quad (i,j,k=1,\dots,6) \qquad (IV.5)$$

Since the $C_{ij}(\{\varepsilon_k\})$ characterize a specific operating strain state of the system, they are so-called ''**local**'' elastic constants. The comparison of the equations IV.5 and IV.3 denotes that the $C_{ij}(\{\varepsilon_k\})$ constitute the correlation coefficients between the $\{\delta\varepsilon_k\}$ and the $\{\delta\sigma_k\}$ components. Taking the above into consideration, if $\{\delta\varepsilon_k\} \ll 1$ then the equation that interrelates $\{\delta\varepsilon_k\}$ and $\{\delta\sigma_k\}$ components should be analogous to the equation IV.1, i.e.

$$\begin{bmatrix}\delta\sigma_1\\ \delta\sigma_2\\ \delta\sigma_3\\ \delta\sigma_4\\ \delta\sigma_5\\ \delta\sigma_6\end{bmatrix} = \begin{bmatrix} C_{11}(\{\varepsilon_k\}) & C_{12}(\{\varepsilon_k\}) & C_{13}(\{\varepsilon_k\}) & C_{14}(\{\varepsilon_k\}) & C_{15}(\{\varepsilon_k\}) & C_{16}(\{\varepsilon_k\})\\ C_{21}(\{\varepsilon_k\}) & C_{22}(\{\varepsilon_k\}) & C_{23}(\{\varepsilon_k\}) & C_{24}(\{\varepsilon_k\}) & C_{25}(\{\varepsilon_k\}) & C_{26}(\{\varepsilon_k\})\\ C_{31}(\{\varepsilon_k\}) & C_{23}(\{\varepsilon_k\}) & C_{33}(\{\varepsilon_k\}) & C_{34}(\{\varepsilon_k\}) & C_{35}(\{\varepsilon_k\}) & C_{36}(\{\varepsilon_k\})\\ C_{41}(\{\varepsilon_k\}) & C_{14}(\{\varepsilon_k\}) & C_{34}(\{\varepsilon_k\}) & C_{44}(\{\varepsilon_k\}) & C_{45}(\{\varepsilon_k\}) & C_{46}(\{\varepsilon_k\})\\ C_{51}(\{\varepsilon_k\}) & C_{25}(\{\varepsilon_k\}) & C_{35}(\{\varepsilon_k\}) & C_{54}(\{\varepsilon_k\}) & C_{55}(\{\varepsilon_k\}) & C_{56}(\{\varepsilon_k\})\\ C_{61}(\{\varepsilon_k\}) & C_{26}(\{\varepsilon_k\}) & C_{36}(\{\varepsilon_k\}) & C_{64}(\{\varepsilon_k\}) & C_{65}(\{\varepsilon_k\}) & C_{66}(\{\varepsilon_k\}) \end{bmatrix} \begin{bmatrix}\delta\varepsilon_1\\ \delta\varepsilon_2\\ \delta\varepsilon_3\\ 2\delta\varepsilon_4\\ 2\delta\varepsilon_5\\ 2\delta\varepsilon_6\end{bmatrix} \qquad (IV.6)$$

As denoted, the $C_{ij}(\{\varepsilon_k\})$ are referred to the initial operation point of the system, whose $\{\varepsilon_k\}$ and $\{\sigma_k\}$ state constitutes the origin for $\{\delta\varepsilon_k\}$ and $\{\delta\sigma_k\}$, respectively. The equation IV.6 implies that Hooke's law can be ''locally'' valid about any reference $\{\varepsilon_k\}$-$\{\sigma_k\}$ state of the system and specifically within an elastic strain range of $\{\varepsilon_k - \delta\varepsilon_k\} < \{\varepsilon\} < \{\varepsilon_k + \delta\varepsilon_k\}$. According to this analysis, the regime of the linear elasticity for a deformed system can be extended by a ''local'' manner up to very large applied strains. According to the above, the validity of equation IV.6 can justify the use of continuum mechanics mathematical formulation in studying the mechanical properties of the fcc aluminium and bcc iron crystals under large applied deformation conditions. However, this hypothesis should be verified for both crystalline systems of interest and under the applied deformation mode and magnitude.

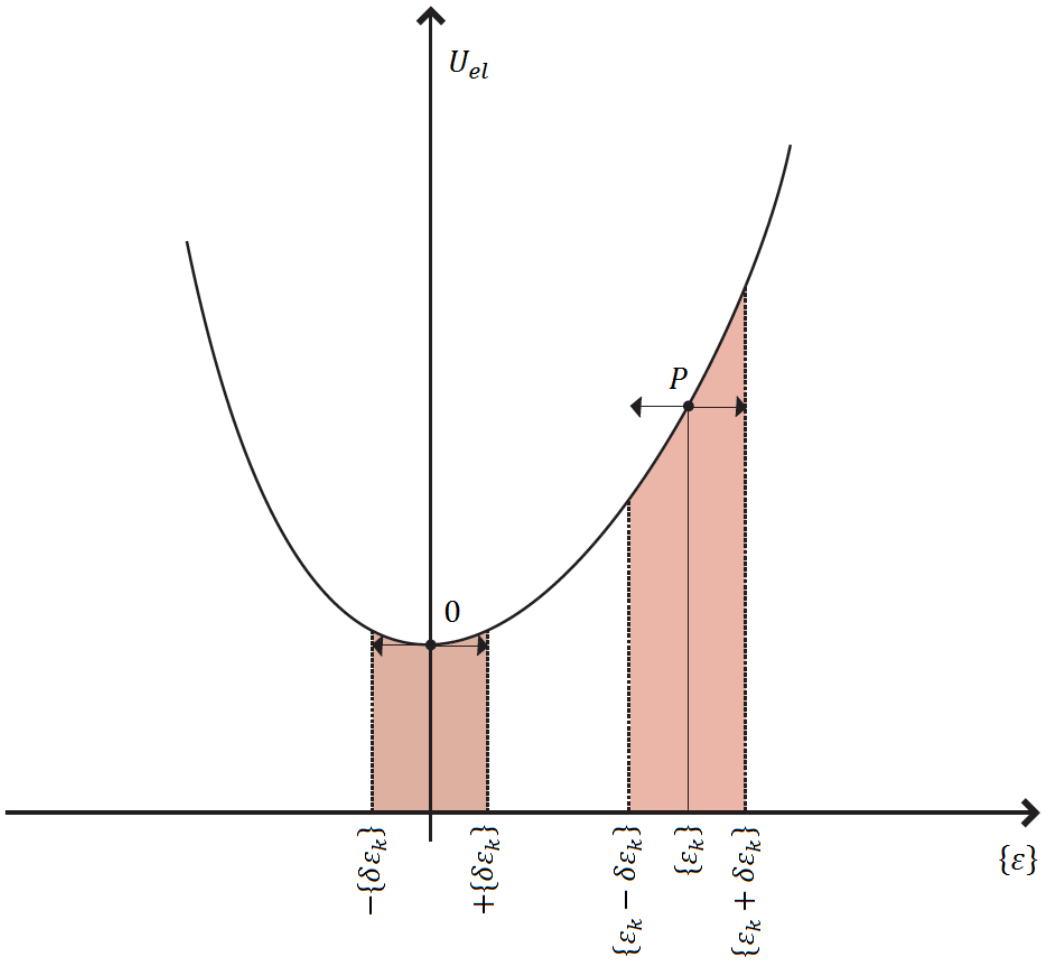

Figure IV.2: Change of the potential energy of an elastic body in respect to the applied strains. The law of Hooke is based to the expansion of elastic strains around the minimum of the potential energy (point 0). This representation is expressed by the equation IV.3 and constitutes the basis for determining the ''equilibrium'' elastic constants corresponding to the minimum of the potential energy or the unstrained state of the body, $C_{ij}(0)$. The same approach is followed to determine the ''local'' elastic constants corresponding at a prescribed homogeneous strain state, $C_{ij}(\{\varepsilon_k\})$. This can be achieved by an expansion of elastic strain increments around the strain state of interest (point P), which is formulated by the equation IV.5.

To this end, the present chapter is devoted to the calculation of $C_{ij}(\varepsilon_{yy})$ of the studied metals in respect to the magnitude of the tensile strain, ε_{yy}, for the plane-strain mode I homogeneous deformation (Appendix A). The calculation has been performed in defect-free atomic models without taking into account the effect of the temperature ($T = 0K$). To ensure the better reliability of the obtaining results, two different methods are being used. The first is an analytic calculation using the inter-atomic potential function (Appendix C) and the second is numerical relying on the elastic energy evaluation of the considered atomistic systems (Appendix B). Both methods have been implemented in fcc aluminium models and the obtained results are displayed in figure IV.3.

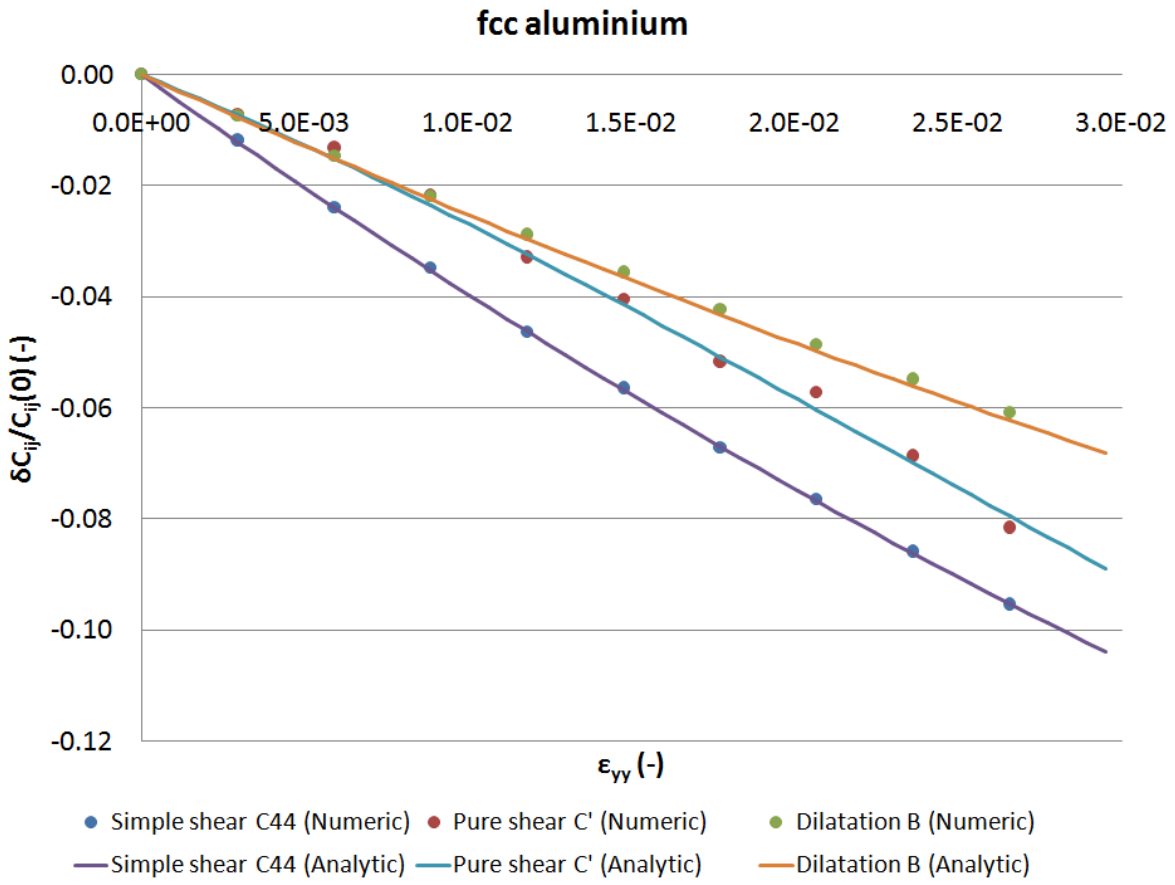

Figure IV.3: Analytic (continuous lines) and numeric (discrete points) determination of the relative change of the simple shear, pure shear and dilatation elastic modulus in fcc aluminium with respect to the magnitude of the mode I tensile strain. The relative change of each elastic modulus is defined as $\delta C_{ij}/C_{ij}(0) = (C_{ij}(\varepsilon_{yy}) - C_{ij}(0))/C_{ij}(0)$, where the $C_{ij}(\varepsilon_{yy})$ and $C_{ij}(0)$ are referred respectively to the strained and unstrained state of the crystalline system.

Figure IV.3 demonstrates that the simple shear, pure shear and dilatation elastic modulus are reduced with increasing the ε_{yy} magnitude. For example, for $\varepsilon_{yy} = 0.025$ the C_{44}, C' and B decrease by 9.1%, 7.4% and 5.9%, respectively, with respect to their unstrained counterparts. Hence, atomistic results imply that the elastic properties of the fcc aluminium change noticeably under large mode I strains. This result suggests that the use of the ''equilibrium'' elastic constants, corresponding to the unstrained state, in studying the elastic properties of aluminium under large applied mode I strains, is not appropriate. The fact that the analytic and numerical methods lead to practically identical results (figure IV.3) gives confidence in the values of the elastic moduli and implies that both methods are equivalent. By using the equations B.6 and B.7, the whole set of cubic elastic constants (i.e. the C_{11}, C_{12} and C_{44}) as function of the ε_{yy} magnitude is obtained. Having calculated the cubic elastic constants in respect to the operating stress-strain states of the system, the validity of the

equation IV.6 can be examined. As already presented, equation IV.6 can provide analytically the stress increments ($\{\delta\sigma_k\}$) compared to an initial operating stress state of the system ($\{\sigma_k\}$), caused by the implementation of elastic strain increments ($\{\delta\varepsilon_k\}$) in respect to the initial operating or reference strain state ($\{\varepsilon_k\}$). The $\{\delta\sigma_k\}$ can also be calculated numerically through the use of the inter-atomic potential [ZAC2017] by comparing the stress states corresponding to the $\{\varepsilon_k\}$ and the $\{\varepsilon_k \pm \delta\varepsilon_k\}$ strain states of the system, i.e.

$$\{\delta\sigma_k\} = \{\sigma_k(\{\varepsilon_k \pm \delta\varepsilon_k\})\} - \{\sigma_k(\{\varepsilon_k\})\},\ (k = 1, \dots, 6) \qquad (IV.7)$$

Both analytic ($\{\delta\sigma_i(ana)\}$, equation IV.6) and numeric ($\{\delta\sigma_i(num)\}$, equation IV.7) calculations have been performed with respect to the reference mode I strain state of $\varepsilon_y^{Ref} = \varepsilon_{yy}^{Ref} = 0.025$. The comparison of their results has been made by utilizing the index:

$$h_i = \frac{\delta\sigma_i(ana) - \delta\sigma_i(num)}{\delta\sigma_i(num) + \sigma_i^{Ref}(num)}, (i = y, z\ or\ yy, zz) \qquad (IV.8)$$

with $\sigma_i^{Ref}(num)$ being the stress components of the reference state, determined through the use of the inter-atomic potential. The investigation was performed for different values of mode I tensile strain increments, $\delta\varepsilon_{yy}$, and the results obtained are presented in figure IV.4. Figure IV.4 demonstrates that for small values of $|\delta\varepsilon_{yy}|$, the results of the analytic and the numerical methods converge. It can be considered that the convergence occurs for $|h| < 5\%$. This result proves that the linear approximation between the $\delta\sigma$ and the $\delta\varepsilon$ components (equation IV.6) is valid around the reference mechanical point examined. In other words, the use of the ''local'' elastic constants that are determined through the equation IV.5, ensures the ''local'' validity of Hooke's law within the elastic region of $\{\varepsilon^{Ref} - \delta\varepsilon(|h| = 5\%)\} < \{\varepsilon^{Ref}\} < \{\varepsilon^{Ref} + \delta\varepsilon(|h| = 5\%)\}$.

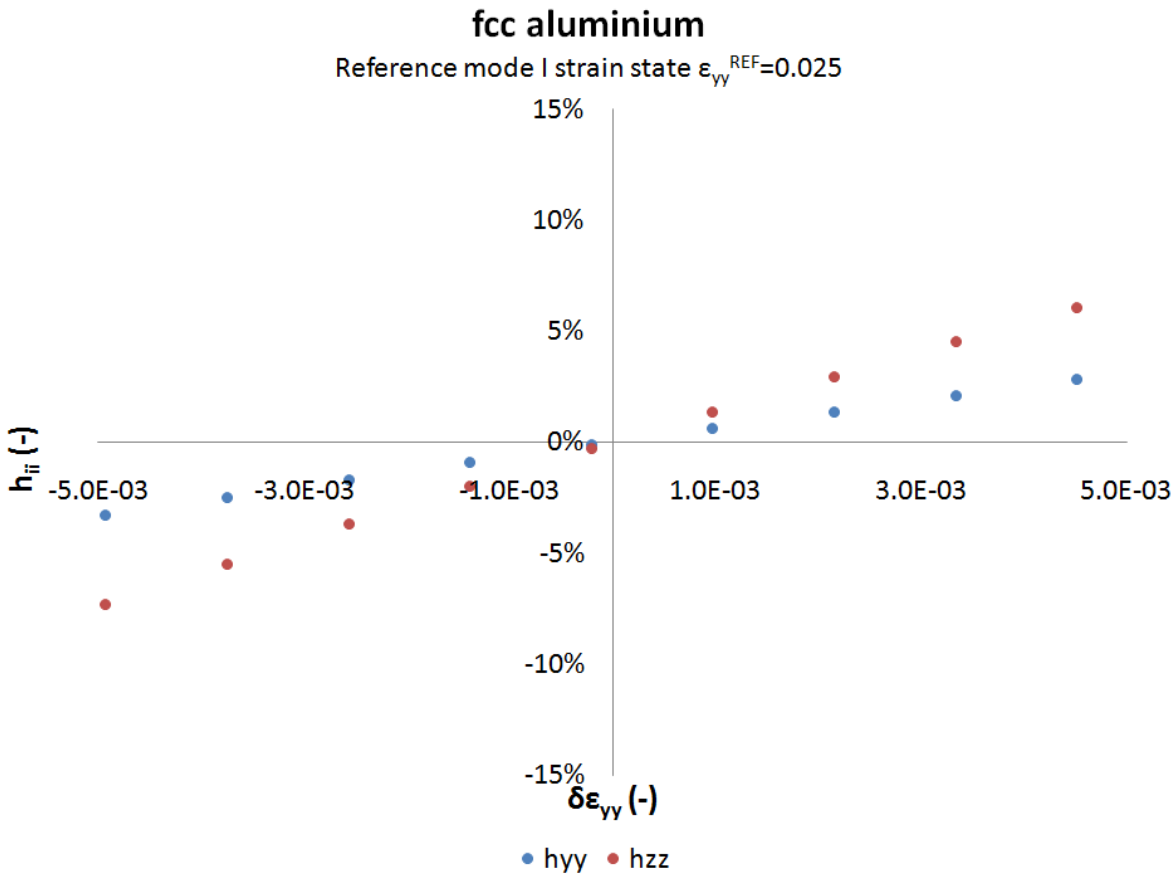

Figure IV.4: The evolution of the index $h_{ii} = [\delta\sigma_{ii}(ana) - \delta\sigma_{ii}(num)]/[\delta\sigma_{ii}(num) + \sigma_{ii}^{Ref}(num)]$ as function of the mode I tensile strain increment, $\delta\varepsilon_{yy}$. The $\delta\varepsilon_{yy}$ components are calculated with respect to the reference mode I strain state of $\varepsilon_{yy}^{Ref} = 0.025$. The investigation has been performed for crystalline fcc aluminium without taking into account the effect of the temperature $(T = 0K)$.

This finding can justify the use of continuum mechanics mathematical formulation in studying the elastic properties of fcc crystalline aluminium under large applied strains. A characteristic example is the calculation of the density of the elastic energy, U_{el}. According to the linear elasticity, the U_{el} of a cubic crystal under mode I plane-strain deformation (Appendix A) is given analytically by the expression:

$$U_{el}(ana) = \frac{C_{11}}{2}\left(\varepsilon_{xx}^2 + \varepsilon_{yy}^2\right) + C_{12}\left(\varepsilon_{xx}\varepsilon_{yy}\right) \qquad (IV.9)$$

The results of this equation are compared with the values of the elastic energy, $U_{el}(num)$, which is calculated numerically by the inter-atomic potential function [ZAC2017].

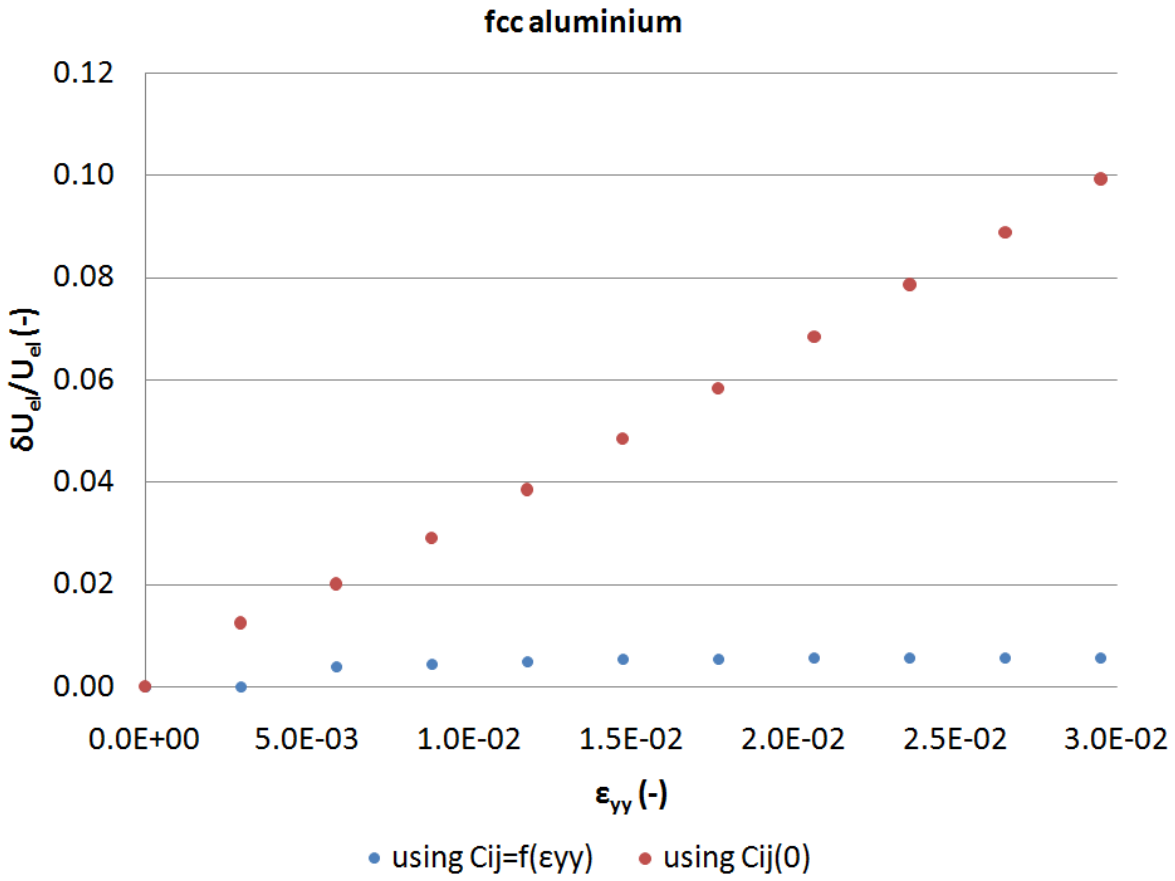

Figure IV.5: The relative change between the analytic and the numeric determination of the density of the elastic energy, $\delta U_{el}/U_{el} = \big(U_{el}(ana) - U_{el}(num)\big)/U_{el}(num)$, as a function of the magnitude of the mode I tensile strain. The analytic calculation of the U_{el} has been made in two ways: the first has been performed by using the equilibrium elastic constants ($C_{ij}(0)$) corresponding to the unstrained state of the system (red data), while the second by the use of the local elastic constants ($C_{ij}(\varepsilon_{yy})$) corresponding to the applied deformation state (blue data). The investigation has been performed for crystalline bcc iron without taking into account the effect of the temperature ($T = 0K$).

Figure IV.5 shows that if the analytic calculation of the elastic energy is performed by the use of the ''equilibrium'' elastic constants that correspond to the unstrained state of the system, $C_{ij}(0)$, then the relative difference between the values of $U_{el}(ana)$ and $U_{el}(num)$ increases significantly with the applied ε_{yy}. On the other hand, if the $U_{el}(ana)$ is calculated by the use of the ''local'' elastic constants, $C_{ij}(\varepsilon_{yy})$, which correspond to the applied deformation state of the system, then the values of $U_{el}(ana)$ and $U_{el}(num)$ are virtually identical, independent of the magnitude of the applied mode I tensile strain. This result ensures that the values of the ''local'' elastic constants, determined for every strain state studied via the equation IV.5, are correct. In addition, it is demonstrated for a second time that the use of the ''local'' elastic constants ensures the local validity of the laws of the linear

elasticity (equation IV.9) in studying the elastic properties of fcc aluminium under large applied strains.

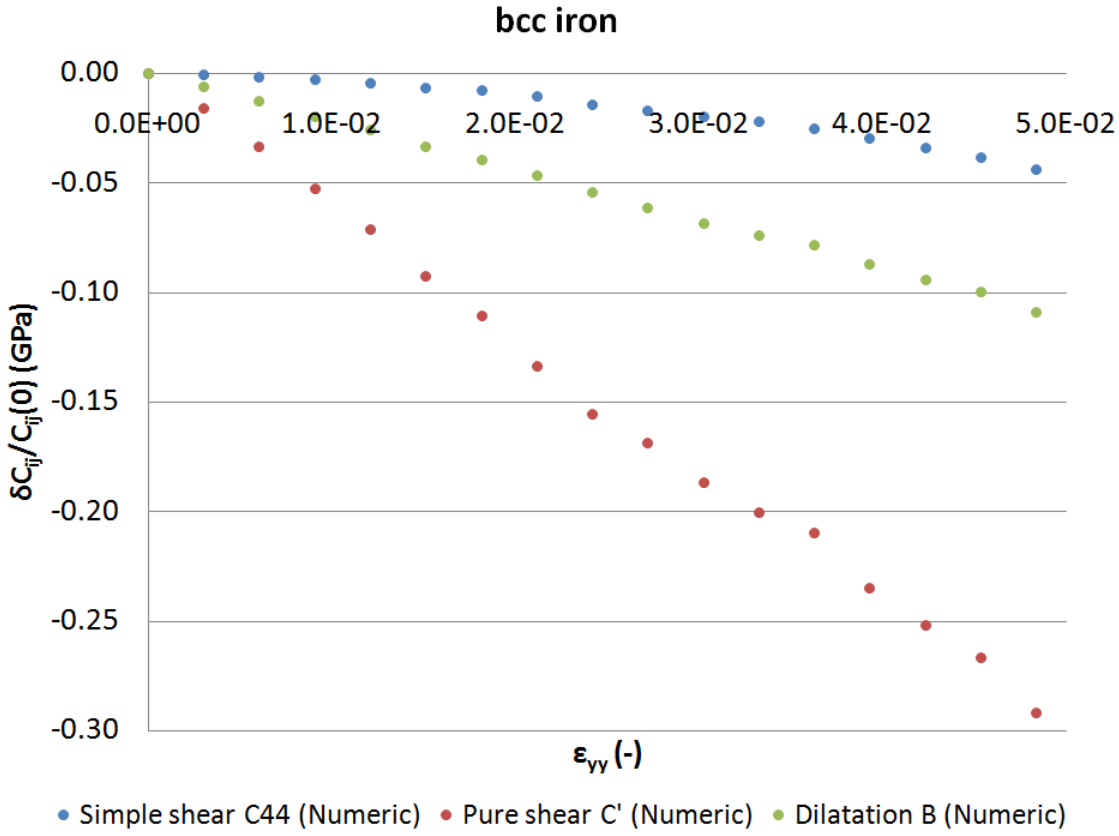

Figure IV.6: Numeric determination of the relative change of the simple shear, pure shear and dilatation elastic modulus in bcc iron with respect to the magnitude of the mode I tensile strain. The relative change of each elastic modulus is defined as $\delta C_{ij}/C_{ij}(0) = (C_{ij}(\varepsilon_{yy}) - C_{ij}(0))/C_{ij}(0)$, where the $C_{ij}(\varepsilon_{yy})$ and $C_{ij}(0)$ are referred respectively to the strained and unstrained states of the crystalline system.

The same investigation has been performed also for the bcc iron model [PON2007]. This time by using only the reliable numerical method (Appendix B), the elastic moduli of simple shear, pure shear and dilatation were calculated as a function of the applied mode I tensile strain, ε_{yy}. Results in figure IV.6 confirm that the crystalline iron also exhibits noticeable change in the elastic constants under large applied mode I strains. For example, for $\varepsilon_{yy} = 0.025$ the C_{44}, C' and B decrease by 1.4%, 15.5% and 5.6%, respectively. Similar to the study of aluminium, the validity of the equation IV.6 was also examined for the model of iron. Analytic and numeric calculations have been conducted with the mode I tensile strain of $\varepsilon_{yy}^{Ref} = 0.025$ as a reference state, and the results obtained are given in figure IV.7.

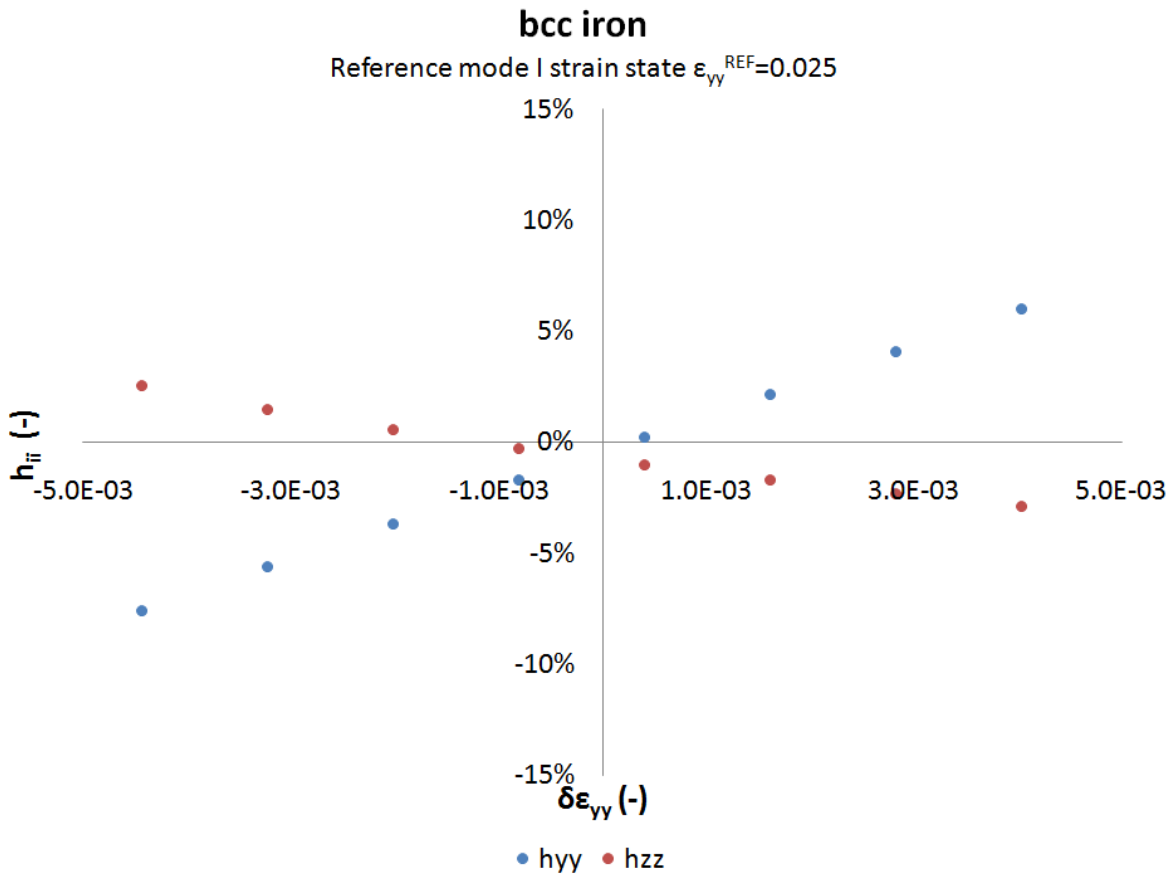

Figure IV.7: The evolution of the $h_{ii} = [\delta\sigma_{ii}(ana) - \delta\sigma_{ii}(num)]/[\delta\sigma_{ii}(num) + \sigma_{ii}^{Ref}(num)]$ as a function of the mode I tensile strain increment, $\delta\varepsilon_{yy}$. The $\delta\varepsilon_{yy}$ components are calculated with respect to the reference mode I strain state of $\varepsilon_{yy}^{Ref} = 0.025$. The investigation has been performed for crystalline bcc iron without taking into account the effect of temperature $(T = 0K)$.

Similar to the aluminium, the results in iron show that for elastic strain increments, with regards to the reference strain state, the law of Hooke (equation IV.6) applies; hence, the ''local'' elastic constants, $C_{ij}(\varepsilon_{yy})$, determined for the reference strain state of the system, are correct. The examination of the equation IV.9 verifies, also, that the use of the ''local'' $C_{ij}(\varepsilon_{yy})$ reproduces correctly the density of the elastic energy for every magnitude of the applied mode I tensile strain (figure IV.8). On the contrary, the determination of the elastic energy is not correct for large applied strains if the equilibrium $C_{ij}(0)$ are used in equation IV.9. Therefore, it can be concluded that the linear elasticity formulation is valid locally under large applied strains, in both fcc aluminium and bcc iron, provided that the ''local'' elastic constants corresponding to the system's mechanical state are used.

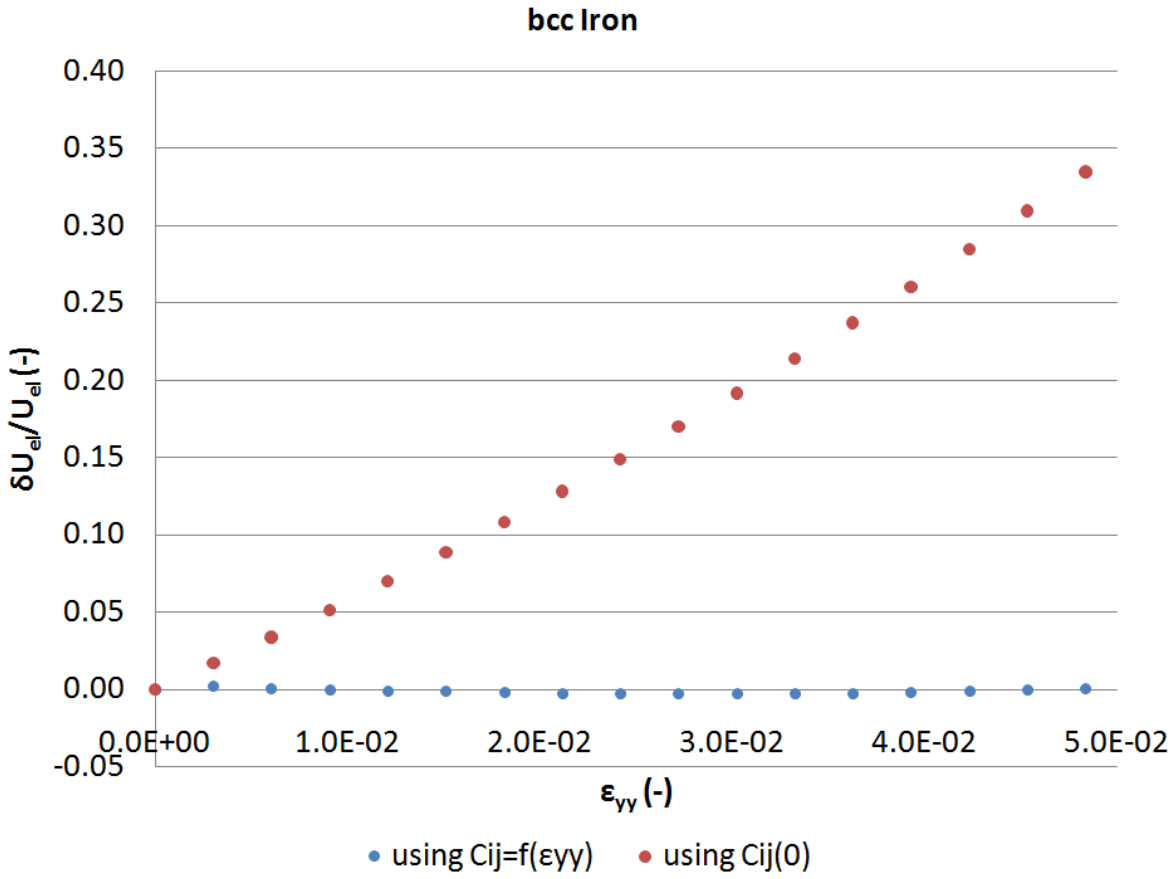

Figure IV.8: The relative change between the analytic and the numeric determination of the density of the elastic energy, $\delta U_{el}/U_{el} = \big(U_{el}(ana) - U_{el}(num)\big)/U_{el}(num)$, as function of the magnitude of the mode I tensile strain. The analytic calculation of the U_{el} has been made in two ways: the first has been performed by using the equilibrium elastic constants ($C_{ij}(0)$) corresponding to the unstrained state of the system (red data), while the second by the use of the local elastic constants ($C_{ij}\big(\varepsilon_{yy}\big)$) corresponding to the applied deformation state (blue data). The investigation has been performed for crystalline bcc iron without taking into account the effect of the temperature ($T = 0K$).

4.3. The elastic constants of the nano-sized crack systems

In the previous paragraph, the study of the elastic constants for the two metals of interest has been conducted in defect-free crystalline models and under the conditions of **homogeneous** applied mode I deformation. On the other hand, a loaded crystal that contains an equilibrium crack is characterized by a **heterogeneous** stress and strain field (Appendix D). This occurs due to the fact that the crack's presence alters the externally applied homogeneous load or deformation, especially close to the vicinity of the crack-tips. The purpose of this paragraph is to evaluate ''elastically'' the crack atomic models of fcc aluminium and bcc iron constructed by the use of the complex variable approach (CVA, Appendix D). Equations IV.3 and IV.5 can be utilized to determine the elastic constants of

homogeneous systems, only; hence they cannot be used directly to determine the overall elastic character of the crack containing models (Chapter III). To this end, we introduce the idea that each atomic crack model is comprised by a mesh of infinitesimal volume elements (figure IV.9). The small size of these volume elements entails that the stress and strain fields within the elements are practically homogeneous. Since the crack field is heterogeneous, the different volume elements of the considered mesh are characterized by a different magnitude of applied homogeneous deformation; hence, according to the §4.2, they correspond to different elastic constants ($C_{ij} = f(\{\varepsilon_k\})$). Therefore, an accurate elastic characterization of each crack model can be achieved by position-dependent elastic constants (figure IV.9). However, the numeric determination of the overall elastic character of the atomic models, as parts of macroscopic loaded crystals, is computationally very expensive by employing this approach.

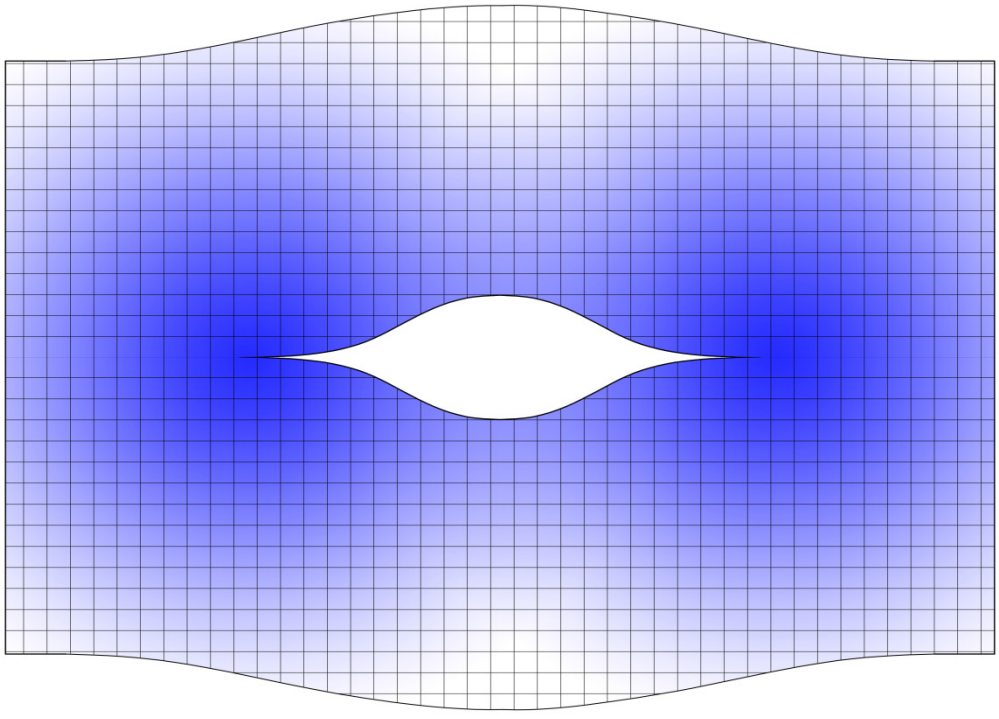

Figure IV.9: Representation of the crack model as a mesh of volume elements. The volume elements are small enough to assume that they are characterized by homogeneous stress and strain states. The intensity of the blue color within each volume element represents the magnitude of the homogeneous deformation and hence the degree of the change of the elastic constants.

To address this issue, an analytic approach is followed. The mathematic analysis of the ''crack problem'', according to the linear elasticity, allows the use of the superposition principle which enables the division of the crack's stress field into two component

parts [WEE2008]: a homogeneous component-field, $\{\sigma_k^{Hom}\}$, due to the applied loading conditions on the crack containing system and a heterogeneous component-field, $\{\sigma_k^{Het}\}$, which describes the alteration of the former due to the presence of the equilibrium crack configuration,

$$\{\sigma_k\} = \{\sigma_k^{Hom}\} + \{\sigma_k^{Het}\} \qquad (IV.10a)$$

Similarly, for the strain field,

$$\{\varepsilon_k\} = \{\varepsilon_k^{Hom}\} + \{\varepsilon_k^{Het}\} \qquad (IV.10b)$$

According to this approach, the $\{\sigma_k^{Het}\}$ describes the stress concentration at the vicinity of the nano-sized crack, which declines with the increase of the distance from the crack faces. CVA results in aluminium and iron show that the $\{\sigma_k^{Het}\}$ and $\{\varepsilon_k^{Het}\}$ of a Griffith's nano-sized crack, with length equal to $a = 100\text{Å}$, becomes practically zero at macroscopic distances ($\sim cm$) from the crack's centre. Hence, it can be assumed that the $\{\sigma_k^{Het}\}$ of a nano-sized crack cannot affect the elastic properties of a macroscopic loaded crystal. On the other hand, the $\{\sigma_k^{Hom}\}$ is spatially constant and therefore it can characterize the stress and strain operation states of the whole macroscopic loaded system. Furthermore, the $\{\sigma_k^{Hom}\}$ is the external condition required for the mechanical stability of a crack with a specific length, a. According to Griffith's criterion [GRI1920], cracks of macroscopic length require low applied mode I $\{\sigma_k^{Hom}\}$ in order to be stabilized. In this case, the formed $\{\varepsilon_k^{Hom}\}$ and $\{\varepsilon_k^{Het}\}$ fields within the crystal are ''elastic'' compared to its perfect state; hence, the system's operation state is located very close to the minimum of the elastic energy curve. Consequently, the linear approximation between the components of the $\{\sigma_k^{Hom} + \sigma_k^{Het}\}$ and the $\{\varepsilon_k^{Hom} + \varepsilon_k^{Het}\}$ fields can be valid by the use of the ''equilibrium'' elastic constants, $C_{ij}(0)$. On the other hand, the applied mode I $\{\sigma_k^{Hom}\}$ required to stabilize cracks of nano-sized length is very large, thus forming large strains ($\{\varepsilon_k^{Hom}\}$) in the system (figure IV.1). In this case, the operation state of the system is not located within the elastic strain range of the minimum of the elastic energy curve, hence, the $C_{ij}(0)$ constants cannot describe it. Nonetheless, the $\{\varepsilon_k^{Hom}\}$ operation state of the system, required to stabilize a nano-sized crack, can be elastically characterized by its ''local'' elastic constants, $C_{ij}(\{\varepsilon_k^{Hom}\})$, determined through the equation IV.5. As it has been shown in §4.2, the $C_{ij}(\{\varepsilon_k^{Hom}\})$ ensure

the validity of the linear approximation between elastic stress and strain increments, with respect to the $\{\varepsilon_k^{Hom}\}$ state. Based on the above, we make the **''working hypothesis**'' that the $\{\varepsilon_k^{Het}\}$ and $\{\sigma_k^{Het}\}$ fields of a nano-sized crack can be linearly interrelated, according to the Hooke's law (equation IV.6), by the use of the system's ''local'' elastic constants ($C_{ij}(\{\varepsilon_k^{Hom}\})$). This working hypothesis is reasonable as both $\{\varepsilon_k^{Het}\}$ and $\{\sigma_k^{Het}\}$ crack fields, for almost the spatial entirety of the crystal, are indeed elastic. Therefore, we can conclude that a macroscopic crystal, containing an equilibrium crack of nano-sized length, can be elastically characterized in its entirety by a single set of elastic constants; the local elastic constants corresponding to the defect-free crystal, under the homogeneously applied loading or deformation conditions which are required to stabilize the nano-sized crack configuration. The result of the analysis above is essential for the purpose of the current thesis because it allows the use of continuum mechanics mathematical formulation in studying the mechanical properties of equilibrium nano-sized cracks in fcc aluminium and bcc iron.

Chapter V: Atomistic simulation of nano-sized cracks

5.1. Space Scale Coupling

The main objective of the present thesis is to understand why aluminium and iron are respectively ductile and brittle upon loading at low temperature. To this end, numerical models of $(010)[001]$ mode I nano-sized cracks (figure V.1) have been constructed by using anisotropic elasticity [SAV1961, LIM2001], in both metals, in order to investigate their mechanical response at $T = 0K$. The crack orientation is chosen in consistency with both the primary cleavage planes of iron and the hypothetically favourable cleavage planes of aluminium (§3.1.1). This investigation is focused at the atomic scale, using atomistic simulations, aiming to study the crystalline lattice effect on the ductile and/or brittle behaviour. The crack models of the studied crystals, despite the crack presence, are defect-free systems and hence do not contain pre-existing dislocations, which are the primary ingredients for the plastic deformation in metals [HIR1982]. Consequently, the stress or strain accommodation of their loaded atomic configurations is characterized by the absence of pre-existing dislocation effects and is determined solely by the crack field.

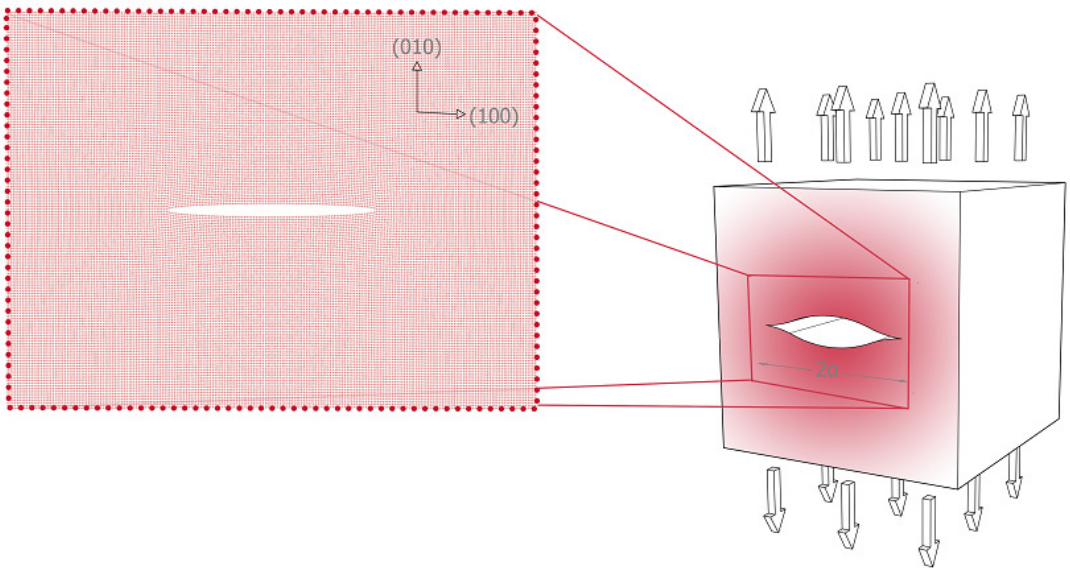

Figure V.1: Infinite plate with a central $(010)[001]$ crack under plane-strain uni-axial mode I loading.

The first issue which arises from this atomistic investigation is the ''space scale problem''. The reason is that the experimentally observed cracks, inside real materials, are meso or macroscopic in dimensions and hence are not compatible with atomistic modelling. Consequently, a legitimate question is: to what extent the simulation findings are able to

correctly describe the behaviour of macroscopic-sized cracks of industrial metals? To address this issue, we investigate if the models of atomic length crack obey the linear elasticity laws, which describe the macroscopic mechanical behaviour of crack-containing bodies. As already described in Chapter II, the energy balance analysis of Griffith [GRI1920] provides the mathematical formulation for the ''mechanical stabilization'' of a crack, under static loading conditions, inside an ideally brittle elastic body. According to his approach, which is based on linear elasticity, each crack configuration of a certain length can be stabilized for a specific level of applied loading or deformation in an unstable mechanical equilibrium state (figure II.7). The crack's mechanical equilibrium condition, which simultaneously corresponds to its critical propagation limit, is defined by means of Griffith's criterion [GRI1920]:

$$\sigma_{yy,c} = \sqrt{\frac{2\gamma}{\pi C a_c}} \Rightarrow a_c = \frac{2\gamma}{\pi} \cdot \frac{1}{C\sigma_{yy,c}^2} \Rightarrow \gamma = \frac{\pi a_c C \sigma_{yy,c}^2}{2} \qquad (V.1)$$

where $\sigma_{yy,c}$ is the critical stress component along the direction of mode I tension (valid for both uni-axial and bi-axial cases), a_c is the critical half-length of the crack, γ is the surface energy of the crack faces and C is the anisotropic elastic coefficient of the deformation mode. For the plane-strain case, the C coefficient is given by the expression [TAD2000]:

$$C = \left(b_{11}b_{22}/2\right)^{1/2} \left[\left(b_{22}/b_{11}\right)^{1/2} + (2b_{12} + b_{66})/2b_{11}\right]^{1/2} \qquad (V.2)$$

where b_{ij} are the compliance constants defined in equations D.28. Additionally, as it further presented in Chapter II, the analysis of Griffith constitutes the base for defining ''mechanical homology'' of the cracks response upon loading independently from the crack size (equation II.12). In particular, we have shown that the mechanical stability of every crack of different length can be described by a master curve (figure II.9), of normalized units, which allow us establishing the scale coupling in space through equation V.1. Hence, if the mechanical response of our crack models can satisfy the criterion of Griffith (equation V.1) then we can conclude that these atomic-sized configurations are mechanically equivalent with macroscopic-sized crack by means of linear elasticity. In such case, the additional simulation findings can consider to be also valid for macroscopic crack configurations, e.g. inside the real metals, thus solving the ''space scale problem''.

Based on the aforementioned, the investigation is focused on the mechanical stability of atomic-sized cracks inside the discrete crystalline lattice of the systems under study. More importantly, the quasi-static loading conditions allow us to appropriately determine the quantities contained in equation V.1 within the thermodynamic regime. The appropriate simulation technique to obtain equilibrium atomistic configurations at $T = 0K$ is the minimization of energy, which has been achieved by using the localized damping method (LDM), as presented in Chapter III. However, like every simulation technique, the LDM is affected by rounding and truncation errors (Appendix I.2.2), which can alter the simulation outcome. This is particularly clear on the effort of stabilizing a crack. As already mentioned (Chapter II), the unstable mechanical equilibrium of a quasi-static crack is represented by a zero-dimensional equilibrium point on the crack's energetics diagram (figure II.7). According to this, if the size of a crack becomes infinitesimally smaller or larger than the critical value (a_c), under specific, constant, applied loading ($\sigma_{yy,c}$), then the crack closes or opens irreversibly. Since the LDM introduces numerical errors on the model's atomic coordinates during the energy minimization process, it is practically impossible to simulate a nano-sized crack with a perfectly constant length, a. Based on the above, the energy minimization process should, normally, not be applied in the investigation of unstable equilibrium Griffith's cracks at $T = 0K$, since it does not allow their stabilization. This ''crack stabilization problem'' constitutes the second issue of our study as it does not allow the study of the equation V.1. With this in mind, one is left wondering whether the scale coupling in space is achievable. Yes it is achievable because, despite the Griffith's critical stress, the crack stabilizes, due to an additional factor, the ''lattice trapping effect'' (LTE) [THO1971, SIN1972, SIN1975, CUR1990]. As already reported (Chapter II), this phenomenon describes the resistance of the crystal lattice against the healing or extension of a pre-existing crack, which is initially in mechanical equilibrium. Corresponding critical stress or strain conditions for the crack to advance or close are known as the upper and the lower trapping limits, respectively. Due to the LTE, a finite stability zone is formed for a crack of any size at its equilibrium state inside discrete crystalline lattice. Consequently, despite the numerical errors of the energy minimization simulation, the LTE allows us to obtain equilibrium nano-sized cracks at the atomic scale; thus, justifying the use of the chosen simulation technique.

5.1.1. Lattice trapping effect at $T = 0K$

Based on the above considerations we have studied quasi-static $(010)[001]$ nano-sized cracks under mode I plane-strain deformation at $T = 0K$. The determination of the equilibrium configurations has been performed by studying the mechanical response of the system. To this end, crack models corresponding to different values of applied stain, or of equivalent stress, field were examined. This investigation has been made for models of different crack lengths aiming at (i) studying the influence of the crack length on the mechanical properties of the systems under study, and (ii) controlling for consistency the models behaviour under different applied loads, thus capturing possible matching errors between static and dynamic regions of the models (§5.3). The computational details of this study concerning both the construction of the atomic models and the simulation procedure have been presented in detail in §3.1 and §3.5, respectively. The mechanical response of the different crack models, upon the energy minimization, with respect to the strain magnitude in the direction of the applied strain tension is presented in figures V.2 and V.3 for fcc aluminium and bcc iron, respectively.

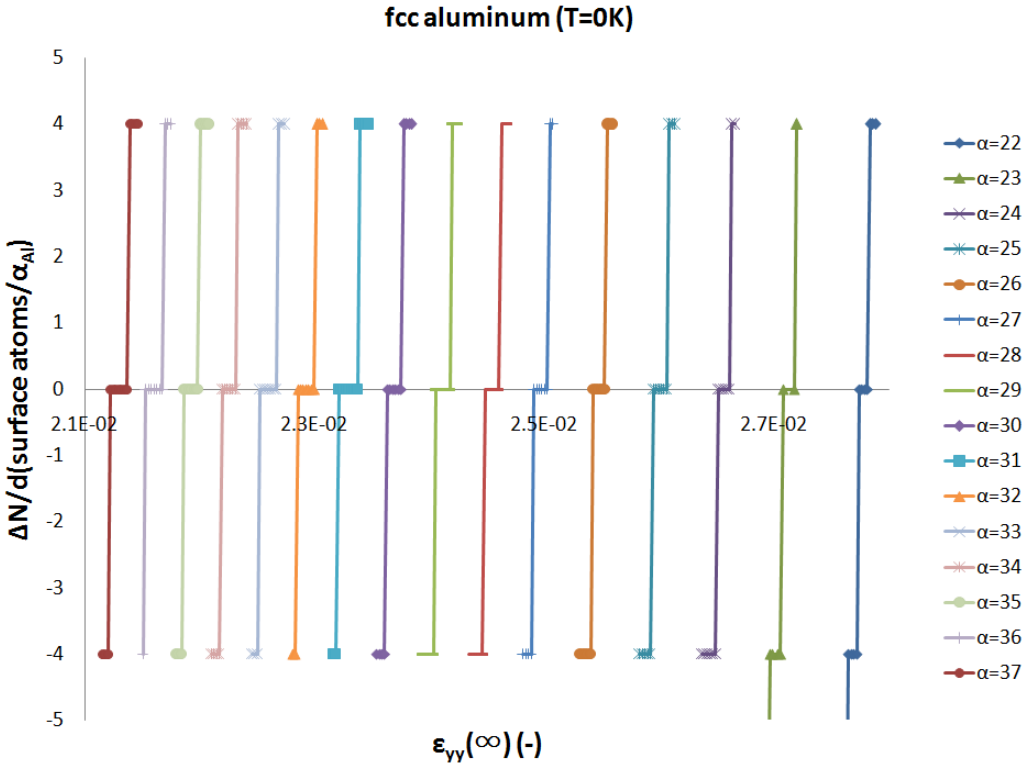

Figure V.2: Mechanical response of $(010)[001]$ nano-sized cracks in fcc aluminium at $T = 0K$. The change in surface atoms per model width, $\Delta N/d$, upon the energy minimization, with association to the strain magnitude in the direction of the applied strain tension. The initial crack half-length according to linear elasticity continuum mechanics is given on the right of the plot in lattice parameters a_{Al} (where $a_{Al} = 4.02\text{Å}$).

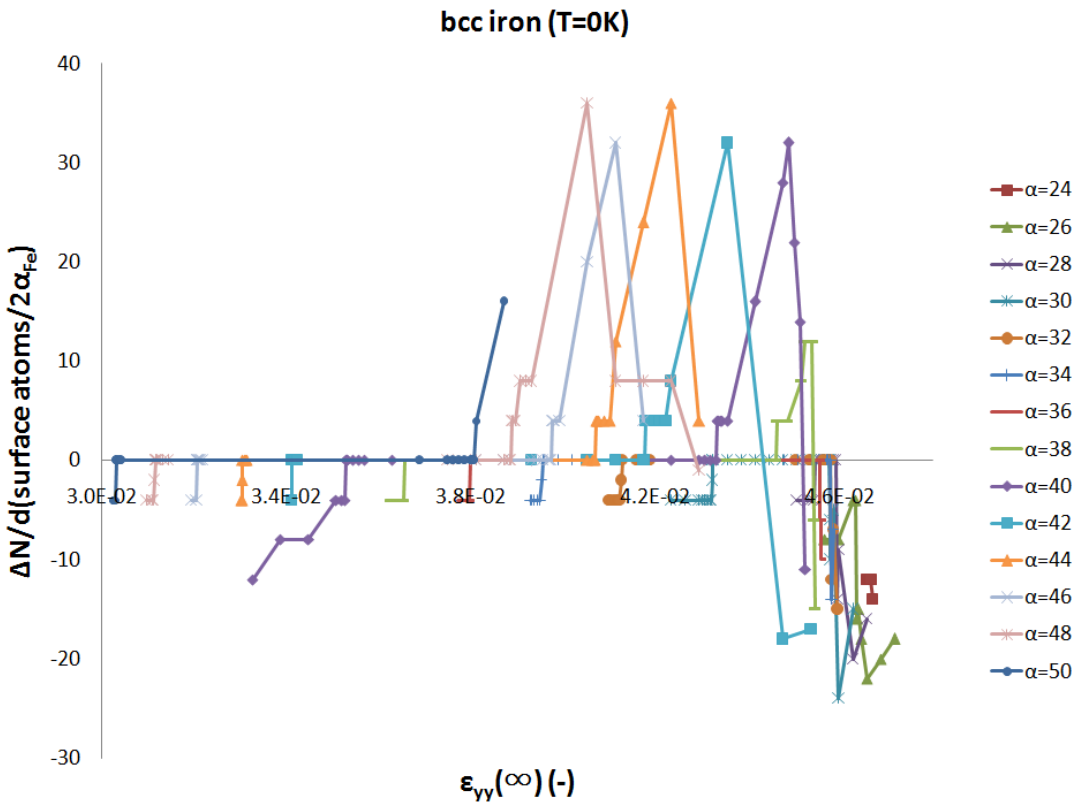

Figure V.3: Mechanical response of $(010)[001]$ nano-sized cracks in bcc iron at $T = 0K$. The change in surface atoms per model width, $\Delta N/d$, upon the energy minimization, with association to the strain magnitude in the direction of the applied strain tension. The initial crack half-length according to linear elasticity continuum mechanics is given on the right of the plot in lattice parameters a_{a-Fe} (where $a_{a-Fe} = 2.86\text{Å}$).

Equilibrium cracks were identified by combining the ''stabilization'' (§3.5.1) and ''relaxation'' (§I.4) criteria. Simulation results revealed that each crack configuration in fcc aluminium remains stable under an applied strain range, indicating the existence of the lattice trapping effect (figure V.4). In addition, atomistic simulations have shown that these crack models present similar mechanical response under quasi-static loading, independently of the crack length or equivalently the applied loading level, with a representative example illustrated in figure V.4. Figure V.4 shows both the stability region as well the evolution of the crack-length and surface-atom number beyond the strain lattice trapping limits. Outside the stability region and above the upper trapping limit, cracks propagate via cleavage (§3.5.3) on the crack plane (010) and along the $[100]$ and $[\bar{1}00]$ direction for the right and left crack-tip, respectively. Conversely, crack healing occurred for the configurations below the lower trapping limit as a reverse propagation process. Both phenomena are constrained by the fixed boundary conditions, becoming increasingly incorrect as the crack evolves. These phenomena are further presented in §5.7.1.

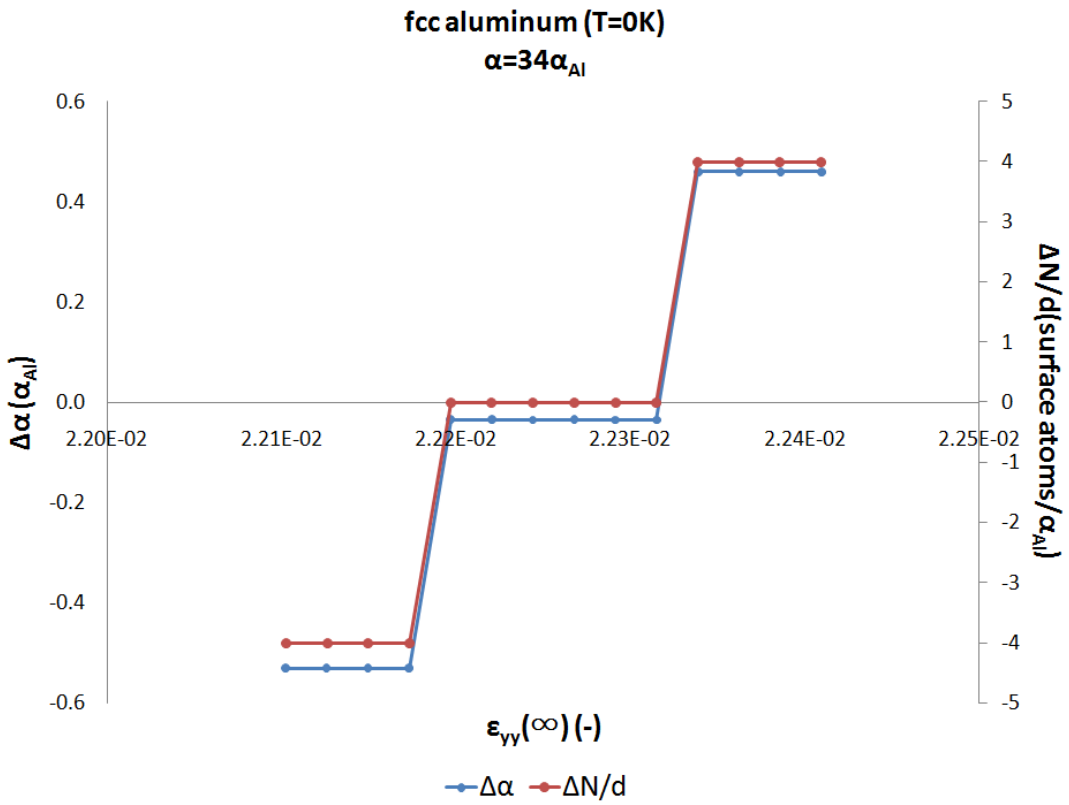

Figure V.4: Evolution of the crack half-length of $(010)[001]$ nano-sized cracks in fcc aluminium in respect to the applied deformation at $T = 0K$. Crack healing, mechanical equilibrium and the cleavage propagation region of the crack configuration with initial half-length equal to 34 lattice parameters are illustrated above.

Upper and lower stability limits can be used for determining the strain-stress conditions required for initiation of crack opening and healing processes, respectively, as function of the crack length (or equivalently the loading level), and hence the lattice trapping strain barrier for propagation of the crack can be obtained (figures V.5 and V.6). Figure V.5 shows that the strain thresholds for these processes are decreasing with the crack length, behaviour in consistency with Griffith's equilibrium criterion [GRI1920], despite the existence of the lattice trapping effect. More importantly, figure V.6 shows that the lattice trapping strain barrier for brittle extension of the cracks in fcc aluminium via cleavage propagation (§3.5.3) is constant, which implies that the lattice resistance for a crack to propagate is an intrinsic property of the system, tightly associated with the applied strain increments $\Delta\varepsilon_{xx(\infty)}$ and $\Delta\varepsilon_{yy(\infty)}$.

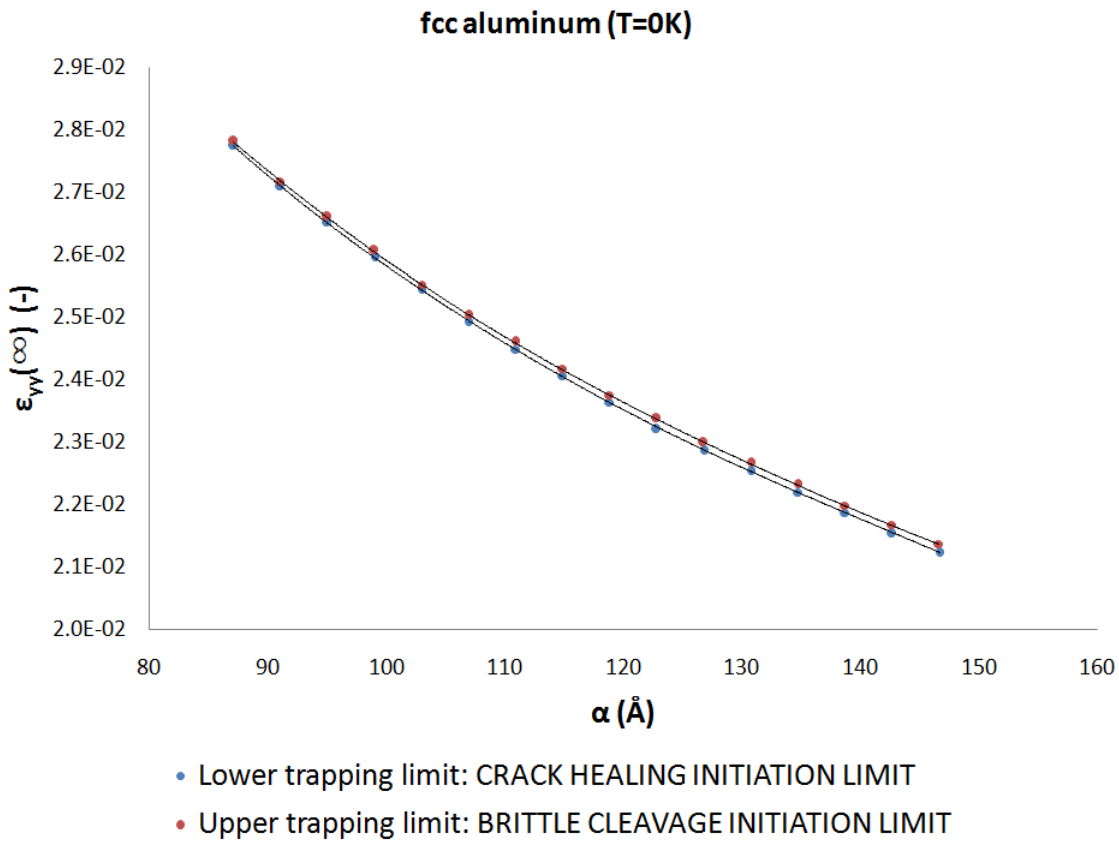

Figure V.5: Lattice trapping effect of $(010)[001]$ nano-sized cracks in fcc aluminium at $T = 0K$. The red circles present the brittle cleavage initiation limit (upper trapping limit), while the blue circles correspond to the crack healing initiation limit (lower trapping limit) of the crack configurations. The strain range between the lower and the upper trapping limit determine the stability region, region where the crack configurations are in a mechanical equilibrium.

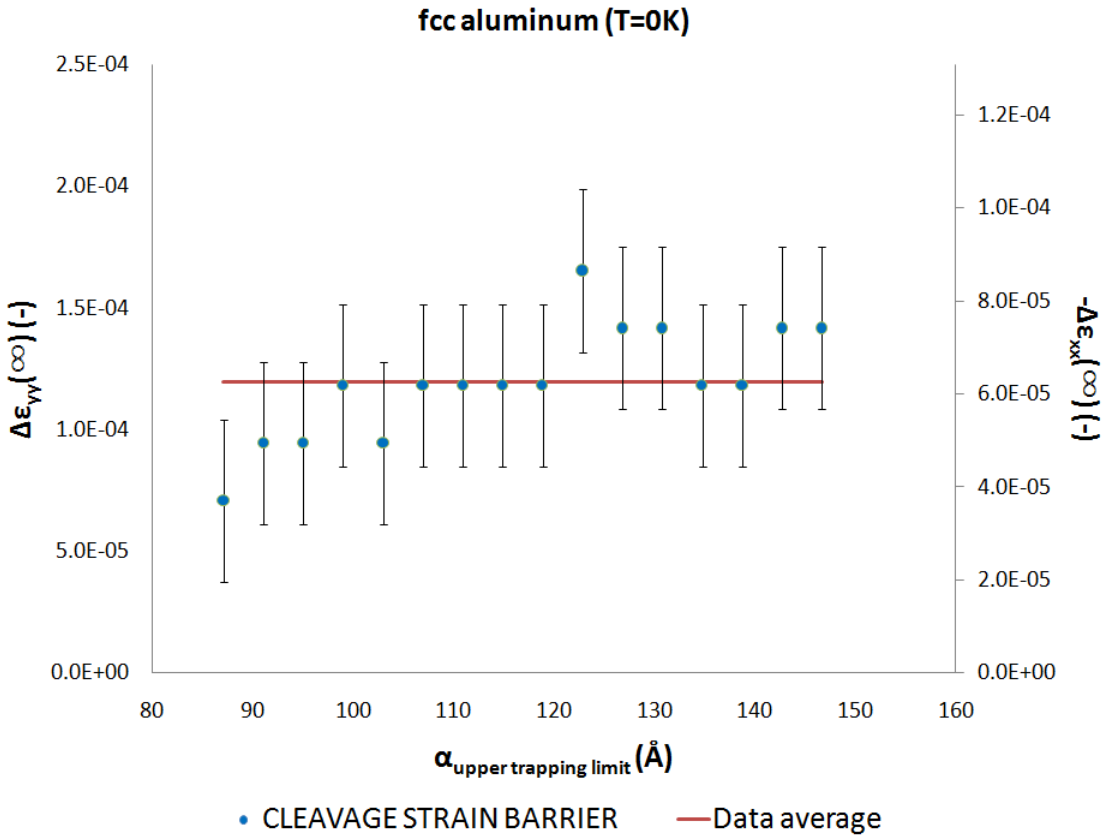

Figure V.6: The strain range of the stability zone of $(010)[001]$ nano-sized cracks in fcc aluminium at $T = 0K$ due to the lattice trapping effect. This strain increment corresponds to the activation barrier for brittle propagation since the upper trapping limit of the stability zone is the threshold of cleavage initiation of the crack configurations.

The lattice trapping effect is also observed in bcc iron crack models. However, simulations revealed significant differences in the mechanical response of cracks in α-iron and aluminium: all cracks in aluminium behave similarly whereas three different mechanical response sequences are observed in α-iron as a function of the crack length. The first (type I) corresponds to models with the shortest cracks, for which none equilibrium configuration exists. In particular, for low applied deformation these models exhibit crack closing, while for high applied deformation they accommodate applied strain by dislocation formation at the crack-tip region. The second (type II) corresponds to cracks with intermediate lengths. In this group a stability region exists between two strain thresholds, separating the crack closing and dislocation generation mechanical responses. This stability region corresponds to a lattice trapping effect which does not characterizes the crack cleavage propagation, since the upper trapping limit relates to the formation of dislocations at the crack-tip region. Finally, a third type of mechanical response sequence (type III) is observed in models with the largest crack lengths. In this group, the lattice trapping effect is present with a similar

fashion to aluminium models, i.e. the upper trapping limit corresponds to crack propagation via cleavage (§3.5.3) on the crack plane. In addition, by increasing the applied deformation, the cleavage propagation transformed to dislocation formation at the crack-tip. Representative examples of the three types of mechanical response sequence are illustrated in figures V.7.

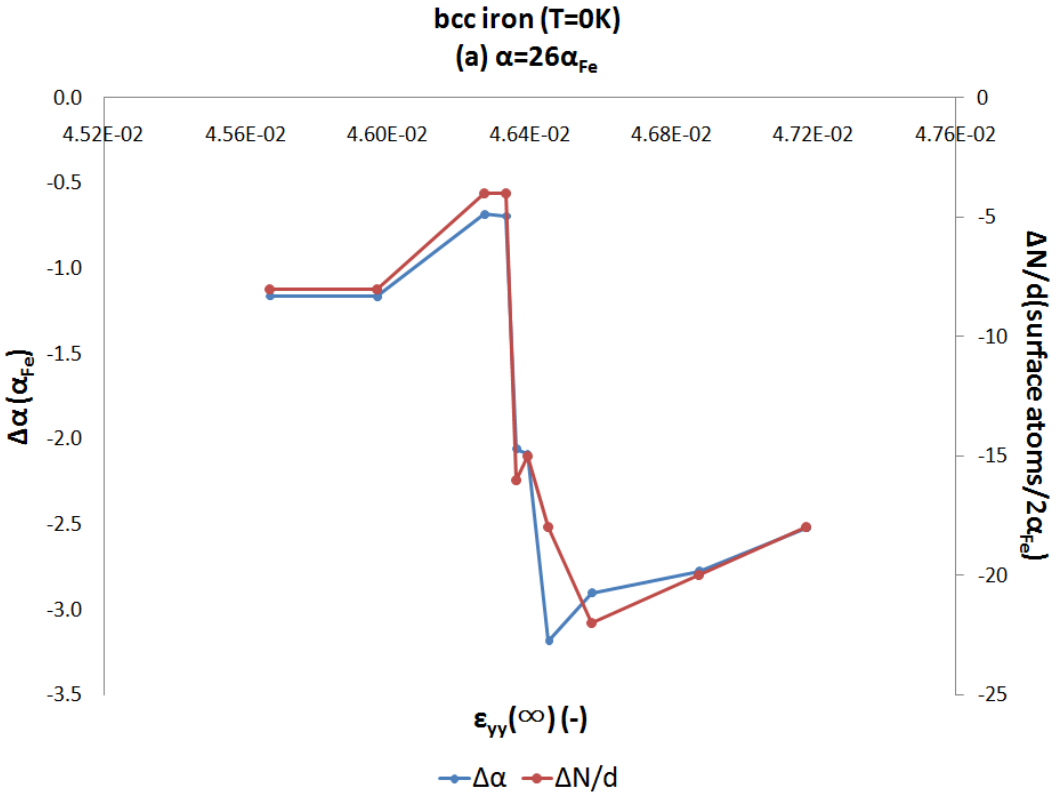

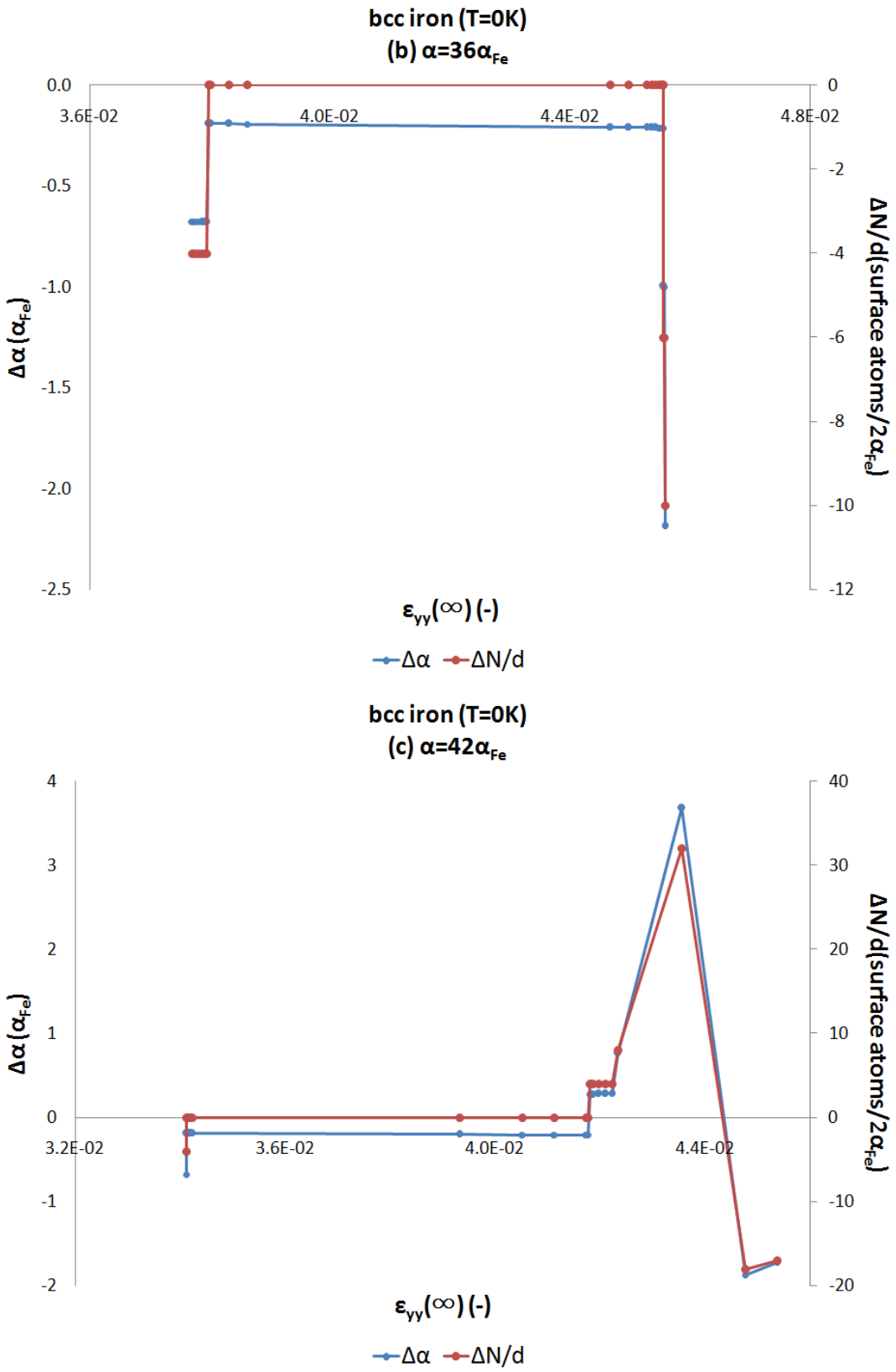

Figure V.7: Evolution of the crack half-length of $(010)[001]$ nano-sized cracks in bcc iron in respect to the applied deformation at $T = 0K$. Representative examples of the different types of mechanical response sequence in (a) short, (b) intermediate and (c) long crack-length models.

All dynamic phenomena associated with non-equilibrium crack configurations will be analyzed in detail later in this chapter (§5.7.1). Starting from equilibrium cracks in bcc iron, the strain conditions for:

(i) the crack healing process,

(ii) the brittle cleavage propagation, and,

(iii) the dislocation generation at the crack-tip region

can be estimated as a function of the crack length as illustrated in figure V.8.

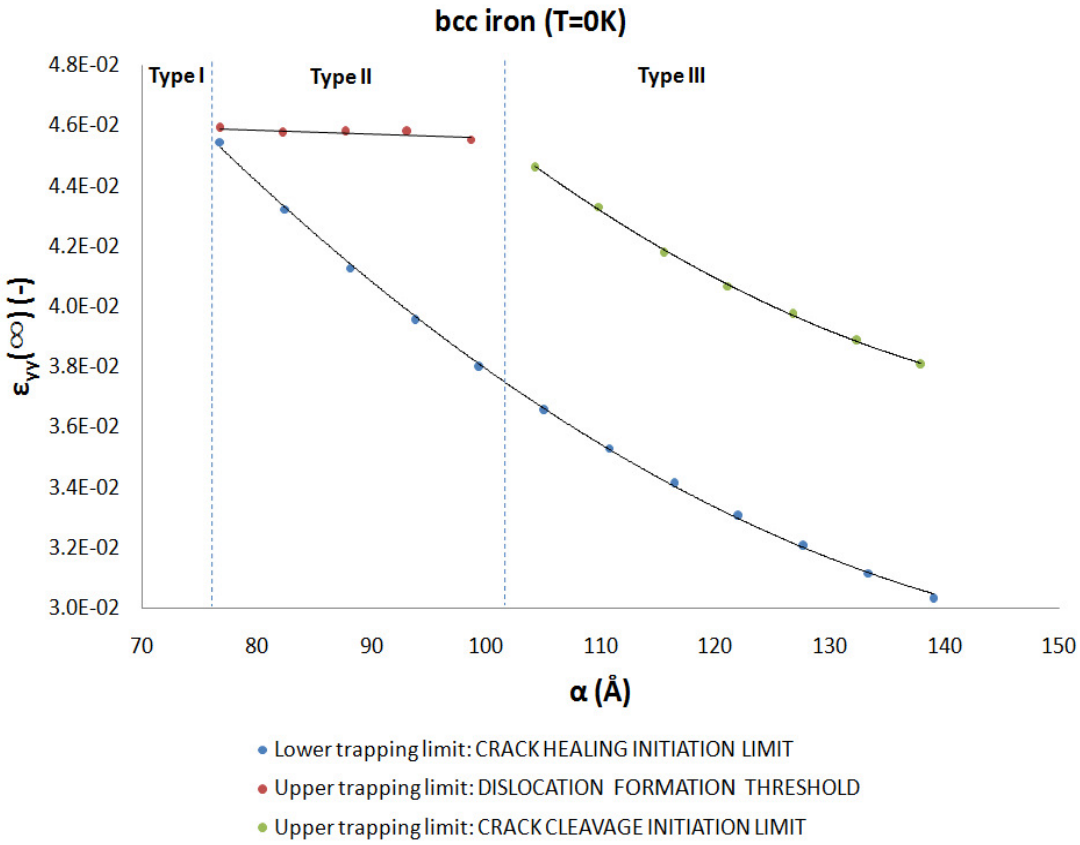

Figure V.8: Lattice trapping effect of $(010)[001]$ nano-sized cracks in bcc iron at $T = 0K$. The red circles present the dislocation formation strain threshold (upper trapping limit), the green circles the brittle cleavage initiation limit (upper trapping limit), while the blue circles correspond to the crack healing initiation limit (lower trapping limit) of the crack configurations in respect to the crack length. The strain range between the lower and the upper trapping limit determine the stability region, region where the crack configurations are in a mechanical equilibrium.

In addition, the lattice trapping strain barriers for dislocation formation and brittle cleavage propagation can be also determined in relation to the crack size (figure V.9).

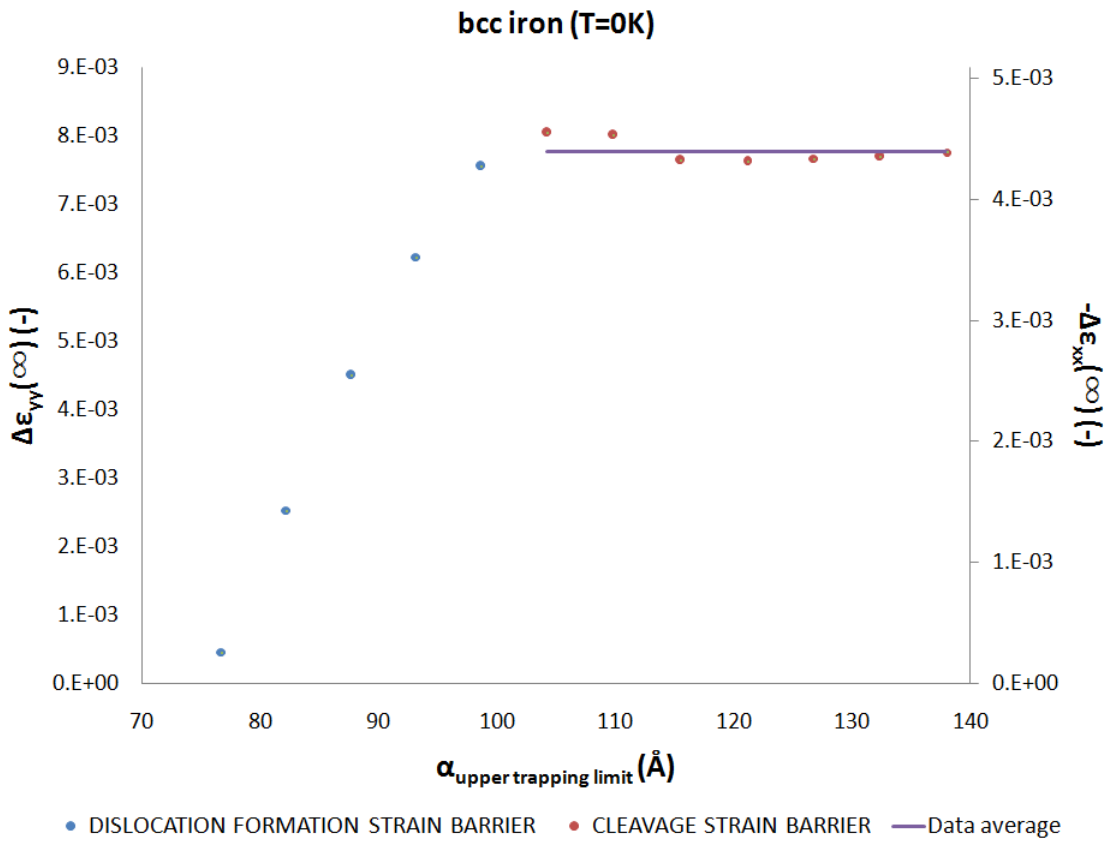

Figure V.9: Strain range of the stability zone of $(010)[001]$ nano-sized cracks in bcc iron at $T = 0K$ due to the lattice trapping effect. The blue circles correspond to the strain barrier for dislocation formation at the crack-tip while the red circles correspond to the strain barriers for brittle cleavage propagation of the crack configurations with respect to the crack length.

Results in figure V.8 show that the crack stability trapping limits for cleavage propagation (green data) and healing (blue data) processes decrease with increasing the crack length, in consistency with Griffith's equilibrium criterion [GRI1920]. Moreover, figure V.8 demonstrates that the strain threshold for dislocation formation at the crack-tip, ε_{yy}^{DIS}, is practically constant (red data). Consequently, the upper trapping limit of the unstable equilibrium cracks divides in to two parts. The first corresponds to the dislocation formation onset at the crack-tip region, while the second corresponds to cleavage propagation (§3.5.3). The ε_{yy}^{DIS} is responsible for the non-existence of equilibrium cracks with half-length less than $\sim 76\text{Å}$. In addition, the existence of ε_{yy}^{DIS} causes reduction of the lattice trapping strain barrier as it can be observed in figure V.9 (blue data). Nevertheless, the complete amplitude of the lattice trapping barrier corresponding to the crack propagation is an almost constant quantity with the crack length (red data on the figure V.9), or equivalently the loading level, suggesting that the resistance for a crack to cleavage is an intrinsic property of the system. Having observed the same behaviour of the lattice trapping

strain barrier for both the studied systems suggest that the statement above has generic validity. More importantly, the comparison of simulation results obtained from the metals studied reveals that the lattice trapping barrier of cracks bcc iron is significantly larger compared to the respectively in fcc aluminium:

$$\frac{\Delta\varepsilon_{yy(\infty)}^{(Fe)}}{\Delta\varepsilon_{yy(\infty)}^{(Al)}} = \frac{\varepsilon_{yy(\infty)}^{Upper(Fe)} - \varepsilon_{yy(\infty)}^{Lower(Fe)}}{\varepsilon_{yy(\infty)}^{Upper(Al)} - \varepsilon_{yy(\infty)}^{Lower(Al)}} \cong 65$$

where $\Delta\varepsilon_{yy(\infty)}$ are the strain increments between the cleavage propagation and healing processes strain thresholds. This result implies that a pre-existing $(010)[001]$ crack inside bcc iron is mechanically much more ''stable'' upon changes in loading compared to the same configuration in fcc aluminium, due to the difference in their lattice trapping barriers.

5.1.2. Empirical examination of nano-sized cracks mechanical stability

By obtaining quasi-static equilibrium cracks in both metals, at the atomic scale, we are allowed to study their mechanical stability. As already mentioned, according to the linear elasticity, the mechanical stability of a mode I crack is described by the criterion of Griffith (equation V.1), which expresses a linear function between the quantities a_c and $1/C\sigma_{yy,c}^2$. According to this stability criterion, the equilibrium state of a crack of a specific length is unique and its nature is unstable (figure II.7). However, simulation results, of the studied metals, have shown that the crystalline lattice gives rise to the lattice trapping phenomenon, which enhances and expands the mechanical stability of cracks around their analytically unstable equilibriums. As already presented, the LTE forms a stability strain (or stress) region for a crack, under mode I deformation, which is bounded by the upper and lower trapping limits. Hence, the LTE transforms the crack's equilibrium from unique and unstable to finite and stable.

Despite of this change on the crack's mechanical stability, we want to examine whether the equilibrium cracks of the studied metals can still be described by a linear relationship, $a = f\left(1/C\sigma_{yy}^2\right)$, in analogy to the elastic approximation of Griffith's criterion (equation V.1). Since every crack has multiple equilibrium configurations within the lattice trapping region, the investigation was performed for those corresponding to the upper and lower trapping limits. Quasi-static configurations, corresponding to both trapping limits, can provide the

values of a as well as the strain components $\varepsilon_{ii}(i = x, y)$ of the applied mode I deformation. In addition, by applying homogeneously the $\varepsilon_{ii}(i = x, y)$ components to a crack-free (or perfect) lattice, the quantities C and σ_{yy}, corresponding to the macroscopic crystal containing the nano-sized crack, can be determined (Chapter IV). Consequently, atomistic results allow the empirical examination of the $a = f\left(1/C\sigma_{yy}^2\right)$ relationship to be performed for the equilibrium crack configurations corresponding to each trapping limit.

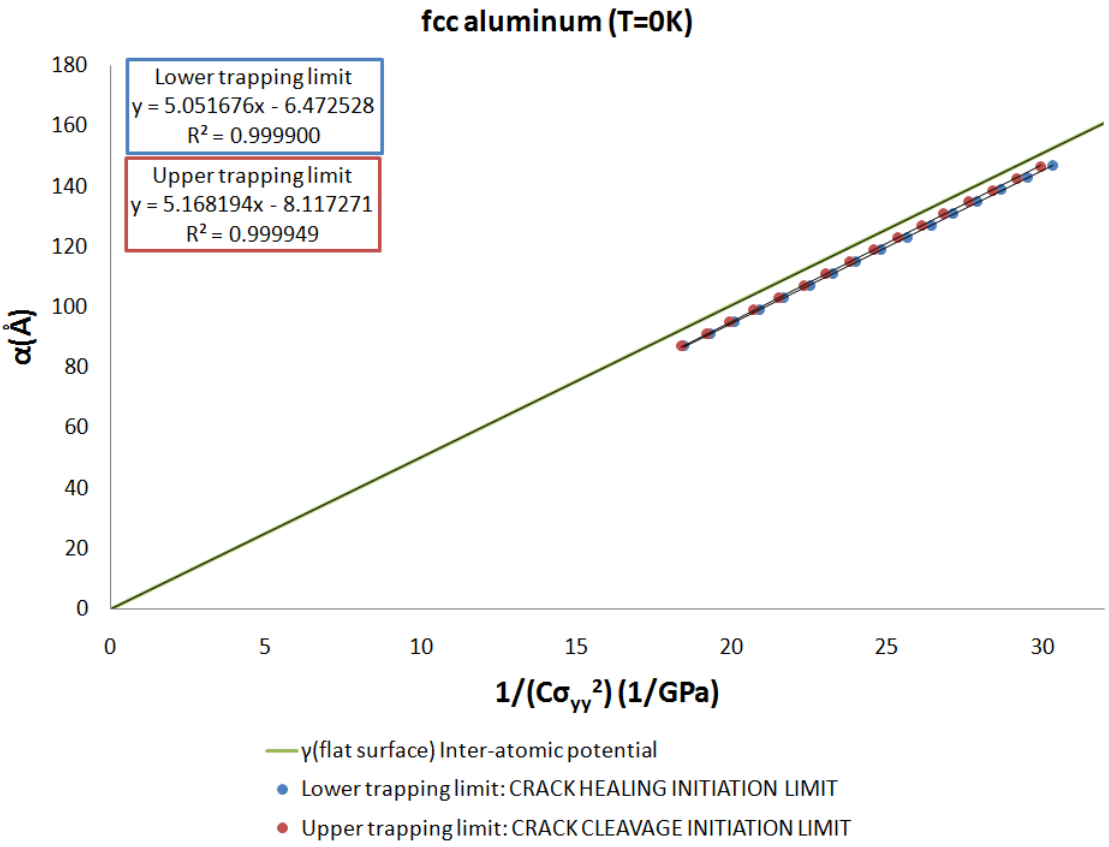

Figure V.10: Examination of the linear relation of the Griffith's criterion from quasi-static $(010)[001]$ nano-sized cracks under mode I deformation in fcc aluminium at $T = 0K$. The red circles present the data correspond to the brittle cleavage initiation limit (upper trapping limit), where the blue circles correspond to the crack healing initiation limit (lower trapping limit) of the crack configurations. In addition, the continuous green line represents the Griffith's criterion by using the surface energy of a perfect flat (010) crystallographic plane given by the inter-atomic potential [ZAC2017].

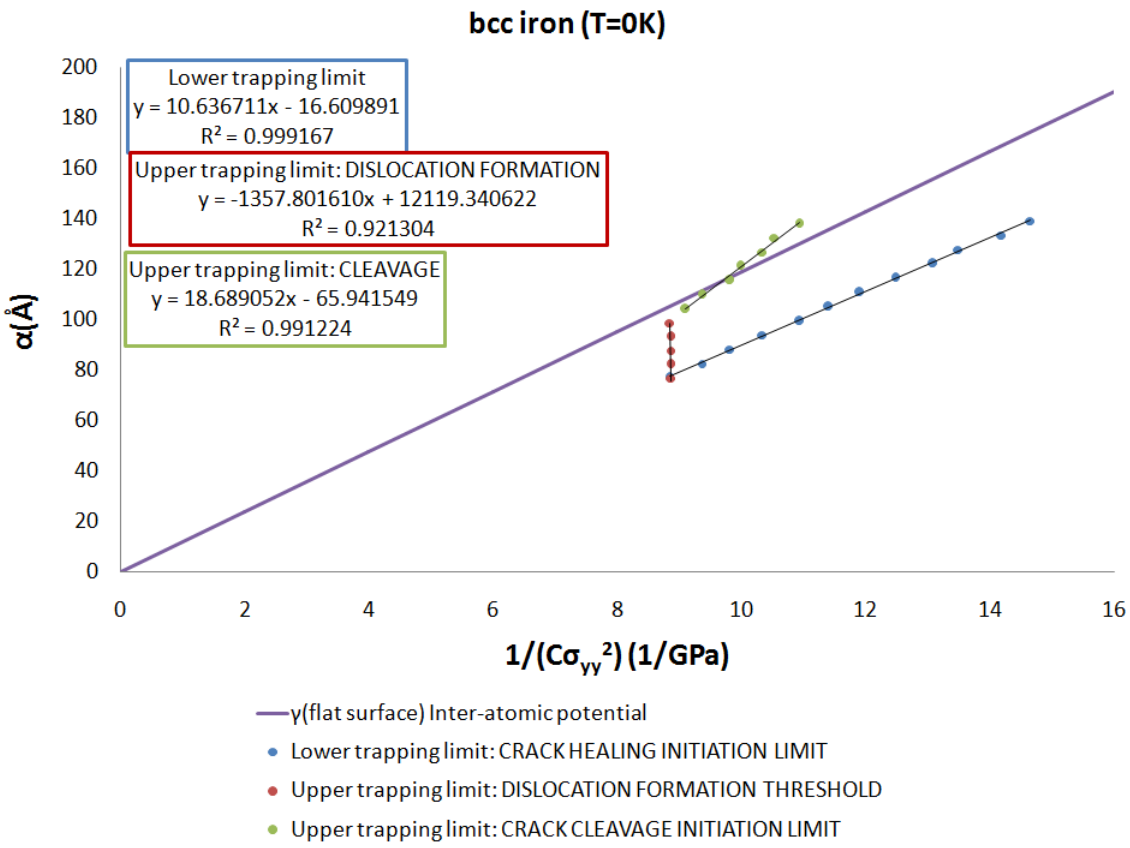

Figure V.11: Examination of the linear relation of the Griffith's criterion from quasi-static $(010)[001]$ nano-sized cracks under mode I deformation in bcc iron at $T = 0K$. The red circles present the data corresponding to the dislocation formation strain threshold (upper trapping limit), the green circles correspond to the brittle cleavage initiation limit (upper trapping limit), while the blue circles correspond to the crack healing initiation limit (lower trapping limit) of the crack configurations. In addition, the continuous violet line represents the Griffith's criterion by using the surface energy of a perfect flat (010) crystallographic plane given by the inter-atomic potential [PON2007].

Simulation results in both metals (figures V.10 and V.11) reveal that the lower trapping limit that corresponds to the healing initiation and the upper trapping limit that corresponds to the cleavage propagation onset demonstrate that the interrelation between the quantities a and $1/C\sigma_{yy}^2$ is practically linear ($R^2 > 0.9999$ for aluminium and $R^2 > 0.99$ for iron). This result demonstrates that despite the fact that the obtained equilibrium nano-sized cracks are different compared to a Griffith's crack (§2.3), in terms of their stability, they still behave elastically to their lattice trapping limits. Based on this result, the slope of the obtained linear equations, $a = f\left(1/C\sigma_{yy}^2\right)$, corresponding to each lattice trapping limit, can be used to approximate an effective value for the surface energy of the crack faces, γ, through the use of equation V.1.

The analysis of the simulation data shows that the effective surface energy of the quasi-static $(010)[001]$ configurations correspond to the lower trapping limit, γ_{Lower}, in fcc

aluminium is almost identical with the free surface energy of the flat $\{100\}$ crystallographic plane, γ_{flat}, calculated by the inter-atomic potential (Table V.1). In addition, the crack configurations of the upper trapping limit correspond to an effective surface energy, γ_{Upper}, which is slightly higher compared to the γ_{Lower}, by an amount equal to $\Delta\gamma = 0.183GPa \cdot \text{Å}$, where $\Delta\gamma = \gamma_{Upper} - \gamma_{Lower}$ (Table V.1). The $\Delta\gamma$ positive increment can be attributed to surface tension terms [MUR1975], since the number of broken bonds is identical for both lower and upper trapping limit configurations. Nevertheless, since the lattice trapping effect in aluminium is characterized by a narrow strain-stress barrier ($\Delta\sigma_{yy}/G_{\langle 010\rangle} \sim 10^{-4}$), the $\Delta\gamma$ between the upper and lower trapping limit is relatively small ($\Delta\gamma = 2.3\% \cdot \gamma_{Lower}$). The fact that both the γ_{Lower} and γ_{Upper} approximate the γ_{flat}, implies that both the lattice trapping limits in aluminium are located very close to Griffith's condition. Hence, the $\gamma_{Lower} \cong \gamma_{Upper} \cong \gamma_{flat}$ empirical result constitutes an ''indirect'' verification of the Griffith's criterion in aluminium, despite the existence of the lattice trapping effect.

For quasi-static $(010)[001]$ cracks in bcc iron the lattice trapping strain barrier is significantly higher compared to aluminium ($\Delta\sigma_{yy}/G_{\langle 010\rangle} \sim 10^{-3}$), hence resulting to larger differentiation in surface tension terms between the two lattice trapping limits. Consequently, the $\Delta\gamma$ between the upper and lower trapping limit is relatively high ($\Delta\gamma = 75.7\% \cdot \gamma_{Lower}$). Hence, despite the fact that the calculated value of γ_{Lower} is relatively close to the value of flat $\{100\}$ crystallographic plane, γ_{flat}, calculated by the inter-atomic potential, the γ_{Upper} is notably larger (Table V.1). This result indicates that the magnitude of the lattice trapping barrier is related to the deviation of the upper trapping limit from Griffith's condition, where $\gamma = \gamma_{flat}$. On the other hand, the simulation results imply that the lower trapping limit is relatively close to Griffith's condition ($\gamma_{Lower}/\gamma_{flat} \cong 0.9$). This finding can be justified from the fact that the lower trapping limit configurations correspond to the minimum applied stress required to stabilize a crack with a specific length; hence, they contain the minimum stored elastic energy into the system, a fact that is minimizing the deviation from Griffith's prediction. Therefore, the $\gamma_{Lower} \approx \gamma_{flat}$ empirical result can considered to be an ''indirect'' verification of the criterion of Griffith in bcc iron.

Table V.1: Calculation of the crack faces surface energy of quasi-static $(010)[001]$ nano-sized cracks under mode I deformation in fcc aluminium and bcc iron at $T = 0K$

Crack faces surface energy	**fcc aluminium**	**bcc iron**
$\gamma_{flat}[GPa \cdot \text{Å}]$ (potentials)	7.898[ZAC2017]	18.678[PON2007]
$\gamma_{Lower(Healing)}[GPa \cdot \text{Å}]$ (calculations)	7.935(+0.47% γ_{flat})	16.708(-10.55% γ_{flat})
$\gamma_{Upper(Cleavage)}[GPa \cdot \text{Å}]$ (calculations)	8.118(+2.79% γ_{flat})	29.357(+57.17% γ_{flat})
$\Delta\gamma[GPa \cdot \text{Å}] = \gamma_{Upper} - \gamma_{Lower}$	0.183	12.649

The comparison of the $\Delta\gamma$ of the studied metals shows that the ratio:

$$\frac{\Delta\gamma^{(Fe)}}{\Delta\gamma^{(Al)}} \cong 69$$

which is of the same order of magnitude with the ratio $\Delta\varepsilon_{yy(\infty)}^{(Fe)}/\Delta\varepsilon_{yy(\infty)}^{(Al)}$. This comparison is another indication that the LTE in crystalline materials can cause an increase of γ. Consequently the critical value of γ, i.e. the γ_{Upper}, which corresponds to the triggering of the crack propagation, is larger compared to γ_{flat}. Simulation findings of the previous paragraphs show that despite the existence of the LTE, which enhances the mechanical stability of a crack, the equilibrium crack models of aluminium and α-iron behave accordingly to the linear elasticity predictions:

(i) linear relation of $a = f\left(1/C\sigma_{yy}^2\right)$ for both the lattice trapping limits, and

(ii) $\gamma_{Lower} \approx \gamma_{flat}$

Based on the linear $a = f\left(1/C\sigma_{yy}^2\right)$ relation holding between the upper and lower trapping limits, it can be concluded that atomic crack models with different a are mechanically equivalent. This conclusion applies for both studied materials. More importantly, by empirically approximating the Griffith's condition at a satisfactory level for the lower trapping limit configurations, in both metals ($\gamma_{Lower}/\gamma_{flat} \cong 1$ for aluminium and $\gamma_{Lower}/\gamma_{flat} \cong 0.9$ for α-iron), allows us to establish a ''mechanical homology'' with macroscopic cracks (Chapter II), more relevant to the experiments. In particular, it can be assumed that the empirical linear $a = f\left(1/C\sigma_{yy}^2\right)$ functions, which were found to characterize the nano-sized cracks corresponding to each lattice trapping limit, have extensive validity up to crack lengths, a, of macroscopic dimensions. Based on this assumption, the equilibrium cracks of macroscopic length, corresponding to the lattice

trapping limits, are located on the linear extrapolation of the respective linear $a = f\left(1/C\sigma_{yy}^2\right)$ function, obtained from the simulation results (figures V.10 and V.11). With the above suggestion, the study of atomic-sized cracks can be considered generic in terms of the obtained results, as well as the conclusions. This kind of ''space scales coupling'' constitutes the cornerstone of the present work.

5.2. Brittle fracture criterion - Working hypothesis

Simulation results have shown that the applied tension required to stabilize the nano-sized $(010)[001]$ cracks, in both metals, is about a few Giga-Pascals (figure V.12).

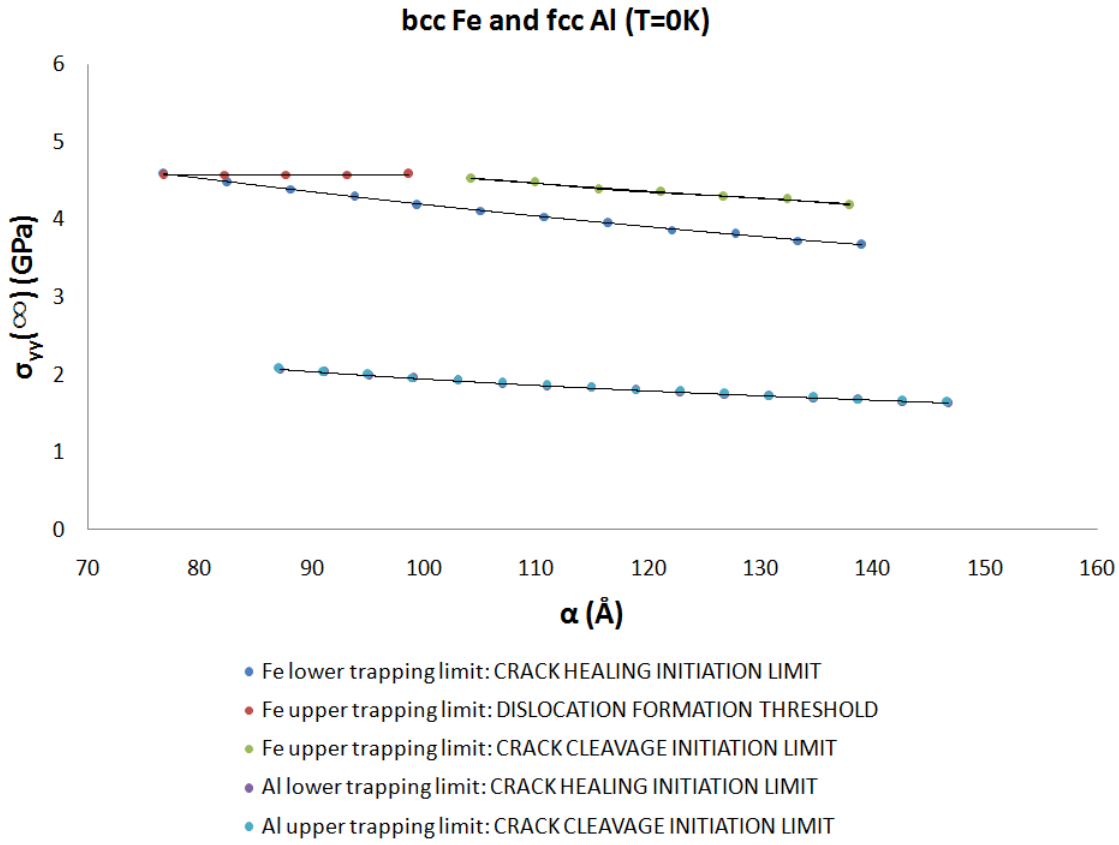

Figure V.12 Lattice trapping effect of $(010)[001]$ nano-sized cracks in fcc aluminium and bcc iron at $T = 0K$. Stability region for both systems corresponds to loading conditions of order of magnitude of Giga-Pascal. Such loading conditions are comparable with the elastic constants of aluminium and iron (Table III.1).

These loading conditions are comparable with the values of the elastic constants (Table IV.1), way above values reached in laboratory experiments, thus suggesting that the present modelling is not related to the experimental reality. However, the above mechanical homology establishes that whenever the atomistic models comply with, these are exactly equivalent to their macroscopic counterparts. According to the empirical $a = f\left(1/C\sigma_{yy}^2\right)$

relations determined in §5.1.2, macroscopic-sized cracks, in both studied metals, amount a few Mega-Pascals; values of loading conditions which can be definitely achieved in mechanical tests. Likewise, the $a = f\left(1/C\sigma_{yy}^2\right)$ relations imply that the extreme loading conditions of the atomistic models are due solely to the nano-sized dimensions of the cracks; a behaviour in consistency to the Griffith's condition. However, the problem is still not solved, how under these extreme loading conditions the mechanical response of the two metals at $T = 0K$ can be handled. In relation with this, it is worth reminding that in literature Griffith's condition is a ''brittle fracture criterion'', as it relates the critical stress for the propagation of a crack with its length [GRI1920, TYS1973, TYS1977b, DEC1983, CHE1990, FIS2001, GUO2006]. This result is based on the fact that the mechanical equilibrium state of a crack within an ideally brittle system is uniquely defined and hence, coincides with the onset of crack's instability. In addition, Griffith's criterion entails that diverging the crack length, the critical applied stress for propagation of the crack via cleavage vanishes:

$$(V.1) \Rightarrow If\ a_c \longrightarrow \infty \Rightarrow \sigma_{yy,c} \longrightarrow 0 \qquad (V.3)$$

Accordingly, all materials containing cracks would be brittle under stress if the lattice trapping effect were not existed! This phenomenon expresses the resistance of the crystalline lattice for the activation of the cleavage propagation of an initially equilibrium crack, which is quantified via a strain or stress barrier, $\Delta\varepsilon_{ii(\infty)}$ (or $\Delta\sigma_{ii(\infty)}$, where $i = x, y, z$). Consequently we can conclude that the Griffith's criterion can describe only the ''mechanical stabilization'' of a crack inside the system, but is unable to provide the additional strain-stress barrier for activating its cleavage propagation (Chapter II). According to this, the critical strain-stress components that correspond to cleavage propagation onset of a crack are given by:

$$\sigma_{ii,critical} = \sigma_{ii(\infty)} + \Delta\sigma_{ii(\infty)} \text{ or } \varepsilon_{ii,critical} = \varepsilon_{ii(\infty)} + \Delta\varepsilon_{ii(\infty)} \qquad (V.4)$$

where the first terms correspond to the stresses-strains required for the crack's mechanical stabilization at the lower trapping limit, which approximates the Griffith's condition (§5.1.2), and the second terms correspond to the stresses-strains required to overcome the lattice trapping barrier. More importantly, based on equation V.3, which constitutes a good approximation for macroscopic-sized cracks, the critical strain-stress conditions are determined for their brittle propagation only by the lattice trapping strain-stress increments:

$$If\ a_c \longrightarrow \infty \Rightarrow \sigma_{ii,critical} = \Delta\sigma_{ii(\infty)}\ \text{ or }\ \varepsilon_{ii,critical} = \Delta\varepsilon_{ii(\infty)} \qquad (V.5)$$

For this reason, in the present study, the lattice trapping barrier substitutes the Griffith's criterion, as the ''criterion of brittleness'' in crystalline systems with pre-existing equilibrium cracks.

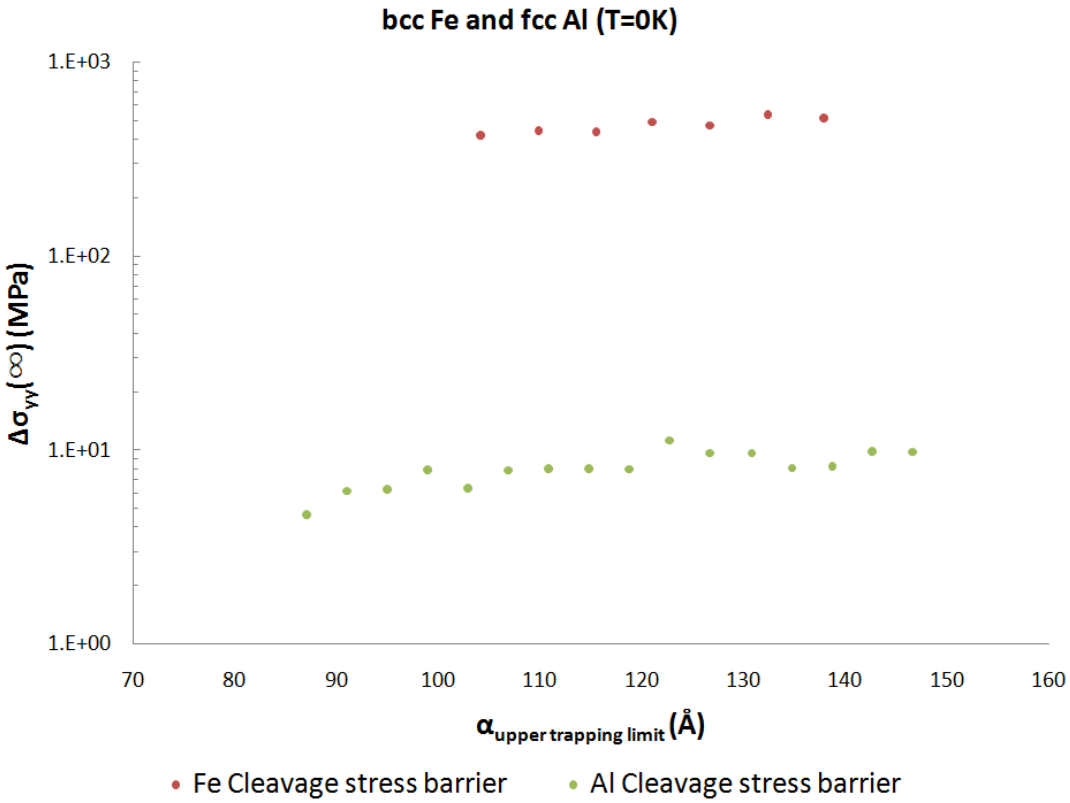

Figure V.13: Lattice trapping stress barriers for cleavage propagation of $(010)[001]$ nano-sized cracks in fcc aluminium and bcc iron at $T = 0K$.

Simulation results (figure V.13) show that the lattice trapping stress increment along the tension direction, $\Delta\sigma_{yy(\infty)}$, in fcc aluminium and bcc iron, amounts Mega-Pascals ($\sim 8MPa$ for aluminium and $\sim 500MPa$ for iron) so that the extreme loading conditions, stabilizing a nano-sized crack, decouple from the much more reasonable strain-stress limits, defining the stability of any given crack, related to lattice trapping. Accordingly, we make the following ''working hypothesis'': We consider that the lattice trapping strain barrier ($\Delta\varepsilon_{ii(\infty)}$, $i = x, y, z$) for cleavage propagation is an intrinsic property of the systems studied; hence, $\Delta\varepsilon_{ii(\infty)}$ are constant and independent from the crack length allowing the description of the mechanical conditions for brittle propagation of the homologous macroscopic-sized equilibrium cracks, which pre-exist inside the systems. In conclusion, the achievement of the scale coupling in space allowing us: (i) first to address the problem of the

extreme loading conditions required to stabilize nano-sized cracks, and, (ii) second to realize that the conditions for the brittle propagation (§3.5.3) of an equilibrium macroscopic-sized crack are determined only by the lattice trapping barrier, which potentially contains the information of the mechanical response of the system.

5.3. Validity of the models: Compatibility at the boundary conditions

Before proceeding to the analysis of the atomistic results it is essential to ensure their reliability through the validity of the numerical models. As described in Chapter III, the atomistic crack configurations were constructed by the use of CVA, in the framework of continuum mechanics. However, it is widely recognized that the obtained crack displacement field is not applicable at the crack-tip region, since the analytic solution of the stress field nearby the crack-tip singularity diverges. Moreover, knowing that the continuum mechanics considers the matter as continuous and homogeneous, the discrete character of the atomistic defect configuration, especially close to the crack-tip and the crack faces, cannot be described appropriately neither. Nevertheless, since the spatial range of non-linearity close to the crack-tip region is atomistic [GUO2006], the far-displacement field of the crack configuration can be appropriately described by continuum mechanics. By using the energy minimization technique, the initial configuration of the crack, according to the CVA, relaxes to its ground state, whose atomic arrangement is based on the inter-atomic interactions. In this way, the atomistic simulation allows addressing the stress singularity at the crack-tip position and simultaneously accounts for the discrete character of the crystalline crack-containing system. A crucial step in this process is the proper integration of the mechanical loading, applied at the macro-scale, on the atomic configuration of the crack. To this end, the crack displacement field, provided by CVA, has been applied on the numerical models through the employment of fixed boundary conditions (Chapter III). However, according to the aforementioned, it is important that the fixed boundaries should be located at a sufficient distance from the crack. In this way, the relaxation of the crack faces and the crack-tip region will not cause a displacement field mismatch at the boundary conditions limit, thus avoiding the induction of non-physical constraints into the model, which possibly affect the applied loading. Despite the precautions that have been taken to address this issue (Chapter III), it is necessary to verify the compatibility between the

dynamic region of the model, where the simulation is performed, and the fixed-displacement boundary conditions.

The confirmation of a valid implementation of the boundary conditions or equivalently of the applied loading can be obtained by either the direct comparison of the initial and relaxed crack displacement fields and/or examining the energy maps of atom sites close to the fixed boundaries. These tests have been systematically employed for all the studied equilibrium crack configurations. The first test consisted in calculating the three-dimensional difference of the atomic positions or misfit, dr, between the initial and relaxed configurations. In aluminium (figure V.14), it is observed that far from crack faces, the misfit is negligibly small and thus indicating that continuum mechanics correctly predicts the displacement field. On the other hand, close to the crack-tip, the corresponding displacement fields are different.

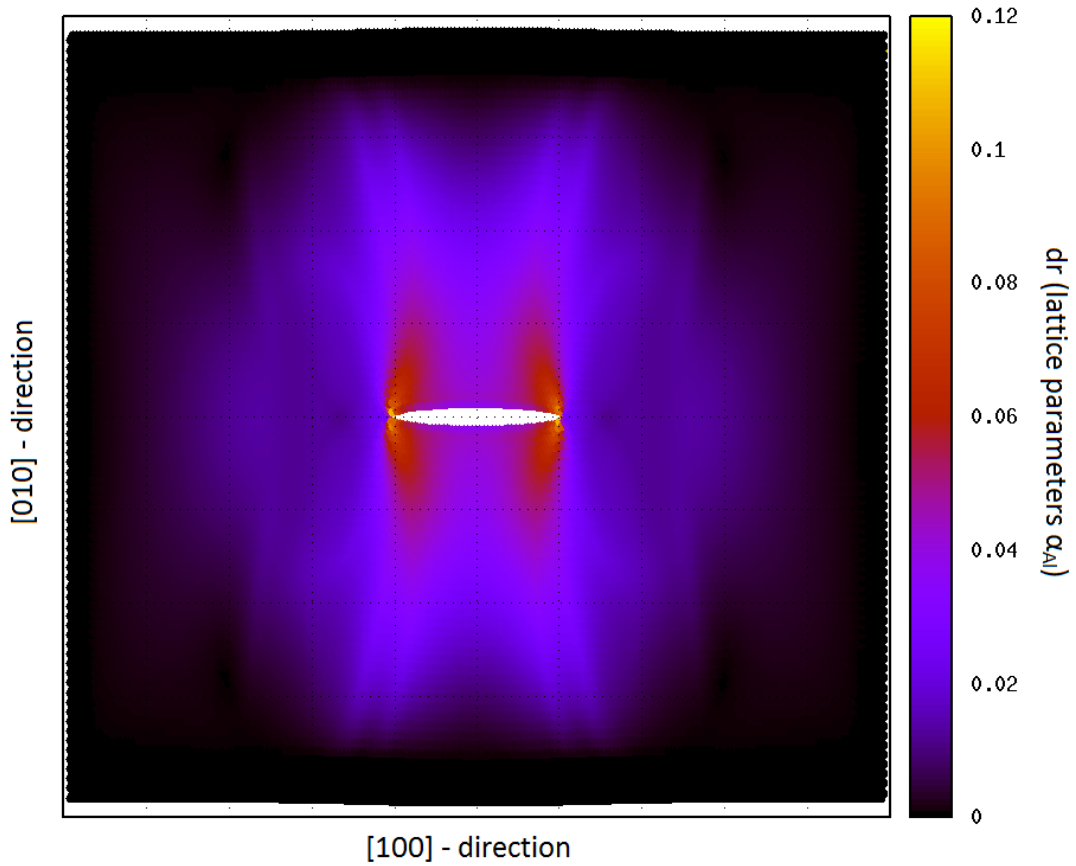

Figure V.14: The difference of 3D-displacements between continuum mechanics and localized-damping minimization of energy for a $(010)[001]$ crack in fcc aluminium at $T = 0K$. The initial crack half-length according to linear elasticity continuum mechanics is equal to 22 lattice parameters a_{Al} (where $a_{Al} = 4.02\text{Å}$).

Simulated cracks in α-iron behave similarly (figure V.15). A comparison of the two systems reveals that the maximum values of misfit in aluminium are located exactly at the crack-tip position, where in α-iron they are located between the $\{110\}$ planes at the crack-tip region.

Moreover, the larger the applied loading on the models, the greater misfit is observed; hence, in iron larger misfit values are found in the crack-tip region as compared to aluminium. However, the misfit observed close to the static boundaries, in both systems, is comparable with the numerical errors of the minimization technique.

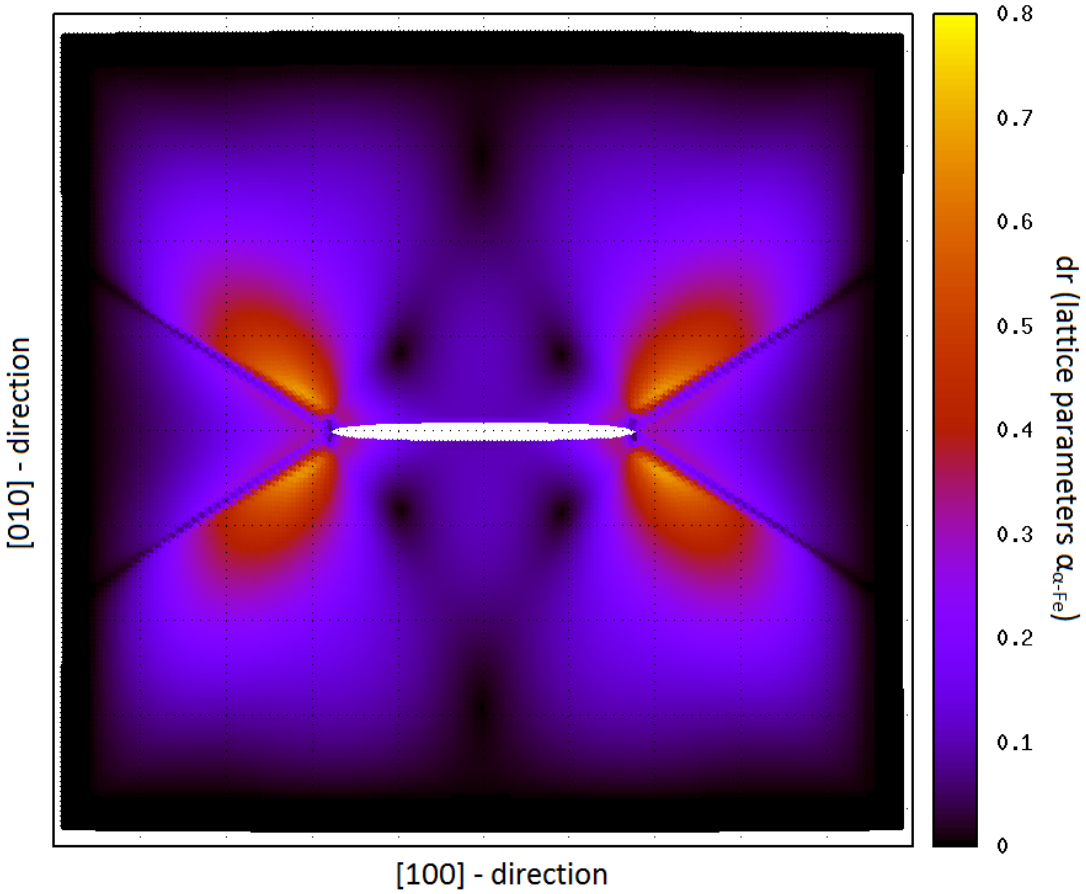

Figure V.15: The difference of 3D-displacements between continuum mechanics and localized-damping minimization of energy for a $(010)[001]$ crack in bcc iron at $T = 0K$. The initial crack half-length according to linear elasticity continuum mechanics is equal to 38 lattice parameters a_{Fe} (where $a_{Fe} = 2.86\text{Å}$).

Analogous results have been obtained using the second test. The investigation of the energy distribution of the crack models, in both metals (figures V.16 and V.17), demonstrates that the potential energy of the atoms varies continuously across the dynamic and static regions in the models! These observations suggest the existence of compatibility, in terms of displacement field and energy, between the free-dynamic region of interest and the fixed-displacement boundary conditions. Therefore, it can be concluded that fixed boundaries do not cause unphysical constraints, thus ensuring that the loading is correctly applied to the crack configuration. This implies that the crack displacement field provided by continuum mechanics is valid at the atomic scale, thus validating the numerical models, the simulation methodology and the reliability of the simulation findings. Threshold strains

defining the stability region of the studied cracks are thus physically correct and suggest that the observed mechanical behaviour of aluminium and α-iron upon loading at $T = 0K$ is realistic.

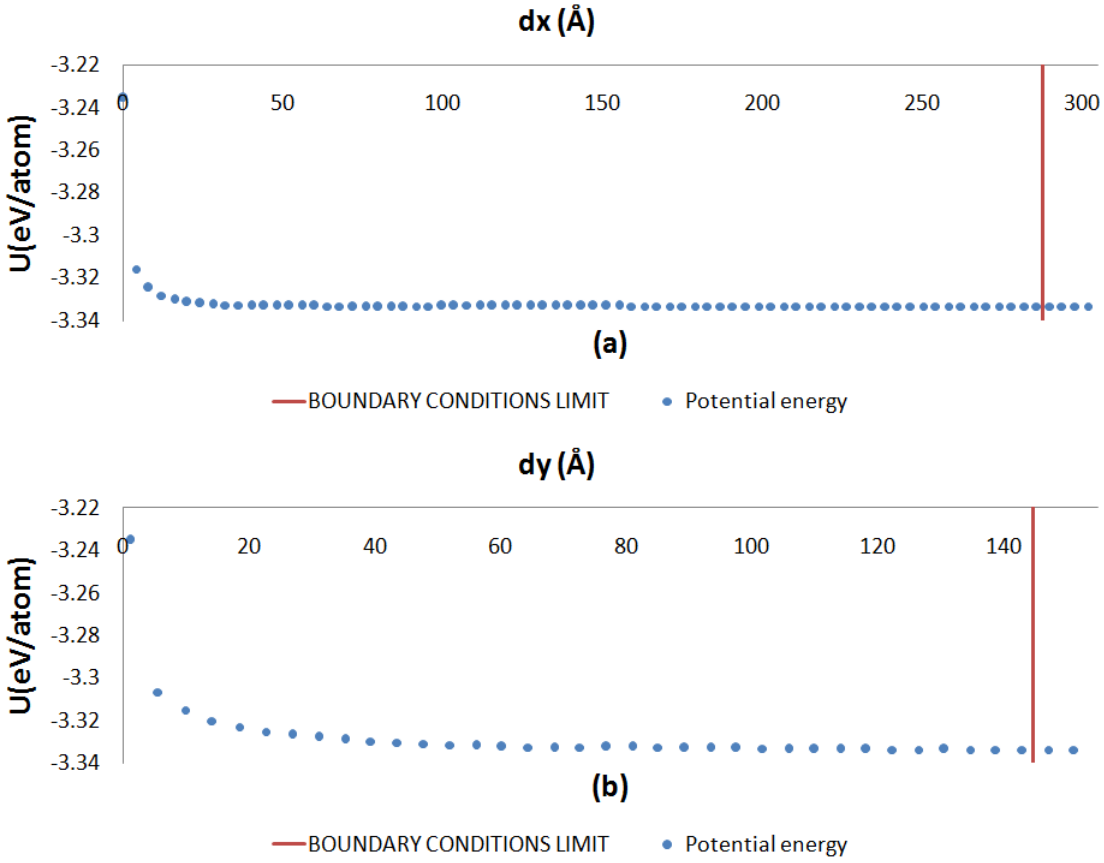

Figure V.16: Investigation of the potential energy of the atoms, of a $(010)[001]$ crack configuration in fcc aluminium, in relation to the distance from the crack-tip along (a) the $x = [100]$ and (b) $y = [010]$ direction. The initial crack half-length to according linear elasticity continuum mechanics is equal to 22 lattice parameters a_{Al} (where $a_{Al} = 4.02\text{Å}$). The boundary conditions' limit between the free-dynamic system and the fixed-displacement conditions is denoted by the red continuous line.

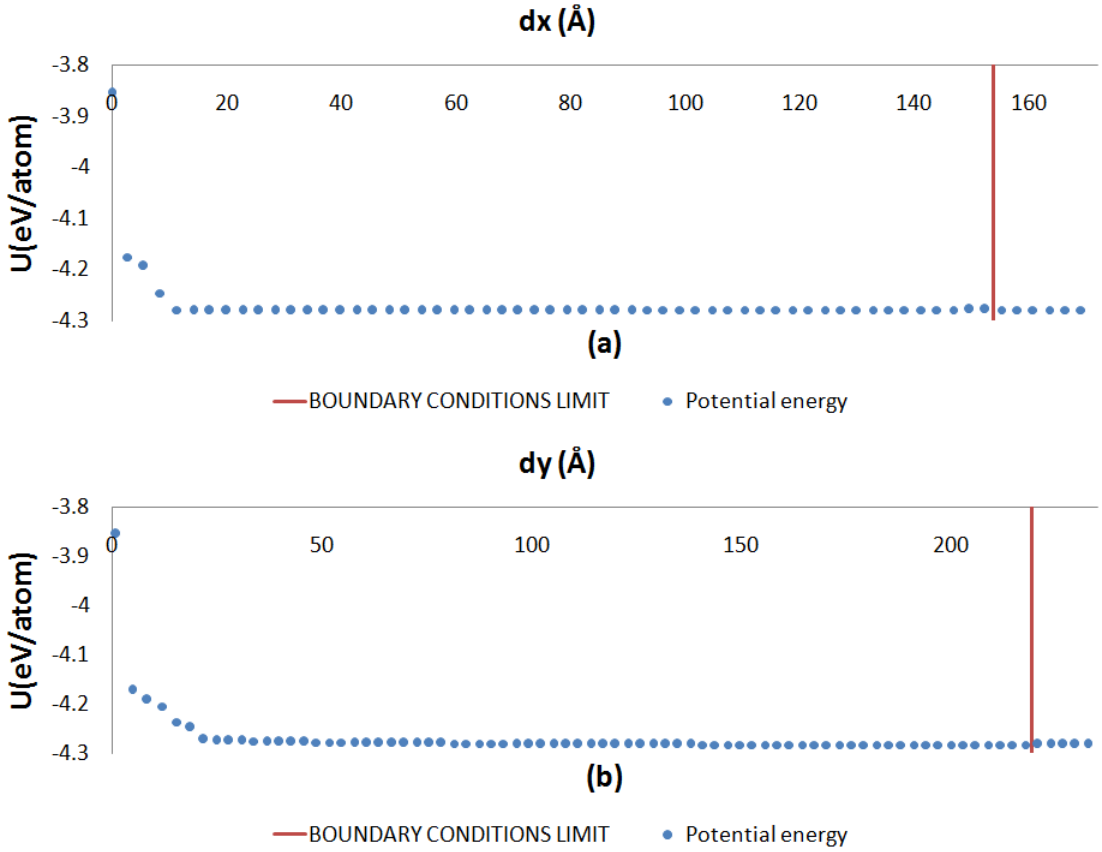

Figure V.17: Investigation of the potential energy of the atoms, of a $(010)[001]$ crack configuration in bcc alpha iron, in relation to the distance from the crack-tip along (a) the $x = [100]$ and (b) $y = [010]$ direction. The initial crack half-length according to linear elasticity continuum mechanics is equal to 38 lattice parameters $a_{\alpha-Fe}$ (where $a_{\alpha-Fe} = 2.86\text{Å}$). The boundary conditions' limit between the free-dynamic system and the fixed-displacement conditions is denoted by the red continuous line.

5.4. Ductility criterion

According to the working hypothesis mentioned above (§5.2), the lattice trapping 3D strain barrier, $\Delta\varepsilon_{ii(\infty)}$ $(i = x, y, z)$, is an intrinsic property of a crystalline system, which expresses the resistance of the lattice to the brittle propagation (§3.5.3) of any-sized pre-existing equilibrium crack. In addition, based on the relation V.5, this barrier approximates the critical strain threshold for brittle propagation of macroscopic-sized cracks, which are found in the samples of the mechanical tests. Hence, as it relates directly to the mechanical conditions required for the brittle fracture of a crack containing crystal, it is considered to be the ''criterion of brittleness'' in the present study. However, in order to interpret the mechanical response of aluminium and iron, an analogous ''ductility criterion'' is also required! In this way, the comparison of the two criteria will reveal the more favourable mechanism of stress-strain accommodation upon mechanical loading, at the atomic scale. In analogy to the ''criterion of brittleness'', the ''ductility criterion'' should be expressed the

resistance of crystalline lattice to the plastic deformation. To this end, the attention should now shift from system's pre-existing cracks to the system's pre-existing dislocations!

These linear structural defects exist in every real single-crystal material and their motion constitutes the primary reason for plastic deformation in metals [HIR1982]. As already presented (Chapter II), dislocation motion in materials is performed through glide on specific crystallographic planes and along specific crystallographic directions, or equivalently *slip systems*, depending on the type of the crystalline lattice (Table II.1). A pre-existing static dislocation may glide in a slip system only if it is subjected to a force which has a component along the respective slip plane and slip direction. Hence, what matters for triggering the dislocation glide inside a loaded crystal is the resolved shear stress (RSS) in its available slip systems due to the applied loading conditions. In the case of tri-axial loading, like the loading mode of the crack models (figure A.2), the RSS of a specific slip system is given by a superposition of three Schmid's laws (Chapter II):

$$\tau_{RSS} = \sigma_x \cdot cos\varphi_x \cdot cos\lambda_x + \sigma_y \cdot cos\varphi_y \cdot cos\lambda_y + \sigma_z \cdot cos\varphi_z \cdot cos\lambda_z \qquad (V.6a)$$

$$\tau_{RSS} = \sigma_x \cdot m_x + \sigma_y \cdot m_y + \sigma_z \cdot m_z \qquad (V.6b)$$

where $\sigma_i (i = x, y, z)$ are the applied stresses in each orthogonal direction, $\varphi_i (i = x, y, z)$ are the angles between each loading axis and the slip plane normal and $\lambda_i (i = x, y, z)$ are the angles between each loading axis and the slip direction (figure V.18). The Schmid-factor of each orthogonal direction takes the values $0 < |m_i| < 0.5$ depending on the relative orientation between the slip system and the respective loading axis. Consequently, the various available slip systems inside the loaded crystalline models correspond to different values of τ_{RSS}. However, as presented in Chapter II, dislocation slip can only be triggered if the τ_{RSS} that acts on a pre-existing static dislocation surpassed a critical value, which is characteristic for every family of slip systems as well as the type of the gliding dislocation (edge or screw). This quantity, known as the critical resolved shear stress, τ_{CRSS}, is a material property which can be determined experimentally at finite temperature. The equivalent form of the τ_{CRSS} at $T = 0K$ is called the Peierls stress, τ_P, and can be determined by theoretical and computational methods. Both τ_{CRSS} and τ_P express the resistance of the crystalline lattice to dislocation motion, thus they define the stress threshold for plastic deformation at the atomic scale. For this reason, they will constitute the

''ductility criterion'' for the crystalline systems of aluminium and iron in the present work. This choice is enhanced also from the fact that both experimental data and simulation results demonstrate the existence of a plastic homology of materials belonging to the same family of crystalline structure. In particular, the τ_P required for triggering dislocation motion in fcc metals is of order of magnitude of $10^{-5}G$ [WAN1996, SUZ1988], where G being the shear modulus. For bcc metals, however, the τ_P is significantly higher and proportional to $10^{-3}G$ [WAN1996, SUZ1999]. The same results are also characterize the yield stress [WAN1996, SUZ1999], which is the experimental quantity representing the τ_{CRSS}. This difference based on the fact that the bcc crystals do not contain truly close-packed planes; hence, despite that the fcc materials contain less available slip systems (12) compared to the bcc (48), the existence of the close-packed planes in the former leads to significantly lower τ_P. At the same time, the magnitude of the τ_P is responsible for the temperature dependence of plasticity in metals. Specifically, experiments have demonstrated that the yield stress in bcc metals decreases significantly by increasing the temperature (figure II.4), suggesting that the glide of dislocations is a thermally-activated process. On the other hand, in fcc metals, the yield stress is not strongly temperature-dependent; hence, dislocation glide is an athermal process, and the low τ_P allows the motion of dislocations to be possible even at $T = 0K$. Table V.2 provides experimental, analytical and numerical results of τ_P from the literature, which will be used to quantify the ''ductility criterion'' for aluminium and α-iron at $T = 0K$ in the further analysis.

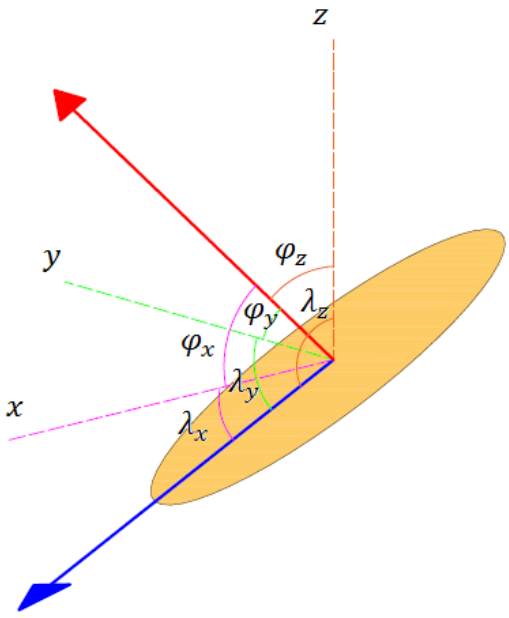

Figure V.18: Schmid's law: the critical resolved shear stress.

Table V.2: Peierls stress of the different slip systems in fcc aluminium and bcc iron

Material	Structure	τ_P/G at $T = 0K$	Slip system	Work	Reference
Al	fcc	4.9×10^{-5} (edge)	$\frac{1}{2}a_0\langle 1\bar{1}0\rangle\{111\}$	First-principles	[SHI2013]
Al	fcc	5.4×10^{-5} (edge)	$\frac{1}{2}a_0\langle 1\bar{1}0\rangle\{111\}$	Experimental	[KOI2000]
Al	fcc	4.0×10^{-5} (edge)	$\frac{1}{2}a_0\langle 1\bar{1}0\rangle\{111\}$	Experimental	[HOW1961]
α-Fe	bcc	5.5×10^{-3}(screw)	$\frac{1}{2}a_0\langle 1\bar{1}\bar{1}\rangle\{110\}$	Experimental	[TAK1982]
α-Fe	bcc	5.2×10^{-3}(screw)	$\frac{1}{2}a_0\langle 1\bar{1}\bar{1}\rangle\{110\}$	Experimental	[KUR1979]
α-Fe	bcc	$24.2\tau_{P\langle 111\rangle\{110\}}$	$\frac{1}{2}a_0\langle 11\bar{1}\rangle\{112\}$	Analytical	[KAS2012]
α-Fe	bcc	$120.3\tau_{P\langle 111\rangle\{110\}}$	$\frac{1}{2}a_0\langle 11\bar{1}\rangle\{123\}$	Analytical	[KAS2012]

5.5. Ductile versus Brittle mechanical behaviour at $T = 0K$

Based on the aforementioned, we suggest that the intrinsically ductile or brittle behaviour of a crystalline system under load is determined by the competition between the activation of a pre-existing crack to cleavage and the glide of pre-existing dislocations. Both mechanisms have been characterized by a stress-strain barrier, through the ''ductility'' and ''brittleness'' criteria, whose comparison will reveal the more favourable process to strain-stress accommodation for the systems studied. To this end, it is necessary to examine if the lattice strain barrier for cleavage activation is sufficient or not to cause glide of pre-existing static dislocations at $T = 0K$. This investigation is performed by applying the following steps:

(i) We start with the ''criterion of brittleness'', i.e. the determination of the strain increments corresponding to the 3D lattice trapping barrier for cleavage propagation of the cracks:

$$\begin{aligned} \Delta\varepsilon_{xx(\infty)} &= \varepsilon_{xx(\infty)}^{Upper} - \varepsilon_{xx(\infty)}^{Lower} \\ \Delta\varepsilon_{yy(\infty)} &= \varepsilon_{yy(\infty)}^{Upper} - \varepsilon_{yy(\infty)}^{Lower} \\ \Delta\varepsilon_{zz(\infty)} &= 0 \end{aligned} \qquad (V.7)$$

where $\varepsilon_{yy(\infty)}^{Upper}$ and $\varepsilon_{yy(\infty)}^{Lower}$ are respectively the upper and lower strain stability trapping limit.

(ii) The next step is to calculate the hydrostatic strain of these increments, given by:

$$\varepsilon_{Hyd} = (\Delta\varepsilon_{xx(\infty)} + \Delta\varepsilon_{yy(\infty)} + \Delta\varepsilon_{zz(\infty)})/3 \qquad (V.8)$$

The reason is that ε_{Hyd} gives rise to hydrostatic pressure into the system, which produces zero τ_{RSS} on the available slip systems and thus cannot trigger the dislocation glide. Therefore, $\Delta\varepsilon_{ii(\infty)}$ should be isolated from hydrostatic terms:

$$\begin{aligned} \Delta\varepsilon'_{xx(\infty)} &= \Delta\varepsilon_{xx(\infty)} - \varepsilon_{Hyd} \\ \Delta\varepsilon'_{yy(\infty)} &= \Delta\varepsilon_{yy(\infty)} - \varepsilon_{Hyd} \\ \Delta\varepsilon'_{zz(\infty)} &= -\varepsilon_{Hyd} \end{aligned} \qquad (V.9)$$

(iii) The corresponding pressure-free stress increments can now be determined by the use of Hooke's law:

$$\begin{aligned} \Delta\sigma'_{xx(\infty)} &= \Delta\varepsilon'_{xx(\infty)} \cdot C_{11}^{Lower} + \Delta\varepsilon'_{yy(\infty)} \cdot C_{12}^{Lower} + \Delta\varepsilon'_{zz(\infty)} \cdot C_{12}^{Lower} \\ \Delta\sigma'_{yy(\infty)} &= \Delta\varepsilon'_{xx(\infty)} \cdot C_{12}^{Lower} + \Delta\varepsilon'_{yy(\infty)} \cdot C_{11}^{Lower} + \Delta\varepsilon'_{zz(\infty)} \cdot C_{12}^{Lower} \\ \Delta\sigma'_{zz(\infty)} &= \Delta\varepsilon'_{xx(\infty)} \cdot C_{12}^{Lower} + \Delta\varepsilon'_{yy(\infty)} \cdot C_{12}^{Lower} + \Delta\varepsilon'_{zz(\infty)} \cdot C_{11}^{Lower} \end{aligned} \qquad (V.10)$$

where the elastic constant C_{11}^{Lower} and C_{12}^{Lower} are the analytically and numerically calculated values corresponding to the lower trapping limit of each crack size reference loading state (Chapter IV).

(iv) Since $\Delta\sigma'_{ii(\infty)}$ are free from hydrostatic pressure, they may be able to trigger the glide of pre-existing static dislocations inside the crystalline system. To evaluate their effect, the generated τ_{RSS} for each available slip system within the crystal (Table II.1) should be calculated. The total resolved shear stress, in normalized units, is given by the relation:

$$\frac{\tau_{RSS}}{G_{\langle 100\rangle}} = \frac{\Delta\sigma'_{xx(\infty)}}{G_{\langle 100\rangle}} cos\varphi_x \cdot cos\lambda_x + \frac{\Delta\sigma'_{yy(\infty)}}{G_{\langle 100\rangle}} cos\varphi_y \cdot cos\lambda_y + \frac{\Delta\sigma'_{zz(\infty)}}{G_{\langle 100\rangle}} cos\varphi_z \cdot cos\lambda_z \quad (V.11)$$

where $\varphi_i (i = x, y, z)$ are the angles between the slip plane normal direction and the cubic axes, $\lambda_i (i = x, y, z)$ are the angles between the slip direction and the

cubic axes and $G_{\langle 100\rangle} = 1/S_{44}$ is the shear modulus along the cubic axes corresponding to the lower trapping limit reference loading point (Chapter IV).

(v) Finally, the intrinsic mechanical response of the system upon loading can be determined by examining if the total τ_{RSS} is sufficient to trigger the glide of dislocations, or in other words to satisfy the ''ductility criterion''. In particular, if the total τ_{RSS} of at least one available slip system is larger compare to the corresponding τ_{CRSS} (τ_P at $T = 0K$):

$$\left(\frac{\tau_{RSS}}{G_{\langle 100\rangle}}\right) > \left(\frac{\tau_{CRSS}}{G_{\langle 100\rangle}}\right) \qquad (V.12\alpha)$$

then glide triggering of a pre-existing dislocation is energetically more favourable compare to the propagation of a pre-existing crack, upon loading, hence the system is consider to be ''intrinsically ductile''. On the other hand, if the total τ_{RSS} of every slip system is smaller compare to the respective values of τ_{CRSS}:

$$\left(\frac{\tau_{RSS}}{G_{\langle 100\rangle}}\right) < \left(\frac{\tau_{CRSS}}{G_{\langle 100\rangle}}\right) \qquad (V.12b)$$

then the propagation of a pre-existing crack is energetically more favourable compare to the glide of a pre-existing static dislocation, upon loading, thus the system is regarded as ''intrinsically brittle''.

For aluminium, simulation results demonstrate the glide of pre-existing dislocations on $\{111\}\langle 110\rangle$ slip systems is the most favourable mechanism of stress-strain accommodation under mode I deformation, than the cleavage triggering of pre-existing equilibrium $(010)[001]$ cracks (figure V.19), since:

$$\left(\frac{\tau_{RSS}}{G_{\langle 100\rangle}}\right)^{T=0K}_{\{111\}\langle 110\rangle} > \left(\frac{\tau_P}{G_{\langle 100\rangle}}\right)^{T=0K}_{\{111\}\langle 110\rangle}$$

The maximum τ_{RSS} is observed on the $(11\bar{1})[011]$, $(1\bar{1}\bar{1})[01\bar{1}]$, $(1\bar{1}1)[011]$ and $(111)[01\bar{1}]$ slip systems, suggesting that these would cause the plastic deformation into the system; hence, they constitute the primary slip systems under plane-strain mode I tension

along the $[010]$ direction. Therefore, atomistic results demonstrate that fcc aluminium is an intrinsically ductile material at $T = 0K$, in agreement with experiments [INT3, TAM2002].

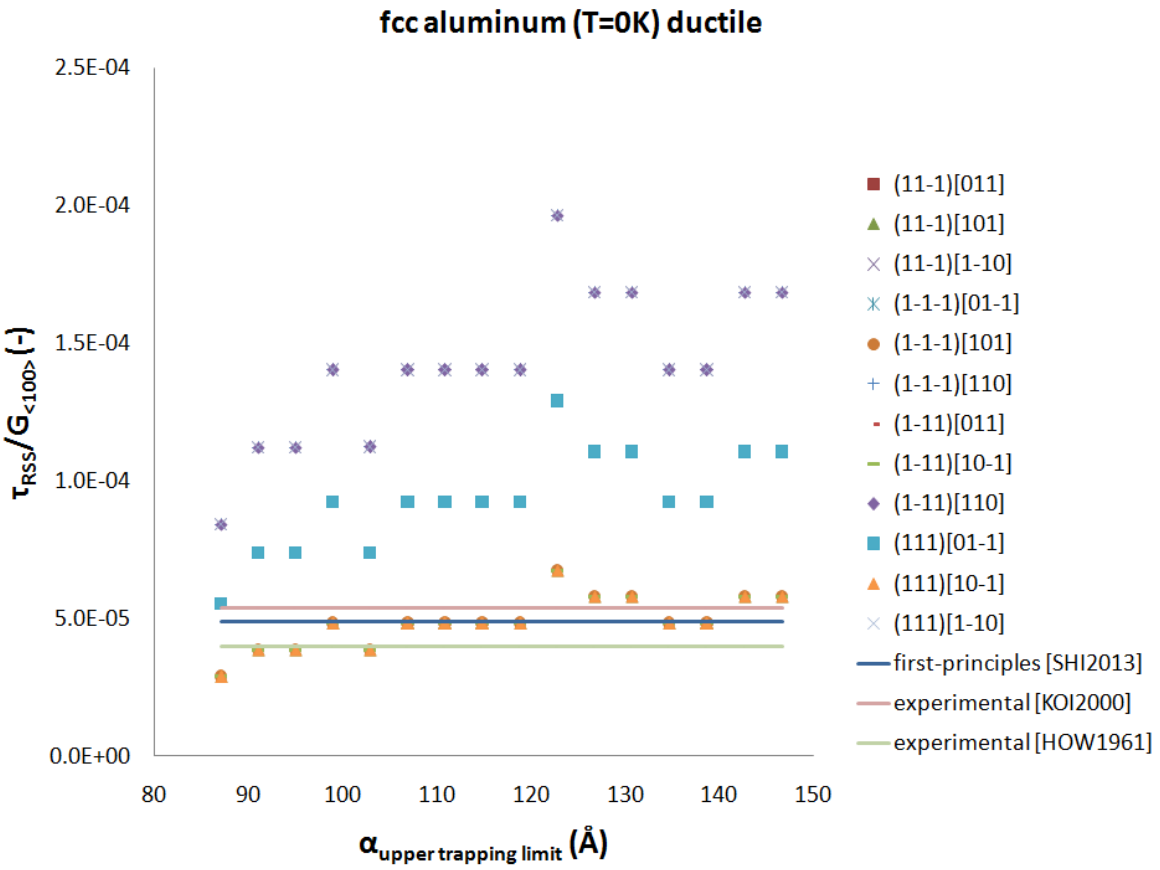

Figure V.19: Comparison between the resolved shear stress on $\{111\}\langle 110\rangle$ slip systems in fcc aluminium, corresponding to the lattice trapping cleavage activation barrier of $(010)[001]$ cracks under mode I deformation, and the critical resolved shear stress for glide of pre-existing edge dislocations on $\{111\}\langle 110\rangle$ slip systems (first-principles simulations [SHI2013] and experimental [KOI2000, HOW1961] results).

Unlike aluminium, atomistic results of iron models demonstrate that the cleavage triggering of pre-existing equilibrium $(010)[001]$ cracks is more preferable mechanism than the triggering of glide of pre-existing dislocations in any available slip system (figure V.20), i.e.:

$$\left(\frac{\tau_{RSS}}{G_{\langle 100\rangle}}\right)^{T=0K}_{\{110\}\langle 111\rangle} < \left(\frac{\tau_{P}}{G_{\langle 100\rangle}}\right)^{T=0K}_{\{110\}\langle 111\rangle}$$

$$\left(\frac{\tau_{RSS}}{G_{\langle 100\rangle}}\right)^{T=0K}_{\{211\}\langle 111\rangle} < \left(\frac{\tau_{P}}{G_{\langle 100\rangle}}\right)^{T=0K}_{\{211\}\langle 111\rangle}$$

$$\left(\frac{\tau_{RSS}}{G_{\langle 100\rangle}}\right)^{T=0K}_{\{123\}\langle 111\rangle} < \left(\frac{\tau_{P}}{G_{\langle 100\rangle}}\right)^{T=0K}_{\{123\}\langle 111\rangle}$$

with

$$\left(\frac{\tau_{RSS}}{G_{\langle 100\rangle}}\right)^{T=0K}_{\{110\}\langle 111\rangle} > \left(\frac{\tau_{RSS}}{G_{\langle 100\rangle}}\right)^{T=0K}_{\{123\}\langle 111\rangle} > \left(\frac{\tau_{RSS}}{G_{\langle 100\rangle}}\right)^{T=0K}_{\{211\}\langle 111\rangle}$$

and

$$\left(\frac{\tau_{P}}{G_{\langle 100\rangle}}\right)^{T=0K}_{\{110\}\langle 111\rangle} < \left(\frac{\tau_{P}}{G_{\langle 100\rangle}}\right)^{T=0K}_{\{211\}\langle 111\rangle} < \left(\frac{\tau_{P}}{G_{\langle 100\rangle}}\right)^{T=0K}_{\{123\}\langle 111\rangle}$$

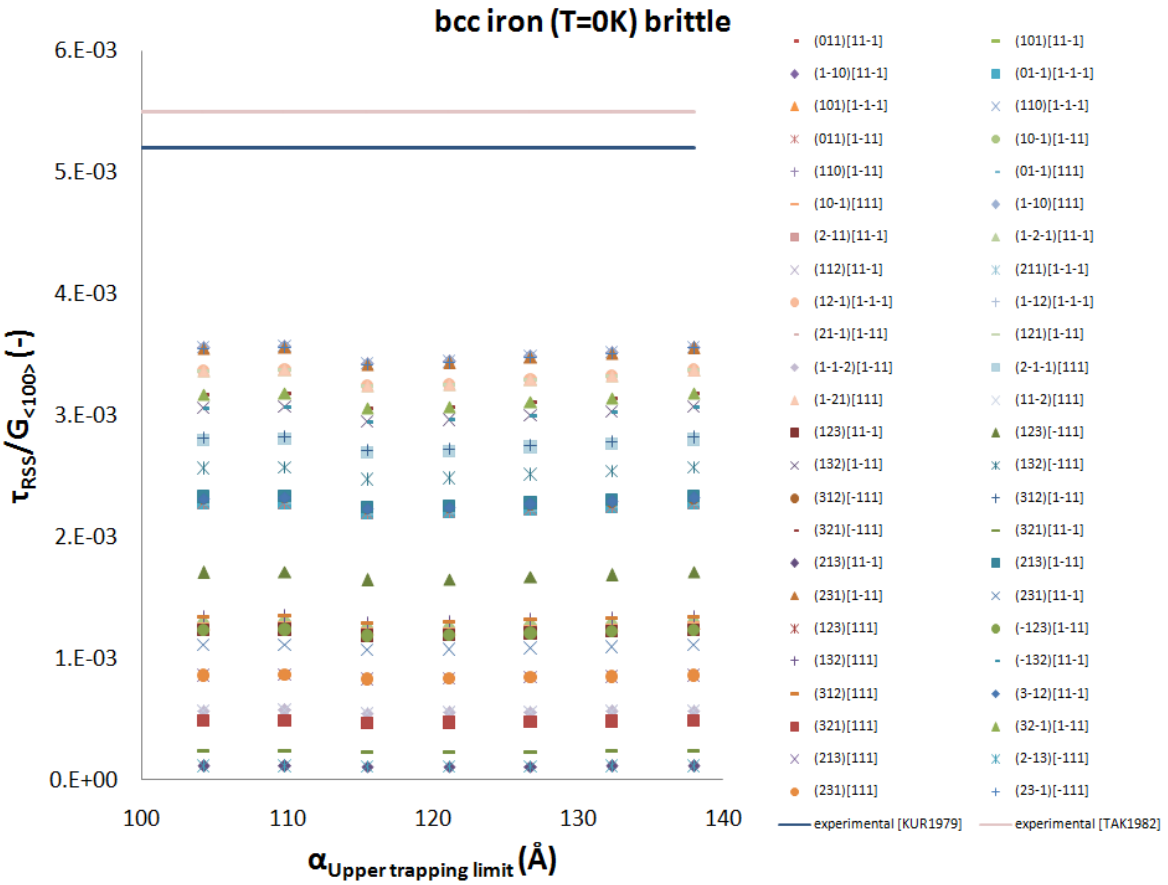

Figure V.20: Comparison between the resolved shear stress on $\{110\}\langle 111\rangle$, $\{211\}\langle 111\rangle$ and $\{123\}\langle 111\rangle$ slip systems in bcc iron, correspond to the lattice trapping cleavage activation barrier of $(010)[001]$ cracks under mode I deformation, and the critical resolved shear stress for glide of pre-existing screw dislocations on the $\{110\}\langle 111\rangle$ slip systems (experimental [KUR1979, TAK1982] results). The $\{110\}\langle 111\rangle$ slip systems in bcc iron are characterized by lower critical resolved shear stress than the $\{211\}\langle 111\rangle$ and $\{123\}\langle 111\rangle$ slip systems [KAS2012].

The maximum τ_{RSS} is observed on the $(1\bar{1}0)[11\bar{1}]$, $(1\bar{1}0)[111]$, $(110)[1\bar{1}1]$ and $(110)[1\bar{1}\bar{1}]$ slip systems, whose slip system family is characterized by the lower τ_P in bcc iron [KAS2012], however it is not sufficient to trigger dislocation glide. Consequently, simulation results suggest that the bcc iron is an intrinsically brittle material at $T = 0K$, in

consistency with experimental data [TAM2002]. Therefore, the approach proposed, i.e. the comparison between the criteria of ''ductility'' and ''brittleness'', can determine and interpret correctly the mechanical response of the two metals under load at $T = 0K$! The next step is to investigate if this approach can work in predicting correctly the mechanical behaviour of aluminium and iron at finite temperature conditions.

5.6. Ductile versus Brittle mechanical behaviour at finite temperature

In order to determine the intrinsic mechanical response of aluminium and iron under loading at finite temperature, the determination of the temperature dependence of the lattice trapping barrier is required. This is made by using molecular dynamics. We have studied the mechanical response of quasi-static $(010)[001]$ cracks under mode I plane-strain deformation at different temperatures, and have estimated the strain-stress barrier for crack brittle propagation, $\Delta\sigma_{ii} = f(T)$. The computational details of this study, including the construction of the numerical models and the simulation procedure, are presented in detail in §3.5.2. The comparison between the $\Delta\sigma_{ii} = f(T)$ and the temperature dependence of the experimental yield stress, $\tau_{CRSS} = f(T)$, will reveal which mechanism is preferred for strain-stress accommodation at finite temperature.

5.6.1. Temperature effect on the lattice trapping barrier

The mechanical response of the nano-sized cracks in aluminium is presented in figure V.21 for $T = 25K$, $75K$ and $125K$. Additional calculations have been performed for the temperatures $50K$ and $100K$. Simulation results revealed the existence of the ''lattice trapping effect'' at every temperature studied. The non-equilibrium configurations, corresponding to applied deformation larger than the upper trapping limit, exhibit crack brittle extension along the $[100]$ and $[\bar{1}00]$ directions (§3.5.3). On the other hand, crack configurations below the lower trapping limit reduced in length via a healing process and eventually close.

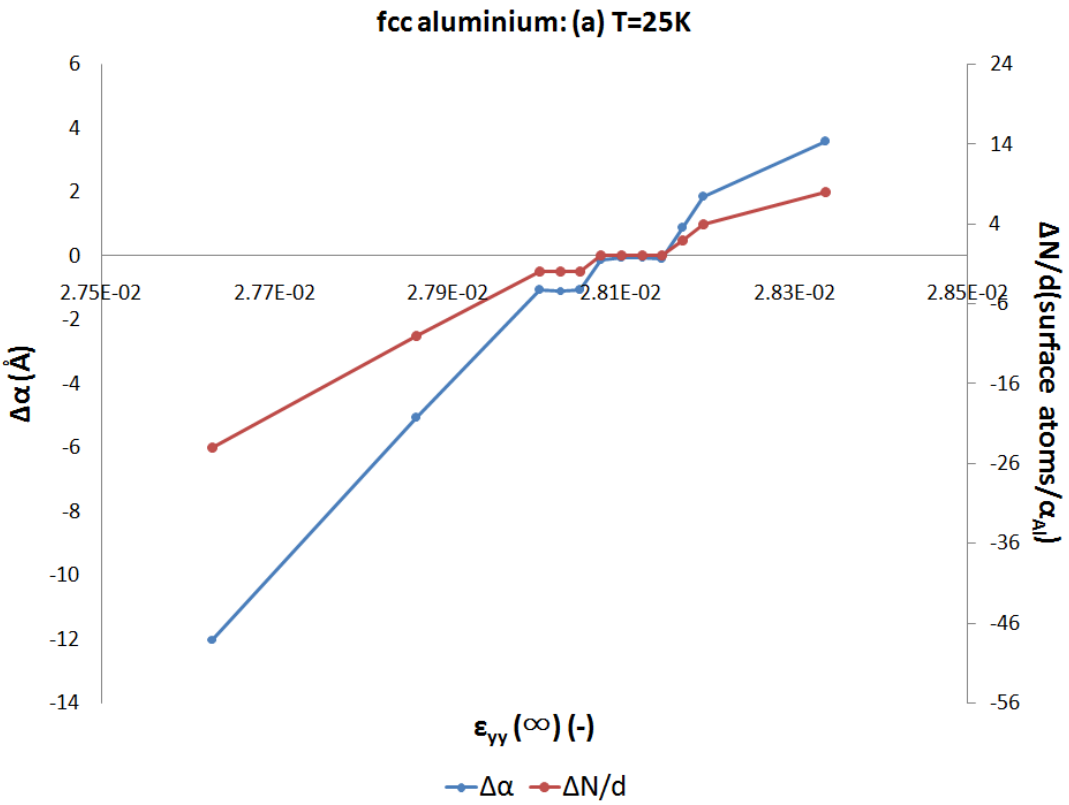
fcc aluminium: (a) T=25K
6
4
2
0
-2
-4
-6
-8
-10
-12
-14
24
14
4
-6
-16
-26
-36
-46
-56
2.75E-02
2.77E-02
2.79E-02
2.81E-02
2.83E-02
2.85E-02
Δα (Å)
ΔN/d(surface atoms/α_Al)
ε_yy (∞) (-)
Δα
ΔN/d

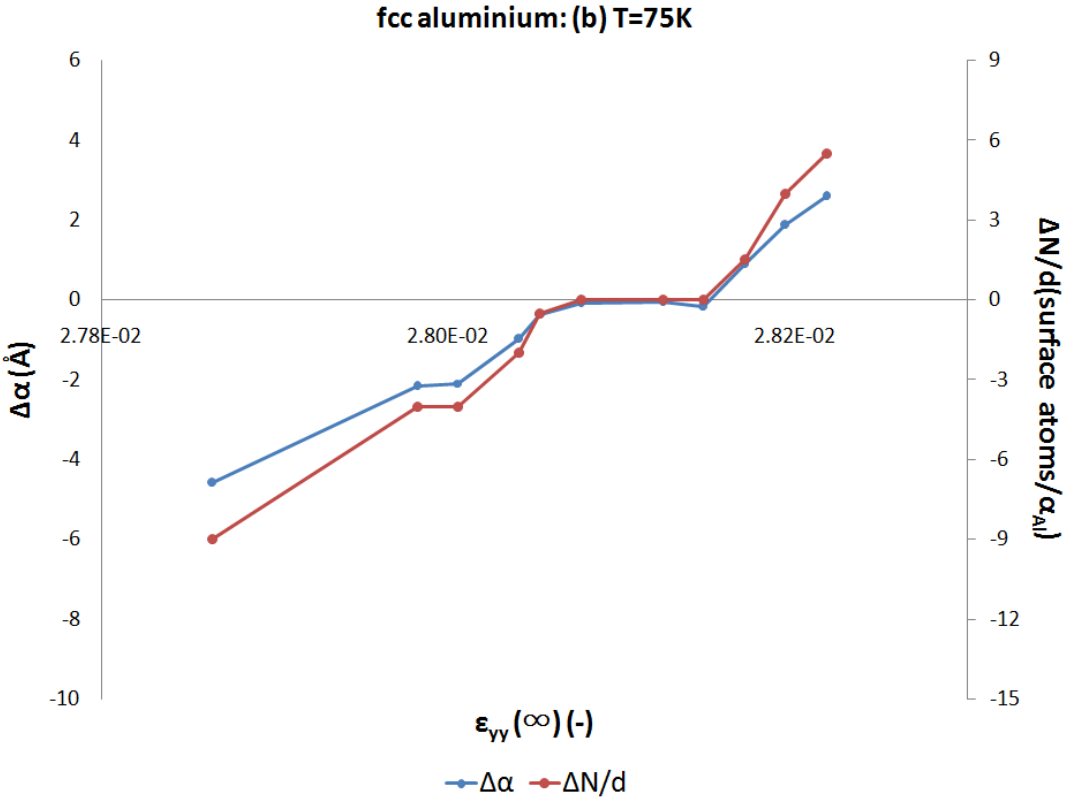
fcc aluminium: (b) T=75K
6
4
2
0
-2
-4
-6
-8
-10
9
6
3
0
-3
-6
-9
-12
-15
2.78E-02
2.80E-02
2.82E-02
Δα (Å)
ΔN/d(surface atoms/α_Al)
ε_yy (∞) (-)
Δα
ΔN/d

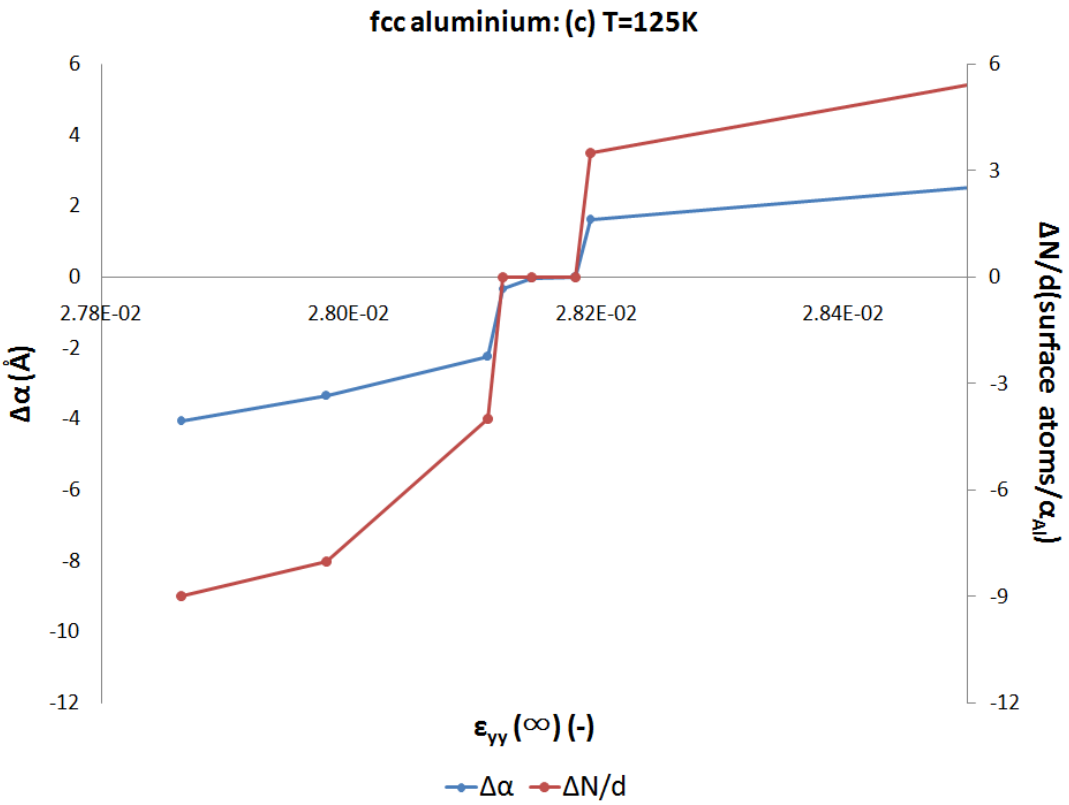

Figure V.21: Evolution of the crack half-length and surface atoms of $(010)[001]$ nano-sized cracks in fcc aluminium in respect to the applied deformation at (a) 25, (b) 75 and (c) 125K. The initial crack half-length of the configurations is equal to 22 lattice parameters, $a(T)$.

More importantly, the equilibrium configurations, correspond to the upper and lower lattice trapping limits (figures V.22 and V.23), can be used to calculate the strain and stress barrier for crack extension in respect to the temperature (figure V.24). Atomistic results show that both the $\Delta\varepsilon_{ii(\infty)}$ and $\Delta\sigma_{ii(\infty)}$ $(i = x, y, z)$ increments are not significantly affected by the temperature increase. This result suggests that the lattice trapping barrier for cleavage propagation of pre-existing cracks is an athermal property of the crystalline aluminium. Since the experimental yield stress of aluminium is also non-activated, we find that there is an analogy between the criteria of ''plasticity'' and ''brittleness'', which may be attributed to the fcc crystalline lattice.

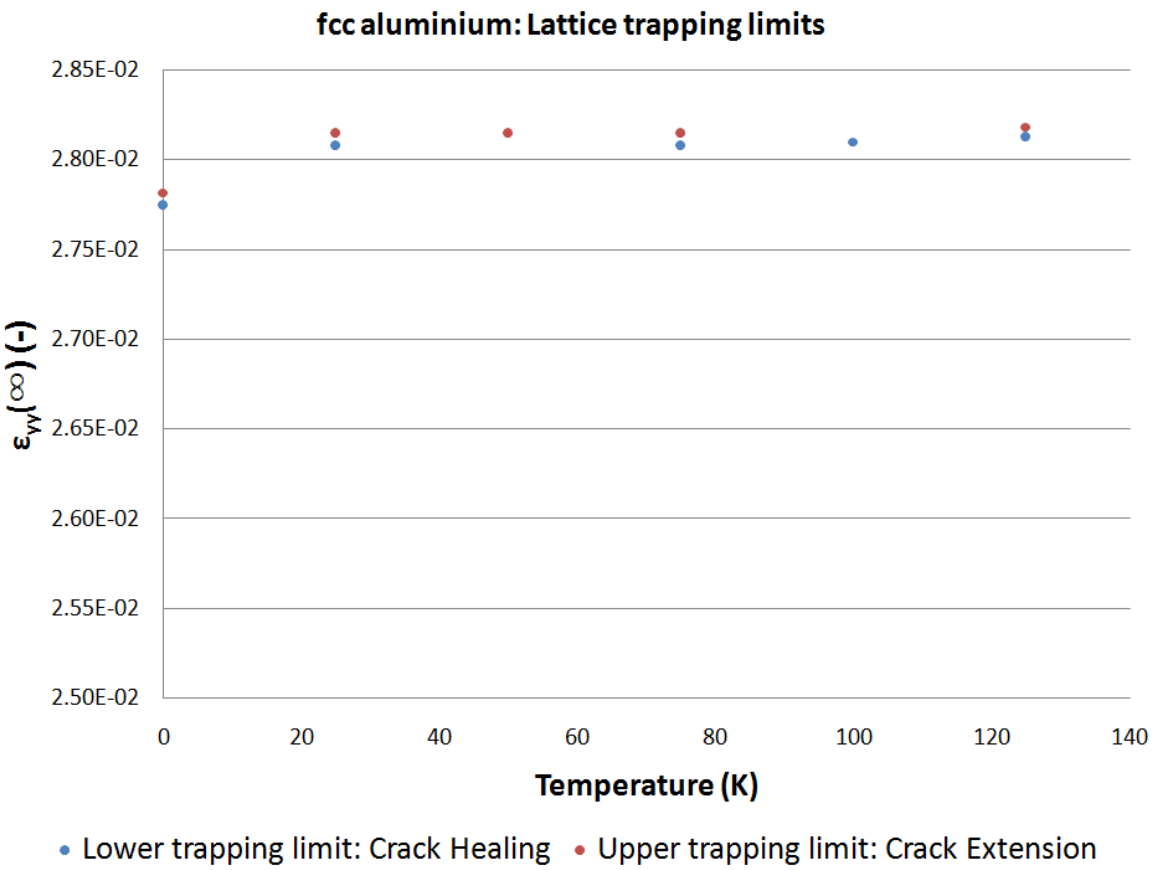

Figure V.22: Lattice trapping effect of $(010)[001]$ nano-sized cracks in fcc aluminium in respect to the temperature. The red circles present the brittle cleavage initiation strain limit (upper trapping limit), while the blue circles correspond to the crack healing initiation strain limit (lower trapping limit) of the crack configurations. The strain range between the lower and the upper trapping limit determine the stability strain region, region where the crack configurations are in a mechanical equilibrium.

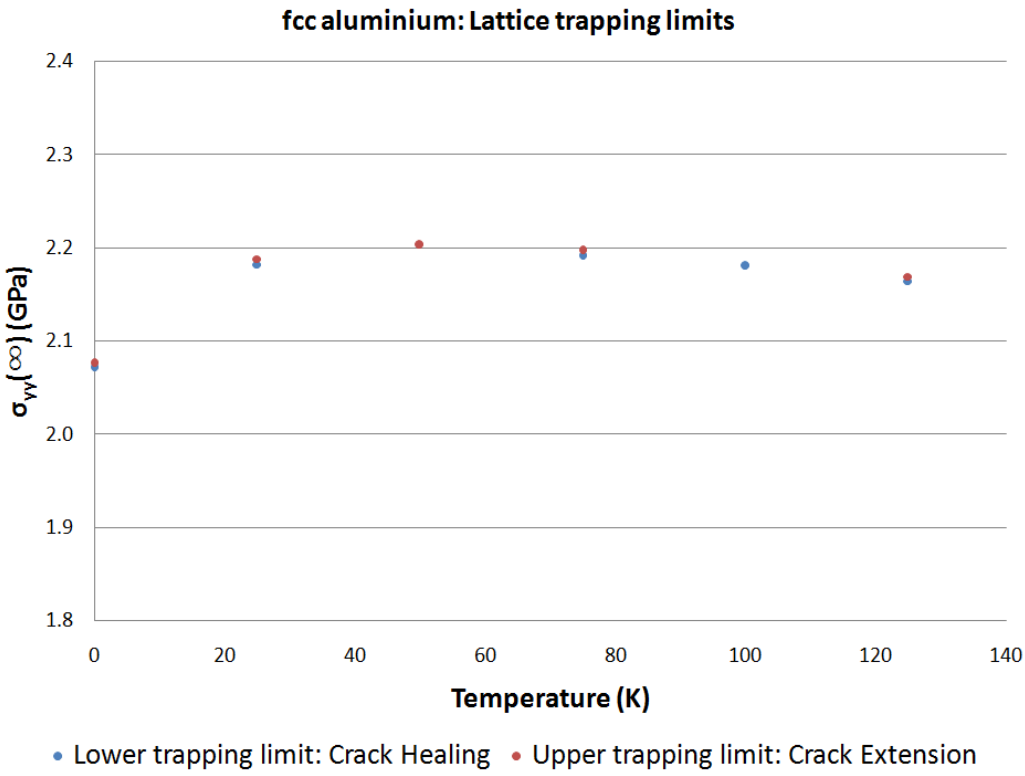

Figure V.23: Lattice trapping effect of $(010)[001]$ nano-sized cracks in fcc aluminium in respect to the temperature. The red circles present the brittle cleavage initiation stress limit (upper trapping limit), while the blue circles correspond to the crack healing initiation stress limit (lower trapping limit) of the crack configurations. The stress range between the lower and the upper trapping limit determine the stability stress region, region where the crack configurations are in a mechanical equilibrium.

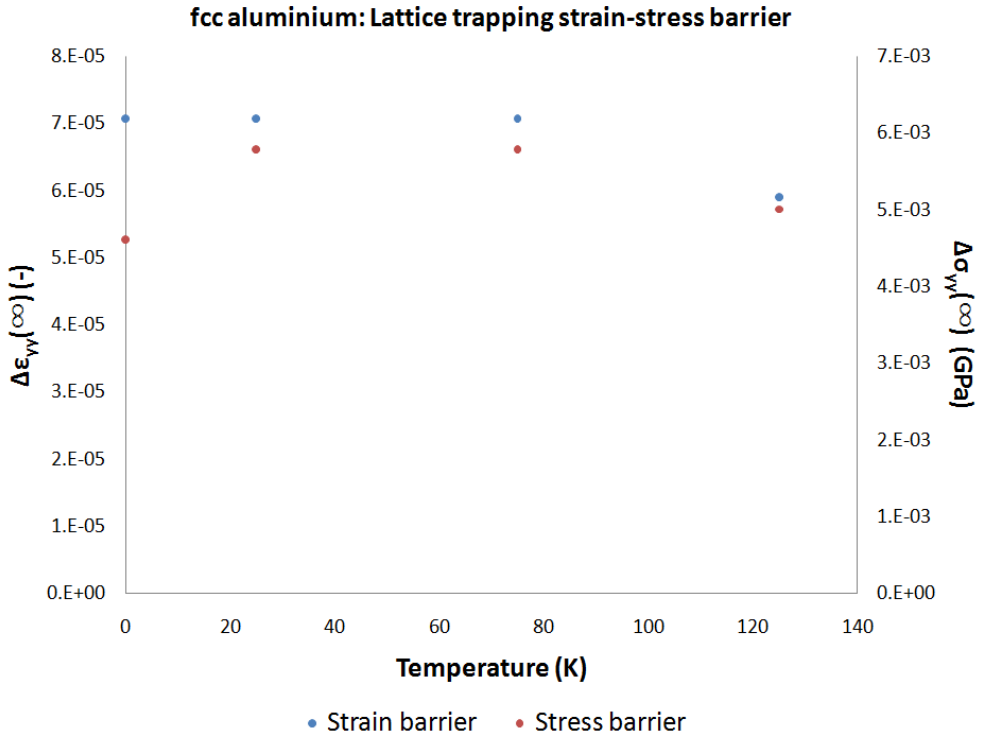

Figure V.24: The strain and stress range of the stability zone of $(010)[001]$ nano-sized cracks in fcc aluminium in respect to the temperature. This strain increment corresponds to the activation barrier for brittle propagation since the upper trapping limit of the stability zone is the threshold of cleavage initiation of the crack configurations.

Despite the success of obtaining equilibrium $(010)[001]$ cracks in aluminium, the investigation in iron showed that the temperature eliminates the stability region of the crack models. In particular, every crack model which investigates at $T = 50K$ accommodates the applied strain-stress field by the generation of partial dislocations and stacking faults (§5.7.1). In addition, the possible motion of the dislocations due to the finite temperature and the applied stress acts as a mechanism of absorption of elastic energy of the system. Hence, every crack model reduces its dimensions and eventually healed (figure V.25) leaving behind the structural defects which generated.

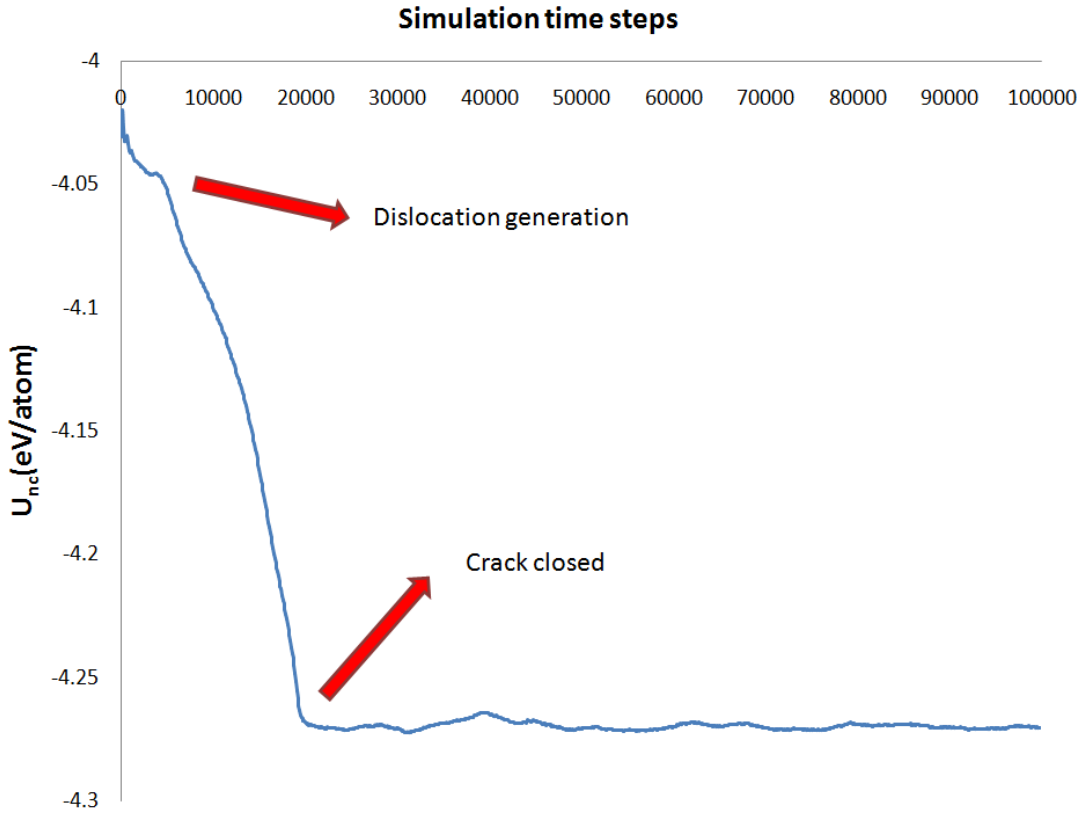

Figure V.25: The change in the potential energy in the near-crack region during the molecular dynamic simulation. The potential energy decreases due to the reduction of the crack surface.

The generation of dislocations at the crack-tip was observed even for applied loading significantly lower compared to the lower trapping limit at the $T = 0K$. This observation suggests that the strain threshold for dislocation generation at the crack-tip, ε_{yy}^{DIS}, which ''snips'' the lattice trapping stability region at $T = 0K$, reduces on increasing the temperature. To avoid reaching ε_{yy}^{DIS}, we should simulate crack configurations with significantly larger length, which they stabilized under lower applied deformation or loading (figure V.11). However, this solution leads to the construction of larger models,

whose simulation is computationally very expensive and time consuming; hence, we did not proceed to it.

5.6.2. Mechanical response of aluminium upon loading at finite temperature

Nevertheless, the achievement of calculating the lattice trapping barrier of cracks in aluminium allows testing the validity of the approach proposed in §5.5, for interpreting the mechanical response of the system under load at finite temperature. To this end, we should examine if the lattice trapping barrier for cleavage activation is sufficient to cause the glide of pre-existing static dislocations on the system's available slip systems. This time, the analysis is performed by using only the stress components, due to the lack of knowledge of the analytic relation between the elastic constants and the temperature. As a result, the investigation is performed by applying the following steps:

(i) The stress increments corresponding to the cleavage activation are determined from the loading conditions of the lattice trapping limits:

$$\begin{aligned} \Delta\sigma_{xx(\infty)} &= \sigma_{xx(\infty)}^{Upper} - \sigma_{xx(\infty)}^{Lower} \\ \Delta\sigma_{yy(\infty)} &= \sigma_{yy(\infty)}^{Upper} - \sigma_{yy(\infty)}^{Lower} \\ \Delta\sigma_{zz(\infty)} &= \sigma_{zz(\infty)}^{Upper} - \sigma_{zz(\infty)}^{Lower} \end{aligned} \qquad (V.13)$$

where $\sigma_{ii(\infty)}^{Upper}$ and $\sigma_{ii(\infty)}^{Lower}$ are respectively the upper and lower stress stability trapping limits.

(ii) The next step is to calculate the hydrostatic stress corresponding to this 3D activation barrier:

$$p_{Hyd} = \left(\Delta\sigma_{xx(\infty)} + \Delta\sigma_{yy(\infty)} + \Delta\sigma_{zz(\infty)}\right)/3 \qquad (V.14)$$

The hydrostatic pressure is not able to cause the glide of pre-existing dislocations; hence, the stress increments of the lattice trapping barriers should be isolated from p_{Hyd}:

$$\Delta\sigma'_{xx(\infty)} = \Delta\sigma_{xx(\infty)} - p_{Hyd}$$

$$\Delta\sigma'_{yy(\infty)} = \Delta\sigma_{yy(\infty)} - p_{Hyd} \qquad (V.15)$$

$$\Delta\sigma'_{zz(\infty)} = \Delta\sigma_{zz(\infty)} - p_{Hyd}$$

(iii) The $\Delta\sigma'_{ii(\infty)}$ are able to generate τ_{RSS} on the available slip systems (Table II.1), which can be calculate by use of equation V.11.

(iv) Eventually, the mechanical response of aluminium under loading in respect to the temperature can be determined by comparing the calculated τ_{RSS} with the experimental yield stress (equivalent to τ_{CRSS}), for every temperature studied. Since the yield is atheral, it can approximately considered to be equal to the Peierls stress at every temperature:

$$\tau_{CRSS}(T) \approx \tau_P \; \forall \; T \qquad (V.16)$$

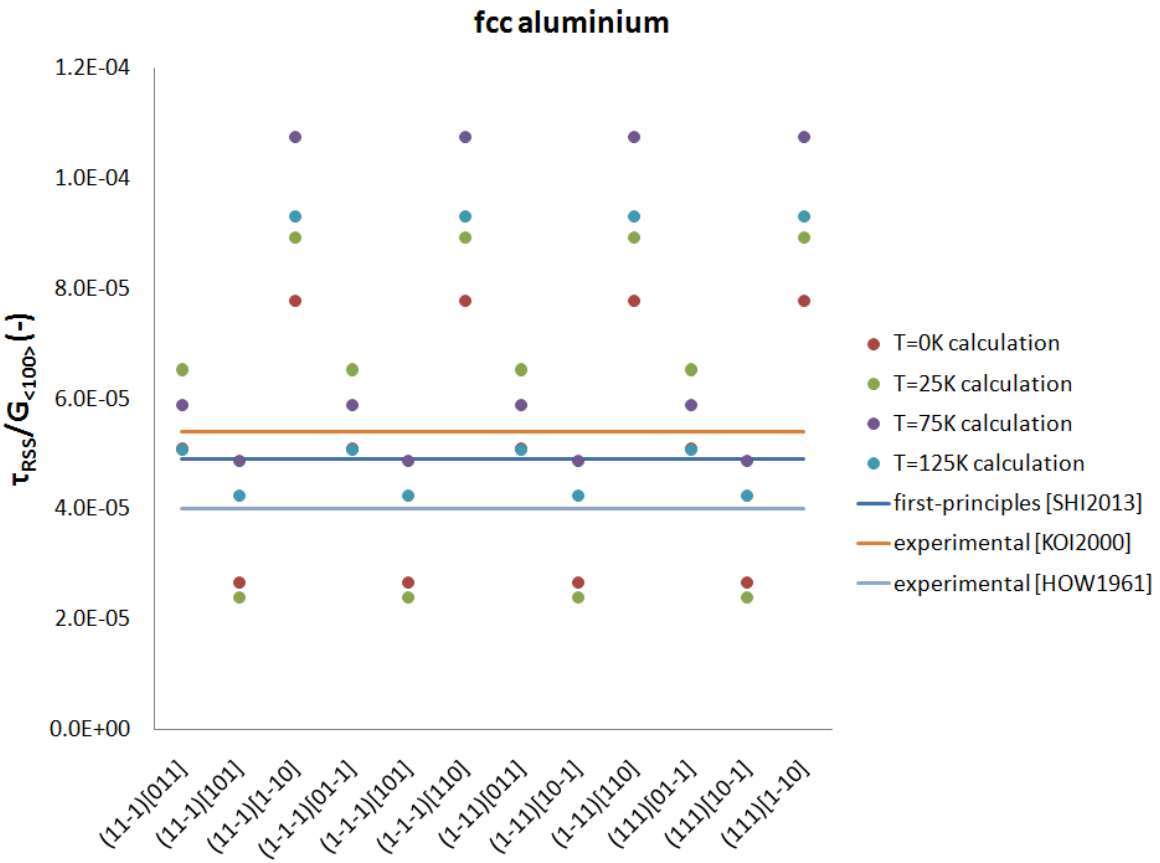

Figure V.26: Comparison between the resolved shear stress on $\{111\}\langle 110\rangle$ slip systems in fcc aluminium, corresponding to the lattice trapping barrier of $(010)[001]$ cracks under mode I deformation for different finite temperatures, and the Peierls stress for glide of pre-existing edge dislocations on these slip systems (first-principles simulations [SHI2013] and experimental [KOI2000, HOW1961] results). The resolved shear stress for every temperature studied ($T = 0K$: red data, $T = 25K$: green data, $T = 75K$: purple data, $T = 125K$: blue data) is larger than the Peierls stress (continuous lines).

Simulation results demonstrate that aluminium is intrinsically ductile in every temperature studied, $T = 0 - 125K$, since the lattice trapping barrier for cleavage activation of the $(010)[001]$ pre-existing cracks is sufficient to trigger the glide of pre-existing dislocations on the $\{111\}\langle 110\rangle$ slip systems (figure V.26):

$$\left(\frac{\tau_{RSS}}{G_{\langle 100\rangle}}\right)^{T}_{\{111\}\langle 110\rangle} > \left(\frac{\tau_{CRSS}}{G_{\langle 100\rangle}}\right)^{T}_{\{111\}\langle 110\rangle} = \left(\frac{\tau_{P}}{G_{\langle 100\rangle}}\right)^{T=0^{\circ}K}_{\{111\}\langle 110\rangle} \quad \forall\, T$$

Atomistic results are in consistent with experimental observations [INT3, TAM2002]; hence, our approach (§5.5) is seems to work also at finite temperature conditions.

5.7. Dynamic response of cracks

The vast majority of studies in the literature focus on the dynamic response of the cracks [DEC1983, CHE1990, MAC1998, MAC2004, BEL2004, CAO2006, BEL2007], in order to interpret the mechanical behaviour of materials under different loading and temperature conditions. However, as already presented in §3.3.1, this approach is characterized by the following issues: Firstly, simulations are performed under conditions outside the thermodynamic regime. This means that the different variables describing the mechanical state of the model, such as the stress, are path-dependent; thus are considered only as quantities, which describe the changes occurring in the system, but not as properties of the systems that are derived by equations of state. Therefore, the simulation results have not quantitative value, but they constitute only qualitative observations of individual mechanical systems. Second, the dynamic response of cracks is simulated under dynamic boundary conditions, with the aim to approximate experimental conditions. However, under this approach the crack configuration undergoes non-physical dynamic loading, which leads to the emergence of new associated non-physical phenomena. Consequently, the evaluation of the obtaining results requires the appropriate precautions. The aim of this paragraph is to investigate if the dynamic response of cracks, inside aluminium and iron, is capable or not to interpret the mechanical behaviour of these metals at $T = 0K$, in the absence of pre-existing dislocations. To this end, we tackle the second issue with the use of quasi-static boundary conditions.

5.7.1. Non-equilibrium cracks in fcc aluminium and bcc iron

The first opportunity to investigate the dynamic response of cracks in the metals of interest was given during the stabilization process, through the non-equilibrium $(010)[001]$ configurations. Non-equilibrium cracks include every configuration outside the lattice trapping region or equivalently correspond to applied deformation within the range:

$$\varepsilon_{yy(\infty)} > \varepsilon_{yy(\infty)}^{Upper} \text{ or } \varepsilon_{yy(\infty)} < \varepsilon_{yy(\infty)}^{Lower}$$

where $\varepsilon_{yy(\infty)}^{Upper}$ and $\varepsilon_{yy(\infty)}^{Lower}$ are the strain components of the upper and lower trapping limit, respectively. The examination of their mechanical response leads to the identification of the micro-mechanisms of stress accommodation, in both studied metals, in the absence of pre-existing dislocations and thus, reveals whether the crack configurations are brittle or ductile (§3.5.3).

Starting with aluminium, crack models that correspond to deformations larger than $\varepsilon_{yy(\infty)}^{Upper}$ exhibit crack extension. Figure V.27 illustrates the resulting atomic configuration of a $(010)[001]$ crack under $1.27\varepsilon_{yy(\infty)}^{Upper}$ applied deformation and after 10^3 time steps of energy minimization simulation. As it can be observed, the crack-tip, whose initial position is denoted by a red circle, has propagated along the $[100]$ crystallographic direction, though maintains its initial sharp shape. Moreover, the potential energy of the crack-tip region (U_{nc}) increases during the propagation process due to the formation of new crack surfaces (figure V.28). Impulses of the potential energy, highlighted by the red arrows in figure V.28, coincide with the crack-tip step-by-step motion during propagation, as well as with the instantaneous increase of the atoms of the crack faces (figure V.29). We therefore conclude that the crack extension proceeds via the cleavage mechanism on the (010) crack plane; hence, the crack configuration it can be considered brittle (§3.5.3).

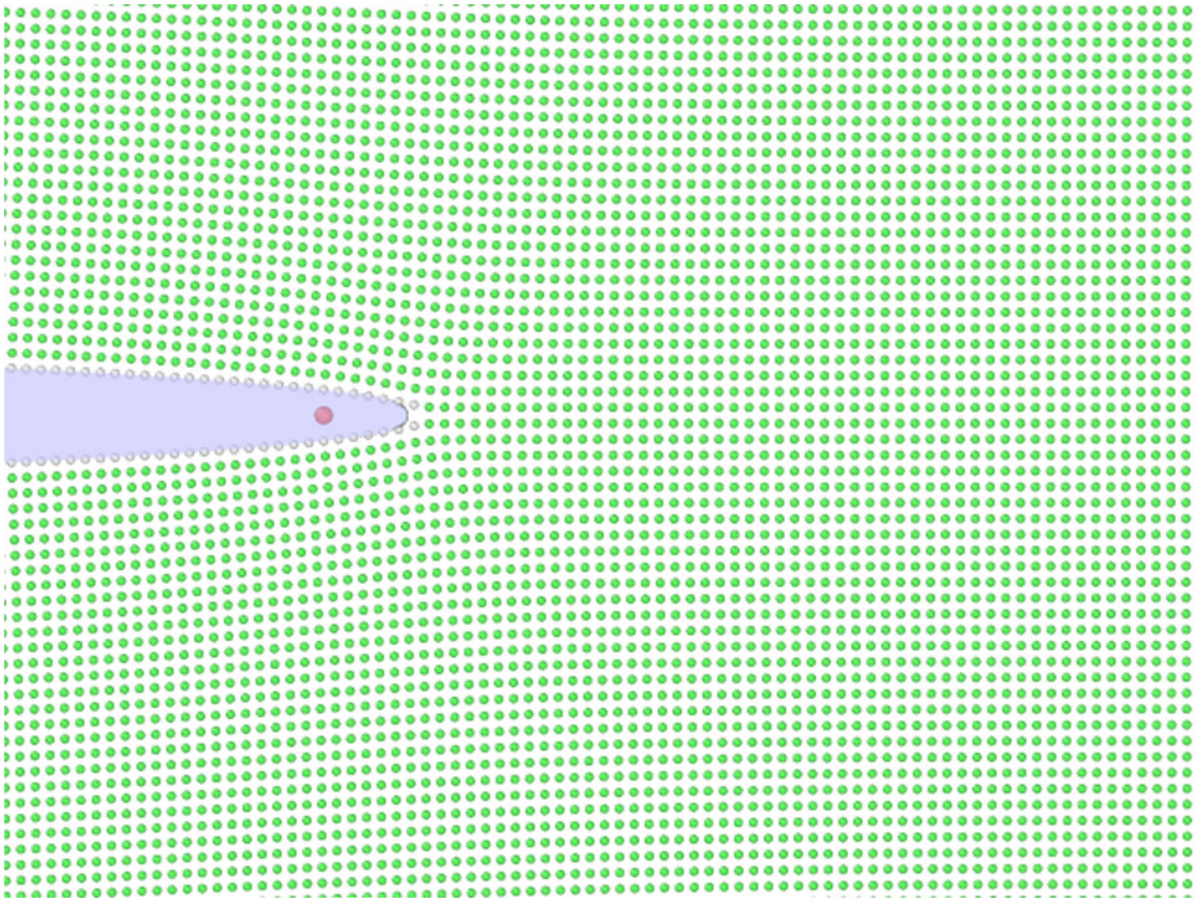

Figure V.27: The evolution of the atomic configuration of a $(010)[001]$ crack under deformation equal to $1.27\varepsilon_{yy(\infty)}^{Upper}$, after relaxation for 1000 time-steps. The initial half-length of the crack was equal to 22 lattice parameters and the initial position of the crack-tip is denoted by a red circle. The crack propagates via brittle cleavage on the (010) crack plane and along the $[100]$ direction.

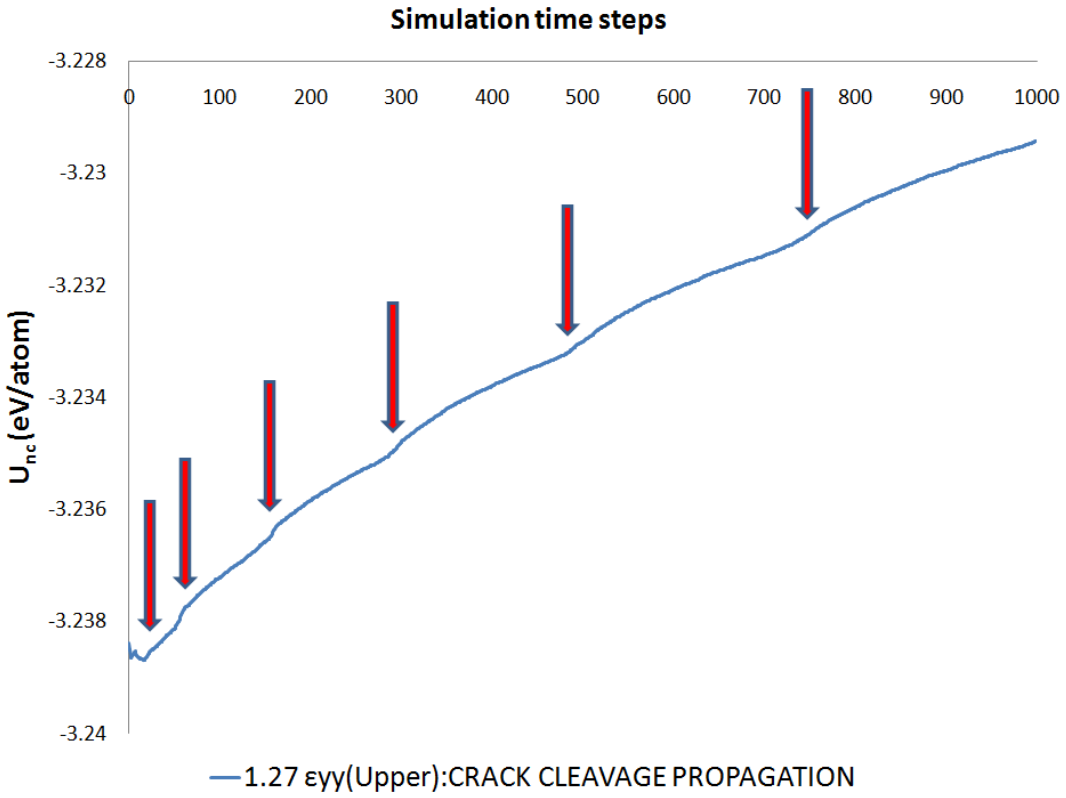

Figure V.28: The change in the potential energy of the near-crack region during the brittle propagation process. The potential energy increases due to the generation of new surfaces. The atomic bonds breaking, which denoted by red arrows, causes a smooth change in slope of the potential energy curve.

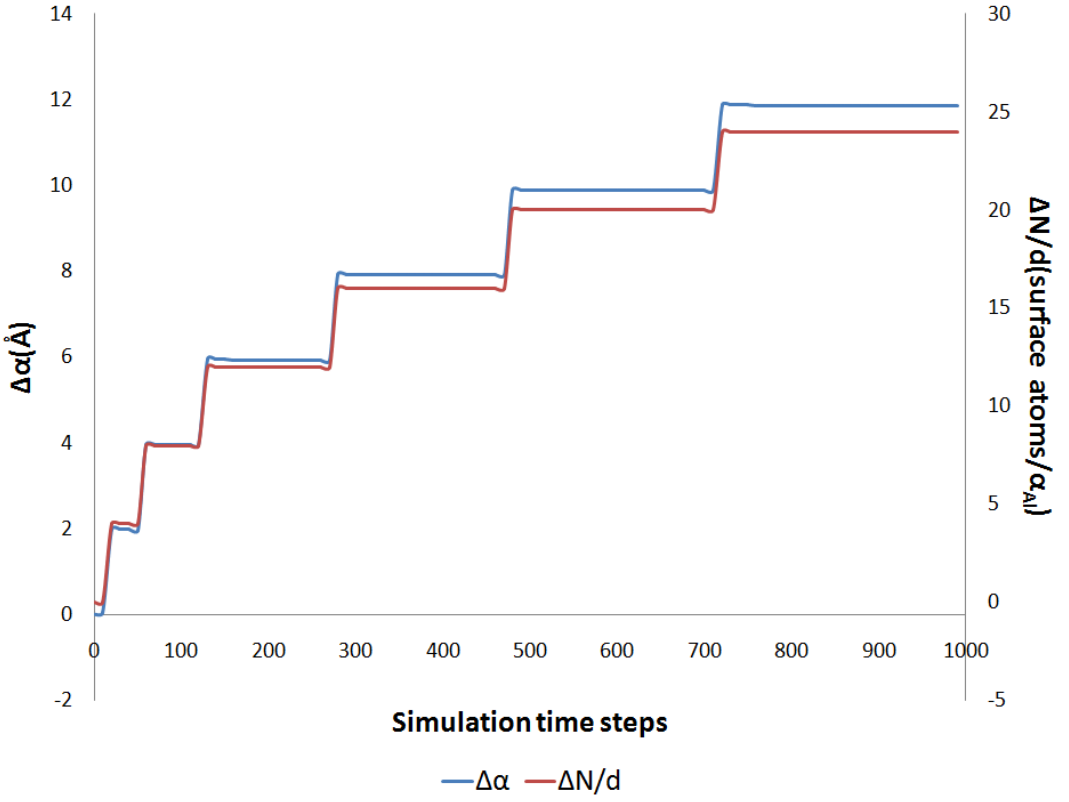

Figure V.29: Evolution of the crack half-length of a $(010)[001]$ crack under deformation equal to $1.27\varepsilon_{yy(\infty)}^{Upper}$ in respect to the relaxation time. The crack configuration is extended through a step-by-step brittle cleavage process.

For aluminium models under higher static deformation the mechanical response of a crack changes from cleavage propagation to dislocation emission from the crack-tip. Figure V.30 presents the structural evolution of a $(010)[001]$ crack under $2.97\varepsilon_{yy(\infty)}^{Upper}$ applied deformation resulting from the relaxation procedure. A part of the potential energy is absorbed (figure V.31) due to the emission of two $1/2\langle 110\rangle$ perfect dislocations of the fcc crystal lattice from the crack-tip (figure V.30). This mechanism of plasticity prevents the crack extension (figure V.32) and causes a blunt shape to the crack-tip (figure V.30); a feature which suggests that the crack configuration is ductile (§3.5.3). The emitted dislocations move away from the tip until their motion is restricted by the fixed-displacement boundary conditions.

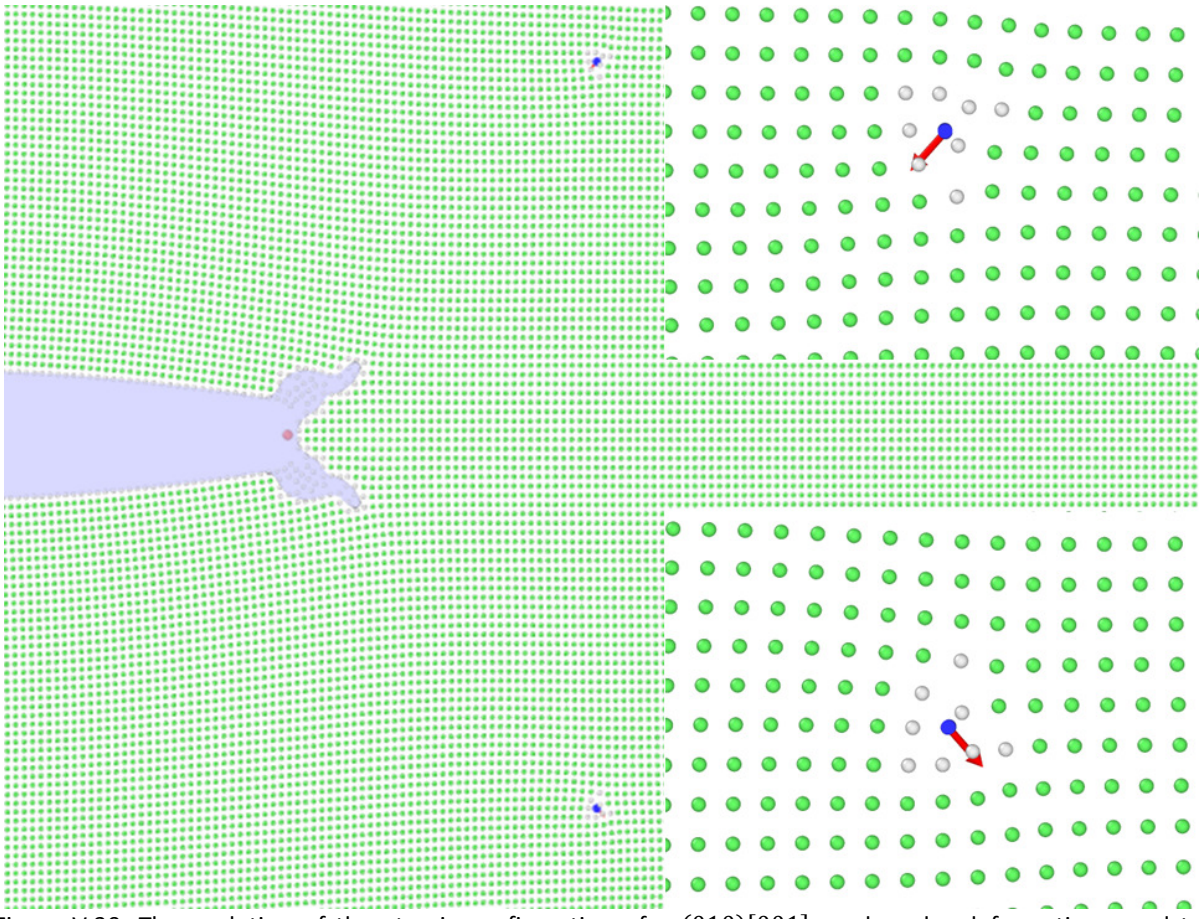

Figure V.30: The evolution of the atomic configuration of a $(010)[001]$ crack under deformation equal to $2.97\varepsilon_{yy(\infty)}^{Upper}$, after relaxation for 1000 time-steps. The initial half-length of the crack was equal to 22 lattice parameters and the initial position of the crack-tip is denoted by a red circle. The crack emits two $1/2[110]$ perfect dislocations from its tip, a plasticity mechanism that prevents the crack extension. The lines of dislocations are illustrated by blue colour, whereas red arrows represent the Burgers vectors.

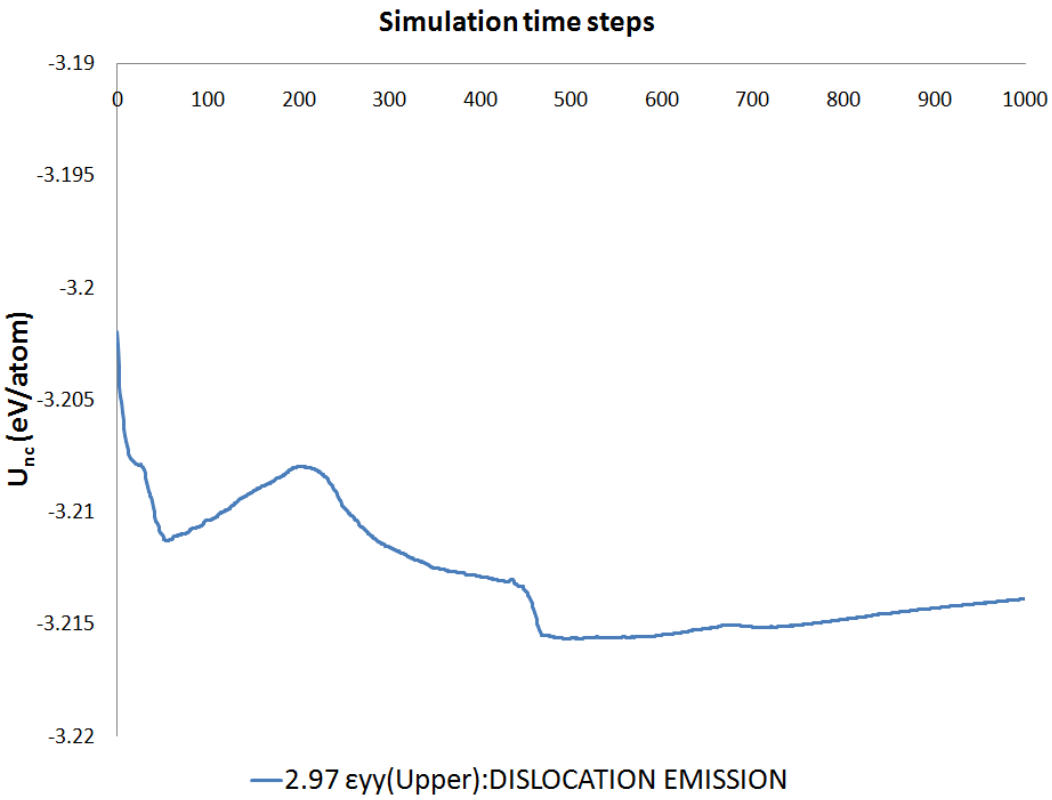

Figure V.31: The change in the potential energy of the near-crack region during the dislocation emission process. The potential energy decreases due to the dislocation emission from the crack-tip.

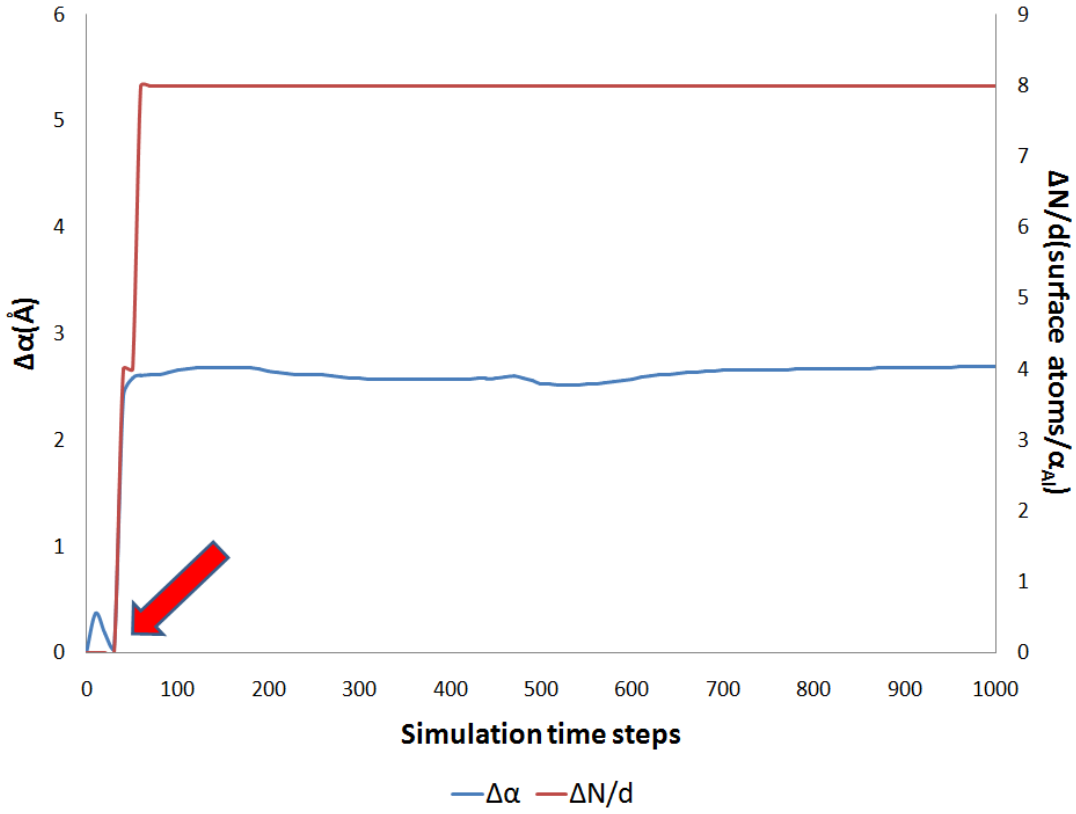

Figure V.32: Evolution of the crack half-length of a $(010)[001]$ crack under deformation equal to $2.97\varepsilon_{yy(\infty)}^{Upper}$, in respect to the relaxation time. The plasticity mechanism of the dislocation emission from the crack-tip, which is activated at the 40th time step (red arrow), prevents the further extension of the crack.

By the increase of the applied static deformation, the number of the emitted dislocations from the crack-tip also increases. A characteristic example is presented in figure V.33 in which a $(010)[001]$ crack under $3.40\varepsilon_{yy(\infty)}^{Upper}$ applied deformation generates six $1/2\langle 110\rangle$ perfect dislocations from its tip.

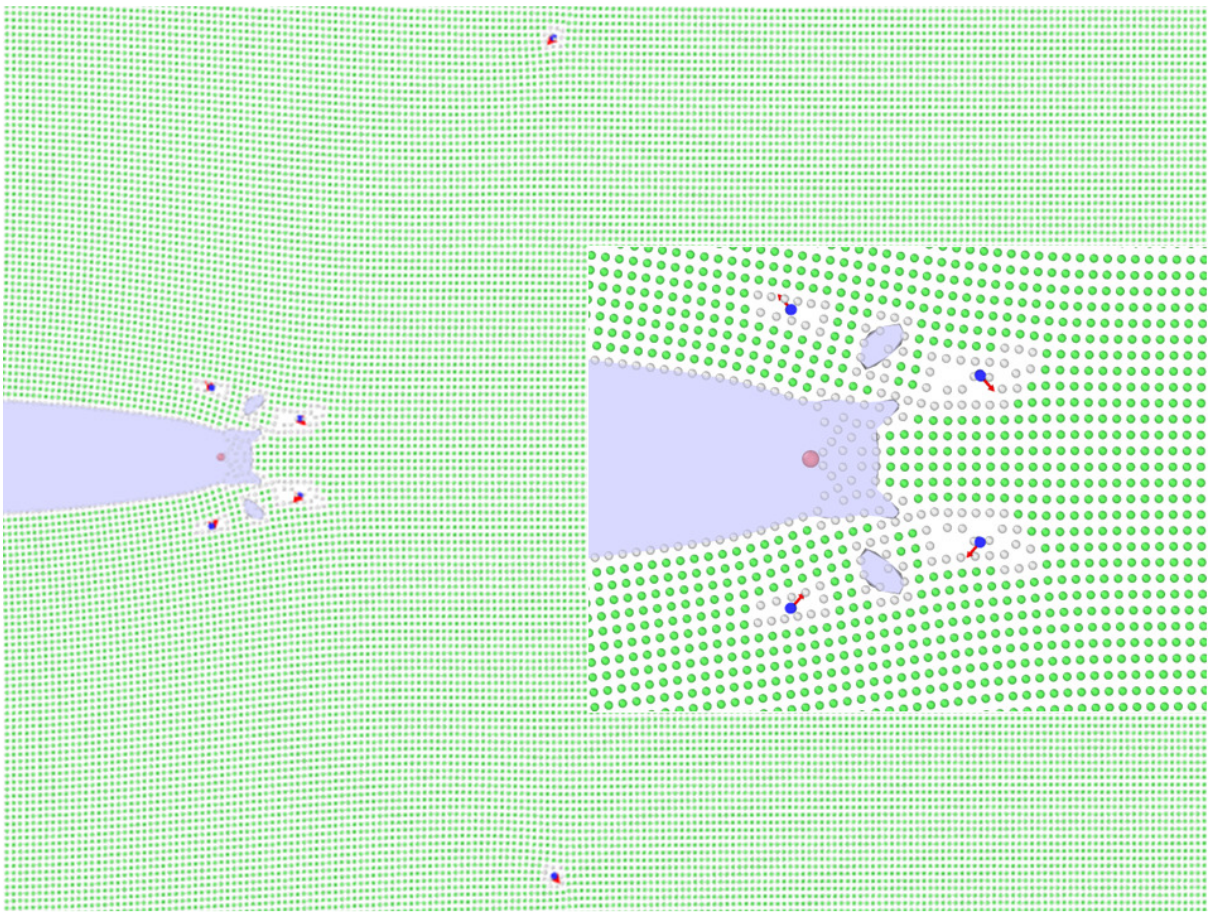

Figure V.33: The evolution of the atomic configuration of a $(010)[001]$ crack under deformation equal to $3.40\varepsilon_{yy(\infty)}^{Upper}$, after relaxation for 1000 time-steps. The initial half-length of the crack was equal to 22 lattice parameters and the initial position of the crack-tip is denoted by a red circle. The crack emits six $1/2[110]$ perfect dislocations from its tip, a plasticity mechanism that prevents the crack extension. The lines of dislocations are illustrated by blue colour, whereas red arrows represent the Burgers vectors.

On the other hand, by applying deformation lower than the $\varepsilon_{yy(\infty)}^{Lower}$ the crack starts closing during energy minimization. Figure V.34 shows the resulting configuration of a $(010)[001]$ crack under $0.85\varepsilon_{yy(\infty)}^{Upper}$ applied deformation and after 10^3 time-steps of simulation. The crack configuration is reduced in length maintaining the sharp shape of its tip. The potential energy of the crack-tip region (U_{nc}) decreases during this ''healing'' process due to the reduction of the crack faces. The decrease rate of the U_{nc} is characterized by a periodic form demonstrating the formation of new atomic bonds at the crack-tip (figure V.35). Moreover, the step-by-step motion of the crack-tip along the $[\bar{1}00]$ crystallographic direction, coincides

with the periodic variation of the U_{nc}, suggesting that the ''healing'' of the crack proceeds via a zipper-like procedure (figure V.36).

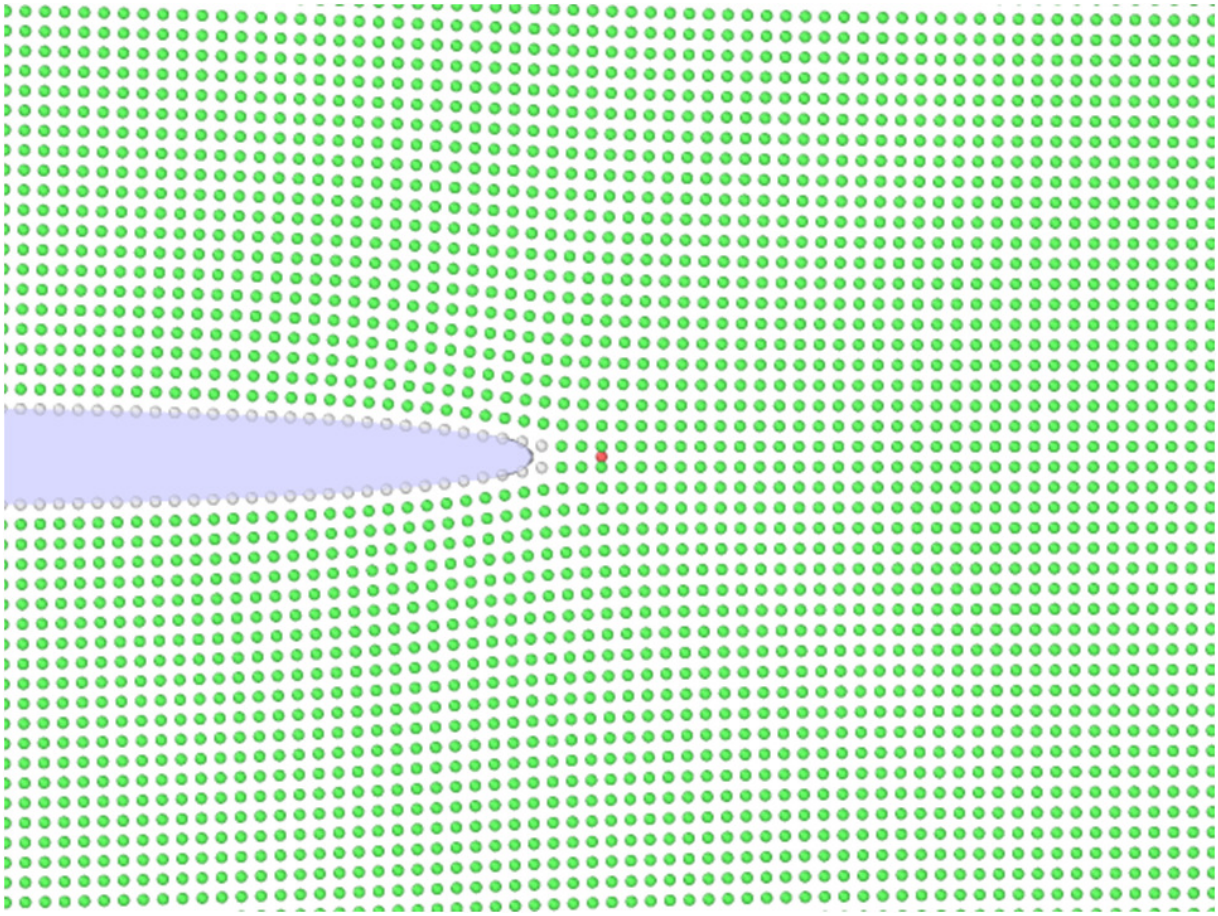

Figure V.34: The evolution of the atomic configuration of a $(010)[001]$ crack under deformation equal to $0.85\varepsilon_{yy(\infty)}^{Upper}$, after relaxation for 1000 time-steps. The initial half-length of the crack was equal to 22 lattice parameters and the initial position of the crack-tip is denoted by a red circle. The crack closes via a zipper-like healing mechanism.

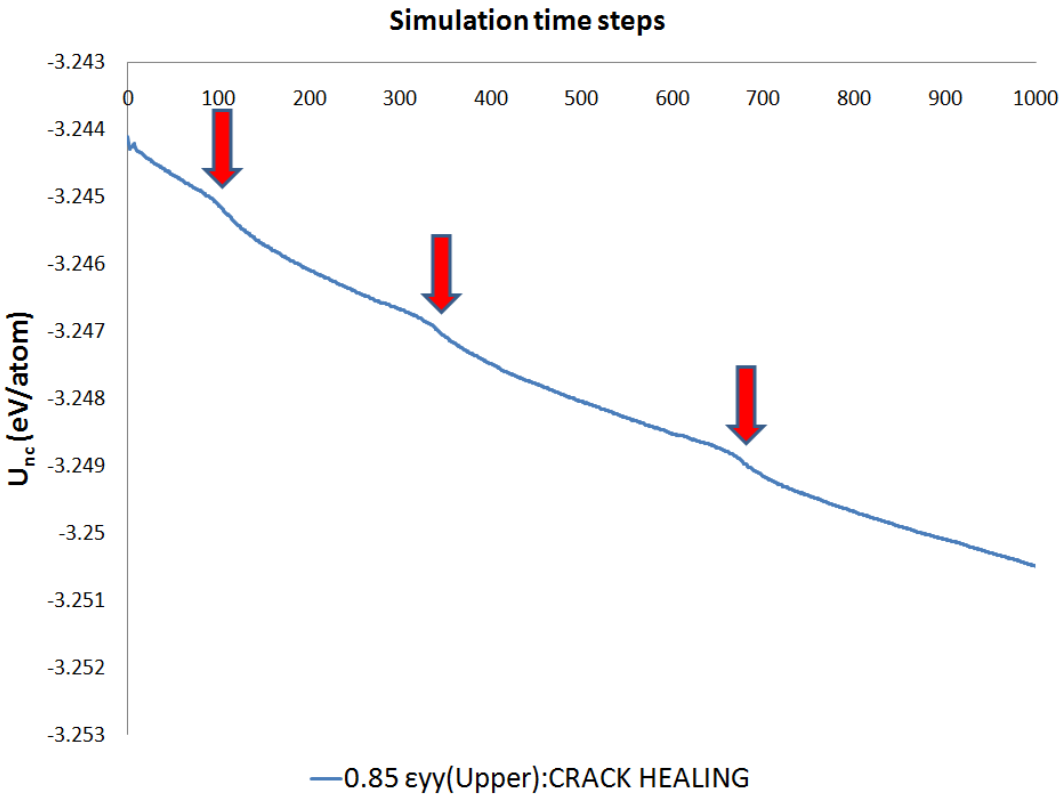

Figure V.35: The change in the potential energy of the near-crack region during the crack healing process. The potential energy decreases due to the reduction of the area of the crack surfaces. The reformation of atomic bonds at the crack-tip, which denoted by red arrows, causes a smooth change in the slope of the potential energy curve.

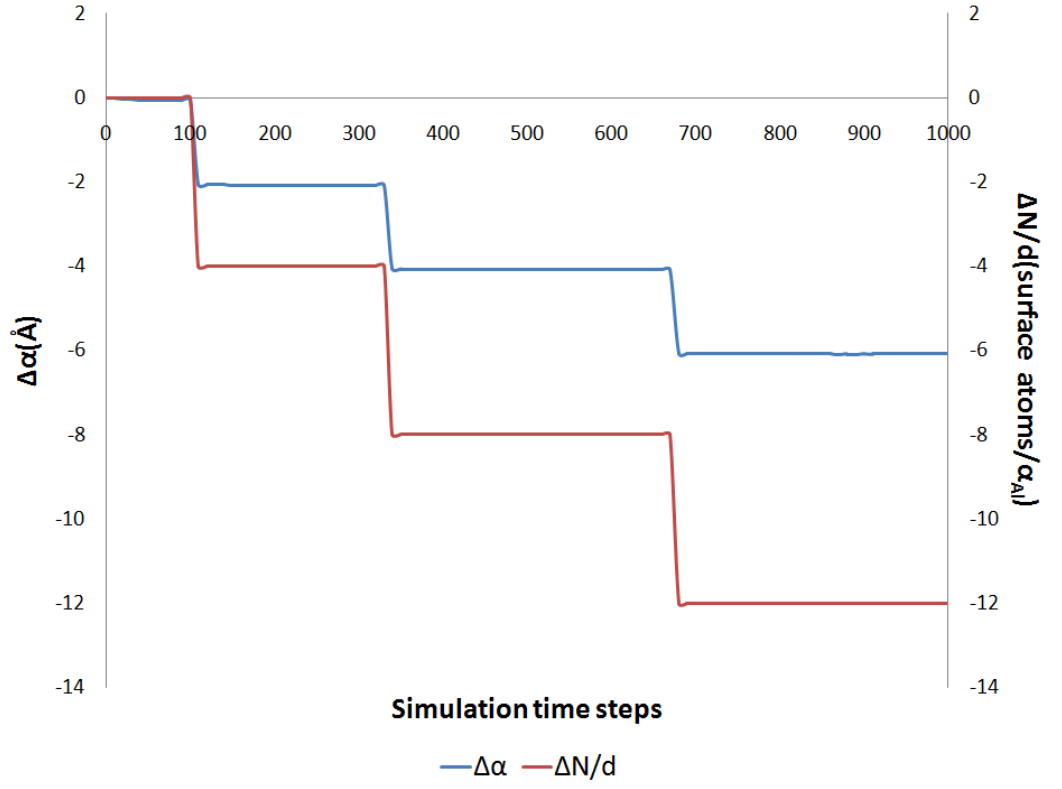

Figure V.36: Evolution of the crack half-length of a $(010)[001]$ crack under deformation equal to $0.85\varepsilon_{yy(\infty)}^{Upper}$ in respect to the relaxation time. The crack configuration is reduced in length through a step-by-step zipper-like process.

For the non-equilibrium configurations in iron, the same analysis has been performed. As it has been mentioned already, simulation results reveal the existence of three types of mechanical response sequences for the crack iron models, depending on the crack length or equivalently the applied loading level (figure V.8). The crack configurations with the largest dimensions (type III) exhibit crack propagation under applied deformation within the finite range:

$$\varepsilon_{yy(\infty)}^{Upper} < \varepsilon_{yy(\infty)} < \varepsilon_{yy(\infty)}^{DIS}$$

where $\varepsilon_{yy(\infty)}^{DIS}$ is the strain threshold required for dislocation formation in the vicinity of the crack-tip. A characteristic example of this mechanical response is given in the figure V.37.

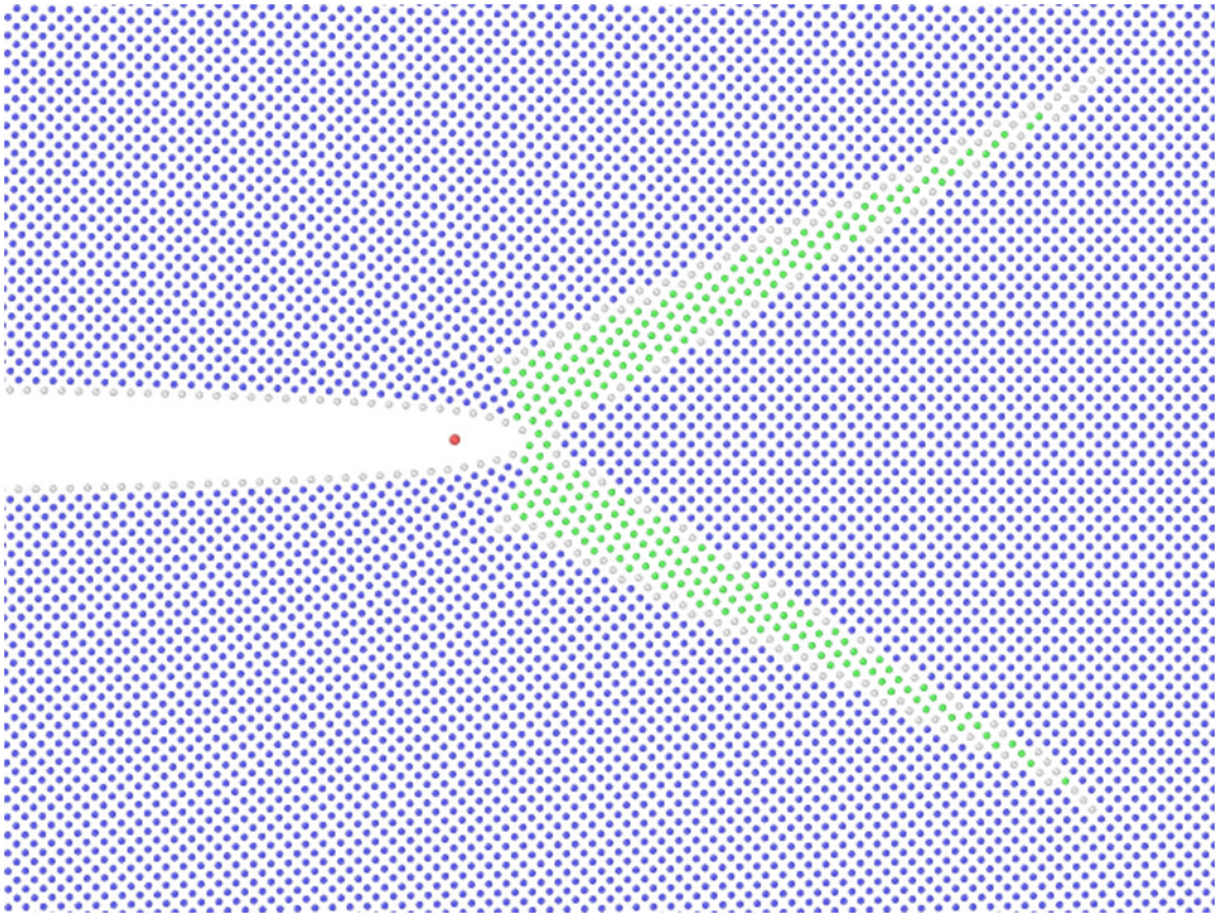

Figure V.37: The evolution of the atomic configuration of a $(010)[001]$ crack under deformation equal to $1.04\varepsilon_{yy(\infty)}^{Upper}$, after relaxation of 1.2×10^5 time-steps. The initial half-length of the crack was equal to 48 lattice parameters and the initial position of the crack-tip is denoted by a red circle. The crack propagates via brittle cleavage on the (010) crack plane and along the $[100]$ direction. The blue and green colour atoms represent the bcc and fcc crystal structure, respectively.

Here, the resulting configuration of a $(010)[001]$ crack under $1.04\varepsilon_{yy(\infty)}^{Upper}$ applied deformation is presented after 1.2×10^5 time-steps of energy minimization simulation. As it can be observed, the crack increases in length, on the (010) crystallographic plane and along the $[100]$ crystallographic direction, maintaining the atomically sharp shape of its tip. Focusing on the energetics of the model, the U_{nc} increases with a step-by-step manner during the crack extension (figure V.38). This behaviour of U_{nc} coincides perfectly with the discrete motion of the crack-tip along the crack plane and the gradual increase of the crack surface atoms (figure V.39). Therefore, simulation results suggest that the crack is propagating via cleavage mechanism (§3.5.3); thus, the crack model can be considered to have brittle response. Indeed, the DXA investigation did not detect the generation of any dislocations during the crack propagation. However, the structural analysis of the model reveals that the crack-tip motion is accompanied by the occurrence of phase transformations (figure V.37).

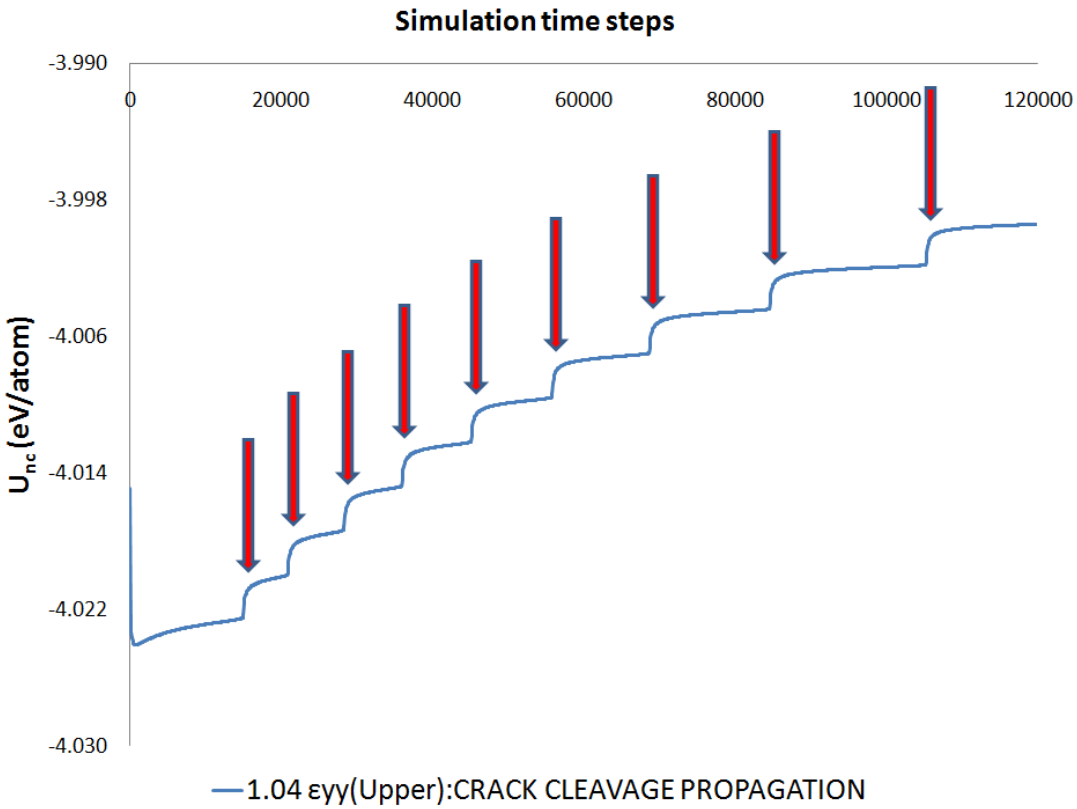

Figure V.38: The change in the potential energy of the near-crack region during the brittle propagation process of the crack. The potential energy increases due to the generation of new surfaces. The atomic bonds breaking at the crack-tip, which denoted by red arrows, causes a discrete gradual increase of potential energy.

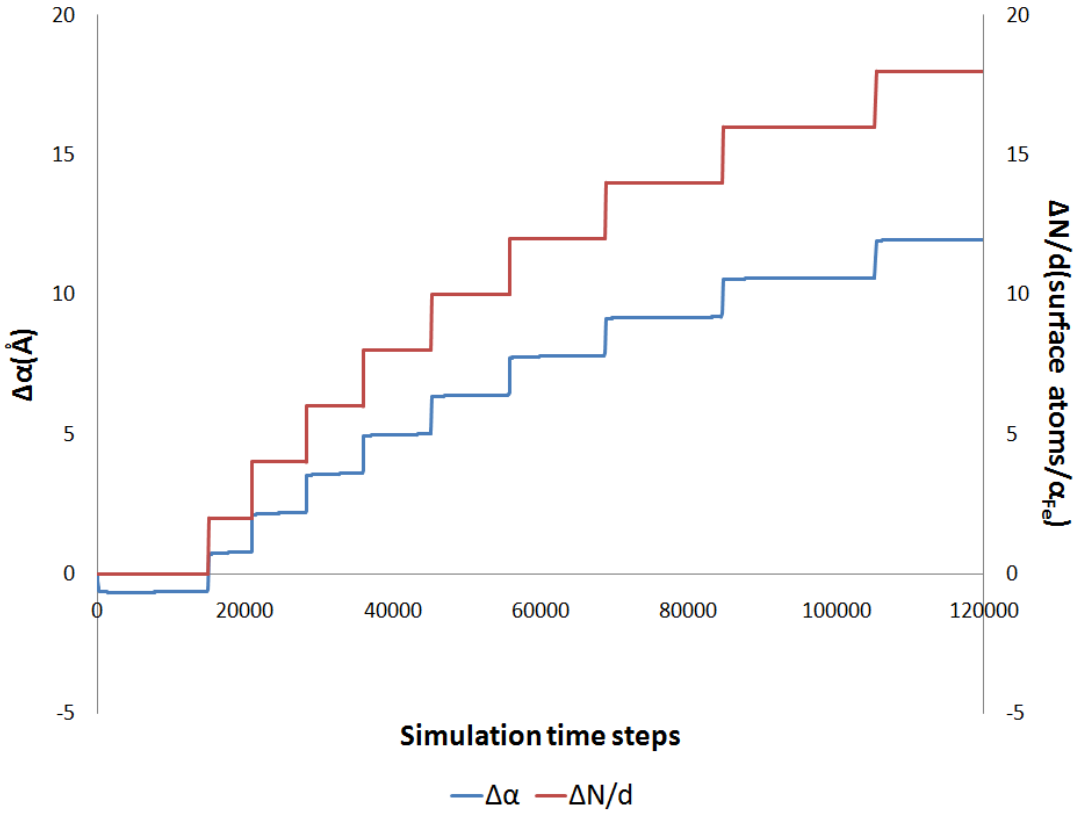

Figure V.39: Evolution of the crack half-length of a $(010)[001]$ crack under deformation equal to $1.04\varepsilon_{yy(\infty)}^{Upper}$ in respect to the relaxation time. The crack configuration is extended through a step-by-step brittle cleavage process on the (010) crack plane and along the $[100]$ direction.

This finding has raised the need for further investigation of the atomistic models, for both the equilibrium and non-equilibrium cracks. Structural analysis of the equilibrium crack configurations, corresponding to the lower trapping limit, shows that the applied deformation is sufficient to cause the formation of two fcc strips in the vicinity of each crack-tip (figure 40a). The increased applied deformation, which is required for the equilibrium crack configurations corresponding to the upper trapping limit, leads to the expansion of these fcc regions within the bcc matrix (figure 40b). Hence, it can be concluded that a bcc→fcc phase transformation is taking place in front of the crack-tip in order to accommodate the increase of the applied strain between the two stability limits. This local phase transformation suggests that the mechanical stability of a crack inside the crystalline iron is related to the energy difference between the bcc and fcc crystal structure of the system at the $T = 0K$, which is an intrinsic property of the system [PON2007]!

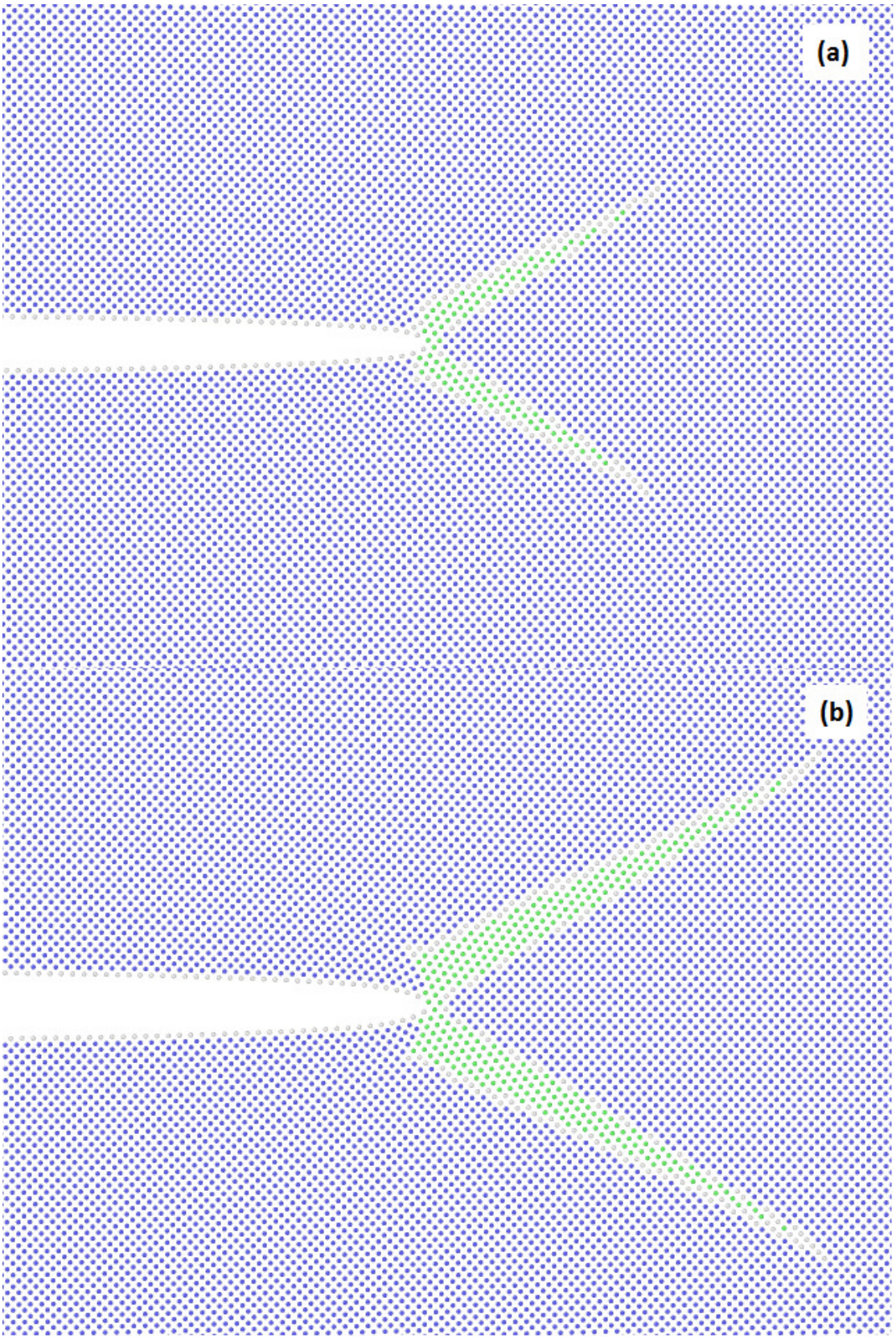

Figure V.40: The (a) lower trapping limit and (b) upper trapping limit equilibrium configurations of a nano-sized $(010)[001]$ crack, in bcc iron, with crack-length equal to 48 lattice parameters. The increased applied deformation, which is required for the equilibrium crack configurations corresponding to the upper trapping limit, leads to the expansion of the fcc regions (green atoms) within the bcc matrix (blue atoms).

Focusing on the cleavage crack propagation, it can be observed (figure V.37) that the fcc regions, which are formed due to the applied deformation level, follow the motion of the crack-tip along the $[100]$ direction. According to this atomic mechanism, the part of the bcc matrix which is located in the front part of the fcc regions, along the crack propagation direction, is transforming into the fcc phase (bcc→fcc), while simultaneously the rear part of the fcc regions, i.e. on the opposite direction, is transforming into the bcc state (fcc→bcc). These phase transformations are continuous, during crack extension, and they cause the movement of the fcc regions through the bcc matrix. This is the route that the crystalline lattice follows in order to accommodate strain at the region ahead of the crack-tip, which results to the cleavage propagation. Similar structural transformations at the vicinity of $(010)[001]$ cracks, inside the bcc Mo, have been recently observed experimentally by Wang et al. [WAN2014]. According to his study, the highly stable bcc structure can be transformed to a meta-stable fcc state, locally, at the region ahead of the crack-tip upon tensile loading. Wang states that this structural change is feasible due to the fact that other shear deformation mechanisms are suppressed or bypassed [WAN2014]. In particular, the crystallographic orientation of the $(010)[001]$ cracks prevents the occurrence of twinning because none of the $\{112\}$ twinning planes are parallel to the crack front, i.e. the $[001]$ crystallographic direction. In addition, the tensile tests were conducted on a pure Mo crystalline film, where dislocation activity was absent. Both the above conditions apply to our atomistic crack models as well. Hence, it can be concluded that our crack models accommodate the accumulated strains by using the easiest deformation mechanism that is available, under the existing simulation conditions. Furthermore, Wang has shown that the higher energy fcc structure can be transformed back to the low-energy bcc state, upon unloading the imposed stresses [WAN2014]. This result suggests that the experimentally observed stress-induced phase transition between the bcc and fcc structures is reversible (bcc↔fcc), a behaviour which is also observed in our atomic crack models during the cleavage mechanism. According to Wang [WAN2014], the experimentally observed bcc↔fcc phase transformations are performed locally through a shear deformation mechanism based on the Nishiyama-Wassermann [NIS1934] and/or the Kurdjumov-Sachs [KUR1930] relationships between the two crystalline structures. The same mechanisms of phase transformation have been obtained numerically by molecular dynamics simulations for nano-crystalline α-iron [LAT2003]. Due to time constraints, the

exact mechanism of the bcc↔fcc transitions [INT4], in our atomic crack models, have not been identified. Nevertheless, this does not prevent us from commenting on the possible consequences of these structural transformations on the mechanical behavior of propagating cracks. Atomistic results in the present study demonstrate that the stress-induced bcc↔fcc transitions and cleavage mechanism, in iron, cooperate at $T = 0K$. This finding suggests that the crystalline lattice resistance to the brittle cleavage propagation of $(010)[001]$ cracks is potentially associated with the energy difference between the stable bcc and the meta-stable fcc structures; hence it is an intrinsic property of the system.

For crack configurations that exceed the $\varepsilon_{yy(\infty)}^{DIS}$ limit (types I-III), the stress concentration in the vicinity of the crack-tip is sufficient to induce plasticity into the single-crystalline system. Simulation results reveal that dislocation formation has been taken place inside the strip regions of the fcc crystalline structure. The generated perfect $1/2[110]$ dislocations are immediately dissociated into pairs of Shockley partials, with Burgers vector equal to $1/6[112]$. The dissociation mechanism leads to the formation of stacking faults, of hexagonal close-packed (hcp) structure with 2 atomic layers of thickness, inside the fcc strip regions. As a result, the crack atomic models characterized by dislocation generation mechanical response under strain, contain three different types of crystalline structures: (i) the bcc, (ii) the fcc and the (iii) hcp. Figure V.41 illustrates the resulting atomic configuration of this plastic deformation mechanism, obtained from a $(010)[001]$ crack under $1.46\varepsilon_{yy(\infty)}^{Upper}$ applied strain and upon relaxation for 3×10^3 time-steps. As it can be observed, the generation of both the Shockley partial dislocations (figure V.42) and the stacking faults (figure V.43) prevent the crack to propagate and increase its dimensions (figure V.44). This is due to the absorption of significant amount of elastic energy that takes place in the crack-tip region (figure V.45) and therefore dislocation formation is the most effective way for the system to accommodate the high applied deformation. These crack configurations can be considered to have ductile mechanical response (§3.5.3).

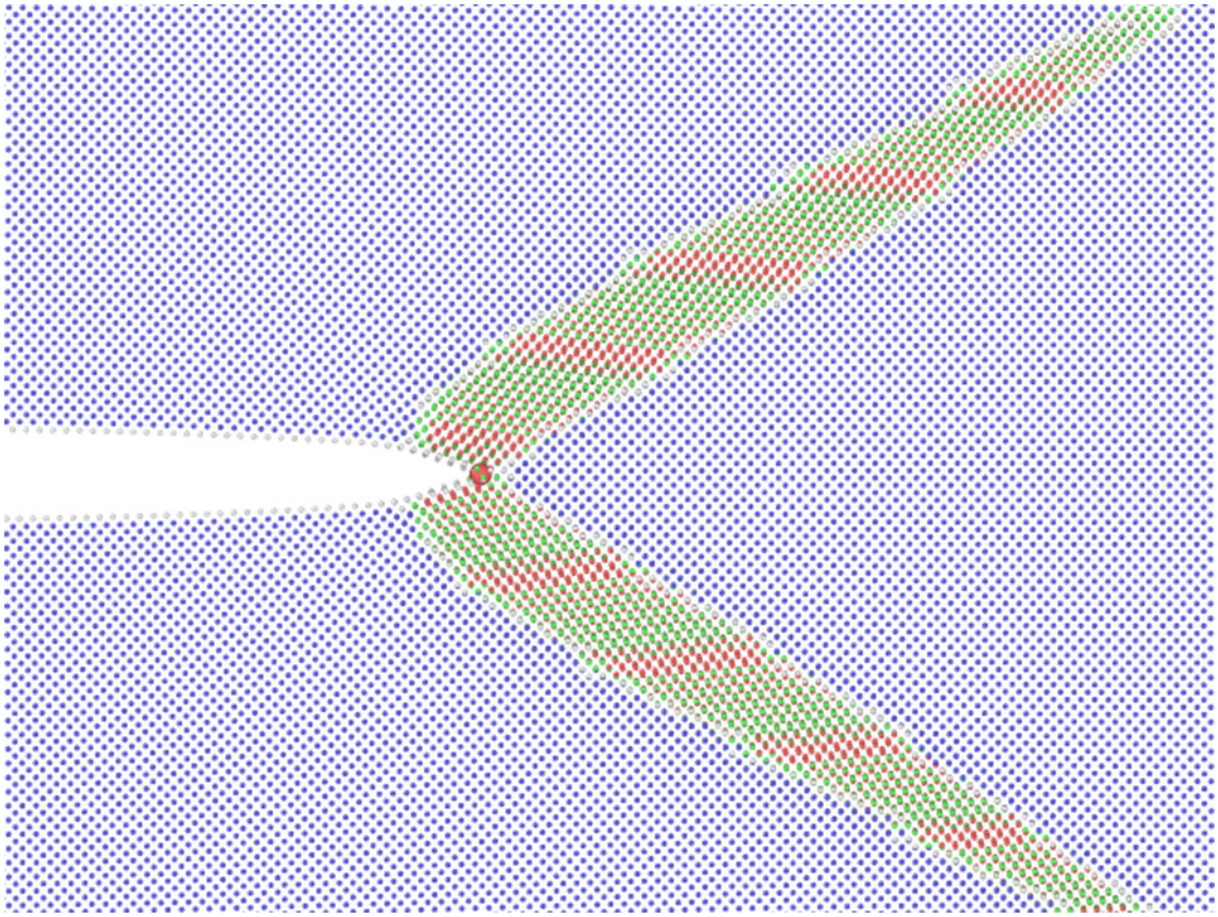

Figure V.41: The evolution of the atomic configuration of a $(010)[001]$ crack under deformation equal to $1.46\varepsilon_{yy(\infty)}^{Upper}$, after relaxation for 3×10^3 time-steps. The initial half-length of the crack was equal to 40 lattice parameters and the initial position of the crack-tip is denoted by a red circle. The generation of stacking faults (red atoms) of hcp structure inside the fcc strip sections (green atoms) prevent the crack propagation to accommodate the applied stain.

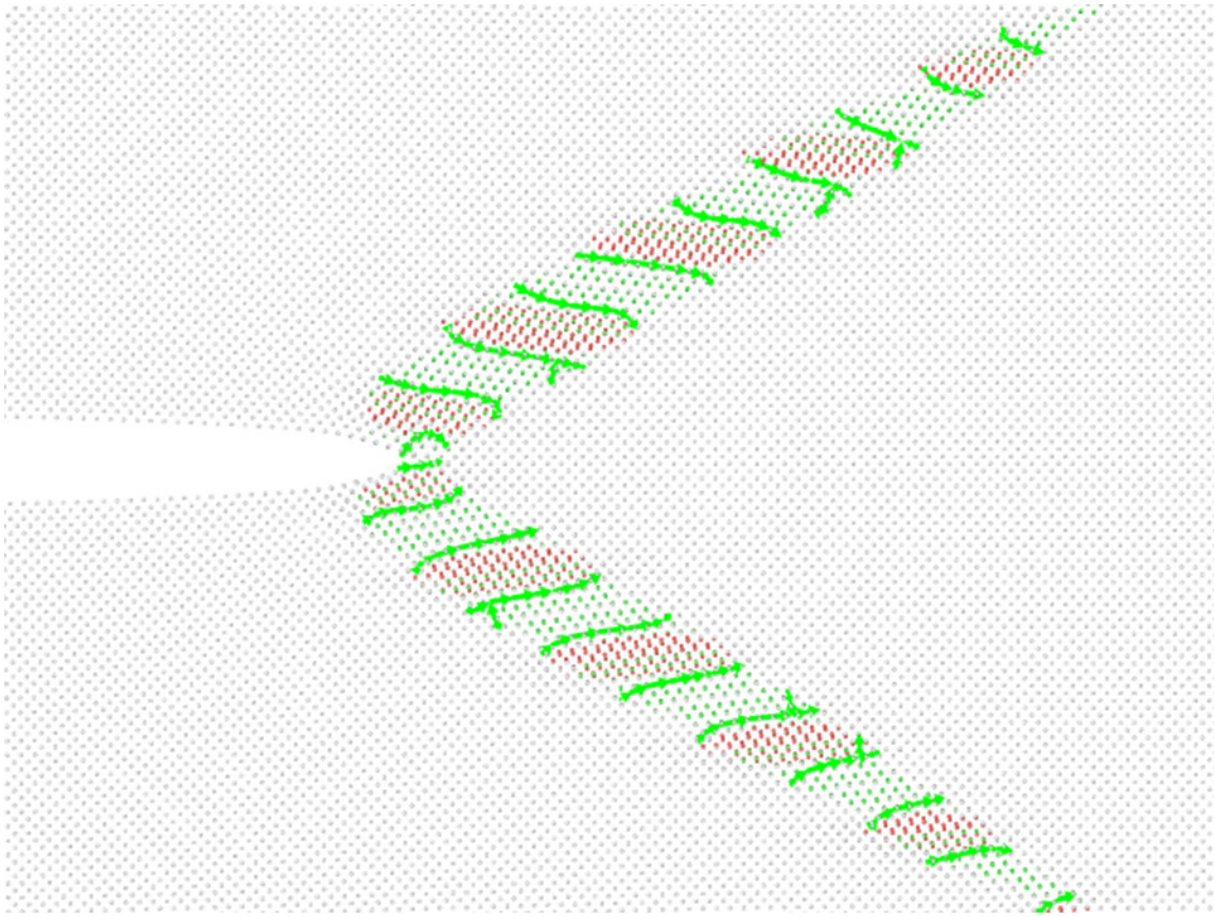

Figure V.42: The evolution of the atomic configuration of a $(010)[001]$ crack under deformation equal to $1.46\varepsilon_{yy(\infty)}^{Upper}$, after relaxation of 3×10^3 time-steps. Shockley partial dislocations, with Burgers vector equal to $1/6[112]$, have been formed inside the fcc structure regions to accommodate the applied strain.

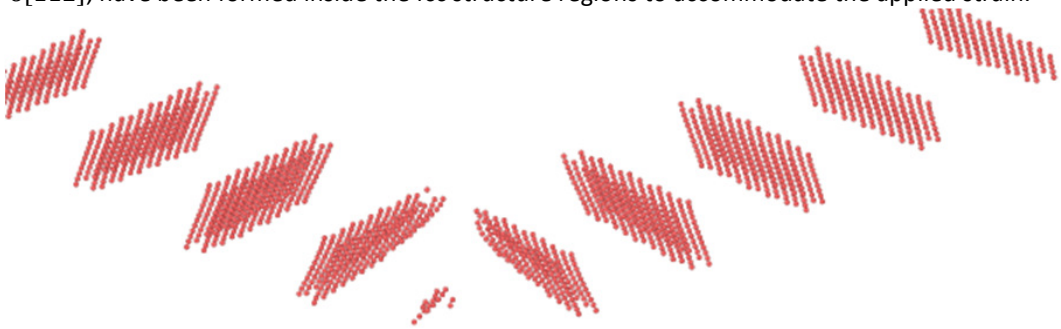

Figure V.43: The dissociation of the Shockley partial dislocations generate hcp stacking faults with 2-layers of thickness inside the fcc structure regions.

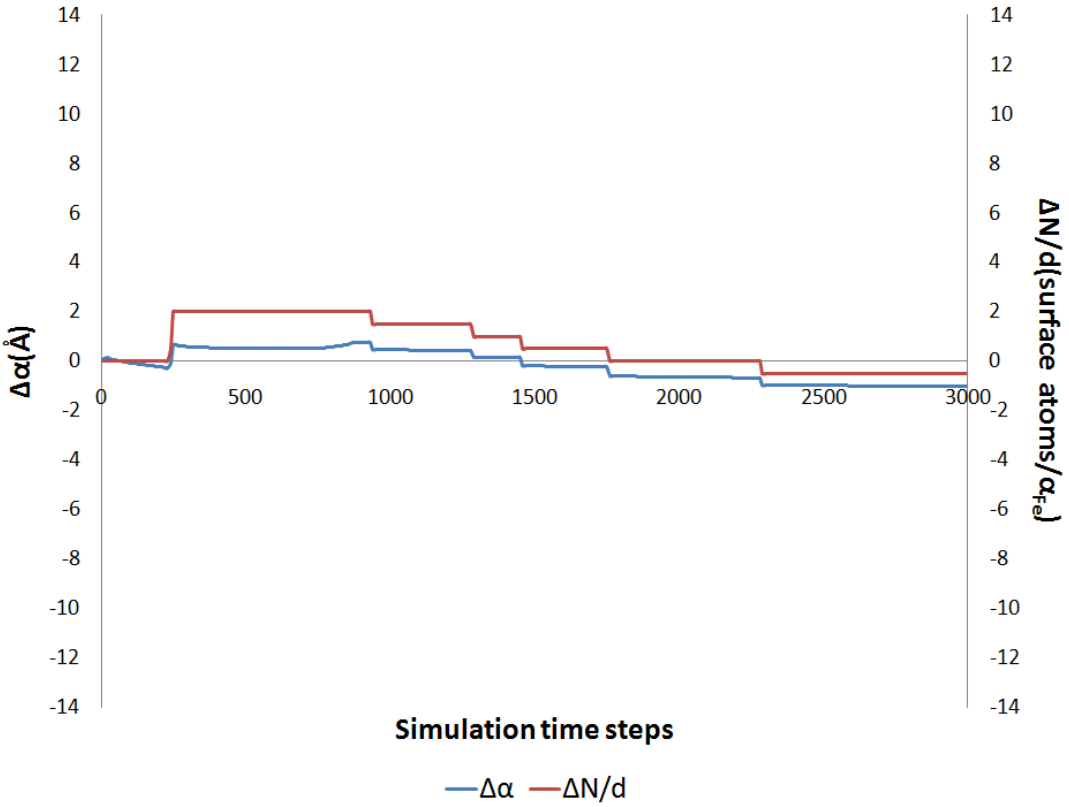

Figure V.44: Evolution of the crack half-length of a $(010)[001]$ crack under deformation equal to $1.46\varepsilon_{yy(\infty)}^{Upper}$ in respect to the relaxation time. The plasticity mechanism of the dislocation and stacking fault formation in the vicinity of the crack-tip prevents the crack extension.

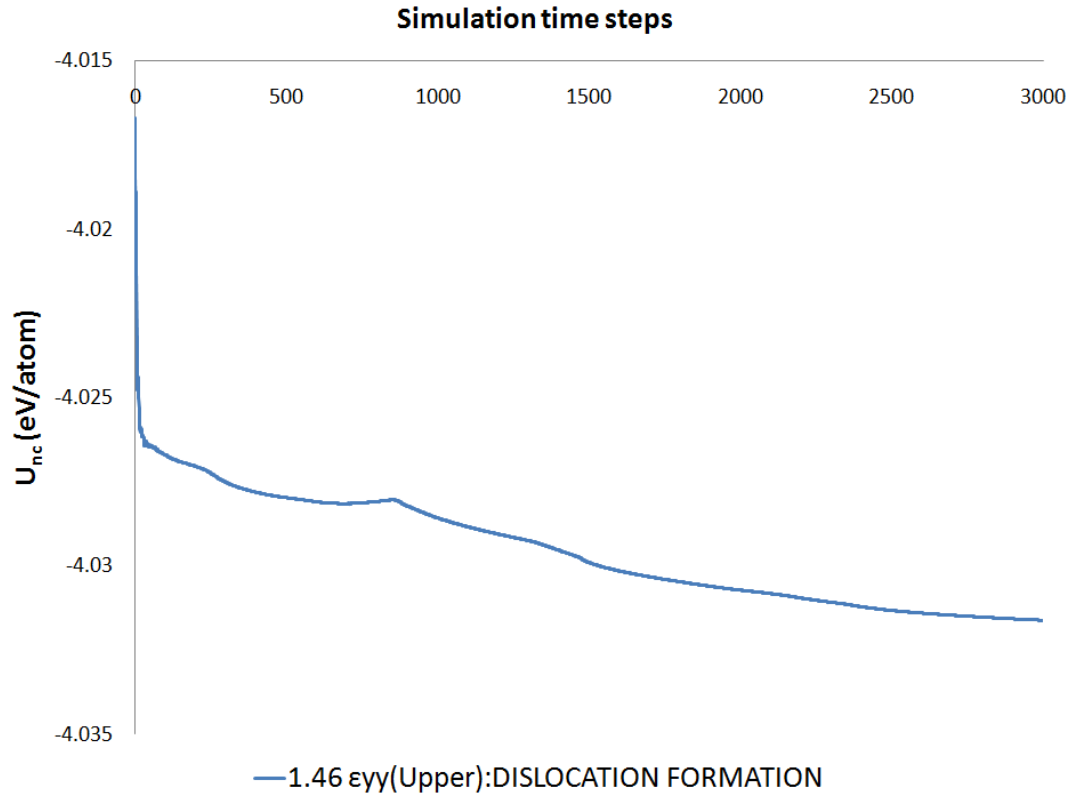

Figure V.45: The change in the potential energy of the near-crack region during the dislocation formation in the vicinity of the crack-tip. The potential energy rabid decrease implies the absorption of significant amount of elastic energy.

Finally, similar to aluminium models, the crack configurations in iron that correspond to applied strain lower than the $\varepsilon_{yy(\infty)}^{Lower}$ (types II and III), are healed during energy minimization simulation. Figure V.46 presents the atomic configuration of a $(010)[001]$ crack obtained via relaxation of 1.2×10^2 time-steps and corresponds to applied strain conditions equal to $0.69\varepsilon_{yy(\infty)}^{Upper}$. Apparently the crack configuration is reduced in length, maintaining the atomically sharp shape of its tip. Moreover, the fcc formed regions in the vicinity of the crack-tip have been restricted in size due to reduction of the stress concentration. The healing procedure is presented in figure V.47 where the crack length is given in respect to the simulation time. As it can be seen, the crack length is decreasing gradually suggesting a zipper-like healing process along the $[\bar{1}00]$ direction. The crack healing is accompanied by reduction in the U_{nc} due to elimination of the crack faces (figure V.48).

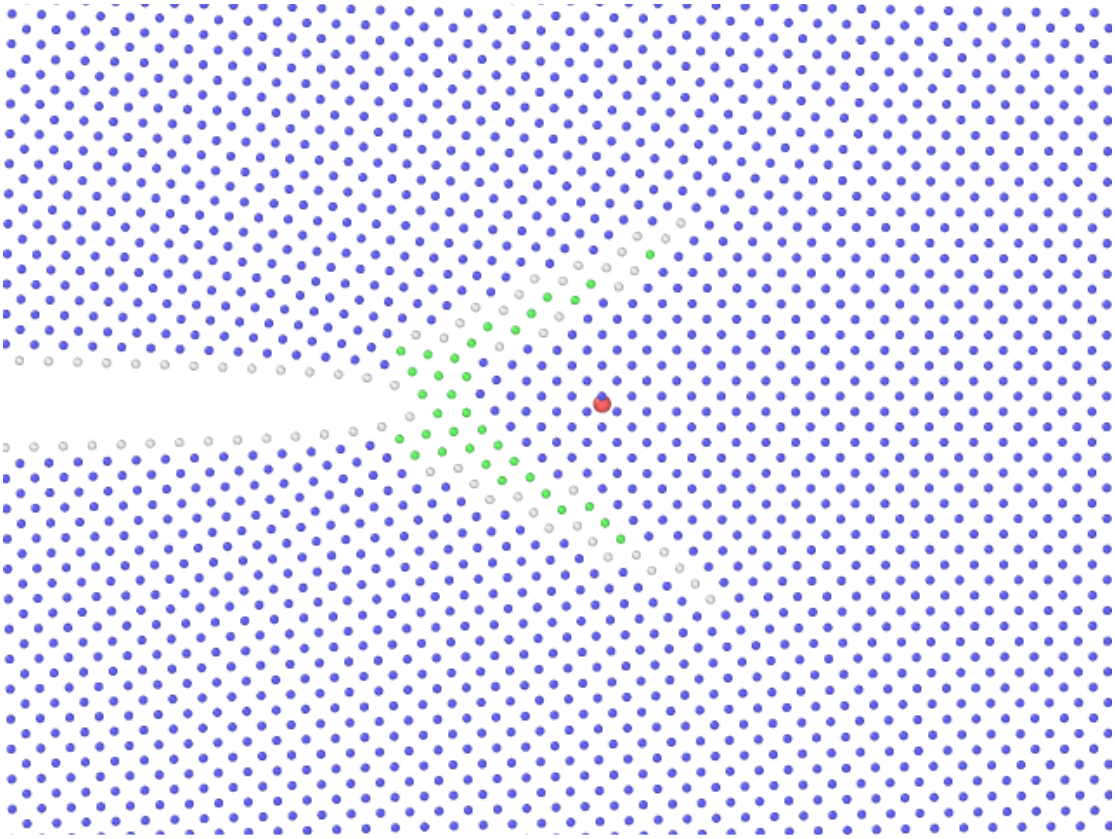

Figure V.46: The evolution of the atomic configuration of a $(010)[001]$ crack under deformation equal to $0.69\varepsilon_{yy(\infty)}^{Upper}$, after relaxation for 1.2×10^2 time-steps. The initial half-length of the crack was equal to 40 lattice parameters and the initial position of the crack-tip is denoted by a red circle. The crack closes via a zipper-like healing mechanism on crack (010) plane and along the $[\bar{1}00]$ direction.

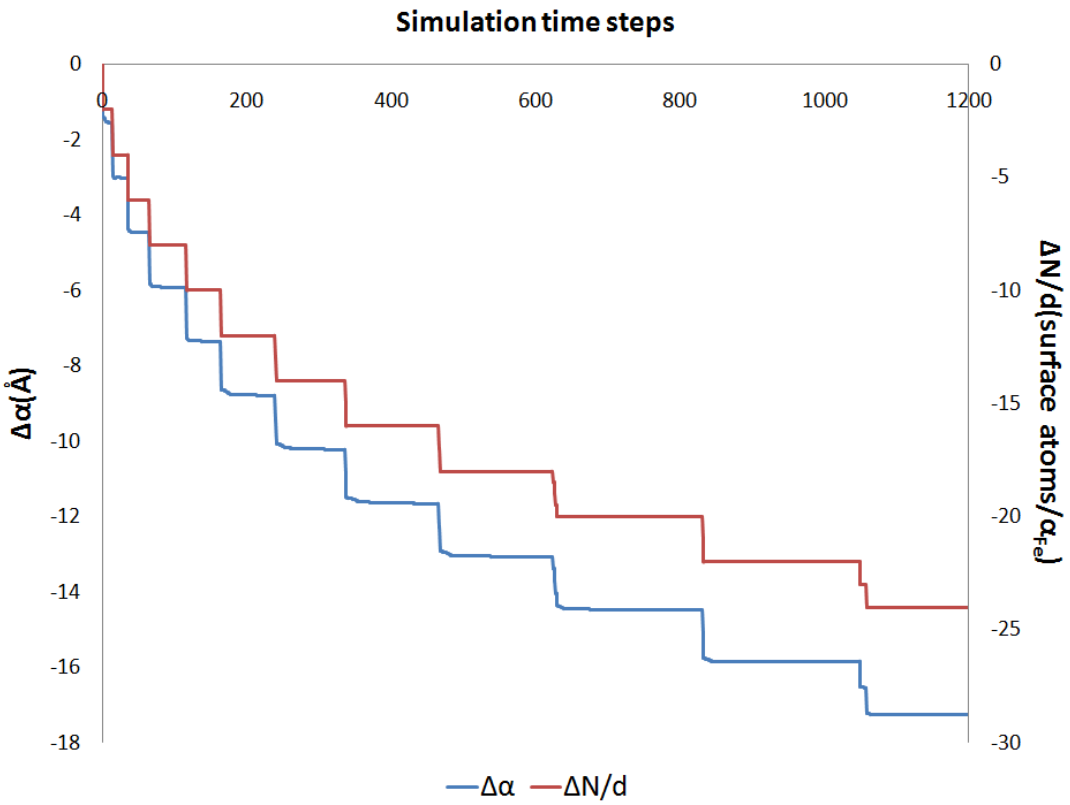

Figure V.47: Evolution of the crack half-length of a $(010)[001]$ crack under deformation equal to $0.69\varepsilon_{yy(\infty)}^{Upper}$ in respect to the relaxation time. The crack configuration is reduced in length through a step-by-step zipper-like process.

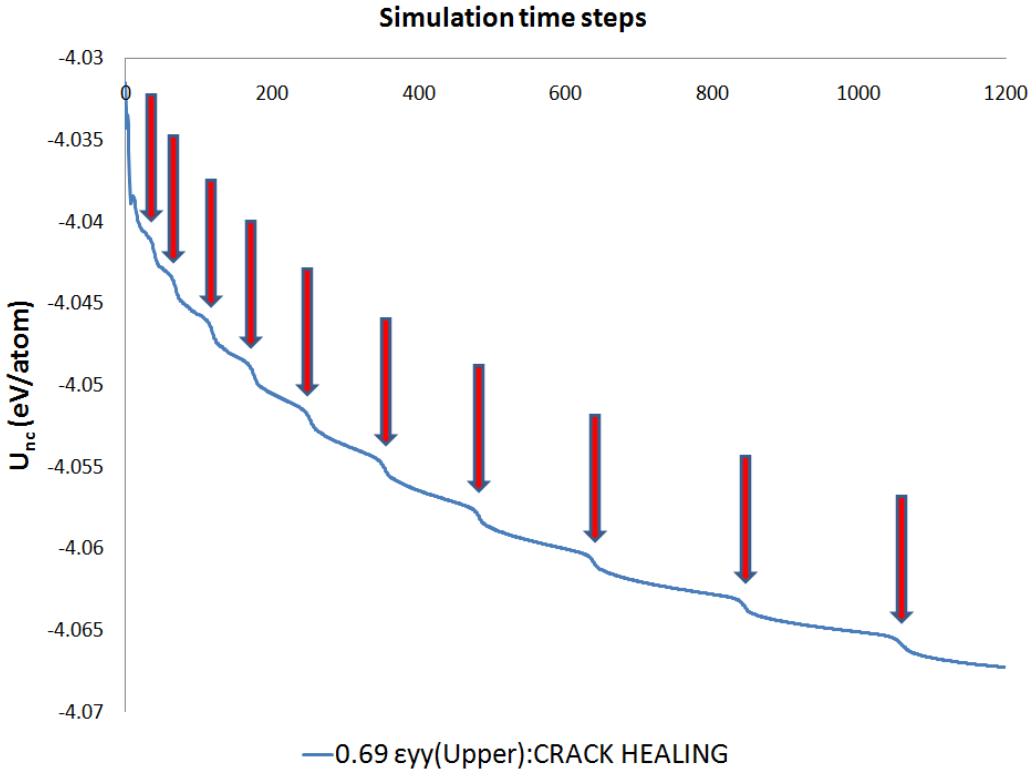

Figure V.48: The change in the potential energy of the near-crack region during the crack healing process. The potential energy decreases due to the reduction of the area of the crack surfaces. The reformation of atomic bonds at the crack-tip, which denoted by red arrows, causes a smooth change in the slope of the potential energy curve.

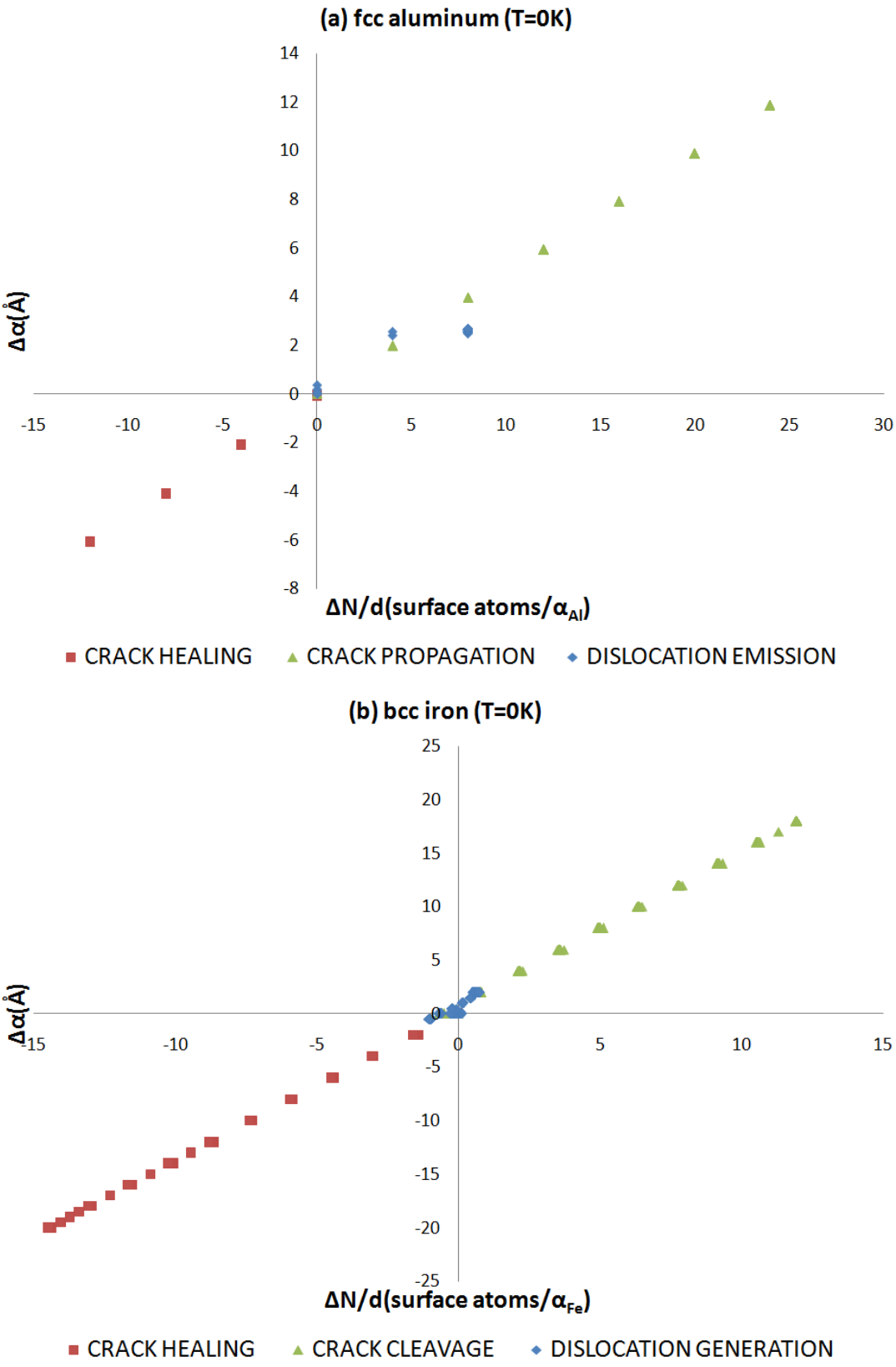

Figure V.49: The criterion of distinguish the mechanical response of cracks under load in (a) fcc aluminium and (b) bcc iron at $T = 0K$.

Figure V.49 illustrates the application of the scheme III.19 in the systems under study. Simulation results in both metals have been shown that the cleavage (§3.5.3) and zipper-like

healing mechanisms are characterized by a linear relation between the quantities $\Delta\alpha$ and ΔN. This linearity is extended due to the uninhibited change in crack length. On the contrary, the dislocation emission and formation mechanisms in aluminium and α-iron respectively, are described by a non-geometric $\Delta\alpha = f(\Delta N)$ relation of restricted range at the origin of the coordinate axis. These results suggest that the III.19 scheme is capable to effectively distinguish the brittle and ductile type of mechanical response of a crack in the absence of pre-existing dislocations. More importantly, atomistic results at $T = 0K$ suggest that the type of the mechanical response of non-equilibrium cracks, in both metals, can be transformed from brittle (cleavage propagation) to ductile (dislocations emission or generation) with increasing static load. Consequently, we have proved that the dynamic behaviour of our crack-containing systems at $T = 0K$ can change depending on the loading level of the system. This result suggests that the association of the dynamic response of crack-containing crystal with the intrinsic mechanical behaviour of this material, without taking into account the loading level of the system, is not correct! This finding constitutes a tool to criticise many studies that exist in literature. To obtain a more ''quantitative'' description of the dynamic response of cracks a different approach has been also followed.

5.7.2. Dynamic response of equilibrium cracks in fcc aluminium and bcc iron

An alternative method to determine the dynamic response of a crack upon loading can be performed by a two-step process:

(i) the stabilization of the crack configuration in a mechanical equilibrium state under specific strain-stress conditions and

(ii) its dynamic evolution upon implementation of additional deformation or loading.

For studying the dynamics of cracks above the stability region, the models corresponding to the upper trapping limit, determined in §5.1.1, have been selected as initial equilibrium configurations. These models were subjected to additional mode I deformation on the $xy = (001)$ plane, where plane-strain conditions are considered in the $z = [001]$ direction (Appendix A). As a result, the atomic coordinates of the additionally deformed crack systems are given by:

$$x_D = x_E\left(1 + \varepsilon^A_{xx(\infty)}\right) \qquad (V.17a)$$

$$y_D = y_E\left(1 + \varepsilon^A_{yy(\infty)}\right) \qquad (V.17b)$$

$$z_D = z_E \qquad (V.17c)$$

where $\varepsilon^A_{ii(\infty)}$ are the strain components of the additional deformation and x_E, y_E, z_E the initial atomic coordinates of every reference equilibrium state. The total applied deformation of the additionally deformed system at the thermodynamic limit is given by:

$$\varepsilon^T_{xx(\infty)} = \varepsilon^I_{xx(\infty)} + \varepsilon^A_{xx(\infty)} + \varepsilon^I_{xx(\infty)} \cdot \varepsilon^A_{xx(\infty)} \approx \varepsilon^A_{xx(\infty)} + \varepsilon^I_{xx(\infty)} \qquad (V.18a)$$

$$\varepsilon^T_{yy(\infty)} = \varepsilon^I_{yy(\infty)} + \varepsilon^A_{yy(\infty)} + \varepsilon^I_{yy(\infty)} \cdot \varepsilon^A_{yy(\infty)} \approx \varepsilon^A_{yy(\infty)} + \varepsilon^I_{yy(\infty)} \qquad (V.18b)$$

where $\varepsilon^I_{ii(\infty)}$ are the strain components of each reference, initial, state. Under this framework, the dynamic response of equilibrium $(010)[001]$ cracks under additional mode I deformation is investigated in both fcc aluminium and bcc iron at $T = 0K$. In this examination we focused on the models with the largest crack dimensions since they are more relevant to the experimental sized cracks, in terms of the loading level.

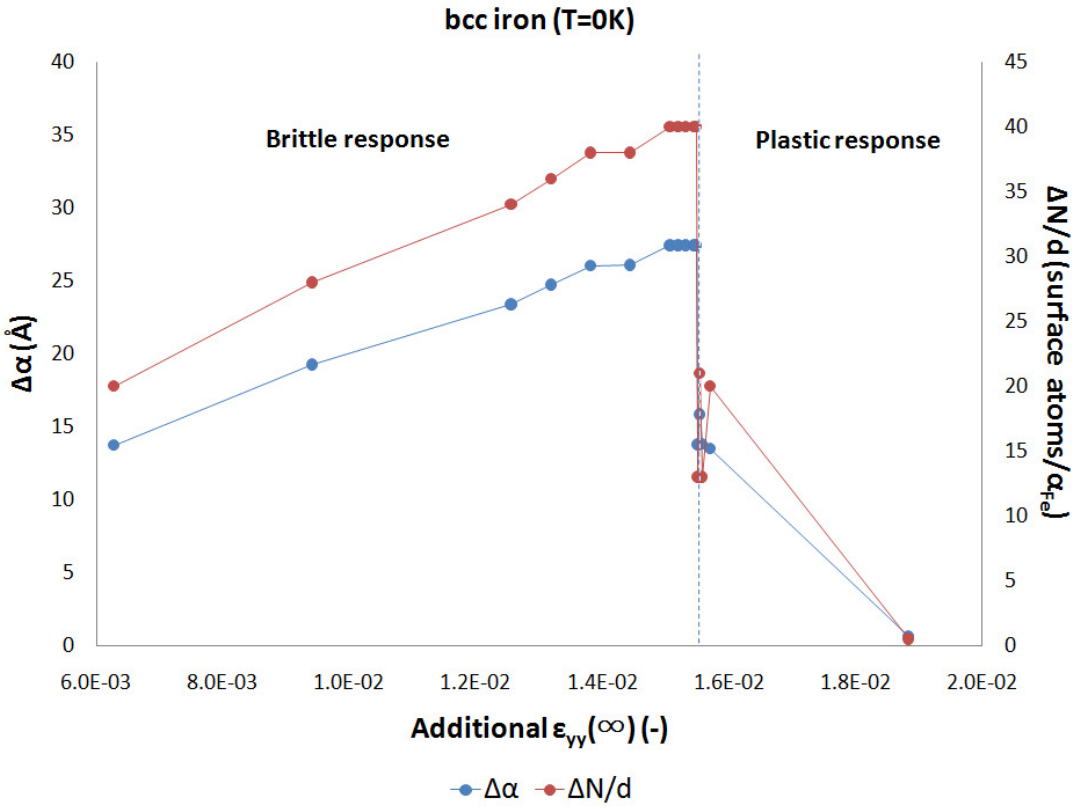

Figure V.50: Evolution of the crack half-length and the surface atoms number of initial equilibrium $(010)[001]$ crack models of α-iron upon additional applied deformation. Every atomic configuration was relaxed for 4×10^4 time steps at $T = 0K$.

Atomistic results reveal that the equilibrium $(010)[001]$ cracks in iron present similar behaviour upon additional deformation, with a characteristic example given in figure V.50. According to figure V.50, the dynamic response of the crack models can be either brittle or/and plastic depending on the $\varepsilon_{ii(\infty)}^{A}$ magnitude. At low values of additional deformation, the crack length increases though maintaining its atomically sharp shape at the crack-tip (figure V.51). In the crack-tip region a significant concentration of stress is seen that leads to the formation of two fcc stripes within the bcc crystal structure (figure V.51). During the crack extension, U_{nc} increases gradually (figure V.52), due to the step-by-step increase of both $\Delta\alpha$ and $\Delta N/d$ (figure V.53). From this behaviour stems a linear relation between $\Delta\alpha$ and $\Delta N/d$ (figure V.54), which is characteristic of the dynamic response of cleavage mechanism. We therefore conclude that the crack propagates through brittle cleavage on the crack plane (010).

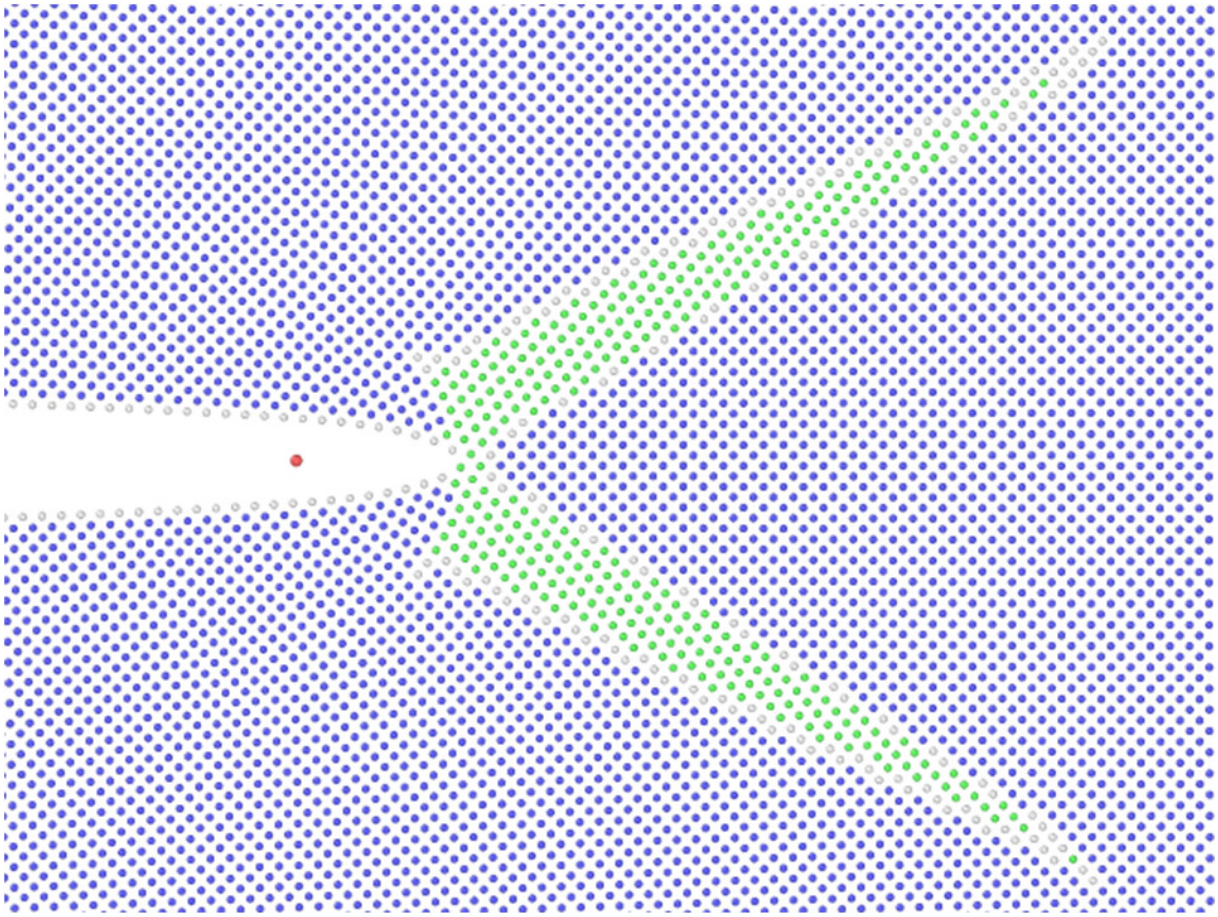

Figure V.51: The structural evolution of an initially equilibrium $(010)[001]$ crack in bcc iron under additional deformation equal to $+0.33\varepsilon_{yy(\infty)}^{Upper}$, and after relaxation of 4×10^4 time steps. The initial half-length of the crack was equal to 50 lattice parameters and the initial position of the crack-tip is denoted by a red circle. The crack propagates via brittle cleavage on the (010) crack plane and along the $[100]$ direction. The blue and green colour atoms represent the bcc and fcc crystal structure, respectively.

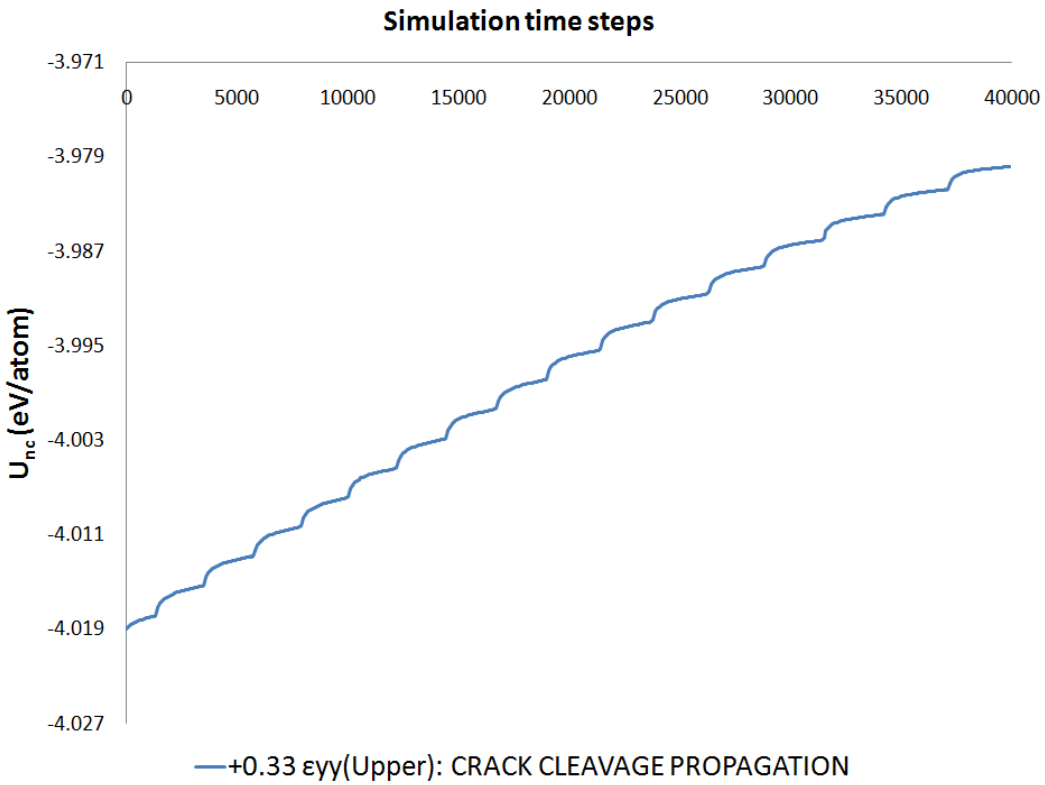

Figure V.52: The change in the potential energy of the near-crack region during the brittle cleavage propagation process. The potential energy increases gradually due to the generation of new surfaces.

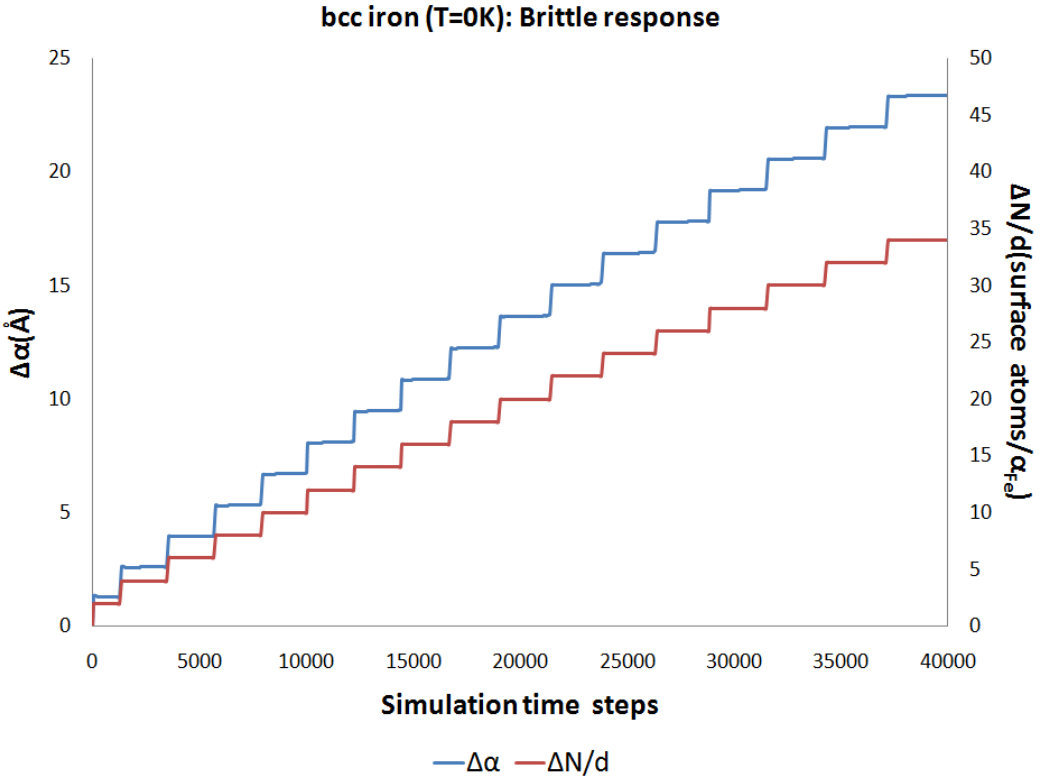

Figure V.53: Evolution of the crack half-length and the surface atoms of an initially equilibrium $(010)[001]$ crack in iron under additional deformation equal to $+0.33\varepsilon_{yy(\infty)}^{Upper}$ in respect to the minimization steps. The crack configuration is extended via brittle cleavage propagation on the (010) crack plane and along the $[100]$ and $[\bar{1}00]$ direction for the right and the left crack-tip, respectively.

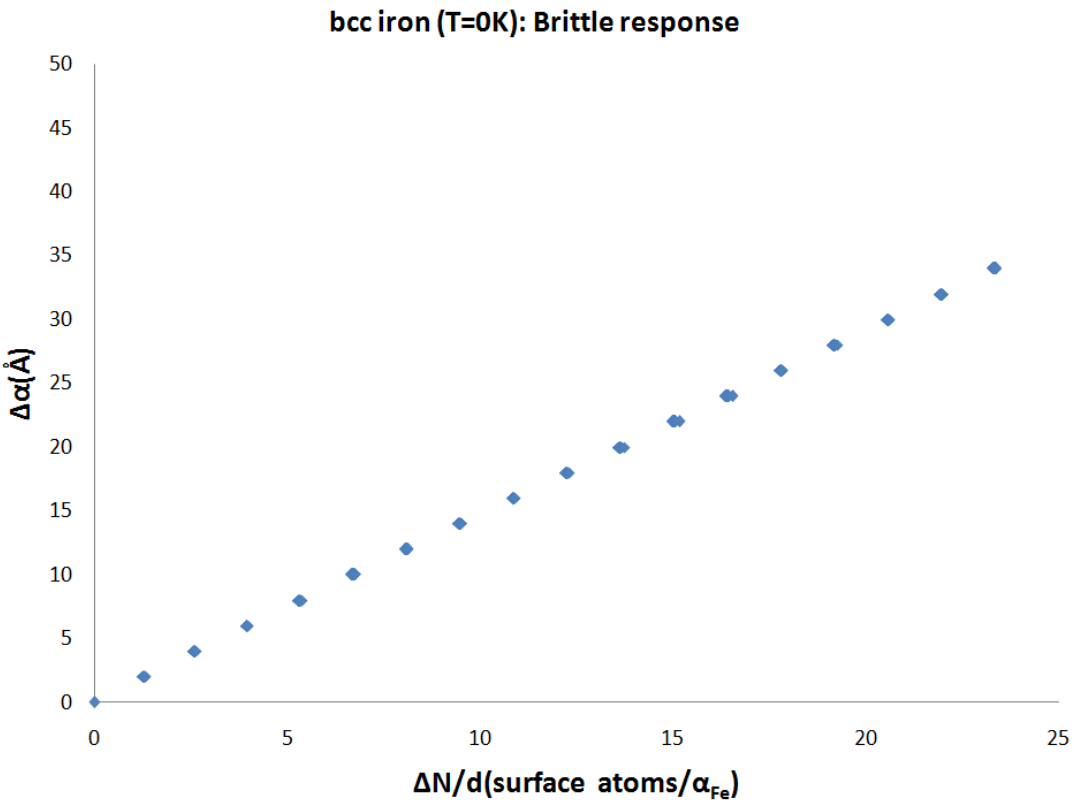

Figure V.54: The extended linear relation between the change in crack length and the surface atoms of the crack faces verify that the crack extension is performed by brittle cleavage propagation.

At high values of additional applied deformation, the stress within the system is sufficient to activate atomistic mechanisms of plasticity. Specifically, the stress concentration ahead of the crack-tip generates dislocations inside the fcc strips (figures V.55), which have been formed during the stabilization process. These dislocations are mainly Shockley partials. Furthermore, their motion under the applied strain-stress conditions leads to the formation of stacking faults, which appear as layers of hcp structure inside the fcc strips (figures V.55). These atomic mechanisms of plasticity absorb significant amount of elastic energy and hence are capable to prevent the crack extension within the model (figures V.56). The plastic response of the models can be also detected from the scheme III.19.

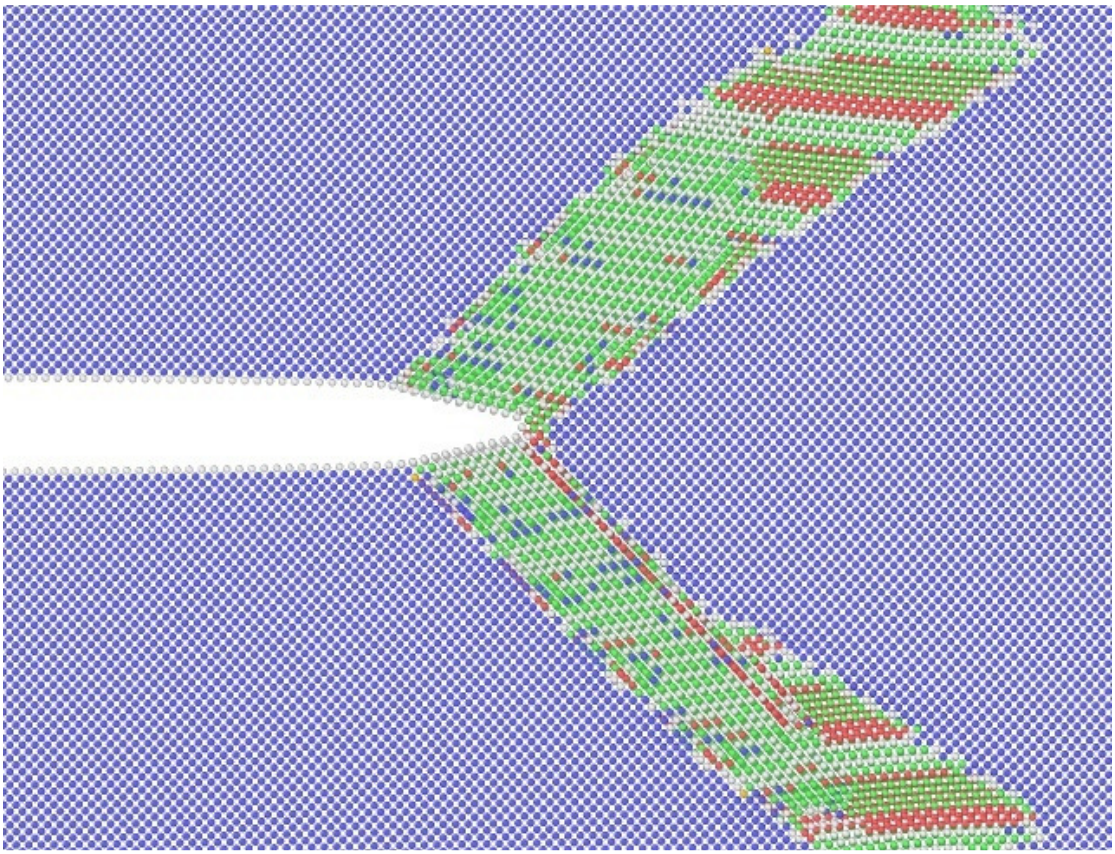

Figure V.55a: The structural evolution of an initially equilibrium $(010)[001]$ crack in bcc iron under additional deformation equal to $+0.50\varepsilon_{yy(\infty)}^{Upper}$, and after relaxation of 4×10^4 time steps. The initial half-length of the crack was equal to 50 lattice parameters. The blue, green and red atoms correspond to the bcc, fcc and hcp crystal structure respectively.

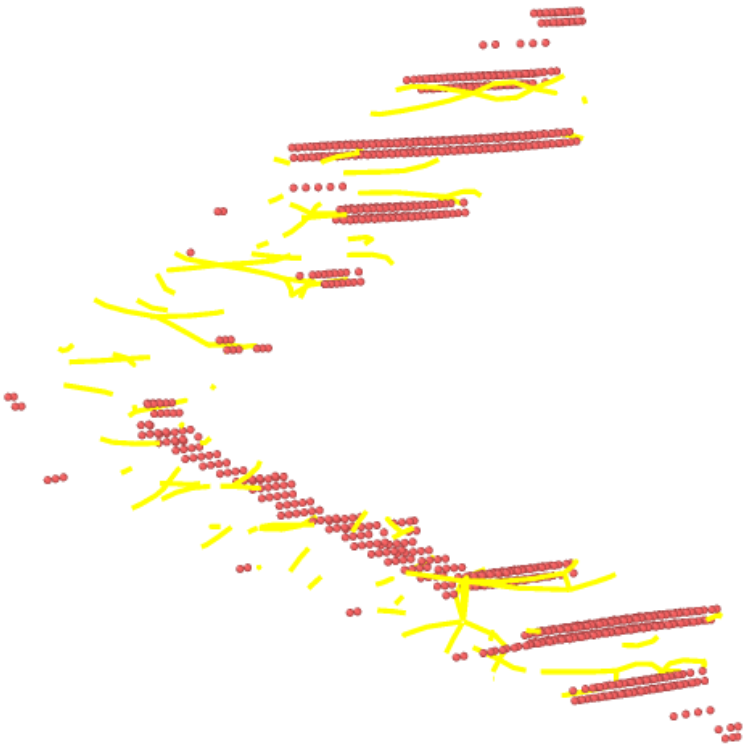

Figure V.55b: Shockley partial dislocations, with Burgers vector equal to $1/6\langle 112\rangle$, have been formed inside the fcc structure regions to accommodate the applied strain.

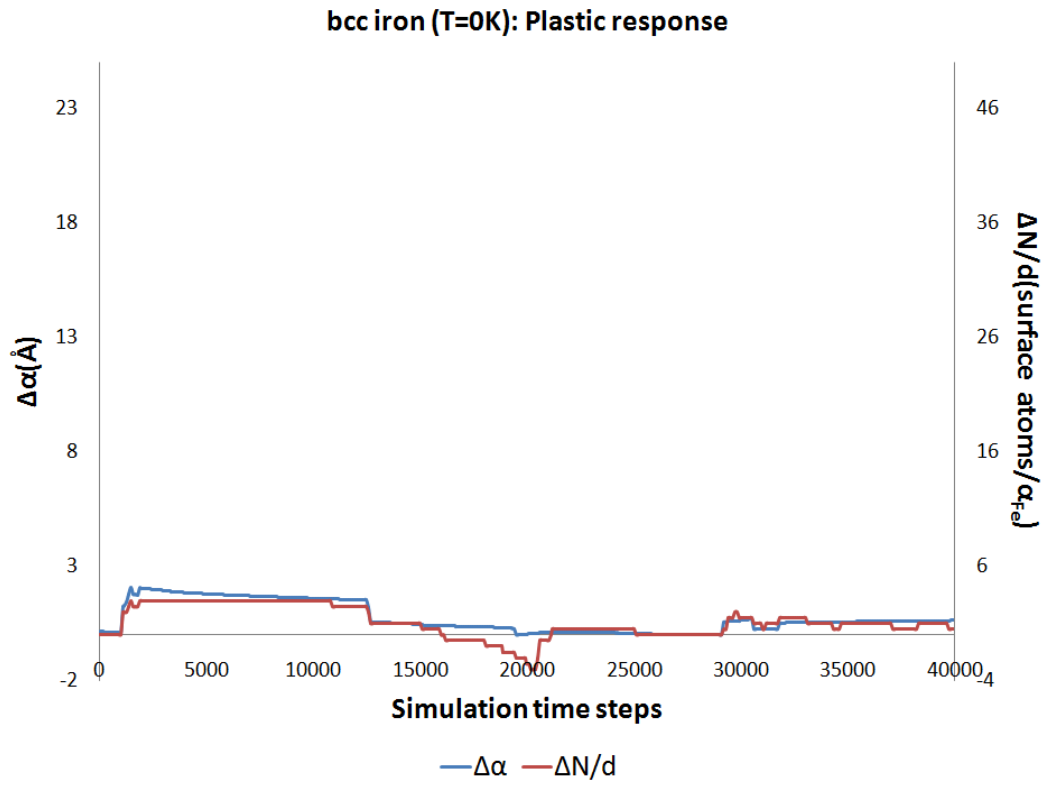

Figure V.56: Evolution of the crack half-length and the surface atoms of an initially equilibrium $(010)[001]$ crack in α-iron under additional deformation equal to $+0.50\varepsilon_{yy(\infty)}^{Upper}$ in respect to the minimization steps. The plasticity mechanisms of the dislocation and stacking fault formation in the vicinity of the crack-tip prevent the crack extension.

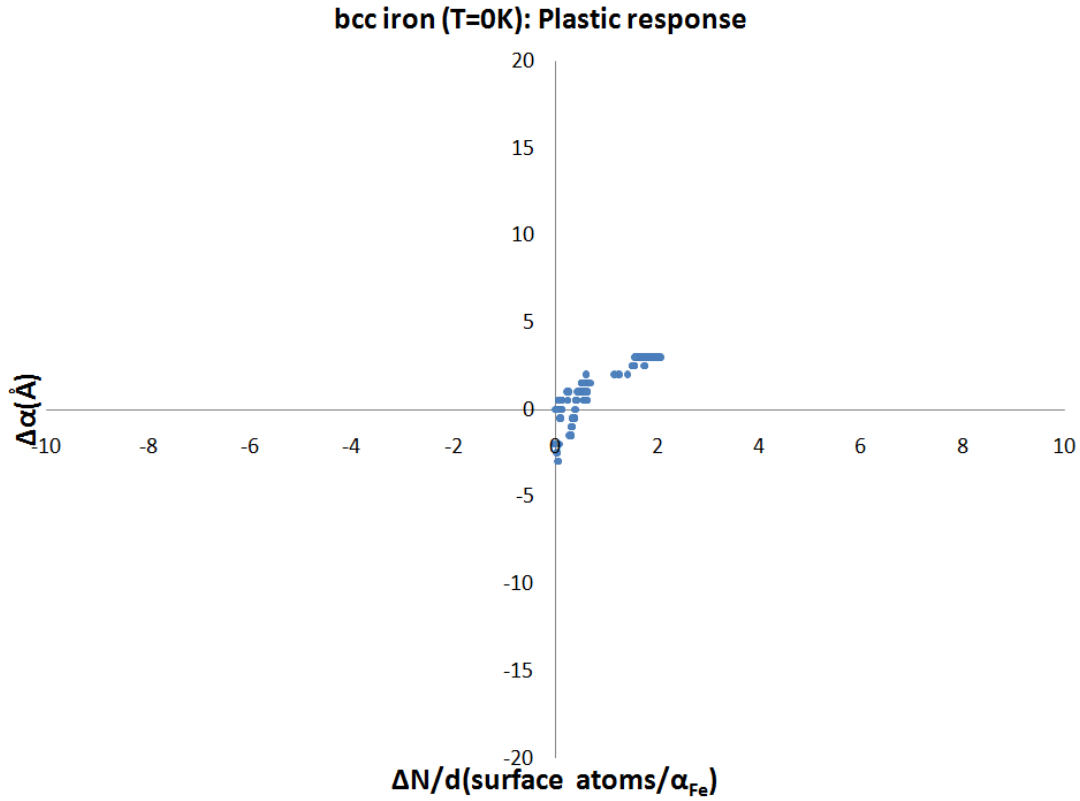

Figure V.57: The narrow-range interrelation between the change in crack length and the surface atoms of the crack faces.

Figure V.57 confirms the existence of a narrow-range mathematical relation between the quantities $\Delta\alpha$ and $\Delta N/d$, which is characteristic of the dislocation processes (§5.7.1). By comparing the dynamic response of cracks with different sizes under additional applied deformation it can be shown that the size of brittle zone increases in respect to the crack half-length, a (figure V.58).

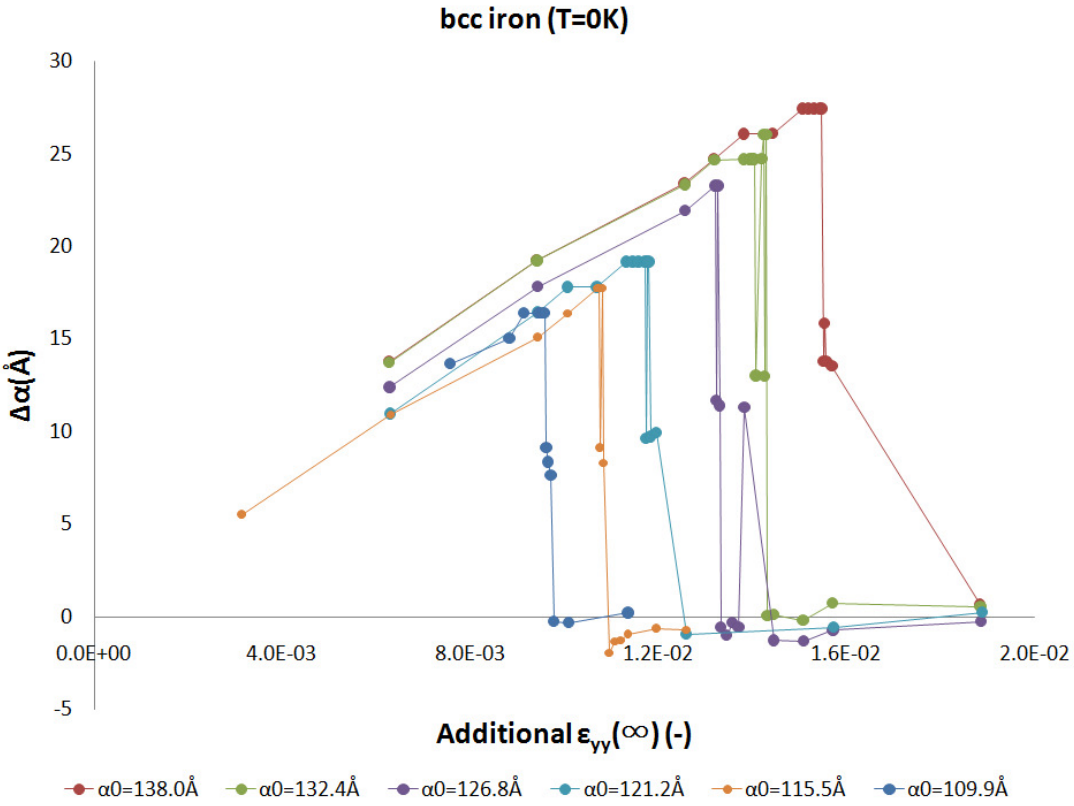

Figure V.58: The evolution of the crack half-length of initial equilibrium $(010)[001]$ crack models in bcc iron in respect to additional applied deformation. Every atomic configuration was relaxed for 4×10^4 time steps at $T = 0K$. The size of the brittle zone increases in relation to the crack length.

This behaviour is due to the fact that the larger the a, the lower the applied deformation of the reference configuration. Consequently, a more accurate description of the dynamic response of the crack in relation to the crack size, requires the expression of the Δa (or $\Delta N/d$) in respect to the total applied deformation on the system, $\varepsilon^T_{ii(\infty)}$. Such a representation (figure V.59) shows the existence of an almost constant threshold of $\varepsilon^T_{ii(\infty)}$, for which a crack configuration behaves plastically independently from its size. More importantly, it is proven for a second time that the mechanical response of crack models can be transform from brittle to ductile under different loading conditions at $T = 0K$. However, the loading conditions required for such a transformation are far away from the reachable experimental conditions. Therefore, a crack configuration of experimental dimensions in bcc

iron is assessed to have a significantly extended brittle zone, in terms of additional applied deformation.

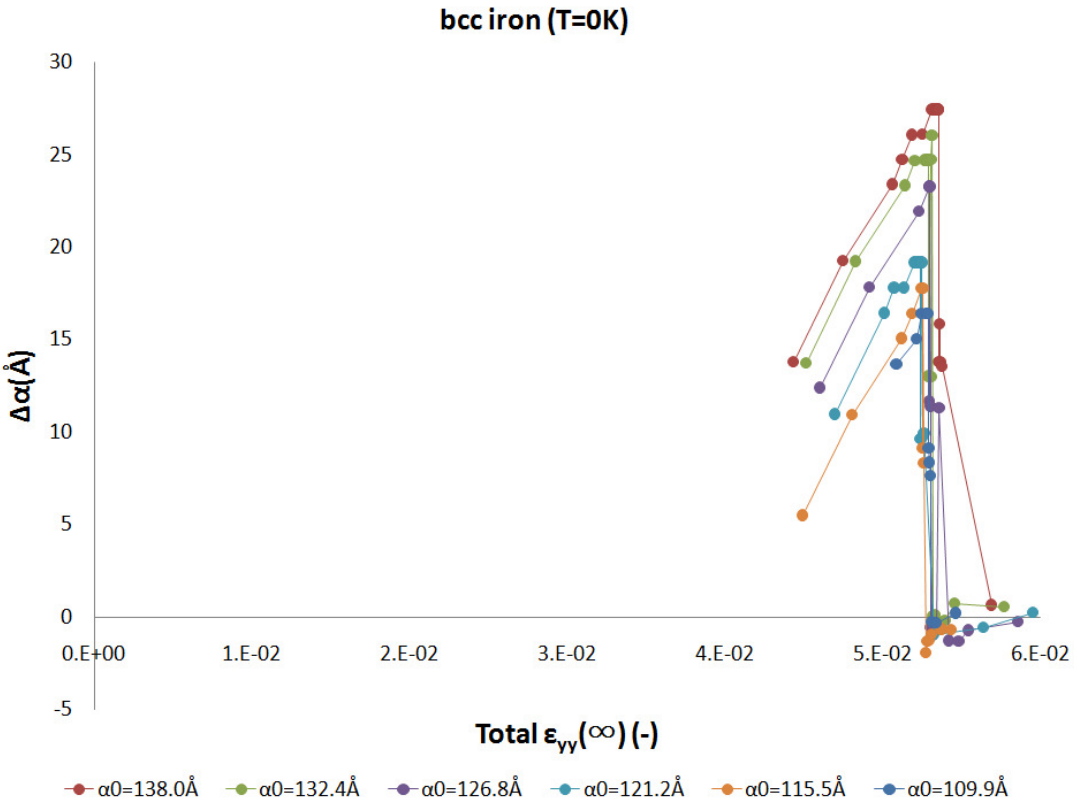

Figure V.59: The evolution of the crack half-length of initial equilibrium $(010)[001]$ crack models in bcc iron in respect to total applied deformation. Every atomic configuration was relaxed for 4×10^4 time steps at $T = 0K$. The size of the brittle zone is almost independent from the crack length.

For the examination of the dynamic response of $(010)[001]$ cracks in fcc aluminium, the same analysis has been followed. Simulation results show that crack configurations of different crack length present similar dynamic behaviour upon additional deformation. A representative example is given in figure V.60. As it can be observed, the crack configuration increases in length through a dynamic propagation process, which is enhanced by the increase of additional deformation. Structural analysis (figure V.61) reveals that the right crack-tip propagates on the crack plane (010) and along the $[100]$ crystallographic direction, maintaining its initial sharp atomic shape. Crack extension is characterized by the quasi-gradual increase of U_{nc} due to the formation of new crack surfaces (figure V.62). The crack extension can be also quantitatively described by monitoring of the physical quantities $\Delta\alpha$ and $\Delta N/d$ (figure V.63). The interrelation of these quantities demonstrates that the dynamic response of the $(010)[001]$ cracks in aluminium is the brittle cleavage mechanism (figure V.64).

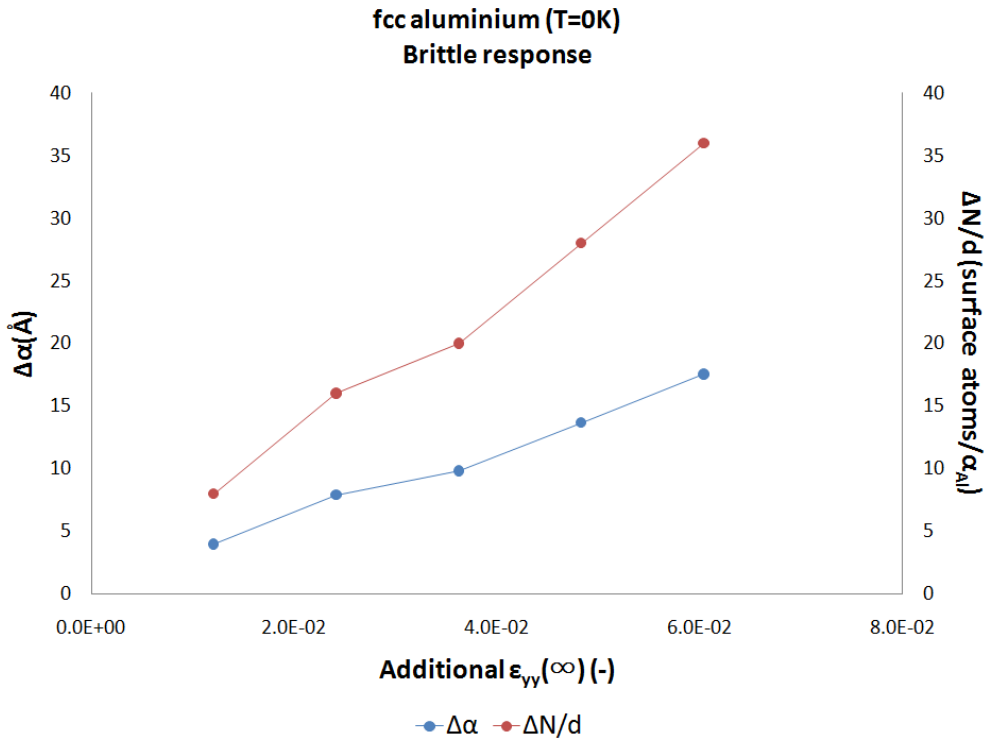

Figure V.60: Evolution of the crack half-length and the surface atoms number of initial equilibrium $(010)[001]$ crack models of fcc aluminium upon additional applied deformation. Every atomic configuration was relaxed for 500 time steps at $T = 0K$.

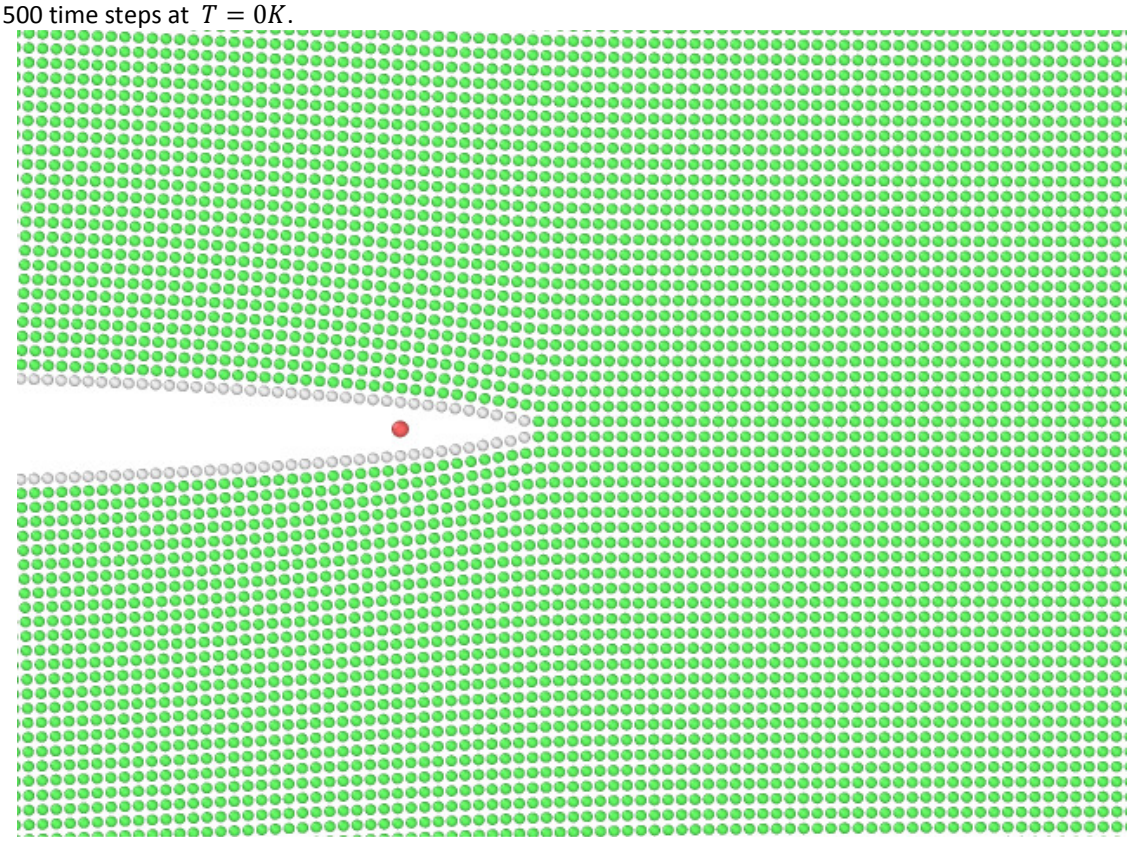

Figure V.61: The structural evolution of an initially equilibrium $(010)[001]$ crack in fcc aluminium under additional deformation equal to $+2.63\varepsilon_{yy(\infty)}^{Upper}$, and after relaxation of 500 picoseconds time steps. The initial half-length of the crack was equal to 32 lattice parameters and the initial position of the crack-tip is denoted by a red circle. The crack propagates via brittle cleavage on the (010) crack plane and along the $[100]$ direction. The green colour atoms represent the fcc crystal structure.

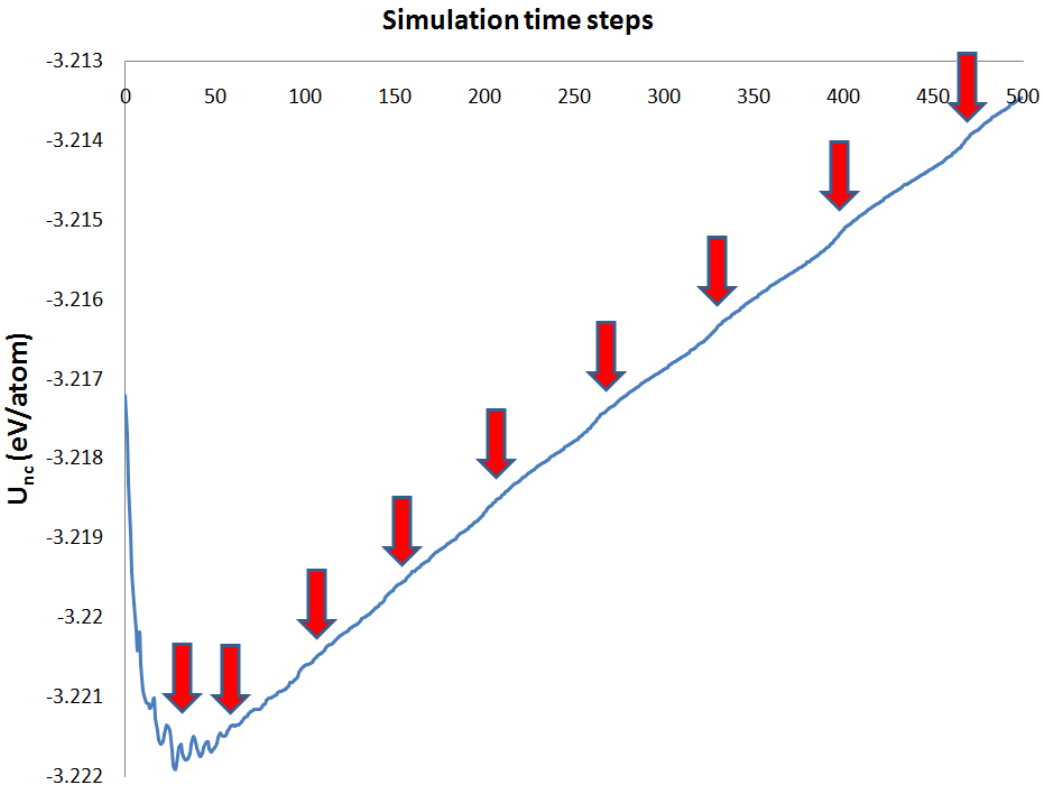

Figure V.62: The change in the potential energy of the near-crack region during the brittle propagation process. The potential energy increases due to the generation of new surfaces. The atomic bonds breaking, which denoted by red arrows, causes a smooth change in slope of the potential energy curve.

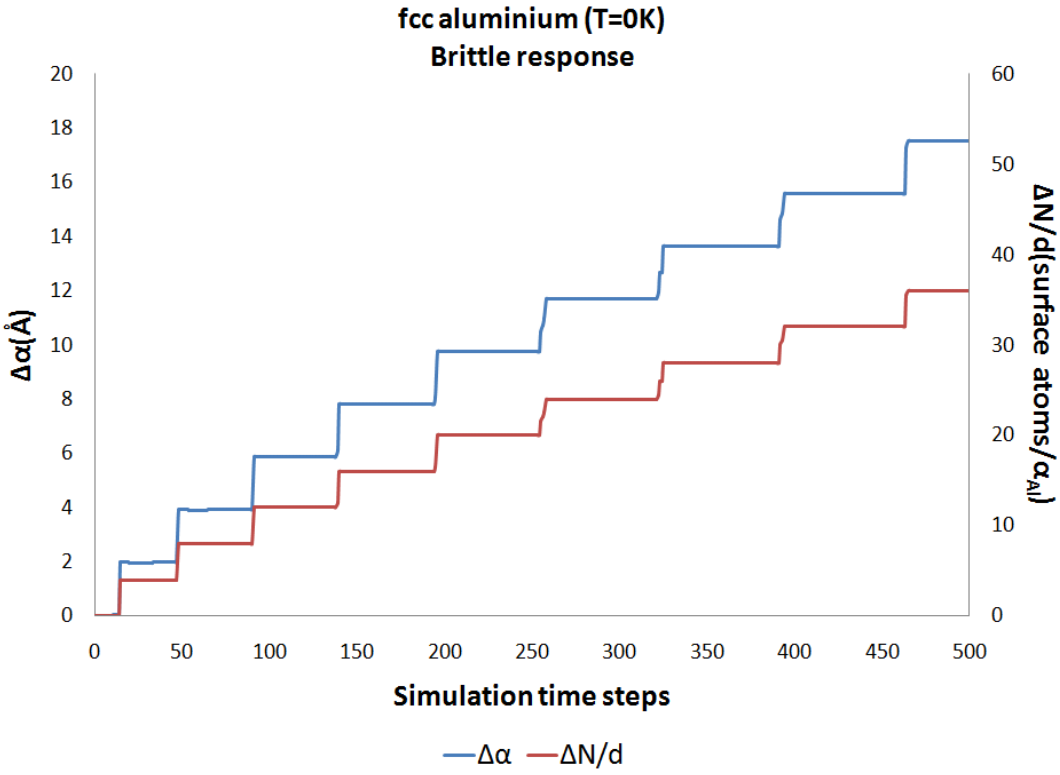

Figure V.63: Evolution of the crack half-length and the surface atoms of an initially equilibrium $(010)[001]$ crack in fcc aluminium under additional deformation equal to $+2.63\varepsilon_{yy(\infty)}^{Upper}$ in respect to the minimization steps. The crack configuration is extended via brittle cleavage propagation on the (010) crack plane and along the $[100]$ and $[\bar{1}00]$ direction for the right and the left crack-tip, respectively.

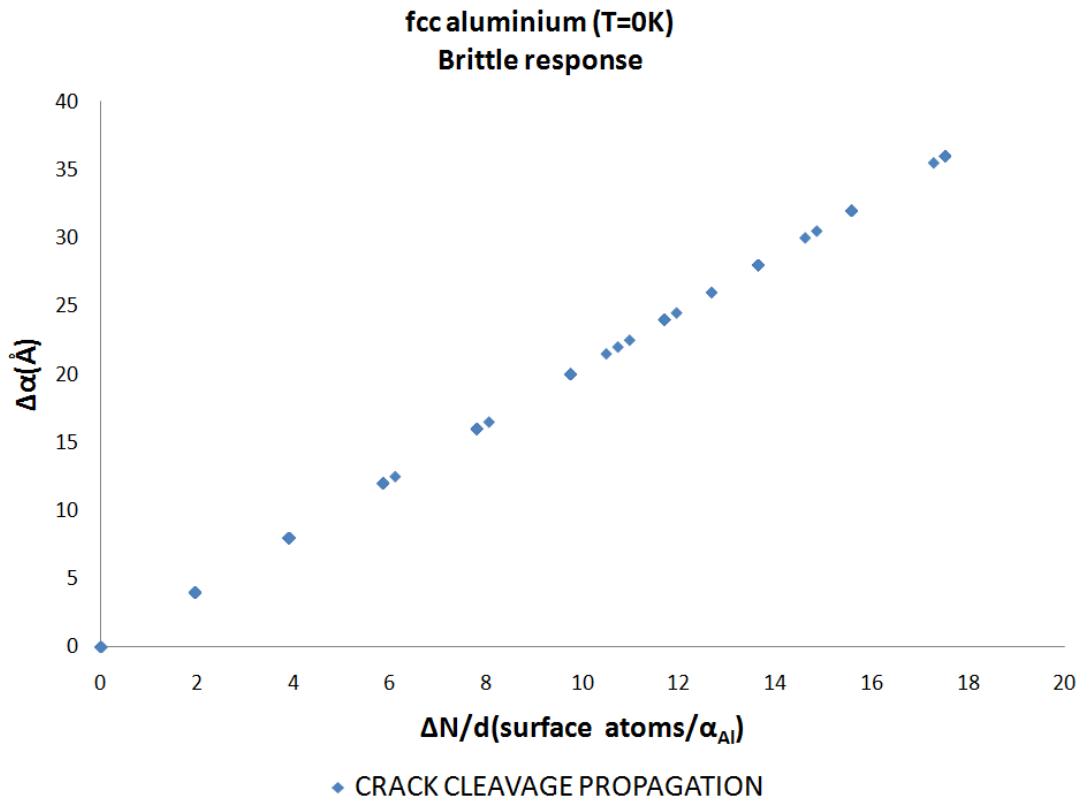

Figure V.64: The extended linear relation between the change in crack length and the surface atoms of the crack faces verify that the crack extension is performed by brittle cleavage propagation.

Considering that:

(i) the cracks of experimental sizes need significantly lower loads to become stable in comparison to cracks at the atomistic scale, tested for the two metals, and

(ii) the achievable experimental loading conditions cannot exceed the range of applied loading used in this study,

it can concluded that the dynamic response of real sized $(010)[001]$ cracks at $T = 0K$, in both metals, and in the absence of pre-existing dislocations is the brittle cleavage propagation (§3.5.3). However, it is well known that aluminium is a ductile material at any temperature [INT3, TAM2002]. Consequently, we conclude that the dynamic response of cracks inside a material cannot constitute the only criterion to interpret its intrinsic mechanical behaviour under specific loading and temperature conditions. In contrast, a more comprehensive interpretation should include both the effects of pre-existing cracks and pre-existing dislocations in the system, something that applies in our approach (§5.5).

Chapter VI: Summary and perspectives

6.1. Results and conclusions

The present thesis is focused on the investigation of the mechanical response, under loading, of mode I $(010)[001]$ cracks in fcc aluminium and bcc iron at the atomic scale. The main objectives of our work are the understanding and interpretation of the ductile behaviour of aluminium and the brittle/ductile behaviour of alpha iron. This section summarizes our results, remarks and conclusions of the present work:

1. **Inter-atomic potential of fcc aluminium (Chapter III)**: As a first result, a phenomenological N-body inter-atomic potential for face-centered cubic aluminium has been optimized [ZAC2017]. This analytic model yields results in excellent agreement with experiments for the lattice parameter a_0, the elastic constants (C', C_{44} and B), the cohesive energy E_c, the vacancy formation energy E_v^f, the intrinsic stacking-fault energy γ_I and the surface excess energies $\gamma_{(hkl)}$. By correctly reproducing C_{ij} and $\gamma_{(hkl)}$, it is suitable for simulating the elastic energy of the crystal under applied load as well as for the effects of free internal or external surfaces. Therefore, it can be considered appropriate for studying the atomistic crack configurations in aluminium.

2. **Validity of linear elasticity at large strains (Chapter IV):** The present study raised up, for the first time, an important issue concerning the modelling of nano-sized cracks. According to Griffith's equilibrium condition [GRI1920], the applied stress that stabilizes a nano-sized crack amounts few giga-Pascals, a value much larger than the experimental elastic limit of the studied metals. Under such loading conditions, the validity of the linear elasticity theory is questionable. To deal with this problem, we proceed to the analytic and/or numeric calculation of the second order elastic constants as function of the applied deformation, $C_{ij} = f(\varepsilon)$. Presented in Chapter IV, the results reveal that the $C_{ij}(\varepsilon)$ deviate progressively from $C_{ij}(0)$ on increasing deformation. Moreover a linear approximation in the neighbourhood of any $\varepsilon \neq 0$ state is possible provided that $C_{ij}(0)$ are replaced by $C_{ij}(\varepsilon)$. This result is

crucial for determining the mechanical properties of a loaded crystal that contains an equilibrium nano-sized crack.

3. **Lattice trapping effect at $T = 0K$ (Chapter V):** The investigation of the mechanical response to mode I loading of $(010)[001]$ nano-sized cracks at $T = 0K$, revealed the existence of the lattice trapping effect in both the studied metals. This phenomenon expresses the resistance of the crystalline lattice for an equilibrium crack to propagate, which is characterized by a stress-strain barrier, in agreement with the literature [THO1971, SIN1972, SIN1975, CUR1990]. The lattice trapping strain barrier, $\Delta\varepsilon_{ii}(i = x, y)$, is independent from the crack length and intrinsically related to the considered material. Finally, the lattice trapping stress barrier in iron ($\Delta\sigma_{yy}/G_{\langle 010\rangle} \sim 10^{-3}$) is found to be significantly larger than in aluminium ($\Delta\sigma_{yy}/G_{\langle 010\rangle} \sim 10^{-4}$), indicating that a pre-existing $(010)[001]$ crack inside iron is mechanically much more ''stable'' upon change in loading compare to the same configuration in aluminium.

4. **Empirical evaluation of cracks mechanical stability at $T = 0K$ (Chapter V)**: Static equilibrium nano-sized cracks have been used to examine if the lattice trapping limits can be described by a linear relationship between the quantities a and $1/C\sigma_{yy}^2$ (where the elastic coefficient $C = f(\varepsilon)$), in analogy to Griffith's condition [GRI1920]. We have shown that these quantities are linearly interrelated for both the studied metals at a very satisfactory level ($R^2 > 0.9999$ for aluminium and $R^2 > 0.99$ for iron). Based on this, an effective surface energy (γ) for both the upper and lower trapping limit configurations has been determined. The values of the lower strain limits correspond to a γ_{Lower} value very close to the energy of the $\{100\}$ terminations (+0.5% for aluminium [ZAC2017] and -10.5% for iron [PON2007]). On the other hand, the upper trapping limit strain values correspond to a $\gamma_{Upper} > \gamma_{Lower}$ in both the studied systems. The difference in γ, $\Delta\gamma = \gamma_{Upper} - \gamma_{Lower}$, can be attributed to surface tension terms [MUR1975] due to the difference in applied loading between the two lattice trapping limits. This statement is strengthen from the fact that the ratios $\Delta\gamma^{(Fe)}/\Delta\gamma^{(Al)}$ and $\Delta\varepsilon_{yy}^{(Fe)}/\Delta\varepsilon_{yy}^{(Al)}$ are of the same order of magnitude. Therefore, we can conclude that

the lattice trapping barrier causes an increase for the critical value of γ (i.e. the γ_{Upper}) corresponding to the initiation of the crack propagation. Additionally, by empirically approximating Griffith's equilibrium condition for the lower trapping limit configurations enables us establishing an ''elastic mechanical homology'' with macroscopic-size cracks, and thus achieving a scale coupling in space (Chapter II). This result allows us to expand the validity of the simulation findings from the atomic scale to the macro-scale.

5. **New criterion of brittleness (Chapter V):** An original approach is adopted in our work to describe the mechanical conditions required for the crack propagation, in respect to the crack size. As explained in Chapters II and V, the traditional Griffith's criterion [GRI1920] describes only the mechanical conditions ($\sigma_{Gr}(a)$ or $\varepsilon_{Gr}(a)$) required for the ''stabilization'' of a crack of a given length, a. According to simulation results, a pre-existing equilibrium crack requires an additional stress-strain increment in order to overcome the resistance of the crystalline lattice for the crack propagation, the lattice trapping barrier ($\Delta\sigma_{LT}$ or $\Delta\varepsilon_{LT}$). Since we have shown that the lower trapping limit approximates the Griffith's condition, the critical mechanical conditions for the crack propagation onset are given by:

$$\sigma_{cr}(a) = \sigma_{Gr}(a) + \Delta\sigma_{LT} \text{ or } \varepsilon_{ii,c}(a) = \varepsilon_{Gr}(a) + \Delta\varepsilon_{LT}$$

Focusing on the first term, the Griffith's stress decreases by increasing the length of the stabilized crack, with the marginal case:

$$If\ a \longrightarrow \infty \Rightarrow \sigma_{Gr}(\infty) \longrightarrow 0$$

This limit constitutes a good approximation for crack configurations with macroscopic dimensions, including those of mechanical test notched samples. Hence, for these configurations, the stress-strain mechanical condition for crack propagation onset becomes equal to the lattice trapping barrier:

$$If\ a \longrightarrow \infty \Rightarrow \sigma_{cr}(\infty) = \Delta\sigma_{LT} \text{ or } \varepsilon_{cr}(\infty) = \Delta\varepsilon_{LT}$$

For this reason, in the present study, the lattice trapping barrier substitutes the Griffith's criterion, as the mechanical condition required for triggering crack

propagation of macroscopic-sized cracks. The main advantage of this approach is that the $\Delta\sigma_{LT}$ amounts Mega-Pascals; hence, the new criterion renders the determination of the mechanical behaviour of the systems under study independent from the extreme loading conditions required to stabilize the nano-sized cracks! Simulation results demonstrate that $\Delta\varepsilon_{LT}$ is constant and independent from a, for the studied nano-sized cracks in both metals. However, computational power limitations do not allow us to verify this result for cracks of macroscopic dimensions. For this reason, we made the working hypothesis that the $\Delta\varepsilon_{LT}$ constitutes an intrinsic constant property of a crystalline system. Despite that this hypothesis is rational more research is required in this direction.

6. **Validity of the crack displacement field at the atomic scale (Chapter V)**: One of the main challenges concerning the simulation of cracks at the atomic scale is the proper implementation of the macroscopically applied loading conditions. This role is undertaken by the boundary conditions of the model, whose appropriate selection and implementation has a significant effect on the obtaining results. The vast majority of the atomistic studies in literature focus only on the crack-tip region, an approach leading to models containing a part of the crack configuration. However, these models employ boundary conditions that do not allow the physical motion of the crack surfaces, keeping them fixed, thus generating in turn non-physical constraints on the crack field. To avoid this problem in our work, atomic models contain the entire crack (Chapter III). In addition, the crack faces are not located within the boundary conditions region and hence are capable to move during the simulation (Chapter III). Despite this improvement, structural relaxation of the atomic crack configuration via energy minimization can potentially cause a mismatch of the crack displacement field at the limit of the boundary conditions (Chapter V). This is another way in which the boundary conditions can affect the applied stress field. Hence, in order to ensure the proper implementation of the macro-scopic loading on the atomic system it is necessary to check for compatibility between the dynamic region of the model and the boundary conditions. The investigation contacted at the boundary limits upon energy minimization shows that compatibility is nearly reached in terms of the displacement field and the potential energy map. This result suggests

that the crack displacement field provided by continuum mechanics [SAV1961, LIM2001] is valid for the two studied crystalline systems at the atomic scale. It is worth noting that most studies in literature do not perform the control of the boundary conditions, even though this is crucial for the validity of the numerical models and the reliability of the simulation results.

7. **Model of interpreting the mechanical behaviour of metals (Chapter V):** The current work has proposed a novel model for interpreting the intrinsic mechanical behaviour of crystalline materials. This model is about the competition between the propagation of an equilibrium crack and the glide motion of dislocations. Both mechanisms are characterized by a stress-strain activation obstacle, with the former being the lattice trapping barrier (''criterion of brittleness'') and the latter being the Peierls stress (''ductility criterion''). According to this model, the comparison of these mechanisms determines the brittle or ductile intrinsic mechanical response of the system upon applied loading. Based on simulation results regarding the lattice trapping barrier and experimental data regarding the Peierls stress, our model is able to predict the ductile behaviour of aluminium and the brittle behaviour of iron at $T = 0K$. This result suggests that the competition of the two mechanisms as function with the temperature can potentially predict the intrinsic mechanical response of a system under loading for every T.

8. **Temperature dependence of the lattice trapping barrier (Chapter V):** The validity of our approach at finite temperature was examined based on the determination of the temperature effect on the lattice trapping barrier. To this end, the mechanical response of nano-sized cracks was investigated for both metals at different temperature via molecular dynamics simulation. Simulation results in aluminium crack models revealed the existence of the lattice trapping effect in every temperature studied ($T = 0,\ 25,\ 50,\ 75,\ 100,\ 125K$). More importantly, the lattice trapping barrier is not significantly affected by the temperature rise, suggesting that it is probably an athermal property of the crystalline aluminium. Based on simulation findings, our model was able to demonstrate that aluminium is ductile for every temperature studied, in consistency with experimental reality [TAM2002]. Unfortunately, simulation results did not allow us to perform the

same analysis for iron. In particular, the investigation of the mechanical response of crack models at $T > 0K$ reveals the elimination of the lattice trapping stability region and thus the non-existence of equilibrium crack configurations. This behaviour may be due to several factors which cannot be excluded, including the inter-atomic potential [PON2007], the simulation parameters, level of applied loading etc. A detailed structural analysis has revealed that the destabilization of the initial crack configurations is due to generation of dislocations at the vicinity of the crack-tip. This plastic mechanism absorbs elastic energy from the atomistic models and thus reducing the applied stress on the crack configurations, which eventually healed. In the event where the elimination of the crack's mechanical stability, observed in our models, is due to the high level of applied loading, the study of equilibrium cracks at finite temperature can be achieved by simulation of significantly larger configurations. However, the particularly demanding computational cost has not allowed us to proceed to the above control.

9. **Dynamic response of cracks (Chapter V):** In the final part of this work the question that has been investigated was whether the dynamic response of the nano-sized cracks, in the absence of pre-existing dislocations, qualitatively determines the mechanical behaviour of aluminium and iron at $T = 0K$. Atomistic results demonstrate that the mechanical response of the crack models in both metals can be changed from brittle to ductile by increasing the load; hence, the type of the dynamic response of a crack under load depends on the applied stress/strain values. This result suggests that the dynamic response of a crack configuration inside a dislocation-free crystal is not directly correlated with the crystal's intrinsic mechanical behaviour. To gain a better view, we further studied the mechanical response of equilibrium cracks under additional applied deformation. Simulation data in both metals demonstrate that the strain-stress range of the brittle dynamic response of a crack increases by increasing the crack length. This result suggests that the dynamic response of macroscopic cracks in both metals under experimental loading at $T = 0K$, and in the absence of pre-existing dislocations is the brittle cleavage propagation. Despite the fact that iron is brittle at low temperatures [TAM2002], it is well known that aluminium is a ductile material at any

temperature [TAM2002]. Consequently, we conclude that the dynamic response of a crack inside a dislocation-free crystalline material cannot constitute the only criterion for interpreting the intrinsic mechanical behaviour of this material under specific loading and temperature conditions. This result suggests that the proper determination of the intrinsic mechanical behaviour of a crystal additionally requires taking into account other atomistic mechanism, including the effect of pre-existing dislocations.

10. **Stress-induced phase transformation in bcc iron (Chapter V):** Atomistic results revealed that the equilibrium nano-sized $(010)[001]$ cracks in α-iron at $T = 0K$ accommodate the applied loading through the formation of two fcc strips in the vicinity of the crack-tip. This local stress-induced bcc→fcc phase transformation is spatially more extensive for the upper trapping limit compared to the lower trapping limit. This result signifies that the mechanical stability of nano-sized $(010)[001]$ cracks in crystalline iron, which is described by the lattice trapping strain barrier, is related to the work required for the extension of the fcc regions within the bcc matrix and thus, to the energy difference between the bcc and fcc crystal structure of the system. Stress-induced phase transformations also occurred during the dynamic crack extension. Atomistic results revealed that during crack cleavage propagation, the simultaneous manifestation of two bcc↔fcc phase transformations (bcc→fcc and fcc→bcc) at the vicinity ahead of the crack-tip cause the movement of the formed meta-stable fcc strips through the stable bcc matrix. This observation shows that the stress-induced bcc↔fcc transitions and the cleavage mechanism cooperate at $T = 0K$. In addition, this observation implies that the crystalline lattice resistance to the brittle cleavage propagation of $(010)[001]$ cracks is potentially associated with the energy difference between the stable bcc and the meta-stable fcc structures.

6.2. Perspectives

Based on the aforementioned, the proposed model is capable to predict that the fcc aluminium and bcc iron are respectively ductile and brittle at $T = 0K$. In addition, it demonstrates that aluminium is maintained plastic at finite temperature ($T > 0K$). These

results are solid evidences that the competition between the propagation of pre-existing equilibrium cracks and the glide of pre-existing static dislocations can indeed interpret the intrinsic mechanical behaviour of crystals. As a result, our work constitutes the starting point for the future improvement, development as well as implementation of this simple model. Proposed future work includes the conduction of:

(i) Search of possible ways for simulating equilibrium $(010)[001]$ cracks of macroscopic length, in both aluminium and α-iron, in order to verify the working hypothesis made in §5.2, stating that the lattice trapping strain barrier is independent from the crack length.

(ii) Search of possible ways for simulating equilibrium $(010)[001]$ cracks in α-iron at $T > 0K$, in order to determine the temperature effect on the lattice trapping barrier. This study will determine the intrinsic mechanical behaviour of iron at finite temperature with respect to the proposed approach (§5.5).

(iii) Study of various geometries of equilibrium cracks on the primary cleavage plane of the studied crystal, aiming to determine their lattice trapping barriers. This investigation will reveal the preferable cleavage direction on the primary cleavage plane under a given loading or deformation mode. In addition, this study can examine the effect of crack's orientation on the outcome of the competition between the propagation of pre-existing equilibrium cracks and the glide of pre-existing static dislocations.

(iv) The implementation of the proposed approach (§5.5) to other body-centered (or face-centered) cubic crystalline systems would extend applicability.

(v) Finally, it is important to examine the effect of presence of different structural defects (e.g. precipitates, impurities, boundaries etc.) at the crack-tip and/or its vicinity on the lattice trapping barrier, with the aim to predict possible alteration of the intrinsic mechanical response of a crystal due to the effect of the micro-structure.

Appendix A: Uni-axial mode I deformation

This appendix presents the linear elasticity formulation concerning the uni-axial mode I deformation in a cubic system. Under this mathematical framework, the mechanical state of the fcc aluminium and the bcc iron is investigated in respect to the strain magnitude and atomistic calculations being compared to the linear elasticity approximation predictions. For the purposes of this appendix, the elastic body is oriented along the cubic axes, i.e. x is the $[100]$, y is the $[010]$ and z is the $[001]$ crystallographic direction.

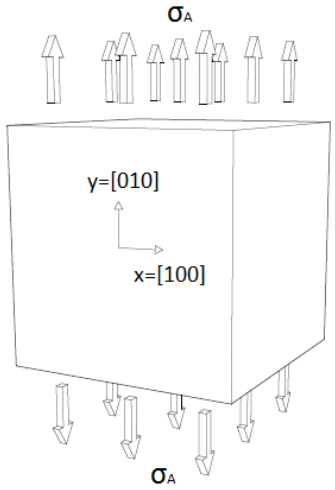

Figure A.1: System under uni-axial mode I loading.

Figure A.1 shows an initially perfect system under uni-axial loading on the xy-plane:

$$\sigma_{xx} = 0, \qquad \sigma_{yy} = \sigma_A \tag{A.1}$$

where σ_A is the magnitude of the uni-axial tension. By considering plane strain conditions along the z-direction, which can be expressed as:

$$\varepsilon_{zz} = \varepsilon_{yz} = \varepsilon_{zx} = 0 \tag{A.2}$$

Hooke's law thus gives the strain components:

$$\varepsilon_{xx} = S_{12}\sigma_A + S_{12}\sigma_{zz} \tag{A.3}$$

$$\varepsilon_{yy} = S_{11}\sigma_A + S_{12}\sigma_{zz} \tag{A.4}$$

$$\varepsilon_{zz} = S_{12}\sigma_A + S_{11}\sigma_{zz} = 0 \tag{A.5}$$

$$\gamma_{yz} = \gamma_{zx} = \gamma_{xy} = 0 \tag{A.6}$$

where S_{11} and S_{12} are the elastic compliances of the perfect cubic system. Using equation A.5 the out-of plane normal stress can be derived:

$$(A.5) \Rightarrow \sigma_{zz} = -S_{12}\sigma_A/S_{11} \qquad (A.7)$$

Therefore, the plane strain mode I loading deformation is described by the following plane stress tensor:

$$\bar{\sigma} = \begin{bmatrix} \sigma_{xx} & \tau_{xy} & \tau_{xz} \\ \tau_{yx} & \sigma_{yy} & \tau_{yz} \\ \tau_{zx} & \tau_{zy} & \sigma_{zz} \end{bmatrix} = \sigma_A \begin{bmatrix} 0 & 0 & 0 \\ 0 & 1 & 0 \\ 0 & 0 & -S_{12}/S_{11} \end{bmatrix} \qquad (A.8)$$

It is worth mentioning that under these loading conditions the system experiences a hydrostatic pressure equal to:

$$p = -\frac{\sigma_{xx} + \sigma_{yy} + \sigma_{zz}}{3} = -\frac{\sigma_A(1 - S_{12}/S_{11})}{3} \qquad (A.9)$$

Using the equations A.3 through A.7, the strain tensor expressed as:

$$\bar{\varepsilon} = \begin{bmatrix} \varepsilon_{xx} & \gamma_{xy} & \gamma_{xz} \\ \gamma_{yx} & \varepsilon_{yy} & \gamma_{yz} \\ \gamma_{zx} & \gamma_{zy} & \varepsilon_{zz} \end{bmatrix} = \sigma_A \begin{bmatrix} (S_{12} - S_{12}^2/S_{11}) & 0 & 0 \\ 0 & (S_{11} - S_{12}^2/S_{11}) & 0 \\ 0 & 0 & 0 \end{bmatrix} \qquad (A.10)$$

can be used to determine the corresponding displacement components:

$$x' = x_0(1 + \varepsilon_{xx}) \Rightarrow u = \varepsilon_{xx}x_0 = \sigma_A x_0(S_{12} - S_{12}^2/S_{11}) \qquad (A.11)$$

$$y' = y_0(1 + \varepsilon_{yy}) \Rightarrow v = \varepsilon_{yy}y_0 = \sigma_A y_0(S_{11} - S_{12}^2/S_{11}) \qquad (A.12)$$

$$z' = z_0(1 + \varepsilon_{zz}) = z_0 \Rightarrow w = 0 \qquad (A.13)$$

where x_0, y_0 and z_0 are the atomic coordinates of the perfect lattice. Using the above mathematical framework of linear elasticity, the stress state of the fcc aluminium and bcc iron under mode I homogeneous deformation is examined using atomistic calculations. The deformation mode of the atomic models is determined through the strain (equation A.10) and displacement (equations A.11-13) components using the elastic compliances of the perfect lattice (Table IV.1). The stress components are analytically-numerically calculated with respect to the magnitude of the applied strain using the Virial theorem [TSA1979] for both metals. For the calculation, three-dimensional periodic boundary conditions were

applied on the atomic models. The comparison between the stress state of the linear continuum mechanics predictions and the analytic-numeric calculation from the potential functions are given in figures A.2a and A.2b for aluminium and iron, respectively.

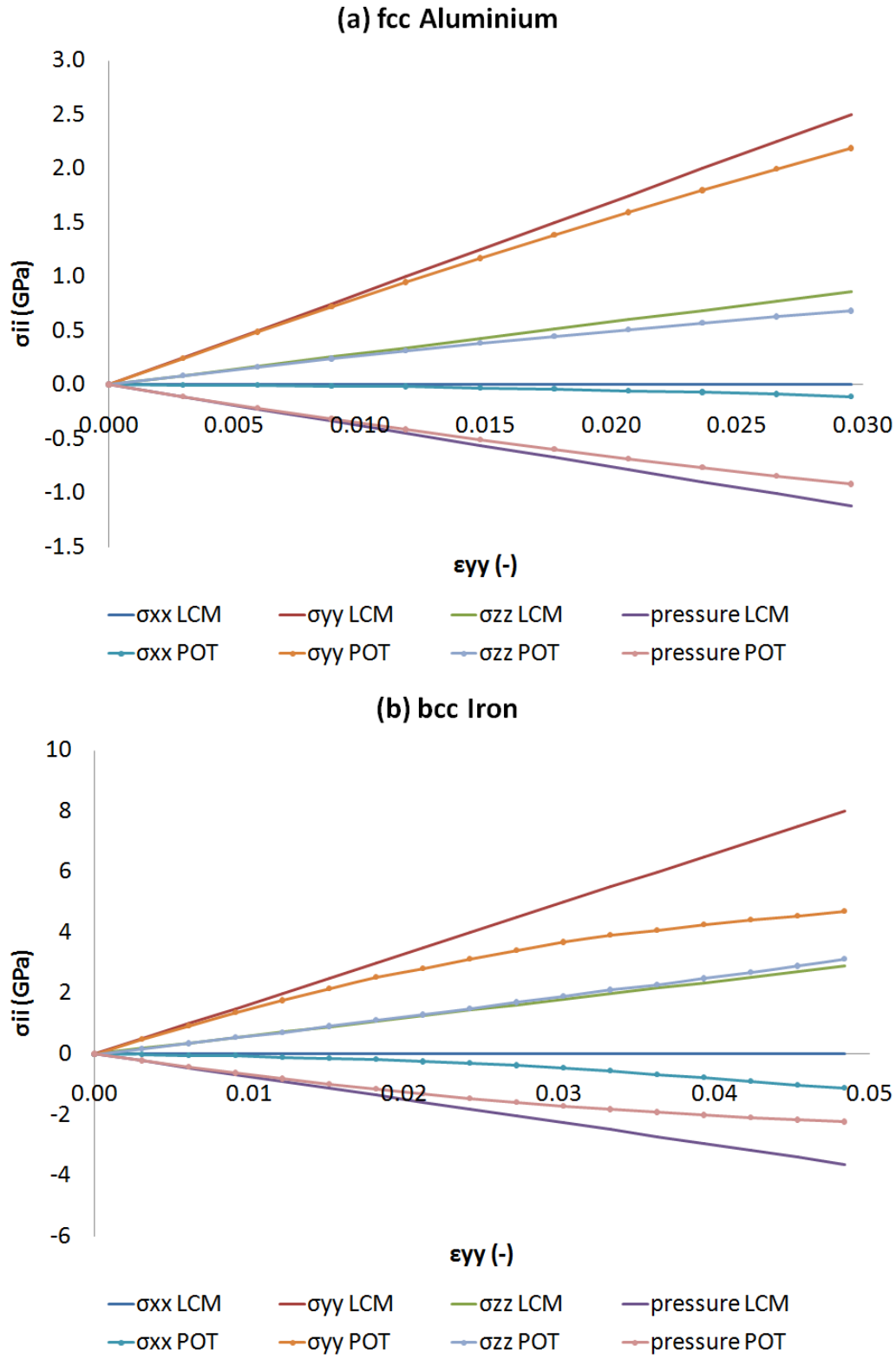

Figure A.2: Comparison of the stress-strain state between the inter-atomic potential results (POT) and linear elasticity predictions (LCM) in (a) fcc aluminium and (b) bcc iron under uni-axial mode I deformation.

By increasing the applied strain of the pure plane strain mode I deformation in both systems, the difference of the stress components between the linear elasticity predictions and the inter-atomic potential results using the Virial theorem increases. This behaviour indicates a deviation from the linear approximation formulation between the stress and the strain components, or, in other words, indicates a change in the elastic constants. More importantly, this behaviour calls into question the validity of linear continuum mechanics (LCM) formulation for the two material systems under large strains.

Appendix B: Numerical determination of the cubic elastic constants

The current appendix presents a numerical methodology for determining the elastic constant of the cubic system (C_{11}, C_{12} and C_{44}) using the dynamic energy calculated from the inter-atomic potential function. This methodology is based on the central difference approximation, which is used to calculate the second order derivative of a mathematical function [INT1], and the definition of the density of elastic energy in cubic systems provided by the linear elasticity. The central difference approximation can be achieved by the use of Taylor's theorem [INT2]. Particularly, the Taylor expansion of a function f around a specific point a, as is illustrated in figure B.1, is equal to:

$$f(a+h) = f(a) + h\frac{df(a)}{dh}\bigg|_{h=0} + \frac{h^2}{2!}\frac{df(a)^2}{d^2h}\bigg|_{h=0} + \frac{h^3}{3!}\frac{df(a)^3}{d^3h}\bigg|_{h=0} + \cdots \qquad (B.1)$$

$$f(a-h) = f(a) - h\frac{df(a)}{dh}\bigg|_{h=0} + \frac{h^2}{2!}\frac{df(a)^2}{d^2h}\bigg|_{h=0} - \frac{h^3}{3!}\frac{df(a)^3}{d^3h}\bigg|_{h=0} + \cdots \qquad (B.2)$$

The central difference approximation can be obtained by the combination of equations B.1 and B.2, where the second derivative of f at the specific point a is given by:

$$\frac{d^2f(a)}{dh^2}\bigg|_{h=0} = \frac{f(a+h) + f(a-h) - 2f(a)}{h^2} + O(h^4) \qquad (B.3)$$

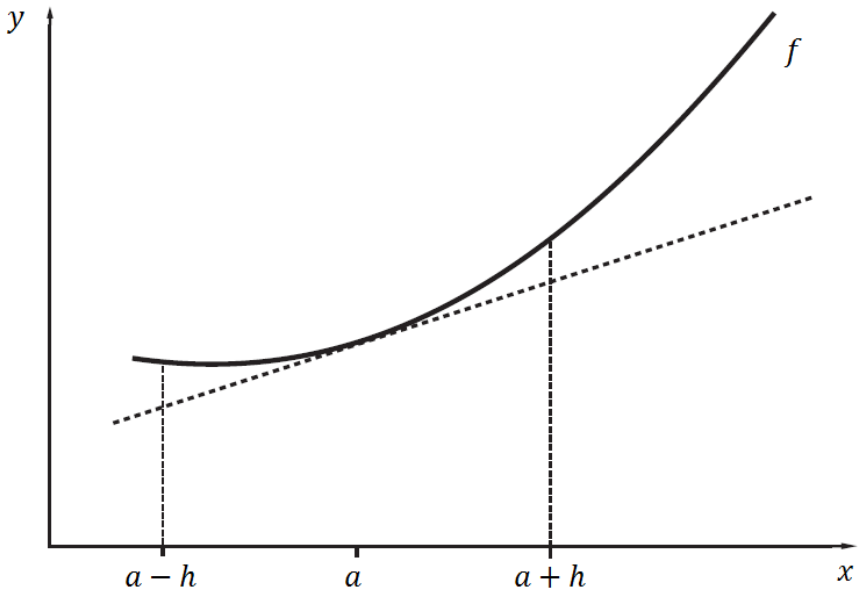

Figure B.1: Central difference approximation.

According to linear elasticity [HIR1982, KIT2004], the density of the elastic energy for the cubic system is given by the following analytical expression:

$$U_{el}(\varepsilon_{ij}, C_{ij}) = \frac{C_{11}}{2}\left(\varepsilon_{xx}^2 + \varepsilon_{yy}^2 + \varepsilon_{zz}^2\right) + C_{12}\left(\varepsilon_{yy}\varepsilon_{zz} + \varepsilon_{zz}\varepsilon_{xx} + \varepsilon_{xx}\varepsilon_{yy}\right) + \frac{C_{44}}{2}\left(\gamma_{yz}^2 + \gamma_{zx}^2 + \gamma_{xy}^2\right) \quad (B.4)$$

where C_{11}, C_{12} and C_{44} are the independent elastic constant and ε_{ij} (or γ_{ij}) are the strain components along the cubic crystallographic axes (i.e. x is $[100]$, y is $[010]$ and z is $[001]$). Thus, for a homogeneous deformation mode the corresponding elastic modulus consists, in the general case, is a combination of the cubic elastic constants. In addition, this elastic modulus is given by the second derivative of the U_{el} in respect to the appropriate strain components. The U_{el} is calculated by the inter-atomic potential function and the atomic volume of the reference pre-deformed configuration. For calculating the whole set of the cubic elastic constants, the following states of deformation must be applied individually to the reference pre-deformed system: (1) the simple shear, (2) the pure shear and (3) the dilatation mode, as presented in figure B.2. The displacement and strain components and the elastic moduli corresponding to these homogeneous deformations are given in Table B.1.

Table B.1: Elastic moduli of simple shear, pure shear and dilatation deformation mode

Deformation	Coordinates	Displacements	Strain tensor	Elastic modulus
Simple shear C_{44}	$x_i = x_0 + \gamma y_0/2$ $y_i = y_0 + \gamma x_0/2$ $z_i = z_0$	$u = \gamma y_0/2$ $v = \gamma x_0/2$ $w = 0$	$\bar{\varepsilon} = \begin{bmatrix} 0 & \gamma & 0 \\ \gamma & 0 & 0 \\ 0 & 0 & 0 \end{bmatrix}$	$\frac{d^2U_{el}}{d\gamma^2} = C_{44}$
Pure shear C'	$x_i = x_0(1 + e/2)$ $y_i = y_0/(1 + e/2)$ $z_i = z_0$	$u = ex_0/2$ $v \cong -ey_0/2$ $w = 0$	$\bar{\varepsilon} = \begin{bmatrix} e/2 & 0 & 0 \\ 0 & -e/2 & 0 \\ 0 & 0 & 0 \end{bmatrix}$	$\frac{d^2U_{el}}{de^2} = \frac{(C_{11} - C_{12})}{2} = C'$
Dilatation B	$x_i = x_0(1 + e/3)$ $y_i = y_0(1 + e/3)$ $z_i = z_0(1 + e/3)$	$u = ex_0/3$ $v = ey_0/3$ $w = ez_0/3$	$\bar{\varepsilon} = \begin{bmatrix} e/3 & 0 & 0 \\ 0 & e/3 & 0 \\ 0 & 0 & e/3 \end{bmatrix}$	$\frac{d^2U_{el}}{de^2} = \frac{(C_{11} + 2C_{12})}{3} = B$

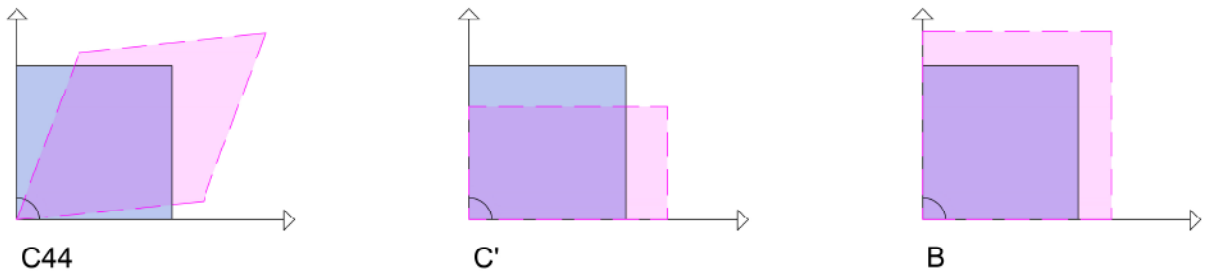

Figure B.2: Deformation modes of simple shear, pure shear and dilatation.

Using the formulation of equation B.3, the elastic constants can be determined numerically by:

$$\left.\frac{d^2U_{el}(r)}{de^2}\right|_{e=0} \cong \frac{U_{el}(+e)+U_{el}(-e)-2U_{el}(0)}{e^2} \qquad (B.5)$$

where the $U_{el}(0)$ and $U_{el}(\pm e)$ are the densities of the elastic energy of the reference pre-deformed and homogeneous deformed configurations, respectively, and e (or γ) is the magnitude of the applied deformation. The results from the numerical method for the perfect lattice of fcc aluminium and bcc iron are shown in figures B.3. As seen in figures B.3 each plot consists of three regions. In region 1, the calculated elastic constants, for small deformations, are incorrect and randomized due to the limited accuracy of calculation of the numerator in equation B.5. For intermediate deformations, in region 2, the calculated elastic constants form a plateau which determines their correct values. In region 3, the calculated elastic constants, for large deformations, deviate from the plateau level due to the negligence of higher order terms (see equation B.3). Finally, the elastic coefficients of the cubic lattice are calculated by:

$$C_{11} = \frac{3B+4C'}{3} \qquad (B.6)$$

$$C_{12} = \frac{3B-2C'}{3} \qquad (B.7)$$

and the results for the perfect lattices of the two metals are summarized in the following table B.2.

Table B.2: Calculated elastic stiffness constants of fcc aluminium and bcc iron

Properties	**Aluminium[ZAC2017]**	**Iron[PON2007]**
Lattice	Face-centered cubic	Body-centered cubic
$C_{44}(GPa)$	29.6	121.8
$C'(GPa)$	27.8	52.8
$B(GPa)$	79.6	172.7
$C_{11}(GPa)$	116.6	243.1
$C_{12}(GPa)$	61.0	137.5

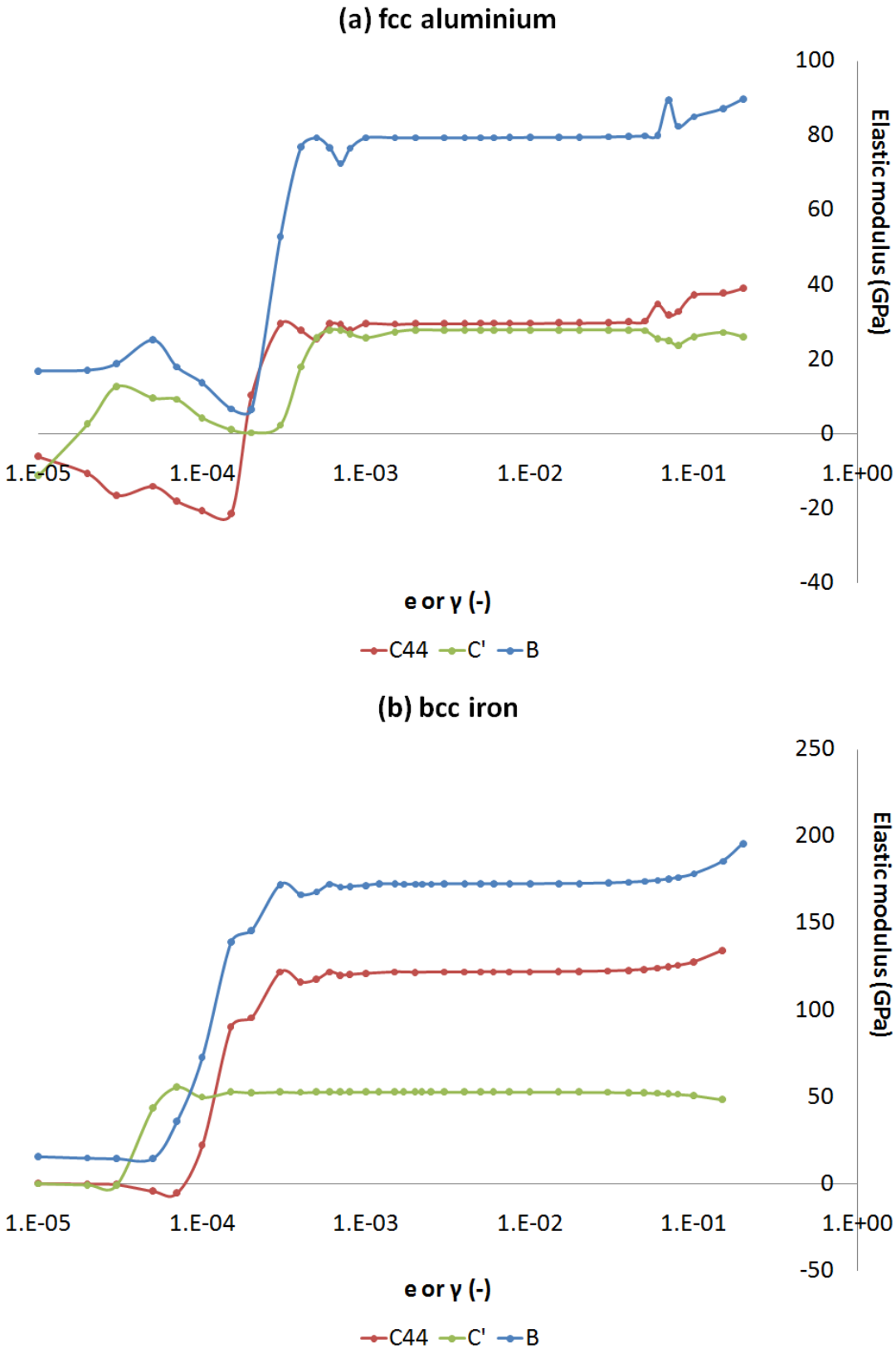

Figure B.3: Numerical determination of elastic constants in (a) fcc aluminium and (b) bcc iron.

Appendix C: Analytic determination of the elastic constants in fcc aluminium

This appendix presents the analytic formulation for determining the elastic constants in fcc aluminium via the inter-atomic potential function. According to linear elasticity, the density of the elastic energy of the crystal can be expressed by the equation:

$$w = \frac{1}{2}\sum_{\alpha=1}^{6}\sum_{\beta=1}^{6} C_{a\beta}\varepsilon_a\varepsilon_\beta \qquad (C.1)$$

where σ_a are the stress components, ε_a are the strain components and $C_{a\beta}$ are the second order elastic constant expressed by Voigt's notation $(\alpha, \beta = 1,2,\dots,6)$. In addition, the total dynamic energy of the crystal can derive through a Taylor expansion in terms of the strain components:

$$U(V,\varepsilon) = U(V_0) + \sum_{\alpha}^{6}\left.\frac{\partial U}{\partial \varepsilon_\alpha}\right|_0 \varepsilon_\alpha + \frac{1}{2}\sum_{\alpha=1}^{6}\sum_{\beta=1}^{6}\left.\frac{\partial^2 U}{\partial\varepsilon_\alpha\partial\varepsilon_\beta}\right|_0 \varepsilon_a\varepsilon_\beta \qquad (C.2a)$$

where V is the volume of the solid and the 0 index denote the reference pre-deformed state. By using equation B.4 the relation C.2a converts to:

$$U(V,\varepsilon) = U(V_0) + V\sum_{\alpha}^{6}\sigma_\alpha\varepsilon_\alpha + \frac{V}{2}\sum_{\alpha=1}^{6}\sum_{\beta=1}^{6} C_{a\beta}\varepsilon_a\varepsilon_\beta \qquad (C.2b)$$

Hence, the second-order elastic constants are approximately determined by equation:

$$C_{\alpha\beta} = \frac{1}{V}\left.\frac{\partial^2 U}{\partial\varepsilon_\alpha\partial\varepsilon_\beta}\right|_0 \qquad (C.3)$$

Considering a homogeneous deformation, each atom in the system is in equivalent mechanical state with all the others, hence, equation C.3 can be transformed to:

$$C_{\alpha\beta} = \frac{1}{V}\sum_{i}^{N_{at}}\left.\frac{\partial^2 U_i}{\partial\varepsilon_\alpha\partial\varepsilon_\beta}\right|_0 = \frac{N_{at}}{V}\left.\frac{\partial^2 U_i}{\partial\varepsilon_\alpha\partial\varepsilon_\beta}\right|_0 = \frac{1}{V_i}\left.\frac{\partial^2 U_i}{\partial\varepsilon_\alpha\partial\varepsilon_\beta}\right|_0 \qquad (C.4)$$

where N_{at} is the total particles of the system and i represents to each individual atom in the homogeneous elastic deformed body. The dynamic energy of the atom i in fcc aluminum is derived from the inter-atomic potential function [ZAC2017]:

$$U_i = \sum_{j \neq i} \left\{ exp\left[-p\left(\frac{r_{ij}}{r_0} - 1\right)\right] + \frac{C_1 cos(2k_F r_{ij})}{\left(r_{ij}/r_0\right)^3} + \frac{S_1 sin(2k_F r_{ij})}{\left(r_{ij}/r_0\right)^4} + \frac{C_2 cos(2k_F r_{ij})}{\left(r_{ij}/r_0\right)^5} \right\}$$

$$- \left[\sum_{j \neq i} \xi^2 \, exp\left[-2q\left(\frac{r_{ij}}{r_0} - 1\right)\right]\right]^{1/2} = \sum_{j \neq i} \varphi(r_{ij}) - \left[\sum_{j \neq i} \psi(r_{ij})\right]^{1/2} = U_i^R - U_i^A \quad (C.5)$$

where U_i^R is the repulsive component, U_i^A is the attractive component and $r_{ij} = \left|\vec{r}_j - \vec{r}_i\right|$ denotes the Euclidean distance between the atoms i and j. All other parameters of equation C.5 can be considered as constants in the further analysis. In order to calculate analytically all the independent cubic elastic constants, the following states of deformation must be applied individually to the reference, pre-deformed system: (a) the simple shear, (b) the pure shear and (c) the dilatation as presented in figure B.2. Based on the formulation in appendix B, the atomic coordinates, displacement and strain components and the elastic moduli corresponding to these homogeneous deformations are given in table C.1.

Table C.1: Elastic moduli of simple shear, pure shear and dilatation deformation mode.

Deformation	Coordinates	Displacements	Strain tensor	Elastic modulus
Simple shear C_{44}	$x_i = x_i^0 + \gamma y_i^0$ $y_i = y_i^0 + \gamma x_i^0$ $z_i = z_i^0$	$u = \gamma y_i^0$ $v = \gamma x_i^0$ $w = 0$	$\bar{\varepsilon} = \begin{bmatrix} 0 & 2\gamma & 0 \\ 2\gamma & 0 & 0 \\ 0 & 0 & 0 \end{bmatrix}$	$\frac{1}{V_i} \cdot \frac{d^2 U_i}{d\gamma^2}\Big\|_0 = 4C_{44}$
Pure shear C'	$x_i = x_i^0(1+e)$ $y_i = y_i^0/(1+e)$ $z_i = z_0$	$u = ex_i^0$ $v \cong -ey_i^0$ $w = 0$	$\bar{\varepsilon} = \begin{bmatrix} e & 0 & 0 \\ 0 & -e & 0 \\ 0 & 0 & 0 \end{bmatrix}$	$\frac{1}{V_i} \cdot \frac{d^2 U_i}{de^2}\Big\|_0 = 2(C_{11} - C_{12}) = 4C'$
Dilatation B	$x_i = x_i^0(1-e)$ $y_i = y_i^0(1-e)$ $z_i = z_i^0(1-e)$	$u = -ex_i^0$ $v = -ey_i^0$ $w = -ez_i^0$	$\bar{\varepsilon} = \begin{bmatrix} -e & 0 & 0 \\ 0 & -e & 0 \\ 0 & 0 & -e \end{bmatrix}$	$\frac{1}{V_i} \cdot \frac{d^2 U_i}{de^2}\Big\|_0 = 3(C_{11} + 2C_{12}) = 9B$

C.1. Simple shear

The Euclidean distance between the atom i and its neighbours j for the simple shear deformation is equal to:

$$r_{ij} = \left[\left(x_j - x_i\right)^2 + \left(y_j - y_i\right)^2 + \left(z_j - z_i\right)^2\right]^{1/2} = \left[\left(x_{ij}^0 + \gamma y_{ij}^0\right)^2 + \left(y_{ij}^0 + \gamma x_{ij}^0\right)^2 + z_{ij}^{0\,2}\right]^{1/2} \quad (C.6)$$

Hence, the first order derivative of r_{ij} with respect to the simple shear deformation is:

$$\frac{dr_{ij}}{d\gamma} = \frac{2y_{ij}^0\left(x_{ij}^0 + \gamma y_{ij}^0\right) + 2x_{ij}^0\left(y_{ij}^0 + \gamma x_{ij}^0\right)}{2\left[\left(x_{ij}^0 + \gamma y_{ij}^0\right)^2 + \left(y_{ij}^0 + \gamma x_{ij}^0\right)^2 + {z_{ij}^0}^2\right]^{1/2}} = \frac{2x_{ij}^0 y_{ij}^0 + \gamma\left({x_{ij}^0}^2 + {y_{ij}^0}^2\right)}{r_{ij}} \qquad (C.7)$$

At the pre-deformed, reference configuration, or for zero deformation, the equation C.7 becomes:

$$\left.\frac{dr_{ij}}{d\gamma}\right|_0 \overset{\gamma\to 0}{\Longrightarrow} \frac{2x_{ij}^0 y_{ij}^0}{{r_{ij}}^0} \qquad (C.8)$$

The second order derivative of r_{ij} with respect to the simple shear deformation is given by:

$$\frac{d^2 r_{ij}}{d\gamma^2} = \frac{\left({x_{ij}^0}^2 + {y_{ij}^0}^2\right)}{r_{ij}} - \frac{2\left[2x_{ij}^0 y_{ij}^0 + \gamma\left({x_{ij}^0}^2 + {y_{ij}^0}^2\right)\right]^2}{2\left[\left(x_{ij}^0 + \gamma y_{ij}^0\right)^2 + \left(y_{ij}^0 + \gamma x_{ij}^0\right)^2 + {z_{ij}^0}^2\right]^{3/2}}$$

$$\frac{d^2 r_{ij}}{d\gamma^2} = \frac{\left({x_{ij}^0}^2 + {y_{ij}^0}^2\right)}{r_{ij}} - \frac{\left[2x_{ij}^0 y_{ij}^0 + \gamma\left({x_{ij}^0}^2 + {y_{ij}^0}^2\right)\right]^2}{\left[\left(x_{ij}^0 + \gamma y_{ij}^0\right)^2 + \left(y_{ij}^0 + \gamma x_{ij}^0\right)^2 + {z_{ij}^0}^2\right]^{3/2}} \qquad (C.9)$$

and at the reference configuration becomes:

$$\left.\frac{d^2 r_{ij}}{d\gamma^2}\right|_0 \overset{\gamma\to 0}{\Longrightarrow} \frac{\left({x_{ij}^0}^2 + {y_{ij}^0}^2\right)}{{r_{ij}}^0} - \frac{\left[2x_{ij}^0 y_{ij}^0\right]^2}{{r_{ij}}^3} = \frac{{x_{ij}^0}^2 + {y_{ij}^0}^2}{{r_{ij}}^0} - \frac{4{x_{ij}^0}^2 {y_{ij}^0}^2}{{r_{ij}}^3} \qquad (C.10)$$

The elastic modulus of simple shear deformation is given by the expression:

$$\left.\frac{d^2 U_i}{d\gamma^2}\right|_0 = \left\{\frac{d}{d\gamma}\left(\frac{dU_i}{d\gamma}\right)\right\}_0 = \left\{\frac{d}{d\gamma}\left(\frac{dU_i^R}{d\gamma} - \frac{dU_i^A}{d\gamma}\right)\right\}_0 = \left.\frac{d^2 U_i^R}{d\gamma^2}\right|_0 - \left.\frac{d^2 U_i^A}{d\gamma^2}\right|_0 = C_{44}^R + C_{44}^A = 4C_{44}V_i^0 \qquad (C.11)$$

where the different terms are determined by using the equations C.8 and C.10. In particular, the repulsive term gives

$$\left.\frac{dU_i^R}{d\gamma}\right|_0 = \sum_{j\neq i}\frac{\partial\varphi(r_{ij})}{\partial r_{ij}}\cdot\left.\frac{dr_{ij}}{d\gamma}\right|_0 = \sum_{j\neq i}\frac{2x_{ij}^0 y_{ij}^0}{{r_{ij}}^0}\cdot\left.\frac{\partial\varphi(r_{ij})}{\partial r_{ij}}\right|_0 \qquad (C.12),$$

and

$$C_{44}^R = \left.\frac{d^2 U_i^R}{d\gamma^2}\right|_0 = \sum_{j\neq i}\left\{\frac{d}{d\gamma}\left(\frac{\partial\varphi(r_{ij})}{\partial r_{ij}}\cdot\frac{dr_{ij}}{d\gamma}\right)\right\}_0 = \sum_{j\neq i}\left\{\frac{d}{d\gamma}\left(\frac{\partial\varphi(r_{ij})}{\partial r_{ij}}\right)\cdot\frac{dr_{ij}}{d\gamma} + \frac{\partial\varphi(r_{ij})}{\partial r_{ij}}\cdot\frac{d}{d\gamma}\left(\frac{dr_{ij}}{d\gamma}\right)\right\}_0$$

$$= \sum_{j\neq i}\left\{\frac{\partial^2\varphi(r_{ij})}{\partial {r_{ij}}^2}\cdot\left(\frac{dr_{ij}}{d\gamma}\right)^2+\frac{\partial\varphi(r_{ij})}{\partial r_{ij}}\cdot\frac{d^2r_{ij}}{d\gamma^2}\right\}_0$$

$$= \sum_{j\neq i}\left\{\left.\frac{\partial^2\varphi(r_{ij})}{\partial {r_{ij}}^2}\right|_0\cdot\left(\frac{2x_{ij}^0y_{ij}^0}{{r_{ij}}^0}\right)^2+\left.\frac{\partial\varphi(r_{ij})}{\partial r_{ij}}\right|_0\cdot\left(\frac{{x_{ij}^0}^2+{y_{ij}^0}^2}{{r_{ij}}^0}-\frac{4{x_{ij}^0}^2{y_{ij}^0}^2}{{r_{ij}}^{0^3}}\right)\right\}$$

$$= \sum_{j\neq i}\left\{\left(\frac{4{x_{ij}^0}^2{y_{ij}^0}^2}{{r_{ij}}^{0^2}}\right)\cdot\left.\frac{\partial^2\varphi(r_{ij})}{\partial {r_{ij}}^2}\right|_0+\left(\frac{{x_{ij}^0}^2+{y_{ij}^0}^2}{{r_{ij}}^0}-\frac{4{x_{ij}^0}^2{y_{ij}^0}^2}{{r_{ij}}^{0^3}}\right)\cdot\left.\frac{\partial\varphi(r_{ij})}{\partial r_{ij}}\right|_0\right\} \qquad (C.13),$$

while the attractive term gives

$$-\left.\frac{dU_i^A}{d\gamma}\right|_0 = -\left\{\frac{d}{d\gamma}\left(\left[\sum_{j\neq i}\psi(r_{ij})\right]^{1/2}\right)\right\}_0 = -\frac{1}{2}\left[\sum_{j\neq i}\psi(r_{ij})\right]^{-1/2}\left.\sum_{j\neq i}\frac{d\psi(r_{ij})}{d\gamma}\right|_0$$

$$= -\frac{1}{2}\left[\sum_{j\neq i}\psi(r_{ij})\right]^{-1/2}\left.\sum_{j\neq i}\frac{\partial\psi(r_{ij})}{\partial r_{ij}}\cdot\frac{dr_{ij}}{d\gamma}\right|_0 = -\frac{1}{2}\left[\sum_{j\neq i}\psi(r_{ij})\right]^{-1/2}\left.\sum_{j\neq i}\frac{2x_{ij}^0y_{ij}^0}{{r_{ij}}^0}\cdot\frac{\partial\psi(r_{ij})}{\partial r_{ij}}\right|_0$$

$$= -\left[\sum_{j\neq i}\psi(r_{ij})\right]^{-1/2}\left.\sum_{j\neq i}\frac{x_{ij}^0y_{ij}^0}{{r_{ij}}^0}\cdot\frac{\partial\psi(r_{ij})}{\partial r_{ij}}\right|_0 \qquad (C.14)$$

and

$$C_{44}^A = -\left.\frac{d^2U_i^A}{d\gamma^2}\right|_0 = \left\{\frac{d}{d\gamma}\left(-\frac{1}{2}\left[\sum_{j\neq i}\psi(r_{ij})\right]^{-1/2}\left.\sum_{j\neq i}\frac{\partial\psi(r_{ij})}{\partial r_{ij}}\cdot\frac{dr_{ij}}{d\gamma}\right|_0\right)\right\}_0$$

$$= -\frac{1}{2}\frac{d}{d\gamma}\left(\left[\sum_{j\neq i}\psi(r_{ij})\right]^{-1/2}\right)\left.\sum_{j\neq i}\frac{\partial\psi(r_{ij})}{\partial r_{ij}}\cdot\frac{dr_{ij}}{d\gamma}\right|_0 - \frac{1}{2}\left[\sum_{j\neq i}\psi(r_{ij})\right]^{-1/2}\sum_{j\neq i}\frac{d}{d\gamma}\left(\frac{\partial\psi(r_{ij})}{\partial r_{ij}}\cdot\frac{dr_{ij}}{d\gamma}\right)_0$$

$$= \left(-\frac{1}{2}\right)\left(-\frac{1}{2}\right)\left[\sum_{j\neq i}\psi(r_{ij})\right]^{-3/2}\left.\sum_{j\neq i}\frac{d\psi(r_{ij})}{d\gamma}\sum_{j\neq i}\frac{\partial\psi(r_{ij})}{\partial r_{ij}}\cdot\frac{dr_{ij}}{d\gamma}\right|_0$$

$$-\frac{1}{2}\left[\sum_{j\neq i}\psi(r_{ij})\right]^{-1/2}\sum_{j\neq i}\left\{\frac{d}{d\gamma}\left(\frac{\partial\psi(r_{ij})}{\partial r_{ij}}\right)\cdot\frac{dr_{ij}}{d\gamma}+\frac{\partial\psi(r_{ij})}{\partial r_{ij}}\cdot\frac{d}{d\gamma}\left(\frac{dr_{ij}}{d\gamma}\right)\right\}_0$$

$$= \frac{1}{4}\left[\sum_{j\neq i}\psi(r_{ij})\right]^{-3/2}\left.\sum_{j\neq i}\frac{\partial\psi(r_{ij})}{\partial r_{ij}}\cdot\frac{dr_{ij}}{d\gamma}\right|_0\left.\sum_{j\neq i}\frac{\partial\psi(r_{ij})}{\partial r_{ij}}\cdot\frac{dr_{ij}}{d\gamma}\right|_0$$

$$-\frac{1}{2}\left[\sum_{j\neq i}\psi(r_{ij})\right]^{-1/2}\sum_{j\neq i}\left\{\frac{\partial^2\psi(r_{ij})}{\partial {r_{ij}}^2}\cdot\left(\frac{dr_{ij}}{d\gamma}\right)^2+\frac{\partial\psi(r_{ij})}{\partial r_{ij}}\cdot\frac{d^2r_{ij}}{d\gamma^2}\right\}_0$$

$$=\frac{1}{4}\left[\sum_{j\neq i}\psi(r_{ij})\right]^{-3/2}\left[\sum_{j\neq i}\frac{\partial\psi(r_{ij})}{\partial r_{ij}}\cdot\frac{dr_{ij}}{d\gamma}\bigg|_0\right]^2-\frac{1}{2}\left[\sum_{j\neq i}\psi(r_{ij})\right]^{-1/2}\sum_{j\neq i}\left\{\frac{\partial^2\psi(r_{ij})}{\partial {r_{ij}}^2}\cdot\left(\frac{dr_{ij}}{d\gamma}\right)^2+\frac{\partial\psi(r_{ij})}{\partial r_{ij}}\cdot\frac{d^2r_{ij}}{d\gamma^2}\right\}_0$$

$$=\frac{1}{4}\left[\sum_{j\neq i}\psi(r_{ij})\right]^{-3/2}\left[\sum_{j\neq i}\frac{2x_{ij}^0y_{ij}^0}{{r_{ij}}^0}\cdot\frac{\partial\psi(r_{ij})}{\partial r_{ij}}\bigg|_0\right]^2$$

$$-\frac{1}{2}\left[\sum_{j\neq i}\psi(r_{ij})\right]^{-1/2}\sum_{j\neq i}\left\{\left(\frac{4{x_{ij}^0}^2{y_{ij}^0}^2}{{r_{ij}^0}^2}\right)\cdot\frac{\partial^2\psi(r_{ij})}{\partial {r_{ij}}^2}\bigg|_0+\left(\frac{{x_{ij}^0}^2+{y_{ij}^0}^2}{{r_{ij}}^0}-\frac{4{x_{ij}^0}^2{y_{ij}^0}^2}{{r_{ij}^0}^3}\right)\cdot\frac{\partial\psi(r_{ij})}{\partial r_{ij}}\bigg|_0\right\}$$

$$=\left[\sum_{j\neq i}\psi(r_{ij})\right]^{-3/2}\left[\sum_{j\neq i}\frac{x_{ij}^0y_{ij}^0}{{r_{ij}}^0}\cdot\frac{\partial\psi(r_{ij})}{\partial r_{ij}}\bigg|_0\right]^2$$

$$-\frac{1}{2}\left[\sum_{j\neq i}\psi(r_{ij})\right]^{-1/2}\sum_{j\neq i}\left\{\left(\frac{4{x_{ij}^0}^2{y_{ij}^0}^2}{{r_{ij}^0}^2}\right)\cdot\frac{\partial^2\psi(r_{ij})}{\partial {r_{ij}}^2}\bigg|_0+\left(\frac{{x_{ij}^0}^2+{y_{ij}^0}^2}{{r_{ij}}^0}-\frac{4{x_{ij}^0}^2{y_{ij}^0}^2}{{r_{ij}^0}^3}\right)\cdot\frac{\partial\psi(r_{ij})}{\partial r_{ij}}\bigg|_0\right\} \quad (C.15)$$

C.2. Pure shear

The Euclidean distance between the atom i and its neighbours j for the pure shear deformation is equal to:

$$r_{ij}=\left[\left(x_j-x_i\right)^2+\left(y_j-y_i\right)^2+\left(z_j-z_i\right)^2\right]^{1/2}=\left[{x_{ij}^0}^2(1+e)^2+\frac{{y_{ij}^0}^2}{(1+e)^2}+{z_{ij}^0}^2\right]^{1/2} \quad (C.16)$$

Thus, the first order derivative of r_{ij} with respect to the pure shear deformation is:

$$\frac{dr_{ij}}{de}=\frac{2{x_{ij}^0}^2(1+e)-\frac{2{y_{ij}^0}^2}{(1+e)^3}}{2\left[{x_{ij}^0}^2(1+e)^2+\frac{{y_{ij}^0}^2}{(1+e)^2}+{z_{ij}^0}^2\right]^{1/2}}=\frac{{x_{ij}^0}^2(1+e)-\frac{{y_{ij}^0}^2}{(1+e)^3}}{\left[{x_{ij}^0}^2(1+e)^2+\frac{{y_{ij}^0}^2}{(1+e)^2}+{z_{ij}^0}^2\right]^{1/2}} \quad (C.17)$$

At the pre-deformed reference configuration, for zero deformation, the equation C.17 becomes:

$$\frac{dr_{ij}}{de}\bigg|_0\overset{e\to0}{\Longrightarrow}\frac{{x_{ij}^0}^2-{y_{ij}^0}^2}{{r_{ij}}^0} \quad (C.18)$$

The second order derivative of r_{ij} with respect to the pure shear deformation is:

$$\frac{d^2 r_{ij}}{de^2} = -\frac{1}{2}\cdot\frac{2{x_{ij}^0}^2(1+e)-\frac{2{y_{ij}^0}^2}{(1+e)^3}}{\left[{x_{ij}^0}^2(1+e)^2+\frac{{y_{ij}^0}^2}{(1+e)^2}+{z_{ij}^0}^2\right]^{3/2}}\cdot\left({x_{ij}^0}^2(1+e)-\frac{{y_{ij}^0}^2}{(1+e)^3}\right)+\frac{{x_{ij}^0}^2+\frac{3{y_{ij}^0}^2}{(1+e)^4}}{\left[{x_{ij}^0}^2(1+e)^2+\frac{{y_{ij}^0}^2}{(1+e)^2}+{z_{ij}^0}^2\right]^{1/2}}$$

$$= -\frac{\left[{x_{ij}^0}^2(1+e)-\frac{{y_{ij}^0}^2}{(1+e)^3}\right]^2}{\left[{x_{ij}^0}^2(1+e)^2+\frac{{y_{ij}^0}^2}{(1+e)^2}+{z_{ij}^0}^2\right]^{3/2}}+\frac{{x_{ij}^0}^2+\frac{3{y_{ij}^0}^2}{(1+e)^4}}{\left[{x_{ij}^0}^2(1+e)^2+\frac{{y_{ij}^0}^2}{(1+e)^2}+{z_{ij}^0}^2\right]^{1/2}} \qquad (C.19)$$

and for zero deformation, it becomes:

$$\left.\frac{d^2 r_{ij}}{de^2}\right|_0 \overset{e\to 0}{\Longrightarrow}\frac{{x_{ij}^0}^2+3{y_{ij}^0}^2}{{r_{ij}}^0}-\frac{\left({x_{ij}^0}^2-{y_{ij}^0}^2\right)^2}{{r_{ij}}^{0^3}} \qquad (C.20)$$

According to table C.1, the elastic modulus for the pure shear deformation is given by the expression:

$$\left.\frac{d^2 U_i}{de^2}\right|_0 = \left\{\frac{d}{de}\left(\frac{dU_i}{de}\right)\right\}_0 = \left\{\frac{d}{de}\left(\frac{dU_i^R}{de}-\frac{dU_i^A}{de}\right)\right\}_0 = \left.\frac{d^2 U_i^R}{de^2}\right|_0 - \left.\frac{d^2 U_i^A}{de^2}\right|_0 = C'^R + C'^A = 4C'V_i^0 \qquad (C.21)$$

where the different terms can be calculated by the use of equations C.18 and C.20. Particularly, the repulsive term is equal to:

$$C'^R = \left.\frac{d^2 U_i^R}{de^2}\right|_0 = \sum_{j\neq i}\left\{\frac{\partial^2\varphi(r_{ij})}{\partial {r_{ij}}^2}\cdot\left(\frac{dr_{ij}}{de}\right)^2+\frac{\partial\varphi(r_{ij})}{\partial r_{ij}}\cdot\frac{d^2 r_{ij}}{de^2}\right\}_0$$

$$= \sum_{j\neq i}\left\{\left[\frac{{x_{ij}^0}^2-{y_{ij}^0}^2}{{r_{ij}}^0}\right]^2\cdot\left.\frac{\partial^2\varphi(r_{ij})}{\partial {r_{ij}}^2}\right|_0+\left(\frac{{x_{ij}^0}^2+3{y_{ij}^0}^2}{{r_{ij}}^0}-\frac{\left[{x_{ij}^0}^2-{y_{ij}^0}^2\right]^2}{{r_{ij}}^{0^3}}\right)\cdot\left.\frac{\partial\varphi(r_{ij})}{\partial r_{ij}}\right|_0\right\} \qquad (C.22)$$

where the attractive term is:

$$C'^A = -\left.\frac{d^2 U_i^A}{de^2}\right|_0 = \frac{1}{4}\left[\sum_{j\neq i}\psi(r_{ij})\right]^{-3/2}\left[\sum_{j\neq i}\frac{\partial\psi(r_{ij})}{\partial r_{ij}}\cdot\left.\frac{dr_{ij}}{de}\right|_0\right]^2$$

$$-\frac{1}{2}\left[\sum_{j\neq i}\psi(r_{ij})\right]^{-1/2}\sum_{j\neq i}\left\{\frac{\partial^2\psi(r_{ij})}{\partial {r_{ij}}^2}\cdot\left(\frac{dr_{ij}}{de}\right)^2+\frac{\partial\psi(r_{ij})}{\partial r_{ij}}\cdot\frac{d^2 r_{ij}}{de^2}\right\}_0$$

$$= \frac{1}{4}\left[\sum_{j\neq i}\psi(r_{ij})\right]^{-3/2}\left[\sum_{j\neq i}\left(\frac{{x_{ij}^0}^2-{y_{ij}^0}^2}{{r_{ij}}^0}\right)\cdot\left.\frac{\partial\psi(r_{ij})}{\partial r_{ij}}\right|_0\right]^2$$

$$-\frac{1}{2}\left[\sum_{j\neq i}\psi(r_{ij})\right]^{-1/2}\sum_{j\neq i}\left\{\left(\frac{{x_{ij}^0}^2-{y_{ij}^0}^2}{{r_{ij}}^0}\right)^2\left.\frac{\partial^2\psi(r_{ij})}{\partial {r_{ij}}^2}\right|_0+\left(\frac{{x_{ij}^0}^2+3{y_{ij}^0}^2}{{r_{ij}}^0}-\frac{\left[{x_{ij}^0}^2-{y_{ij}^0}^2\right]^2}{{r_{ij}}^{0^3}}\right)\left.\frac{\partial\psi(r_{ij})}{\partial r_{ij}}\right|_0\right\} \quad (C.23)$$

C.3. Dilatation

The volume of an atom i under dilatation deformation is equal to:

$$V_i = x_i y_i z_i = x_i^0 y_i^0 z_i^0 (1-e)^3 = V_i^0 (1-e)^3 \quad (C.24)$$

Thus, the first order derivative of the volume of an atom with respect to the dilatation deformation is:

$$\frac{dV_i}{de} = -3V_i^0(1-e)^2 \Rightarrow \frac{de}{dV_i} = -\frac{1}{3V_i^0}(1-e)^{-2} \quad (C.25)$$

and for zero deformation becomes:

$$\left.\frac{de}{dV_i}\right|_0 = -\frac{1}{3V_i^0} \quad (C.26)$$

In addition, the second order derivative is equal to:

$$\frac{d^2e}{dV_i^2} = \frac{2}{3V_i^0}(1-e)^{-3}\left(-\frac{de}{dV_i}\right) = \frac{2}{9{V_i^0}^2}(1-e)^{-5} \quad (C.27)$$

and at the reference state becomes:

$$\left.\frac{d^2e}{dV_i^2}\right|_0 = \frac{2}{9{V_i^0}^2} \quad (C.28)$$

Similarly, the Euclidean distance between the atom i and its neighbours j for the dilatation deformation is equal to:

$$r_{ij} = \left[\left(x_j - x_i\right)^2 + \left(y_j - y_i\right)^2 + \left(z_j - z_i\right)^2\right]^{1/2}$$

$$r_{ij} = (1-e)\left[\left(x_j^0 - x_i^0\right)^2 + \left(y_j^0 - y_i^0\right)^2 + \left(z_j^0 - z_i^0\right)^2\right]^{1/2} = r_{ij}^0(1-e) \quad (C.29)$$

with first and second derivatives

$$\frac{dr_{ij}}{d\varepsilon} = -r_{ij}^0 \tag{C.30}$$

and

$$\frac{d^2 r_{ij}}{d\varepsilon^2} = 0 \tag{C.31}$$

The pressure in the system is defined as

$$p = -\frac{\partial U}{\partial V}\Big|_0 \tag{C.32}$$

Since,

$$V = N_{at} V_i \Longrightarrow dV = N_{at} dV_i \Longrightarrow \frac{dV_i}{dV} = \frac{1}{N_{at}} \tag{C.33}$$

equation C.32 becomes

$$p = -\sum_i \frac{\partial U_i}{\partial V}\Big|_0 = -\sum_i \frac{\partial U_i}{\partial V_i} \cdot \frac{dV_i}{dV}\Big|_0 = -\frac{1}{N_{at}} \sum_i \frac{\partial U_i}{\partial V_i} \cdot\Big|_0 = -\frac{N_{at}}{N_{at}} \frac{dU_i}{dV_i}\Big|_0 = -\frac{dU_i}{dV_i}\Big|_0 \tag{C.34}$$

because all the atoms have the same mechanical state in the system. Hence,

$$p = -\frac{dU_i^R}{dV_i}\Big|_0 + \frac{dU_i^A}{dV_i}\Big|_0 = -\sum_{j \neq i} \frac{d\varphi(r_{ij})}{dV_i}\Big|_0 + \left\{ \frac{d}{dV_i} \left[\sum_{j \neq i} \psi(r_{ij}) \right]^{1/2} \right\}_0 = p^R + p^A \tag{C.35}$$

where

$$p^R = -\sum_{j \neq i} \frac{\partial \varphi(r_{ij})}{\partial r_{ij}} \cdot \frac{dr_{ij}}{de} \cdot \frac{de}{dV_i}\Big|_0 = -\sum_{j \neq i} \frac{\partial \varphi(r_{ij})}{\partial r_{ij}}\Big|_0 \left(-r_{ij}^0\right) \left(-\frac{1}{3V_i^0}\right)$$

$$= -\frac{1}{3V_i^0} \sum_{j \neq i} r_{ij}^0 \cdot \frac{\partial \varphi(r_{ij})}{\partial r_{ij}}\Big|_0 \tag{C.36}$$

and

$$p^A = \frac{1}{2} \left[\sum_{j \neq i} \psi(r_{ij}) \right]^{-1/2} \sum_{j \neq i} \frac{d\psi(r_{ij})}{dV_i}\Big|_0 = \frac{1}{2} \left[\sum_{j \neq i} \psi(r_{ij}) \right]^{-1/2} \sum_{j \neq i} \frac{\partial \psi(r_{ij})}{\partial r_{ij}} \cdot \frac{dr_{ij}}{de} \cdot \frac{de}{dV_i}\Big|_0$$

$$= \frac{1}{2} \left[\sum_{j \neq i} \psi(r_{ij}) \right]^{-1/2} \sum_{j \neq i} \frac{\partial \psi(r_{ij})}{\partial r_{ij}}\Big|_0 \cdot \left(-r_{ij}^0\right) \cdot \left(-\frac{1}{3V_i^0}\right)$$

$$= \frac{1}{6V_i^0}\left[\sum_{j\neq i}\psi(r_{ij})\right]^{-1/2}\sum_{j\neq i} r_{ij}^0 \cdot \frac{\partial\psi(r_{ij})}{\partial r_{ij}}\bigg|_0 \qquad (C.37)$$

Therefore, pressure is:

$$p = p^R + p^A = -\frac{1}{3V_i^0}\sum_{j\neq i} r_{ij}^0 \cdot \frac{\partial\varphi(r_{ij})}{\partial r_{ij}}\bigg|_0 + \frac{1}{6V_i^0}\left[\sum_{j\neq i}\psi(r_{ij})\right]^{-1/2}\sum_{j\neq i} r_{ij}^0 \cdot \frac{\partial\psi(r_{ij})}{\partial r_{ij}}\bigg|_0 \qquad (C.38)$$

The definition of bulk modulus is given by the expression:

$$B = -V_0\left(\frac{dp}{dV}\right)_0 \qquad (C.39)$$

By using equations C.33 to C.35, equation C.39 becomes:

$$B = -V_0\left(\frac{dp}{dV_i}\frac{dV_i}{dV}\right)_0 = -\frac{V_0}{N_{at}}\left(\frac{dp^R}{dV_i}+\frac{dp^A}{dV_i}\right)_0 = -V_i^0\left(\frac{dp^R}{dV_i}+\frac{dp^A}{dV_i}\right)$$

$$= -V_i^0\frac{d}{dV_i}\left(-\sum_{j\neq i}\frac{\partial\varphi(r_{ij})}{\partial r_{ij}}\cdot\frac{dr_{ij}}{de}\cdot\frac{de}{dV_i}\bigg|_0 + \frac{1}{2}\left[\sum_{j\neq i}\psi(r_{ij})\right]^{-1/2}\sum_{j\neq i}\frac{\partial\psi(r_{ij})}{\partial r_{ij}}\cdot\frac{dr_{ij}}{de}\cdot\frac{de}{dV_i}\bigg|_0\right)$$

$$= V_i^0\sum_{j\neq i}\frac{d}{dV_i}\left\{\frac{\partial\varphi(r_{ij})}{\partial r_{ij}}\cdot\frac{dr_{ij}}{de}\cdot\frac{de}{dV_i}\bigg|_0\right\} - \frac{V_i^0}{2}\frac{d}{dV_i}\left\{\left[\sum_{j\neq i}\psi(r_{ij})\right]^{-1/2}\sum_{j\neq i}\frac{\partial\psi(r_{ij})}{\partial r_{ij}}\cdot\frac{dr_{ij}}{de}\cdot\frac{de}{dV_i}\bigg|_0\right\}$$

$$B = B^R + B^A \qquad (C.40)$$

where the repulsive part is given by

$$B^R = V_i^0\sum_{j\neq i}\frac{d}{dV_i}\left\{\frac{\partial\varphi(r_{ij})}{\partial r_{ij}}\cdot\frac{dr_{ij}}{de}\cdot\frac{de}{dV_i}\bigg|_0\right\}$$

$$= V_i^0\sum_{j\neq i}\left\{\frac{d}{dV_i}\left(\frac{\partial\varphi(r_{ij})}{\partial r_{ij}}\right)\cdot\frac{dr_{ij}}{de}\cdot\frac{de}{dV_i} + \frac{\partial\varphi(r_{ij})}{\partial r_{ij}}\cdot\frac{d}{dV_i}\left(\frac{dr_{ij}}{de}\right)\cdot\frac{de}{dV_i} + \frac{\partial\varphi(r_{ij})}{\partial r_{ij}}\cdot\frac{dr_{ij}}{de}\cdot\frac{d}{dV_i}\left(\frac{de}{dV_i}\right)\right\}_0$$

$$= V_i^0\sum_{j\neq i}\left\{\frac{\partial^2\varphi(r_{ij})}{\partial {r_{ij}}^2}\cdot\left(\frac{dr_{ij}}{de}\right)^2\cdot\left(\frac{de}{dV_i}\right)^2 + \frac{\partial\varphi(r_{ij})}{\partial r_{ij}}\cdot 0\cdot\frac{de}{dV_i} + \frac{\partial\varphi(r_{ij})}{\partial r_{ij}}\cdot\frac{dr_{ij}}{de}\cdot\frac{d^2e}{{dV_i}^2}\right\}_0$$

$$= V_i^0\sum_{j\neq i}\left\{\frac{\partial^2\varphi(r_{ij})}{\partial {r_{ij}}^2}\bigg|_0\cdot\left(-r_{ij}^0\right)^2\cdot\left(-\frac{1}{3V_i^0}\right)^2 + \frac{\partial\varphi(r_{ij})}{\partial r_{ij}}\bigg|_0\cdot\left(-r_{ij}^0\right)\cdot\left(\frac{2}{9{V_i^0}^2}\right)\right\}$$

$$= V_i^0 \cdot \frac{1}{9{V_i^0}^2} \sum_{j \neq i} \left\{ {r_{ij}^0}^2 \cdot \left. \frac{\partial^2 \varphi(r_{ij})}{\partial {r_{ij}}^2} \right|_0 - 2 r_{ij}^0 \cdot \left. \frac{\partial \varphi(r_{ij})}{\partial r_{ij}} \right|_0 \right\}$$

$$= \frac{1}{9V_i^0} \sum_{j \neq i} \left\{ {r_{ij}^0}^2 \cdot \left. \frac{\partial^2 \varphi(r_{ij})}{\partial {r_{ij}}^2} \right|_0 - 2 r_{ij}^0 \cdot \left. \frac{\partial \varphi(r_{ij})}{\partial r_{ij}} \right|_0 \right\} \qquad (C.41)$$

and the attractive part is given by

$$B^A = -\frac{V_i^0}{2} \frac{d}{dV_i} \left\{ \left[\sum_{j \neq i} \psi(r_{ij}) \right]^{-1/2} \sum_{j \neq i} \left. \frac{\partial \psi(r_{ij})}{\partial r_{ij}} \cdot \frac{dr_{ij}}{de} \cdot \frac{de}{dV_i} \right|_0 \right\}$$

$$= -\frac{V_i^0}{2} \left\{ -\frac{1}{2} \left[\sum_{j \neq i} \psi(r_{ij}) \right]^{-3/2} \sum_{j \neq i} \left. \frac{d\psi(r_{ij})}{dV_i} \right|_0 \sum_{j \neq i} \left. \frac{\partial \psi(r_{ij})}{\partial r_{ij}} \cdot \frac{dr_{ij}}{de} \cdot \frac{de}{dV_i} \right|_0 \right.$$

$$\left. + \left[\sum_{j \neq i} \psi(r_{ij}) \right]^{-1/2} \sum_{j \neq i} \frac{d}{dV_i} \left(\left. \frac{\partial \psi(r_{ij})}{\partial r_{ij}} \cdot \frac{dr_{ij}}{de} \cdot \frac{de}{dV_i} \right)_0 \right\} = B^{A1} + B^{A2} \qquad (C.42)$$

The first part of the repulsive term is

$$B^{A1} = \frac{V_i^0}{4} \left[\sum_{j \neq i} \psi(r_{ij}) \right]^{-3/2} \left(\sum_{j \neq i} \left. \frac{\partial \psi(r_{ij})}{\partial r_{ij}} \cdot \frac{dr_{ij}}{de} \cdot \frac{de}{dV_i} \right|_0 \right) \left(\sum_{j \neq i} \left. \frac{\partial \psi(r_{ij})}{\partial r_{ij}} \cdot \frac{dr_{ij}}{de} \cdot \frac{de}{dV_i} \right|_0 \right)$$

$$= \frac{V_i^0}{4} \left[\sum_{j \neq i} \psi(r_{ij}) \right]^{-3/2} \left[\sum_{j \neq i} \left. \frac{\partial \psi(r_{ij})}{\partial r_{ij}} \cdot \frac{dr_{ij}}{de} \cdot \frac{de}{dV_i} \right|_0 \right]^2$$

$$= \frac{V_i^0}{4} \left[\sum_{j \neq i} \psi(r_{ij}) \right]^{-3/2} \left[\sum_{j \neq i} \left. \frac{\partial \psi(r_{ij})}{\partial r_{ij}} \right|_0 \cdot \left(-r_{ij}^0 \right) \cdot \left(-\frac{1}{3V_i^0} \right) \right]^2$$

$$= \frac{1}{36V_i^0} \left[\sum_{j \neq i} \psi(r_{ij}) \right]^{-3/2} \left[\sum_{j \neq i} r_{ij}^0 \cdot \left. \frac{\partial \psi(r_{ij})}{\partial r_{ij}} \right|_0 \right]^2 \qquad (C.43)$$

while the second part is equal to,

$$B^{A2} = -\frac{V_i^0}{2} \left[\sum_{j \neq i} \psi(r_{ij}) \right]^{-1/2} \sum_{j \neq i} \frac{d}{dV_i} \left(\left. \frac{\partial \psi(r_{ij})}{\partial r_{ij}} \cdot \frac{dr_{ij}}{de} \cdot \frac{de}{dV_i} \right|_0 \right)$$

$$= -\frac{V_i^0}{2}\left[\sum_{j\neq i}\psi(r_{ij})\right]^{-1/2}\sum_{j\neq i}\left\{\frac{d}{dV_i}\left(\frac{\partial\psi(r_{ij})}{\partial r_{ij}}\right)\cdot\frac{dr_{ij}}{de}\cdot\frac{de}{dV_i}\Big|_0+\frac{\partial\psi(r_{ij})}{\partial r_{ij}}\cdot\frac{d}{dV_i}\left(\frac{dr_{ij}}{de}\right)\cdot\frac{de}{dV_i}\Big|_0 + \frac{\partial\psi(r_{ij})}{\partial r_{ij}}\cdot\frac{dr_{ij}}{de}\cdot\frac{d}{dV_i}\left(\frac{de}{dV_i}\right)\Big|_0\right\}$$

$$= -\frac{V_i^0}{2}\left[\sum_{j\neq i}\psi(r_{ij})\right]^{-1/2}\sum_{j\neq i}\left\{\frac{\partial^2\psi(r_{ij})}{\partial {r_{ij}}^2}\cdot\left(\frac{dr_{ij}}{de}\right)^2\cdot\left(\frac{d\varepsilon}{dV_i}\right)^2\Big|_0+\frac{\partial\psi(r_{ij})}{\partial r_{ij}}\cdot\left(\frac{d}{dV_i}\frac{dr_{ij}}{de}\right)\cdot\frac{de}{dV_i}\Big|_0 + \frac{\partial\psi(r_{ij})}{\partial r_{ij}}\cdot\frac{dr_{ij}}{de}\cdot\frac{d^2e}{{dV_i}^2}\Big|_0\right\}$$

$$= -\frac{V_i^0}{2}\left[\sum_{j\neq i}\psi(r_{ij})\right]^{-1/2}\sum_{j\neq i}\left\{\frac{\partial^2\psi(r_{ij})}{\partial {r_{ij}}^2}\Big|_0\cdot\left(-r_{ij}^0\right)^2\cdot\left(-\frac{1}{3V_i^0}\right)^2+\frac{\partial\psi(r_{ij})}{\partial r_{ij}}\Big|_0\cdot 0\cdot\left(-\frac{1}{3V_i^0}\right)+\frac{\partial\psi(r_{ij})}{\partial r_{ij}}\Big|_0\cdot\left(-r_{ij}^0\right)\cdot\left(\frac{2}{9{V_i^0}^2}\right)\right\}$$

$$= -\frac{V_i^0}{2}\cdot\frac{1}{9{V_i^0}^2}\left[\sum_{j\neq i}\psi(r_{ij})\right]^{-1/2}\sum_{j\neq i}\left\{{r_{ij}^0}^2\cdot\frac{\partial^2\psi(r_{ij})}{\partial {r_{ij}}^2}\Big|_0-2r_{ij}^0\cdot\frac{\partial\psi(r_{ij})}{\partial r_{ij}}\Big|_0\right\}$$

$$= -\frac{1}{18V_i^0}\left[\sum_{j\neq i}\psi(r_{ij})\right]^{-1/2}\sum_{j\neq i}\left\{{r_{ij}^0}^2\cdot\frac{\partial^2\psi(r_{ij})}{\partial {r_{ij}}^2}\Big|_0-2r_{ij}^0\cdot\frac{\partial\psi(r_{ij})}{\partial r_{ij}}\Big|_0\right\} \qquad (C.44)$$

By combining the equations C.38, C.41, C.43 and C.44, the bulk modulus is proven to be related with the pressure of the system as follows

$$B = B^{RL} + B^{AL} + \frac{2}{3}p \qquad (C.45)$$

where

$$B^{RL} = \frac{1}{9V_i^0}\sum_{j\neq i}{r_{ij}^0}^2\cdot\frac{\partial^2\varphi(r_{ij})}{\partial {r_{ij}}^2}\Big|_0$$

and

$$B^{AL} = \frac{1}{36V_i^0}\left[\sum_{j\neq i}\psi(r_{ij})\right]^{-3/2}\left[\sum_{j\neq i}r_{ij}^0\cdot\frac{\partial\psi(r_{ij})}{\partial r_{ij}}\Big|_0\right]^2-\frac{1}{18V_i^0}\left[\sum_{j\neq i}\psi(r_{ij})\right]^{-1/2}\sum_{j\neq i}{r_{ij}^0}^2\cdot\frac{\partial^2\psi(r_{ij})}{\partial {r_{ij}}^2}\Big|_0$$

Appendix D: Crack configuration in anisotropic media

D.1. Fundamental equations of linear elasticity [LOV1944, SIH1968, HIR1982]

This appendix focuses on the mathematical analysis of mode-I crack 2D-displacement field in an ideally homogeneous anisotropic medium. This relies on the fundamental equations of the classical linear elasticity [LOV1944, HIR1982]. In a Cartesian coordinate system, with x, y, z (or x_i where $i = 1,2,3$) the orthogonal coordinates, the state of stress of at a point inside an elastic body is defined by the Cauchy stress tensor:

$$\sigma = \begin{bmatrix} \sigma_{11} & \sigma_{12} & \sigma_{13} \\ \sigma_{21} & \sigma_{22} & \sigma_{23} \\ \sigma_{31} & \sigma_{32} & \sigma_{33} \end{bmatrix} = \begin{bmatrix} \sigma_{xx} & \sigma_{xy} & \sigma_{xz} \\ \sigma_{yx} & \sigma_{yy} & \sigma_{yz} \\ \sigma_{zx} & \sigma_{zy} & \sigma_{zz} \end{bmatrix} \quad (D.1)$$

where σ_{ij} (with $i, j = 1,2,3$ or x, y, z) denotes the component of stress acting on the jth-plane of an infinitesimal volume element and parallel to the i direction, as illustrated on figure D.1. Under mechanical equilibrium, in each infinitesimal volume element inside the body the following relation holds:

$$\sigma_{ij} = \sigma_{ji} (i, j = 1,2,3) \quad (D.2)$$

Additionally, in absence of net force acting on the element, the following relation applies:

$$\frac{\partial \sigma_{1i}}{\partial x_i} + \frac{\partial \sigma_{2i}}{\partial x_2} + \frac{\partial \sigma_{3i}}{\partial x_3} + f_i = 0, \ \ (i = 1,2,3) \quad (D.3)$$

where f_i is the i-th component of the body force per unit volume constituting the equations of classical elasticity. Under stress the body deforms with displacement components, u_i $(i = 1,2,3)$. The corresponding symmetric strains are given by:

$$\varepsilon_{ij} = \frac{1}{2}\left(\frac{\partial u_i}{\partial x_j} + \frac{\partial u_j}{\partial x_i}\right), (i, j = 1,2,3) \quad (D.4)$$

For convention, the shear strains components (i.e. $i \neq j$) given by equation D.4 are the half of the shear strains γ_{ij} defined in engineering:

$$\gamma_{ij} = 2\varepsilon_{ij}, \ \ (i \neq j) \quad (D.5)$$

Accordingly, rigid rotation components are:

$$\omega_{ij} = \frac{\partial u_i}{\partial x_j} - \frac{\partial u_j}{\partial x_i}, (i,j = 1,2,3) \qquad (D.6)$$

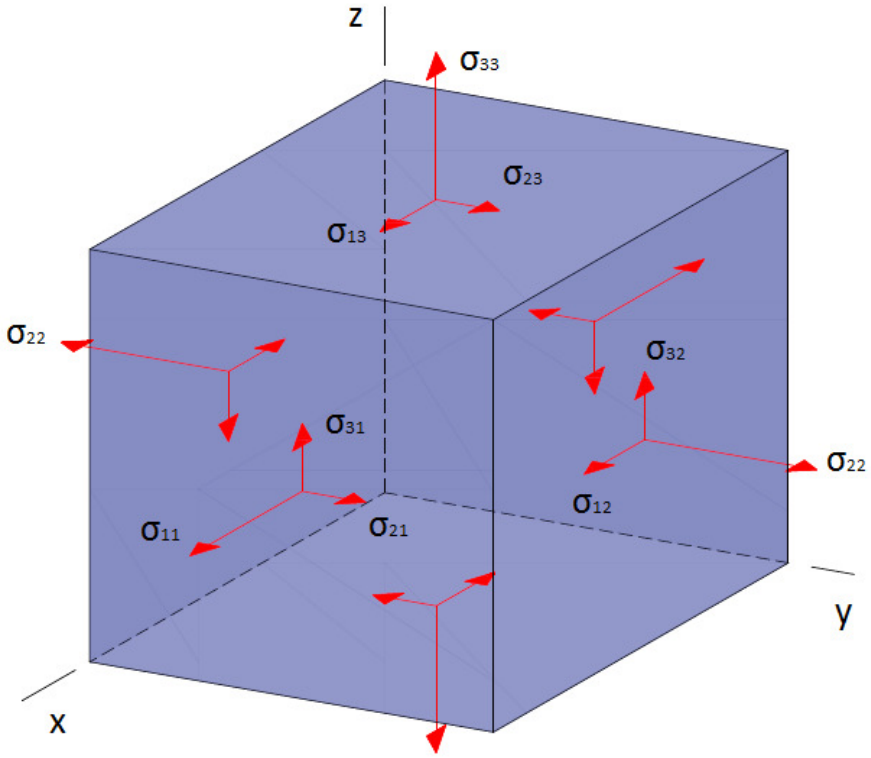

Figure D.1: Stress distribution on an infinitesimal volume element [HIR1982].

Equations D.3, D.4 and D.6 hold for small (elastic) displacements and form the starting point of the linear theory of elasticity. Under this approximation, the stress components are linearly related to the strain components, leading to the generalized Hooke's law:

$$\sigma_{ij} = \sum_{k=1}^{3}\sum_{l=1}^{3} C_{ijkl}\varepsilon_{kl}\,, (i,j = 1,2,3) \qquad (D.7)$$

The coefficients C_{ijkl} are the elastic constants of the elastic body. Now, since $\sigma_{ij} = \sigma_{ji}$ and $\varepsilon_{kl} = \varepsilon_{lk}(i,j,k,l = 1,2,3)$,

$$C_{ijkl} = C_{jikl} = C_{ijlk} = C_{jilk} \qquad (D.8)$$

Considering the strain energy, the work done by stresses σ_{ij} on an element of unit volume deforming it reversible by differential strain increments $d\varepsilon_{ij}$, expressed with,

$$dw = \sigma_{ij}d\varepsilon_{ij} = \sum_{k=1}^{3}\sum_{l=1}^{3} C_{ijkl}\varepsilon_{kl}d\varepsilon_{ij}, \quad (i,j,k,l = 1,2,3) \qquad (D.9)$$

For an isothermal and reversible deformation, the differential work of the element is equal to the differential change in Helmholtz free energy:

$$dw = dF \qquad (D.10)$$

Thus, the stress components are given by:

$$\sigma_{ij} = \frac{\partial F}{\partial \varepsilon_{ij}} = \frac{\partial w}{\partial \varepsilon_{ij}} \qquad (D.11)$$

and the elastic constants of stiffness

$$C_{ijkl} = \frac{\partial^2 F}{\partial \varepsilon_{ij} \partial \varepsilon_{kl}} = \frac{\partial^2 w}{\partial \varepsilon_{ij} \partial \varepsilon_{kl}} = \frac{\partial \sigma_{ij}}{\partial \varepsilon_{ij}} \qquad (D.12)$$

Since F is a state function and dF is a perfect differential, the order of the differentiation in equation D.12 is irrelevant, which implies:

$$C_{ijkl} = C_{klij} \qquad (D.13)$$

By integrating the equation D.9, the density of the strain energy of the element is given analytically by:

$$w = \frac{1}{2} \sum_{k=1}^{3} \sum_{l=1}^{3} C_{ijkl} \varepsilon_{kl} \varepsilon_{ij}, \quad (i,j = 1,2,3) \qquad (D.14)$$

The generalized Hooke's law (equation D.7) can also be expressed in terms of matrices, by using the following notation:

$$\begin{matrix} (kl) \rightarrow \\ \{\sigma_{ij}\} = (ij)\{C_{ijkl}\}\{\varepsilon_{kl}\}, \\ \downarrow \end{matrix} \qquad (i,j,k,l = 1,2,3) \qquad (D.15)$$

where the $\{C_{ijkl}\}$ is a symmetric 9×9 matrix relating the nine stress elements σ_{ij} to the nine strain elements ε_{kl}. Moreover, the elastic constants can also be written in a contracted matrix notation C_{mn}, given by Voigt [VOI1966], where each of the index m and n corresponds to a pair of indices ij or kl, according to the following reduction:

$$\begin{array}{cccccccccc} ij\ or\ kl = & 11 & 22 & 33 & 23 & 31 & 12 & 32 & 13 & 21 \\ \Downarrow & \Downarrow & \Downarrow & \Downarrow & \Downarrow & \Downarrow & \Downarrow & \Downarrow & \Downarrow & \Downarrow \\ m\ or\ n = & 1 & 2 & 3 & 4 & 5 & 6 & 7 & 8 & 9 \end{array} \qquad (D.16)$$

As indicated by equations D.8 and D.13, from the 81 elastic constants in C_{mn} only 21 are independent [KIT2004]. Hence, equation D.15 gives,

$$\begin{bmatrix} \sigma_{11} \\ \sigma_{22} \\ \sigma_{33} \\ \sigma_{23} \\ \sigma_{31} \\ \sigma_{12} \\ \sigma_{32} \\ \sigma_{13} \\ \sigma_{21} \end{bmatrix} = \begin{bmatrix} C_{11} & C_{12} & C_{13} & C_{14} & C_{15} & C_{16} & C_{14} & C_{15} & C_{16} \\ C_{12} & C_{22} & C_{23} & C_{24} & C_{25} & C_{26} & C_{24} & C_{25} & C_{26} \\ C_{13} & C_{23} & C_{33} & C_{34} & C_{35} & C_{36} & C_{34} & C_{35} & C_{36} \\ C_{14} & C_{14} & C_{34} & C_{44} & C_{45} & C_{46} & C_{44} & C_{45} & C_{46} \\ C_{15} & C_{25} & C_{35} & C_{54} & C_{55} & C_{56} & C_{54} & C_{55} & C_{56} \\ C_{16} & C_{26} & C_{36} & C_{64} & C_{65} & C_{66} & C_{64} & C_{65} & C_{66} \\ C_{14} & C_{14} & C_{34} & C_{44} & C_{45} & C_{46} & C_{44} & C_{45} & C_{46} \\ C_{15} & C_{25} & C_{35} & C_{54} & C_{55} & C_{56} & C_{54} & C_{55} & C_{56} \\ C_{16} & C_{26} & C_{36} & C_{64} & C_{65} & C_{66} & C_{64} & C_{65} & C_{66} \end{bmatrix} \begin{bmatrix} \varepsilon_{11} \\ \varepsilon_{22} \\ \varepsilon_{33} \\ \varepsilon_{23} \\ \varepsilon_{31} \\ \varepsilon_{12} \\ \varepsilon_{32} \\ \varepsilon_{13} \\ \varepsilon_{21} \end{bmatrix} \qquad (D.17)$$

Symmetry considerations lead to the following reduced form:

$$\begin{bmatrix} \sigma_{11} \\ \sigma_{22} \\ \sigma_{33} \\ \sigma_{23} \\ \sigma_{31} \\ \sigma_{12} \end{bmatrix} = \begin{bmatrix} C_{11} & C_{12} & C_{13} & C_{14} & C_{15} & C_{16} \\ C_{12} & C_{22} & C_{23} & C_{24} & C_{25} & C_{26} \\ C_{13} & C_{23} & C_{33} & C_{34} & C_{35} & C_{36} \\ C_{14} & C_{14} & C_{34} & C_{44} & C_{45} & C_{46} \\ C_{15} & C_{25} & C_{35} & C_{54} & C_{55} & C_{56} \\ C_{16} & C_{26} & C_{36} & C_{64} & C_{65} & C_{66} \end{bmatrix} \begin{bmatrix} \varepsilon_{11} \\ \varepsilon_{22} \\ \varepsilon_{33} \\ \gamma_{23} \\ \gamma_{31} \\ \gamma_{12} \end{bmatrix} \qquad (D.18)$$

The 6×6 and 9×9 representations express the same C_{mn} occurring in the matrix. Therefore, there is symmetry along the diagonal also for the 6×6 matrix. It is noteworthy that γ_{ij} is used for shear strains in the reduce scheme instead of the ε_{ij} values. The Voigt notation can also be used to denote the strain and stress components:

$$\begin{bmatrix} \sigma_1 \\ \sigma_2 \\ \sigma_3 \\ \sigma_4 \\ \sigma_5 \\ \sigma_6 \end{bmatrix} = \begin{bmatrix} \sigma_{11} \\ \sigma_{22} \\ \sigma_{33} \\ \sigma_{23} \\ \sigma_{31} \\ \sigma_{12} \end{bmatrix} \text{ and } \begin{bmatrix} \varepsilon_1 \\ \varepsilon_2 \\ \varepsilon_3 \\ 2\varepsilon_4 \\ 2\varepsilon_5 \\ 2\varepsilon_6 \end{bmatrix} = \begin{bmatrix} \varepsilon_{11} \\ \varepsilon_{22} \\ \varepsilon_{33} \\ \gamma_{23} \\ \gamma_{31} \\ \gamma_{12} \end{bmatrix} \qquad (D.19)$$

for the reduced 6×6 scheme. Alternatively, one may express the strain components as a linear combination of the stress components,

$$\varepsilon_{ij} = \sum_{k=1}^{3} \sum_{l=1}^{3} S_{ijkl} \sigma_{kl}\,, (i, j = 1,2,3) \qquad (D.20)$$

giving rise to the inverse form of the Hooke's law. In this case, $\{S_{ijkl}\}$ is called the elastic compliance tensor and its elements are called compliances. Similarly to equation D.18, the inverse Hooke's law tensional form can be also expressed with the reduce 6×6 scheme:

$$\begin{bmatrix} \varepsilon_{11} \\ \varepsilon_{22} \\ \varepsilon_{33} \\ \gamma_{23} \\ \gamma_{31} \\ \gamma_{12} \end{bmatrix} = \begin{bmatrix} S_{11} & S_{12} & S_{13} & S_{14} & S_{15} & S_{16} \\ S_{12} & S_{22} & S_{23} & S_{24} & S_{25} & S_{26} \\ S_{13} & S_{23} & S_{33} & S_{34} & S_{35} & S_{36} \\ S_{14} & S_{14} & S_{34} & S_{44} & S_{45} & S_{46} \\ S_{15} & S_{25} & S_{35} & S_{54} & S_{55} & S_{56} \\ S_{16} & S_{26} & S_{36} & S_{64} & S_{65} & S_{66} \end{bmatrix} \begin{bmatrix} \sigma_{11} \\ \sigma_{22} \\ \sigma_{33} \\ \sigma_{23} \\ \sigma_{31} \\ \sigma_{12} \end{bmatrix} \qquad (D.21)$$

According to equations D.18 and D.21, the elastic coefficient tensors $\{C_{ijkl}\}$ and $\{S_{ijkl}\}$ have the same symmetry and are related by the expression

$$\sum_{k=1}^{3} \sum_{l=1}^{3} C_{ijkl} S_{klmn} = I_{ijmn}, (i, j, m, n = 1,2,3) \qquad (D.22)$$

where I is a fourth-rank identify tensor. The elastic coefficients C and S are assumed to be position-independent inside the elastic body. Hence, these coefficients are constant for a given coordinate system and such a body is considered elastically homogeneous.

D.2. Plane Stress and Plane Strain deformation [SIH1968]

Concerning the crack problem, it is pertinent to reduce the number of equations in relations D.18 and D.21 for simplicity. The most convenient approach is the assumption of certain stress and strain states leading to the plane crack problem. These are the plane stress and plane strain deformation states. The ''plane stress'' state in an elastic body is defined by the conditions:

$$\sigma_{zz} = \sigma_{yz} = \sigma_{zx} = 0$$

$$\sigma_{xx} = \sigma_{xx}(x, y),\ \sigma_{yy} = \sigma_{yy}(x, y),\ \sigma_{xy} = \sigma_{xy}(x, y) \qquad (D.23)$$

This loading mode corresponds to a thin flat plate with major dimensions in the xy coordinate plane and with stress-free surfaces normal to the z direction. Under this condition, the in-plane strain components depend solely from the in-plane stresses:

$$\varepsilon_{xx} = S_{11}\sigma_{xx} + S_{12}\sigma_{yy} + S_{16}\sigma_{xy}$$

$$\varepsilon_{yy} = S_{12}\sigma_{xx} + S_{22}\sigma_{yy} + S_{26}\sigma_{xy} \qquad (D.24)$$

$$\gamma_{xy} = 2\varepsilon_{xy} = S_{16}\sigma_{xx} + S_{26}\sigma_{yy} + S_{66}\sigma_{xy}$$

Similarly, an elastic body is in ''plane strain'' state, i.e. $\varepsilon_{zz} = \gamma_{yz} = \gamma_{zx} = 0$, if the displacement components satisfy:

$$u_x = u_x(x,y),\ u_y = u_y(x,y),\ u_z = 0 \qquad (D.25)$$

Such deformation mode corresponds to that of a long cylindrical body, with axial the z direction, and loaded uniformly on the xy plane. In this case, Hooke's law reads:

$$\sigma_{yz} = \sigma_{zx} = 0, \quad \sigma_{zz} = -(S_{33})^{-1}\left(S_{13}\sigma_{xx} + S_{23}\sigma_{yy} + S_{26}\sigma_{xy}\right) \qquad (D.26)$$

and:

$$\varepsilon_{xx} = b_{11}\sigma_{xx} + b_{12}\sigma_{yy} + b_{16}\sigma_{xy}$$

$$\varepsilon_{yy} = b_{21}\sigma_{xx} + b_{22}\sigma_{yy} + b_{26}\sigma_{xy} \qquad (D.27)$$

$$\gamma_{xy} = 2\varepsilon_{xy} = b_{61}\sigma_{xx} + b_{62}\sigma_{yy} + b_{66}\sigma_{xy}$$

where the constants b_{ij} are given by:

$$b_{11} = \frac{S_{11}S_{33} - S_{13}^2}{S_{33}}, \qquad b_{12} = b_{21} = \frac{S_{12}S_{33} - S_{13}S_{23}}{S_{33}}$$

$$b_{22} = \frac{S_{22}S_{33} - S_{23}^2}{S_{33}}, \qquad b_{16} = b_{61} = \frac{S_{16}S_{33} - S_{13}S_{36}}{S_{33}} \qquad (D.28)$$

$$b_{66} = \frac{S_{66}S_{33} - S_{36}^2}{S_{33}}, \qquad b_{26} = b_{62} = \frac{S_{26}S_{33} - S_{23}S_{36}}{S_{33}}$$

Hence, the stress-strain relationship for the general plane problem can be formulated in terms of compliance coefficients as:

$$\begin{pmatrix} \varepsilon_{xx} \\ \varepsilon_{yy} \\ \gamma_{xy} \end{pmatrix} = \begin{bmatrix} a_{11} & a_{12} & a_{16} \\ a_{12} & a_{22} & a_{26} \\ a_{16} & a_{26} & a_{66} \end{bmatrix} \begin{pmatrix} \sigma_{xx} \\ \sigma_{yy} \\ \tau_{xy} \end{pmatrix} \qquad (D.29)$$

where, $a_{ij} = S_{ij}$ for plane stress and $a_{ij} = b_{ij} = S_{ij} - S_{i3}S_{3j}/S_{33}$ for plane strain deformation mode. Due to the diagonal symmetry of the compliance matrix there are six

independent constants in total. A comparison between the equations D.24 and D.27 reveals that they are of the same type. Hence, if the constants S_{ij} everywhere replace b_{ij}, then the solution found for any case of plane stress state will be the solution for the corresponding case of a plane strain state. As an arbitrary choice, the constants a_{ij} will be used in the following analysis. By applying the plane stress or plane strain approximation into the strain energy density function given by:

$$w = \frac{1}{2}\left(\sigma_{xx}\varepsilon_{xx} + \sigma_{yy}\varepsilon_{yy} + \sigma_{zz}\varepsilon_{zz} + \sigma_{yz}\gamma_{yz} + \sigma_{zx}\gamma_{zx} + \sigma_{xy}\gamma_{xy}\right) \qquad (D.30)$$

it can be proven that the products of the components,

$$\sigma_{xz}\left(\frac{\partial u_x}{\partial z} + \frac{\partial u_z}{\partial x}\right), \sigma_{yz}\left(\frac{\partial u_y}{\partial z} + \frac{\partial u_z}{\partial y}\right), \sigma_{zz}\frac{\partial u_z}{\partial z} \qquad (D.31)$$

are equal to zero [LOV1944]. Hence, the total amount of strain energy stored in an elastic body, under plane stress or plane strain deformation, is given by,

$$W = \iiint_D w = \frac{1}{2}\iint_D \left[\sigma_{xx}\frac{\partial u_x}{\partial x} + \sigma_{yy}\frac{\partial u_y}{\partial y} + \sigma_{xy}\left(\frac{\partial u_y}{\partial x} + \frac{\partial u_x}{\partial y}\right)\right] dS \qquad (D.32)$$

where the number of integrals refers to the different dimensions and dS is the integral for the two-dimensional plate surface. Consequently, the equations of equilibrium in the absence of body forces are become:

$$\frac{\partial \sigma_{xx}}{\partial x} + \frac{\partial \sigma_{xy}}{\partial y} = 0 \qquad (D.33a)$$

$$\frac{\partial \sigma_{xy}}{\partial x} + \frac{\partial \sigma_{yy}}{\partial y} = 0 \qquad (D.33b)$$

where the in-plane xy components of stress depends solely on x and y coordinates of the system.

D.3. Plane crack problem in a homogeneous anisotropic elastic body

The equilibrium conditions, given in equations D.33, constitute the ''mathematical cornerstone'' of the central crack 2D-problem in an anisotropic homogeneous medium under plane stress or plane strain conditions (figure D.2).

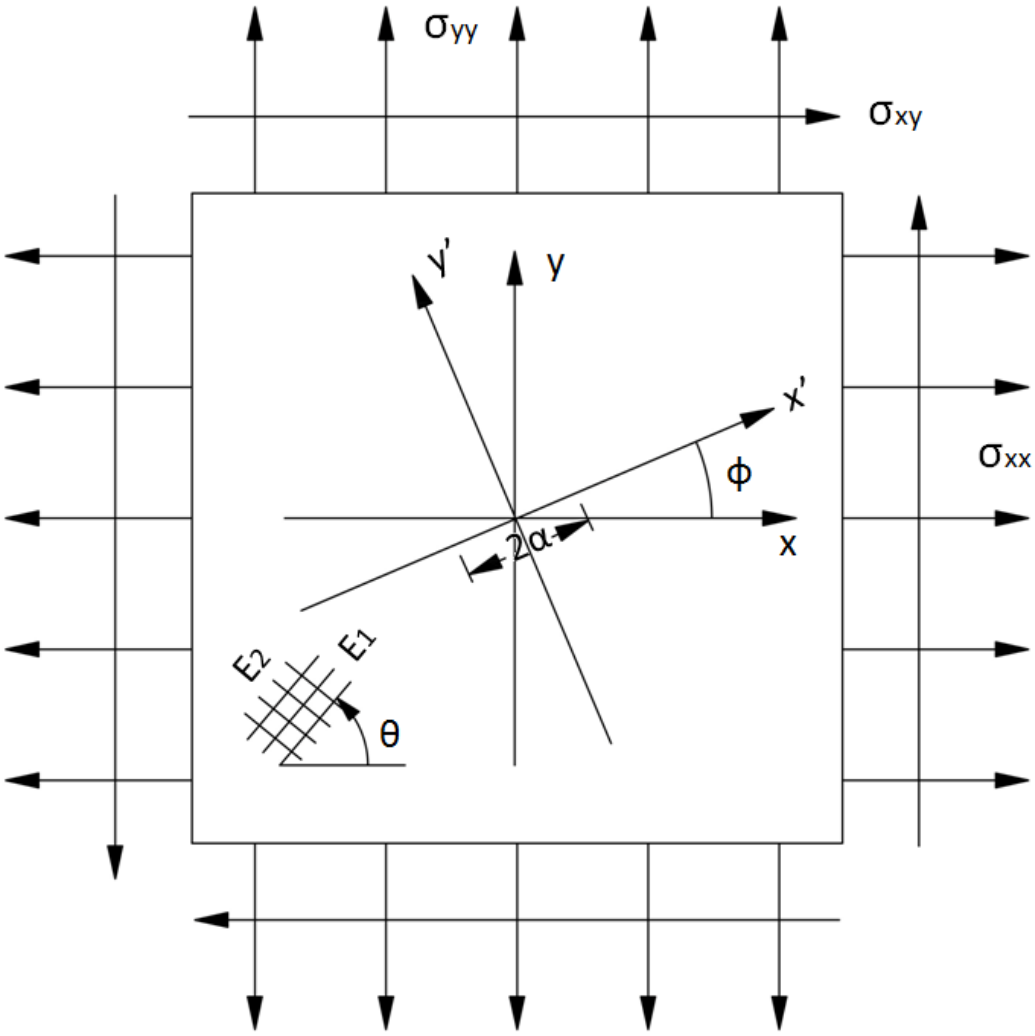

Figure D.2: Two-dimensional anisotropic plate with a crack configuration with half-length equal to a. θ is the angle between the coordinate axes (the directions of x and y) and the elasticity axes (the directions of E_1 and E_2). φ is the angle between the coordinate axes and the crack orientation axes (the directions of crack length x' and crack plane y') [SUN2003].

Equations D.33 can be satisfied if the following definition of stress function $U(x, y)$ is introduced:

$$\sigma_{xx} = \frac{\partial^2 U}{\partial y^2}, \qquad \sigma_{yy} = \frac{\partial^2 U}{\partial x^2}, \qquad \sigma_{xy} = -\frac{\partial^2 U}{\partial x \partial y} \tag{D.34}$$

a function that depends on both material properties and applied loading conditions. By substituting the ε_{xx}, ε_{yy}, γ_{xy} expressions from the stain-stress relations (equation D.29) and the σ_{xx}, σ_{yy}, σ_{xy} components, according to equations D.34, in the compatibility equation

$$\frac{\partial^2 \varepsilon_{xx}}{\partial y^2} + \frac{\partial^2 \varepsilon_{yy}}{\partial x^2} - \frac{\partial^2 \gamma_{xy}}{\partial x \partial y} = 0 \tag{D.35}$$

the governing differential equation of the plane problem of the anisotropic elasticity is obtained:

$$a_{22}\frac{\partial^4 U}{\partial x^4} - 2a_{26}\frac{\partial^4 U}{\partial x^3 \partial y} + (2a_{12} + a_{66})\frac{\partial^4 U}{\partial x^2 \partial y^2} - 2a_{16}\frac{\partial^4 U}{\partial x \partial y^3} + a_{11}\frac{\partial^4 U}{\partial y^4} = 0 \quad (D.36)$$

This equation can also be formulated in terms of differential operators:

$$D_1 D_2 D_3 D_4 U(x, y) = 0 \quad (D.37)$$

where,

$$D_j = \left(\frac{\partial}{\partial y} - \mu_j \frac{\partial}{\partial x}\right), \quad (j = 1,2,3,4) \quad (D.38)$$

and μ_i are the roots solution of the characteristic equation:

$$a_{11}\mu_j^4 - 2a_{16}\mu_j^3 + (2a_{12} + a_{66})\mu_j^2 - 2a_{26}\mu_j + a_{22} = 0 \quad (D.39)$$

Lekhnitskii [LEK1963], proved that equation D.39 could have either complex, or purely imaginary roots but could not have real roots in the case of any ideal elastic body. The following special conditions represent the only exceptions in this argument and will be excluded in future consideration:

(i) $a_{22} = a_{26} = 0,$

(ii) $a_{22} = a_{26} = 2a_{12} + a_{66} = a_{16} = 0,$

(iii) $a_{11} = a_{16} = 0,$

(iv) $a_{11} = a_{16} = 2a_{12} + a_{66} = a_{26} = 0$

It is noted that in the first two cases two and all four roots, respectively, are equal to zero. Additionally for the remaining cases, two or all four roots diverge. Therefore, the general form of the characteristic roots can be denoted as,

$$\mu_1 = a_1 + i\beta_1, \qquad \mu_2 = a_2 + i\beta_2,$$

$$\mu_3 = \bar{\mu}_1 = a_1 - i\beta_1, \qquad \mu_4 = \bar{\mu}_2 = a_2 - i\beta_2 \quad (D.40)$$

The quantities of μ_1 and μ_2 are called the complex parameters of the first order of plane stress or, plane strain respectively. Complex parameters are numbers that describe the anisotropy of an elastic body oriented along a given coordinate system and can be used to quantify its effect on mechanical plane problems. According to their values it can be evaluated how much a given body departs from isotropy, for which the μ_1 and μ_2 are equal to i.

D.4. Classification of the Complex Parameters [SUN2003]

Sun [SUN2003] has demonstrated that the roots solution of the characteristic equation D.39 can be grouped into four fundamental cases based upon different material properties:

Case I: The real parts of the roots are all equal to zero, and the imaginary parts are unequal ($a_1 = a_2 = 0,\ \beta_1 \neq \beta_2$)

Case II: The real parts of the roots are all equal to zero, and the imaginary parts are equal ($a_1 = a_2 = 0,\ \beta_1 = \beta_2$)

Case III: The real parts of the roots are negative and the imaginary parts are equal ($a_1 = -a_2 = 0,\ \beta_1 = \beta_2$)

For the above three cases, all the material systems are orthotropic and the directions of the axes x and y coincide with the principal directions of elasticity (directions of E_1 and E_2). Orthotropic problems are illustrated in figures D.2 and D.3(a) where the angles, $|\theta - \varphi| = 0°$ or $90°$.

Case IV: Both the real and the imaginary parts of the complex roots differ ($a_1 \neq a_2$, $\beta_1 \neq \beta_2$).

The case IV is obtained when principal directions of elasticity are not aligned with the directions of the axes x and y, or $|\theta - \varphi| \neq 0°$ or $90°$ as illustrated on figures D.2 and D.3(b).

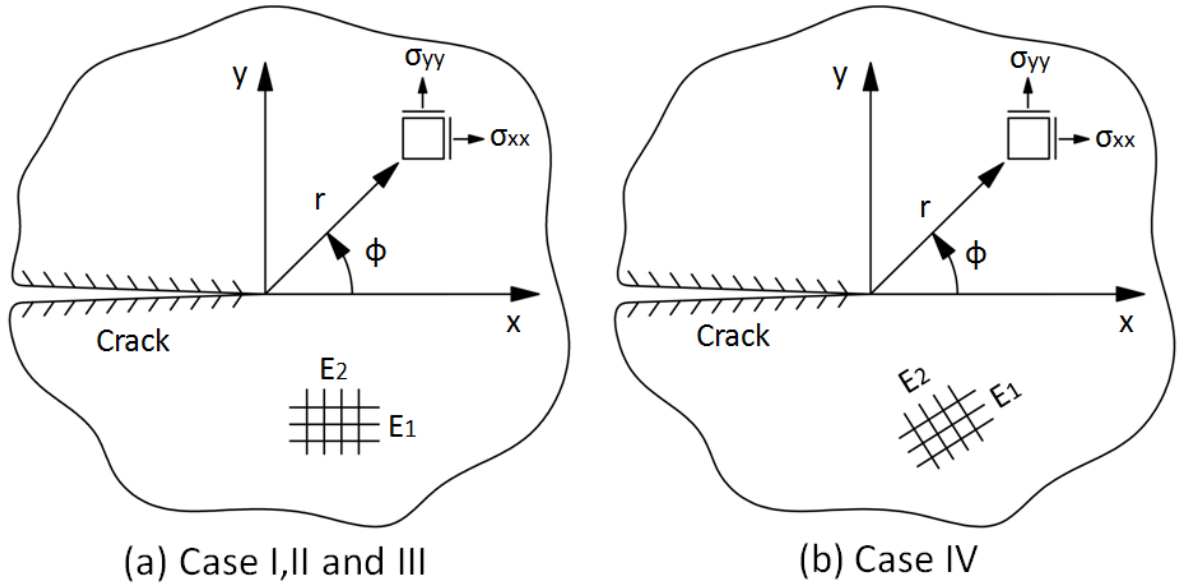

Figure D.3: Classification of problems concerned. The directions of E_1 and E_2coincide with the principal directions of elasticity [SUN2003].

Moreover, with reference to the characteristic equation D.39 orthotropic problems (cases I, II and III) imply that $a_{16} = a_{26} = 0$. Denoting as a_{ij} the no zero compliance terms in the orthotropic case, equation D.39 can be simplified as:

$$x_i^2 + \frac{2a_{12} + a_{66}}{a_{11}} x_i + \frac{a_{22}}{a_{11}} = 0 \qquad (D.41)$$

where $x_i = \mu_i^2$. The different solutions of the above second-order equation are given by:

$$x_{1,2} = -\frac{2a_{12} + a_{66}}{2a_{11}} \pm \sqrt{\left[\frac{2a_{12} + a_{66}}{2a_{11}}\right]^2 - \frac{a_{22}}{a_{11}}} \qquad (D.42)$$

Introducing the notations of $A = (2a_{12} + a_{66})/2a_{11}$ and $B = a_{22}/a_{11}$, solutions are obtained by:

$$x_{1,2} = -A \pm \sqrt{A^2 - B} \Rightarrow \mu_j = \pm\sqrt{-A \pm \sqrt{A^2 - B}}\,, (j = 1,2,3,4) \qquad (D.43)$$

Hence, the three cases of orthotropic crack problems can be found by the different relations between A and B, and the corresponding roots μ_1 and μ_2 for each case can be written explicitly as follows,

Case I: when $A^2 - B > 0$,

$$\mu_1 = i\sqrt{A + \sqrt{A^2 - B}} \text{ and } \mu_2 = i\sqrt{A - \sqrt{A^2 - B}} \qquad (D.44)$$

Case II: when $A^2 - B = 0$,

$$\mu_1 = \mu_2 = i\sqrt{\sqrt{A}} \qquad (D.45)$$

Case III: when $A^2 - B < 0$,

$$\mu^2 = -A \pm i\sqrt{B - A^2}$$

$$\mu_1 = \sqrt{-A \pm \sqrt{B - A^2}} = a_1 + i\beta_1 \text{ and } \mu_2 = -a_1 + i\beta_1 \qquad (D.46)$$

Case IV refers to a random geometric orientation between the elasticity axes and the coordinate axes on the xy plane (figure D.3b). In such a case, coordinate system and the elasticity axes do not coincide with each other; hence equation D.39 will be a fourth order equation. To avoid dealing with such complex equation, Lekhnitskii [LEK1968] has been show that a simple transformation formula can be used to obtain the complex parameters in the coordinate system of $x'oy'$ from those in xoy corresponding to an orthotropic case (figure D.4). In particular, the complex roots of the coordinate system of $x'oy'$ can be expressed as:

$$\mu_1' = \frac{\mu_1 \cos\theta - \sin\theta}{\cos\theta + \mu_1 \sin\theta}, \qquad \mu_2' = \frac{\mu_2 \cos\theta - \sin\theta}{\cos\theta + \mu_2 \sin\theta} \qquad (D.47)$$

where μ_1 and μ_2 are the corresponding complex parameters in the xoy and can be obtain from equations D.44 to D.46.

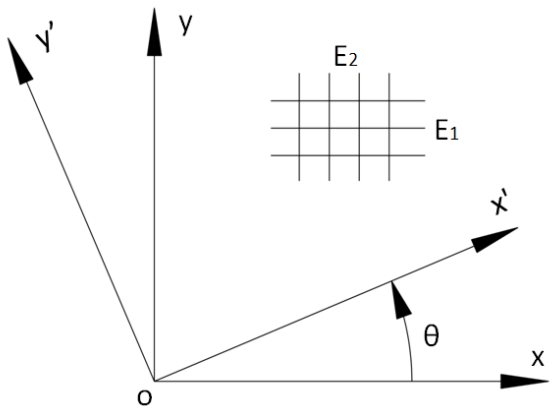

Figure D.4: The complex parameters in two coordinates. The directions of E_1 and E_2coincide with the principal directions of elasticity [SUN2003].

The classification of the four cases of anisotropic plane problems, in terms of different type of complex parameters, is summarized in Table D.1.

Table D.1: Classification of anisotropic crack problems based on the complex parameters [SUN2003]

Case	Orientation of elasticity axes	Coefficients of the compliance matrix	The complex parameters
I	Orthotropy and coincident with the coordinate axis $\lvert\theta-\varphi\rvert = 0°$ or $90°$	$a_{11}, a_{22}, a_{66}, a_{12} \neq 0$ $a_{16} = a_{26} = 0$	$\mu_1 = i\sqrt{A+\sqrt{A^2-B}} = i\beta_1\mu_2 = i\sqrt{A-\sqrt{A^2-B}} = i\beta_2$
II			$\mu_1 = i\sqrt{\sqrt{A}} = i\beta$ $\mu_2 = \mu_1$
III			$\mu_1 = \sqrt{-A \pm \sqrt{B-A^2}} = \alpha + i\beta$ $\mu_2 = -\alpha + i\beta$
IV	Orthotropy but not coincident with the coordinate axis $\lvert\theta-\varphi\rvert \neq 0°$ and $90°$	$a_{11}, a_{22}, a_{66}, a_{12}$, $a_{16}, a_{26} \neq 0$	$\mu_1' = \frac{\mu_1\cos\theta - \sin\theta}{\cos\theta + \mu_1\sin\theta} = \alpha_1 + i\beta_1$ $\mu_2' = \frac{\mu_2\cos\theta - \sin\theta}{\cos\theta + \mu_2\sin\theta} = \alpha_2 + i\beta_2$

D.5. Global Interpolation functions [SIH1968, SUN2003]

The general solution of equation D.36 in plane elasticity problems can be written in terms of complex variables z_i. In fact, the four cases of complex parameters can be divided into two main stress function solutions. According to Lekhinitskii [LEK1968], in the case of unequal complex parameters (cases I, III and IV), the stress function $U(x,y)$ defined by equation D.34 should have the following expression:

$$U(x,y) = U_1(z_1) + U_2(z_2) + U_3(z_3) + U_4(z_4)$$

or

$$U(x,y) = U_1(z_1) + U_2(z_2) + U_3(\bar{z}_1) + U_4(\bar{z}_2) \qquad (D.48)$$

where $U_1(z_1)$ and $U_2(z_2)$ are the arbitrary functions of the complex variables:

$$z_1 = x + \mu_1 y \text{ and } z_2 = x + \mu_2 y \qquad (D.49)$$

set by system coordinates x, y and the complex parameter μ_1, μ_2, respectively. As the stress function should be a real function of coordinate components x and y, $U(x,y)$ can be further simplified as:

$$U(x,y) = 2Re[U_1(z_1) + U_2(z_2)] \qquad (D.50)$$

In order to avoid the subscript notation of $U_j(z_j)$, the new sub-functions

$$\varphi(z_1) = dU_1/dz_1 \text{ and } \psi(z_2) = dU_2/dz_2 \qquad (D.51)$$

are introduced. By substituting the stress function from equation D.50 into D.34 and taking into account the relations D.51, the stress components in terms of $\varphi(z_1)$ and $\psi(z_2)$ can be expressed as:

$$\sigma_{xx} = 2Re[\mu_1^2\varphi'(z_1) + \mu_2^2\psi'(z_2)] \qquad (D.52a)$$

$$\sigma_{yy} = 2Re[\varphi'(z_1) + \psi'(z_2)] \qquad (D.52b)$$

$$\sigma_{xy} = -2Re[\mu_1\varphi'(z_1) + \mu_2\psi'(z_2)] \qquad (D.52c)$$

where $\varphi'(z_1) = d\varphi(z_1)/dz_1$ and $\psi'(z_2) = d\psi(z_2)/dz_2$. From equations D.52 and the strain-stress relations (equations D.29), a simple integration gives the displacement components u_x and v_y along the x and y coordinate axes, respectively:

$$u = 2Re[p_1\varphi(z_1) + p_2\psi(z_2)] + rigid\ body\ terms \qquad (D.53a)$$

$$v = 2Re[q_1\varphi(z_1) + q_2\psi(z_2)] + rigid\ body\ terms \qquad (D.53b)$$

where

$$p_k = a_{11}\mu_k^2 + a_{12} - a_{16}\mu_k, (k = 1,2) \qquad (D.54a)$$

and

$$q_k = a_{12}\mu_k + \frac{a_{22}}{\mu_k} - a_{26}, (k = 1,2) \qquad (D.54b)$$

In the rare case of pair-wise equal imaginary parameters (case II), the stress function $U = U(x, y)$ should have the following expression [LEK1968]:

$$U = U_1(z_1) + \bar{z}_1U_2(z_1) + U_3(\bar{z}_1) + z_1U_4(\bar{z}_1) \qquad (D.55)$$

where $z_1 = x + \mu y = x + i\beta y$. It is noted that case II problems differ from isotropic case (where $\mu_1 = \mu_2 = i$ and $z_1 = x + iy$) only by one coefficient on β. By considering that the stress function should be a real function of variables x and y, the case II solution of equation D.34 can be expressed as:

$$U(x,y) = 2Re[U_1(z_1) + \bar{z}_1 U_2(z_1)] \qquad (D.56)$$

The stress components from equations D.34 can thus be written in terms of the stress function as:

$$\sigma_{xx} = -2\beta^2 Re[\varphi'(z_1) - 2\psi(z_1) + \bar{z}_1\psi'(z_1)] \qquad (D.57a)$$

$$\sigma_{yy} = 2Re[\varphi'(z_1) + 2\psi(z_1) + \bar{z}_1\psi'(z_1)] \qquad (D.57b)$$

$$\sigma_{xy} = -2\beta Im\big[\mu\big(\varphi'(z_1) + \bar{z}_1\psi'(z_1)\big)\big] \qquad (D.57c)$$

After integration of the strain-stress equations D.29 combined by equations D.57 the displacements are obtained as:

$$u = 2Re\big[p_1\varphi(z_1) + p_2 U_2(z_1) + p_1\big(\bar{z}_1\psi(z_1) - U_2(z_1)\big)\big] + rigid\ body\ terms \quad (D.58a)$$

$$v = 2Re\big[q_1\varphi(z_1) + q_2 U_2(z_1) + q_1\big(\bar{z}_1\psi(z_1) + U_2(z_1)\big)\big] + rigid\ body\ terms \quad (D.58b)$$

where

$$p_1 = a_{11}\mu^2 + a_{12} = -a_{11}\beta^2 + a_{12},\ \ p_2 = -2a_{11}\mu^2 + 2a_{12} = 2a_{11}\beta^2 + 2a_{12} \quad (D.59a)$$

and

$$q_1 = a_{12}\mu + \frac{a_{22}}{\mu} = i\left(a_{12}\beta - \frac{a_{22}}{\beta}\right), q_2 = -2a_{12}\mu + 2\frac{a_{22}}{\mu} = -i\left(2a_{12}\beta + 2\frac{a_{22}}{\beta}\right) \quad (D.59b)$$

The displacements of equation D.58 can be further formulated as:

$$u = 2m_1 Re[\varphi(z) + \bar{z}\psi(z)] + 2m_2 Re[U_2(z)] + rigid\ body\ terms \qquad (D.60a)$$

$$v = 2n_1 Im[\varphi(z) + \bar{z}\psi(z)] + 2n_2 Im[U_2(z)] + rigid\ body\ terms \qquad (D.60b)$$

where

$$m_1 = -a_{11}\beta^2 + \alpha_{12},\ m_2 = 3a_{11}\beta^2 + \alpha_{12} \qquad (D.61a)$$

and

$$n_1 = -a_{12}\beta + \frac{a_{22}}{\beta},\ n_2 = a_{12}\beta + \frac{3a_{22}}{\beta} \qquad (D.61b)$$

When β equals to unity, it can be proved that the stress and displacement components derived from equations D.57 and D.60 can recover the corresponding isotropic case,

$$\sigma_{xx} + \sigma_{yy} = 8Re[\psi(z_1)] = 4[\psi(z_1) + \bar{\psi}(z_1)] \qquad (D.62)$$

$$\sigma_{xx} - \sigma_{yy} + 2i\sigma_{xy} = 4[\bar{z}_1\psi'(z_1) + \varphi'(z_1)] \qquad (D.63)$$

$$2G(u + iv) = 2[\kappa U_2(z_1) - z_1\bar{\psi}(z_1) - \bar{\varphi}(z_1)] \qquad (D.64)$$

where G is the shear modulus and ν is the Poisson's ratio for the isotropic case and

$$\kappa = \frac{3 - \nu}{1 + \nu} \qquad (D.65)$$

$$\kappa = 3 - 4\nu \qquad (D.66)$$

is the κ factor for the plane stress and plane strain condition, respectively. The plane problem of the anisotropic cracked material is now reduced to the determination of the two complex stress sub-functions $\varphi(z_1)$ and $\psi(z_2)$ that must satisfy the boundary conditions on the contour of the body. The boundary conditions are defining by the loading situation of the body, and namely for the mode I deformation is the uni-axial or bi-axial tension.

D.6. Analytic functions of a horizontal central crack inside an infinite anisotropic plate under uni-axial and bi-axial loading [LIM2001]

In order to determine the analytic function φ and ψ in anisotropic crack problem under uniaxial and biaxial loading, an elliptical hole inside an infinite plate under tension is considered (figure D.5). When an elliptical hole in a plate is subjected to uni-axial tension at an angle α in respect to the x-axis, the analytic stress functions are given according Savin [SAV1961] as follows:

$$\varphi^{(\alpha)}(z_1) = \varphi_0^{(\alpha)}(z_1) + B^{*(\alpha)}z_1 \qquad (D.67a)$$

$$\psi^{(\alpha)}(z_2) = \psi_0^{(\alpha)}(z_2) + \left[B'^{*(\alpha)} + iC'^{*(\alpha)}\right]z_2 \qquad (D.67b)$$

where $\varphi_0^{(\alpha)}(z_1)$, $\psi_0^{(\alpha)}(z_2)$, $B^{*(\alpha)}$, $B'^{*(\alpha)}$, and $C'^{*(\alpha)}$ are defined as:

$$\varphi_0^{(\alpha)}(z_1) = -\frac{i\sigma^{\infty}(a - is_1b)}{4(s_1 - s_2)}\left\{\frac{b(s_2 sin2\alpha + 2cos^2\alpha)}{z_1 + \sqrt{z_1^2 - (a^2 + s_1^2b^2)}} + \frac{ia(2s_2 sin^2\alpha + sin2\alpha)}{z_1 + \sqrt{z_1^2 - (a^2 + s_1^2b^2)}}\right\} (D.68a)$$

$$\psi_0^{(\alpha)}(z_2) = \frac{i\sigma^{\infty}(a - is_2 b)}{4(s_1 - s_2)}\left\{\frac{b(s_1 sin2\alpha + 2cos^2\alpha)}{z_2 + \sqrt{z_2^2 - (a^2 + s_2^2 b^2)}} + \frac{ia(2s_1 sin^2\alpha + sin2\alpha)}{z_2 + \sqrt{z_2^2 - (a^2 + s_2^2 b^2)}}\right\} \quad (D.68b)$$

$$B^{*(\alpha)} = \sigma^{\infty}\frac{cos^2\alpha + (\alpha_2^2 + \beta_2^2)sin^2\alpha + \alpha_2 sin2\alpha}{2[(\alpha_2 - \alpha_1)^2 + (\beta_2 - \beta_1)^2]} \quad (D.68c)$$

$$B'^{*(\alpha)} = \sigma^{\infty}\frac{[(\alpha_1^2 - \beta_1^2) - 2\alpha_1\alpha_2]sin^2\alpha - cos^2\alpha - \alpha_2 sin2\alpha}{2[(\alpha_2 - \alpha_1)^2 + (\beta_2 - \beta_1)^2]} \quad (D.68d)$$

$$C'^{*(\alpha)} = \sigma^{\infty}\left\{\frac{(\alpha_2 - \alpha_1)cos^2\alpha + [\alpha_2(\alpha_1^2 - \beta_1^2) - \alpha_1(\alpha_2^2 - \beta_2^2)]sin^2\alpha}{2\beta_2[(\alpha_2 - \alpha_1)^2 + (\beta_2 - \beta_1)^2]}\right.$$
$$\left. + \frac{[(\alpha_1^2 - \beta_1^2) - (\alpha_2^2 - \beta_2^2)]sin\alpha \cdot cos2\alpha}{2\beta_2[(\alpha_2 - \alpha_1)^2 + (\beta_2 - \beta_1)^2]}\right\} \quad (D.68e)$$

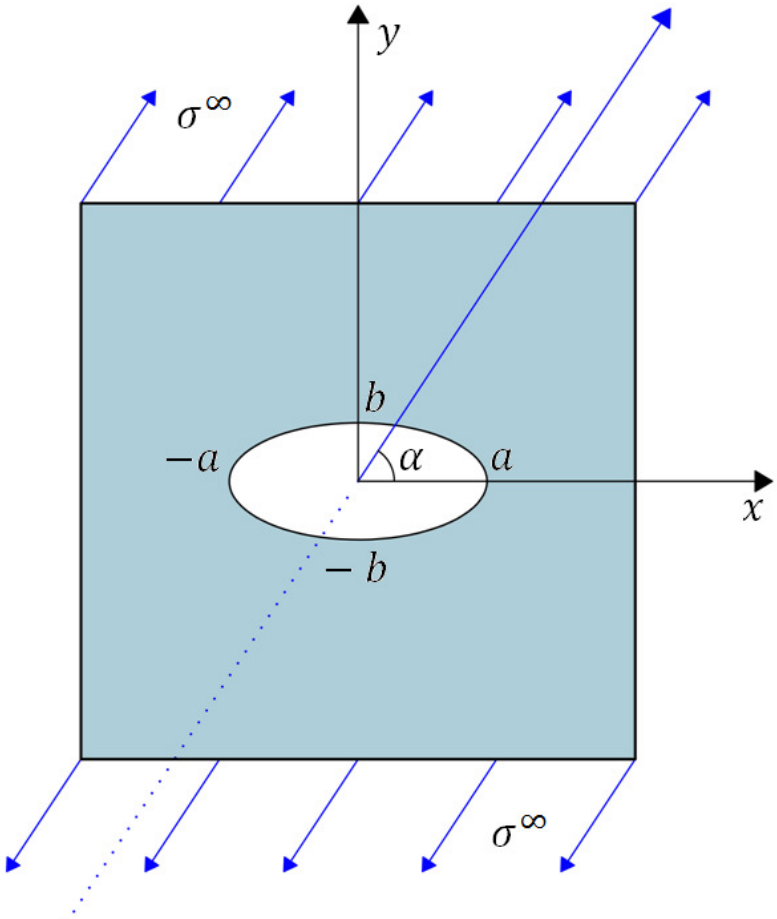

Figure D.5: Anisotropic plate with an elliptical hole under tension. The minor half-axis of the ellipse denoted with b where the major half-axis with a [LIM2001].

Hence, if angle α equals $\pi/2$, the analytic function can represented as:

$$\varphi^{(\alpha=\pi/2)}(z_1) = \varphi_0^{(\alpha=\pi/2)}(z_1) + B^{*(\alpha=\pi/2)}z_1 \quad (D.69a)$$

$$\psi^{(\alpha=\pi/2)}(z_2) = \psi_0^{(\alpha=\pi/2)}(z_2) + \left[B'^{*(\alpha=\pi/2)} + iC'^{*(\alpha=\pi/2)}\right]z_2 \quad (D.69b)$$

where $\varphi_0^{(\alpha=\pi/2)}(z_1)$, $\psi_0^{(\alpha=\pi/2)}(z_2)$, $B^{*(\alpha=\pi/2)}$, $B'^{*(\alpha=\pi/2)}$, and $C'^{*(\alpha=\pi/2)}$ are defined as:

$$\varphi_0^{(\alpha=\pi/2)}(z_1) = -\frac{i\sigma^{\infty}(a - is_1 b)}{4(s_1 - s_2)}\left\{\frac{i2as_2}{z_1 + \sqrt{z_1^2 - (a^2 + s_1^2 b^2)}}\right\} \qquad (D.70a)$$

$$\psi_0^{(\alpha=\pi/2)}(z_2) = \frac{i\sigma^{\infty}(a - is_2 b)}{4(s_1 - s_2)}\left\{\frac{i2as_1}{z_1 + \sqrt{z_1^2 - (a^2 + s_1^2 b^2)}}\right\} \qquad (D.70b)$$

$$B^{*(\alpha=\pi/2)} = \sigma^{\infty}\frac{\sigma^{\infty}(\alpha_2^2 + \beta_2^2)}{2[(\alpha_2 - \alpha_1)^2 + (\beta_2 - \beta_1)^2]} \qquad (D.70c)$$

$$B'^{*(\alpha=\pi/2)} = \frac{\sigma^{\infty}[(\alpha_1^2 - \beta_1^2) - 2\alpha_1\alpha_2]}{2[(\alpha_2 - \alpha_1)^2 + (\beta_2 - \beta_1)^2]} \qquad (D.70d)$$

$$C'^{*(\alpha=\pi/2)} = \frac{\sigma^{\infty}[\alpha_2(\alpha_1^2 - \beta_1^2) - \alpha_1(\alpha_2^2 - \beta_2^2)]}{2\beta_2[(\alpha_2 - \alpha_1)^2 + (\beta_2 - \beta_1)^2]} \qquad (D.70e)$$

In the case of $\alpha = 0$, the analytic function is determined similarly from equations D.67 and is given as:

$$\varphi^{(\alpha=0)}(z_1) = \varphi_0^{(\alpha=0)}(z_1) + B^{*(\alpha=0)}z_1 \qquad (D.71a)$$

$$\psi^{(\alpha=0)}(z_2) = \psi_0^{(\alpha=0)}(z_2) + \left[B'^{*(\alpha=0)} + iC'^{*(\alpha=0)}\right]z_2 \qquad (D.71b)$$

where $\varphi_0^{(\alpha=0)}(z_1)$, $\psi_0^{(\alpha=0)}(z_2)$, $B^{*(\alpha=0)}$, $B'^{*(\alpha=0)}$, and $C'^{*(\alpha=0)}$ are defined as:

$$\varphi_0^{(\alpha=0)}(z_1) = -\frac{ik\sigma^{\infty}(a - is_1 b)}{4(s_1 - s_2)}\left\{\frac{2b}{z_1 + \sqrt{z_1^2 - (a^2 + s_1^2 b^2)}}\right\} \qquad (D.72a)$$

$$\psi_0^{(\alpha=0)}(z_2) = \frac{ik\sigma^{\infty}(a - is_2 b)}{4(s_1 - s_2)}\left\{\frac{2b}{z_2 + \sqrt{z_2^2 - (a^2 + s_2^2 b^2)}}\right\} \qquad (D.72b)$$

$$B^{*(\alpha=0)} = \frac{k\sigma^{\infty}}{2[(\alpha_2 - \alpha_1)^2 + (\beta_2 - \beta_1)^2]} \qquad (D.72c)$$

$$B'^{*(\alpha=0)} = \frac{-k\sigma^{\infty}}{2[(\alpha_2 - \alpha_1)^2 + (\beta_2 - \beta_1)^2]} \qquad (D.72d)$$

$$C'^{*(\alpha=0)} = \frac{k\sigma^{\infty}(\alpha_1 - \alpha_2)}{2\beta_2[(\alpha_2 - \alpha_1)^2 + (\beta_2 - \beta_1)^2]} \qquad (D.72e)$$

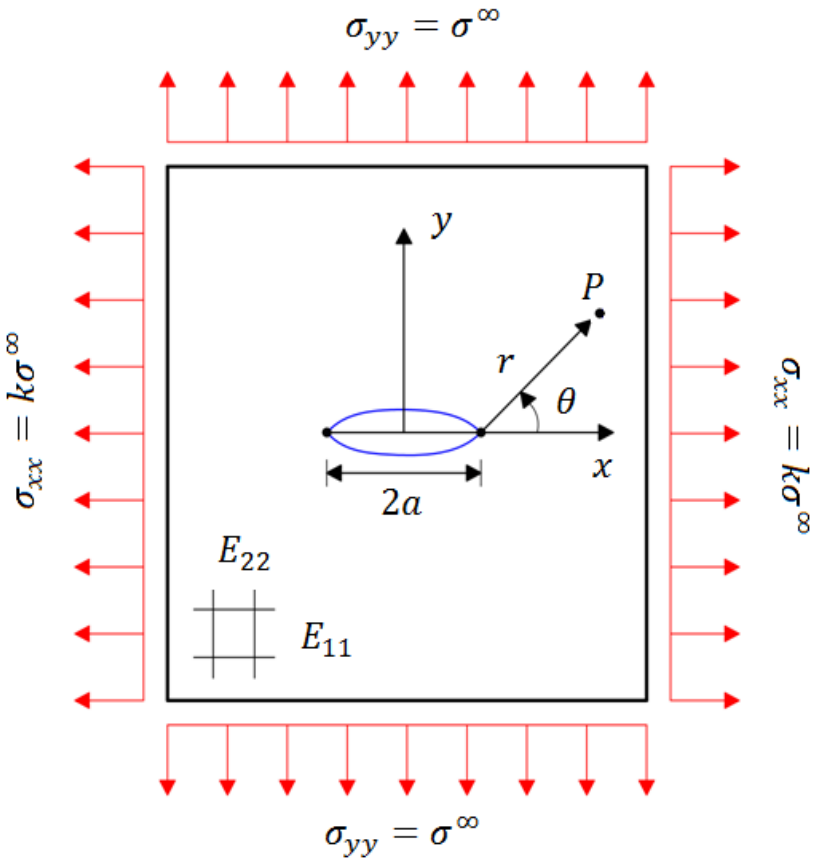

Figure D.6: Plane bi-axially loaded central crack geometry [LIM2001].

Therefore, the analytic functions for a horizontal-crack configuration under biaxial loading as shown in figure D.6 can be obtained by combing the function given in equations D.69 and D.71. In addition, by substituting zero for the short radius of elliptical hole, i.e., $b = 0$, the problem is converted to the Griffith-Inglis crack [WEE2008]. Henceforth, the analytic function for central sharp crack can be expressed as:

$$\varphi(z_1) = \frac{\sigma^{\infty} s_2}{2(s_1 - s_2)}\left[z_1 - \sqrt{z_1^2 - a^2}\right] + \Gamma_1 z_1 \qquad (D.73a)$$

$$\psi(z_2) = -\frac{\sigma^{\infty} s_1}{2(s_1 - s_2)}\left[z_2 - \sqrt{z_2^2 - a^2}\right] + \Gamma_2 z_2 \qquad (D.73b)$$

where $\Gamma_1 = B^*$ and $\Gamma_2 = (B'^* + iC'^*)$. B^*, B'^* and C'^* are constants depending from material properties and external applied loading conditions:

$$B^* = \frac{k\sigma^{\infty} + (\alpha_2^2 + \beta_2^2)\sigma^{\infty}}{2[(\alpha_2 - \alpha_1)^2 + (\beta_2 - \beta_1)^2]} \qquad (D.74a)$$

$$B'^{*} = \frac{[(\alpha_1^2 - \beta_1^2) - 2\alpha_1\alpha_2]\sigma^{\infty} - k\sigma^{\infty}}{2[(\alpha_2 - \alpha_1)^2 + (\beta_2 - \beta_1)^2]} \qquad (D.74b)$$

$$C'^{*} = \left\{\frac{(\alpha_1 - \alpha_2)\, k\sigma^{\infty}\sigma^{\infty}[\alpha_2(\alpha_1^2 - \beta_1^2) - \alpha_1(\alpha_2^2 - \beta_2^2)]\sigma^{\infty}}{2\beta_2[(\alpha_2 - \alpha_1)^2 + (\beta_2 - \beta_1)^2]}\right\} \qquad (D.74c)$$

Appendix E: Crystallographic formulas for the cubic lattices

The present appendix summarizes the basic crystallographic geometrical features of the face-centered cubic (fcc) and the body-centered cubic (bcc) types of crystal lattices. In the formulas below, the lattices are referred to cubic axes (i.e. the $[100]$, $[010]$ and $[001]$ crystallographic direction), with h, k, l denoted the Miller crystallographic indices and a_{uc} the length of the cubic unit cell. The basic features of the cubic lattices are:

1. the volume of the cubic unit cell per atom, given by:

$$V = a_{uc}^3/4, \text{ for the fcc lattice} \qquad (E.1a)$$

$$V = a_{uc}^3/2, \text{ for the bcc lattice} \qquad (E.1b)$$

2. the spacing between (hkl) crystallographic planes, through lattice points, expressed by:

$$d_{hkl} = \frac{a_{uc}}{Q\sqrt{h^2 + k^2 + l^2}} \qquad (E.2)$$

where for fcc lattice for bcc lattice

$Q = 1$ if h, k, l are all odd if $h + k + l$ is even,

$Q = 2$ if h, k, l are of mixed parity if $h + k + l$ is odd.

3. the identity period along the $[hkl]$ crystallographic direction, which is equal to:

$$I_{[hkl]} = \frac{a_{uc}}{2} Q^* \sqrt{h^2 + k^2 + l^2} \qquad (E.3)$$

where for fcc lattice for bcc lattice

$Q^* = 1$ if $h + k + l$ is even if h, k, l are all odd,

$Q^* = 2$ if $h + k + l$ is odd if h, k, l are all of mixed parity.

4. the angle between $(h_1k_1l_1)$ or $[h_1k_1l_1]$ and $(h_2k_2l_2)$ or $[h_2k_2l_2]$:

$$cos\varphi = \frac{(h_1h_2 + k_1k_2 + l_1l_2)}{\sqrt{(h_1^2 + k_1^2 + l_1^2)(h_2^2 + k_2^2 + l_2^2)}} \qquad (E.4)$$

Appendix F: Programs

This appendix presents the two codes developed in the present thesis in order to construct the atomic models of cracks in fcc aluminium and in bcc iron, respectively. The codes are written in FORTRAN programming language and they are capable to create the $(010)[001]$ crack configuration under mode I plane-strain loading conditions, based on the complex variable approach (Appendix D).

F.1. Program fccAlaniccrack.f

```
C     ------------------------------------------------------------------
C     |   Construction of the FACE-CENTERED-CUBIC lattice of ALUMINIUM   |
C     |   with a crack configuration under mode I plane-strain loading   |
C     ------------------------------------------------------------------
C     | Coordinates system: x=[ 1  0  0], y=[ 0  1  0], z=[ 0  0  1]     |
C     | Atomic positions - normalized units: divided by lattice constant |
C     | Crack geometry (010)[001] - FULL ELASTIC DISPLACEMENT FIELD      |
C     | ANISOTROPIC MEDIA APPROACH = Complex variable approach           |
C     | Fixed boundary conditions: xy  Periodic boundary conditions: z   |
C     ------------------------------------------------------------------
C     | Program: fccAlaniccrack.f          M. Zacharopoulos - 28/11/2013 |
C     ------------------------------------------------------------------
C
      IMPLICIT DOUBLE PRECISION (A-H,O-Z)
      PARAMETER (LA=200,LB=80,LC=6,NP=4*LA*LB*LC)
      PARAMETER (ND=1)
C
      COMMON/C1/PI,TPI,RSQ2,RSQ3,RSQ6
C
      DIMENSION ZL(3),ZLS2(3),TR(3),RCM(3),RRCM(3),SX(ND),SY(ND)
      DIMENSION XP(NP,3),IP(NP,3),XPD(NP,3),UN(NP,3),UNT(NP,3),L(NP)
      DIMENSION M(NP)
C
      CALL C_INIT
C
C     Construction of perfect crystal lattice
C     (coordinares system : X//[100] - Y//[010] - Z//[001])
C
      ZL(1) = DBLE(LA)                              ![100]
      ZL(2) = DBLE(LB)                              ![010]
      ZL(3) = DBLE(LC)                              ![001]
      ZLS2  = 0.5D0*ZL
C
      CALL RES100(NP,LA,LB,LC,ZLS2,TR,XP,IP,L,M)
C
      EN = DBLE(NP)
      PRINT *,'EN',EN
C
C     Position of (mode I) the crack's center (center of the ellipse)
C
      SX(1) =  0.D0
      SY(1) =  0.D0
C
C     Displacement field calculation
C
      UNT = 0.D0
      UN  = 0.D0
      CALL  DIS_FL(NP,XP,SX(1),SY(1),UN)
      UNT = UNT + UN
C
      XPD = XP + UNT
C
C     Writing transformed positions
C
      DO I = 1, NP
        WRITE(30,FMT='(I6,9(2X,F15.8),2X,3I5)')
```

```
     $           I, (XPD(I,IC),IC=1,3), (UNT(I,IC),IC=1,3),
     $          (XP(I,IC),IC=1,3), (IP(I,IC),IC=1,3)
      END DO
C
C     Centering the system
C
      DO IC = 1, 3
        RCM(IC) = SUM(XPD(1:NP,IC))/EN
        XPD(1:NP,IC) = XPD(1:NP,IC) - RCM(IC)
      END DO
      PRINT *,'Center of mass: defore centering the system'
      PRINT *,'[100]', RCM(1)
      PRINT *,'[010]', RCM(2)
      PRINT *,'[001]', RCM(3)
C
      DO IC = 1, 3
        RRCM(IC) = SUM(XPD(1:NP,IC))/EN
      END DO
      PRINT *,'Center of mass: after centering the system'
      PRINT *,'[100]', RRCM(1)
      PRINT *,'[010]', RRCM(2)
      PRINT *,'[001]', RRCM(3)
C
C     Writing transformed positions with centered atoms
C
      DO I = 1, NP
       WRITE(60,FMT='(I6,3(2X,F22.15),2X,5I5)')
     $   I,(XPD(I,IC),IC=1,3),(IP(I,IC),IC=1,3),L(I),M(I)
      END DO
C
C     Fixed/Criterion atoms CONTROL
C
      DO I=1,NP
C       IF (L(I) .EQ. 1) THEN
        IF (M(I) .EQ. 1) THEN
          WRITE(61,FMT='(I6,2X,3(F22.15,1X),5I5)')
     $        I,(XPD(I,J),J=1,3),(IP(I,IC),IC=1,3),L(I),M(I)
        END IF
      END DO
C
      CALL FIXORD(NP,XPD,IP,L,M)
C
      WRITE(*,FMT='(/,A,/)') '  PROGRAM FINISHED   '
C
      END
C     ------------------------------------------------------------------
      SUBROUTINE RES100(NP,LA,LB,LC,ZLS2,TR,XP,IP,L,M)
C     crystal lattice construction
C     ------------------------------------------------------------------
      IMPLICIT DOUBLE PRECISION (A-H,O-Z)
      COMMON/C1/PI,TPI,RSQ2,RSQ3,RSQ6
      COMMON/C2/A11,A12,A16,A26,A22,A66,AS,FK,CHL
C
      DIMENSION BZ(3),TR(3),U(4,3),XP(NP,3),ZLS2(3),IP(NP,3),L(NP)
      DIMENSION M(NP)
C
      DATA U/0.D0,1.D0,1.D0,0.D0,                              ! [100]
     $       0.D0,1.D0,0.D0,1.D0,                              ! [010]
     $       0.D0,0.D0,1.D0,1.D0/                              ! [001]
C
      WRITE(*,FMT='(/,A,/,4(3F5.0,/))')
     $             '  MATRICE U(4,3)   ',((U(I,J), J = 1, 3),I = 1, 4)
C
      TR(1) = ZLS2(1) - 0.25D0                                 ! [100]
      TR(2) = ZLS2(2) - 0.25D0                                 ! [010]
      TR(3) = ZLS2(3) - 0.25D0                                 ! [001]
C
C     Fixed boundary conditions
C     (along X//[100] and Y//[010] directions)
C
      XMAX =   ZLS2(1) - 5.D0
      XMIN = -(ZLS2(1) - 5.D0)
      YMAX =   ZLS2(2) - 5.D0
      YMIN = -(ZLS2(2) - 5.D0)
C
C     Minimization criterion
C     (along X//[100] and Y//[010] directions)
```

```
C
      YCH =   1.5D0
      YCL =  -1.5D0
      XCH =   CHL + 10.D0
      XCL = -(CHL + 10.D0)
C
      I = 0
      DO JA = 1, LA
        BZ(1) = DBLE(JA)
        DO JB = 1, LB
          BZ(2) = DBLE(JB)
          DO JC = 1, LC
            BZ(3) = DBLE(JC)
            DO JD = 1, 4
              I = I + 1
C
              XP(I,1) = U(JD,1)*0.5D0 + (BZ(1)-1.D0) - TR(1)
              XP(I,2) = U(JD,2)*0.5D0 + (BZ(2)-1.D0) - TR(2)
              XP(I,3) = U(JD,3)*0.5D0 + (BZ(3)-1.D0) - TR(3)
              PX = 1.D0 + 2.D0*(U(JD,1)*0.5D0 + BZ(1) - 1.D0)
              PY = 1.D0 + 2.D0*(U(JD,2)*0.5D0 + BZ(2) - 1.D0)
              PZ = 1.D0 + 2.D0*(U(JD,3)*0.5D0 + BZ(3) - 1.D0)
              IP(I,1) = IDNINT(PX)
              IP(I,2) = IDNINT(PY)
              IP(I,3) = IDNINT(PZ)
C
C             Fixed boundary conditions
C
              IF (XP(I,1) .GE. XMAX .OR. XP(I,1) .LE. XMIN) THEN
                L(I) = 1
           ELSE IF (XP(I,2) .GE. YMAX .OR. XP(I,2) .LE. YMIN) THEN
                L(I) = 1
              ELSE
                L(I) = 0
              END IF
C
C             Minimization criterion
C
              IF (XP(I,1) .LE. XCH .AND. XP(I,1) .GE. XCL  .AND.
     $            XP(I,2) .LE. YCH .AND. XP(I,2) .GE. YCL) THEN
                M(I) = 1
              ELSE
                M(I) = 0
              END IF
C
              WRITE(20,FMT='(I5,2X,6(G15.8,1X),4I5)')
     $             I,(XP(I,J),J=1,3),
     $             PX,PY,PZ,(IP(I,IC),IC=1,3),L(I)
C
            END DO
          END DO
        END DO
      END DO
C
      WRITE(*,*) 'RES100 : Lattice construction OK IM =',I,' atoms'
C
C     Fixed/Criterion atoms CONTROL
C
      DO I=1,NP
        IF (L(I) .EQ. 1) THEN
!       IF (M(I) .EQ. 1) THEN
          WRITE(21,FMT='(I5,2X,6(G15.8,1X),5I5)')
     $             I,(XP(I,J),J=1,3),
     $             PX,PY,PZ,(IP(I,IC),IC=1,3),L(I),M(I)
        END IF
      END DO
C
      RETURN
      END
C     ------------------------------------------------------------------
      SUBROUTINE DIS_FL(IM,XP,SHX,SHY,UN)
C     Displacement field calculation
C     ------------------------------------------------------------------
      IMPLICIT DOUBLE PRECISION (A-H,O-Z)
C
      COMPLEX(KIND(1.D0))  YY,Y1,Y2,R1,R2,R3,R4
      COMPLEX(KIND(1.D0))  S1,S2,P1,P2,Q1,Q2,Z1,Z2
```

```
      COMPLEX(KIND(1.D0))  GF1,GF2,FC,PC,FZ1,PZ2
C
      COMMON/C1/PI,TPI,RSQ2,RSQ3,RSQ6
      COMMON/C2/A11,A12,A16,A26,A22,A66,AS,FK,CHL
C
      DIMENSION XP(IM,3),UN(IM,3),RRP(3,2),RRUN(3,2),RRPT(3,2)
C     XP perfect crystal position, UV displacements
C
C     complex roots calculation (S1,S2)
C
      AA = (0.5D0*A66+A12)/A11
      BB = DSQRT(A22/A11)
C
      PRINT *,'A=',AA
      PRINT *,'B=',BB
      PRINT *,'A**2 - B**2 = ',AA**2 - BB**2,' CASE III'
C
      YY  =  CDSQRT(DCMPLX(AA**2 - BB**2,0.D0))
      Y1 = -AA + YY
      Y2 = -AA - YY
      R1 =  CDSQRT(Y1)
      R2 =  CDSQRT(Y2)
      R3 = -CDSQRT(Y1)
      R4 = -CDSQRT(Y2)
C
      PRINT *,'CMPLX ROOT R1',R1
      PRINT *,'CMPLX ROOT R2',R2
      PRINT *,'CMPLX ROOT R3',R3
      PRINT *,'CMPLX ROOT R4',R4
C
      S1 =  R1
      A1 =  DBLE(S1)
      B1 =  DIMAG(S1)
      S2 =  R4
      A2 =  DBLE(S2)
      B2 =  DIMAG(S2)
C
      PRINT *,'CMPLX ROOT S1',S1
      PRINT *,'Re part',A1
      PRINT *,'Im part',B1
      PRINT *,'CMPLX ROOT S2',S2
      PRINT *,'Re part',A2
      PRINT *,'Im part',B2
C
C     Stress function constants
C
      DOM     = 2.D0*((A2 - A1)**2 + (B2**2 - B1**2))
      BSCNUM  = AS*FK + AS*(A2**2 + B2**2)
      BSCDOM  = DOM
      BSC     = BSCNUM/BSCDOM
      BTSCNUM = ((A1**2 - B1**2) - 2.D0*A1*A2)*AS - FK*AS
      BTSCDOM = DOM
      BTSC    = BTSCNUM/BTSCDOM
      CTSCNUM = (A1-A2)*FK*AS+(A2*(A1**2-B1**2)-A1*(A2**2-B2**2))*AS
      CTSCDOM = DOM*B2
      CTSC    = CTSCNUM/CTSCDOM
C
      GF1 = DCMPLX(BSC,0.D0)
      GF2 = DCMPLX(BTSC,CTSC)
C
      FC  =  AS*S2/(2.D0*(S1 - S2))
      PC  = -AS*S1/(2.D0*(S1 - S2))
C
      PRINT *,'B*',BSC
      PRINT *,'B"*',BTSC
      PRINT *,'C"*',CTSC
      PRINT *,'FC',FC
      PRINT *,'PC',PC
      PRINT *,'GAMMA 1',GF1
      PRINT *,'GAMMA 2',GF2
C
C     Displacement function constants
C
      P1 = A11*S1**2 + A12 - A16*S1
      P2 = A11*S2**2 + A12 - A16*S2
C
      Q1 = (A12*S1**2 + A22 - A26*S1)/S1
```

```
      Q2 = (A12*S2**2 + A22 - A26*S2)/S2
C
      ZER = 0.D0
C
      PRINT *,'P1',P1
      PRINT *,'P2',P2
      PRINT *,'Q1',Q1
      PRINT *,'Q2',Q2
C
C       Calculate rigid rotation
C
C      Point P
       RRP (1,1) = -10000000000.D0
       RRP (1,2) = -10000000000.D0
C      Point R1
       RRP (2,1) =  10000000000.D0
       RRP (2,2) = -10000000000.D0
C      Point R2
       RRP (3,1) = -10000000000.D0
       RRP (3,2) =  10000000000.D0
C
      DO I = 1, 3
C
C       Position with referece the crack center
C
        X = RRP(I,1) - SHX
        Y = RRP(I,2) - SHY
        R = DSQRT(X**2 + Y**2)
C
        CALL DATG(1.D0,X,Y,TH)
        COTH  = DCOS(TH)
        SITH  = DSIN(TH)
C
        Z1 = R*(COTH + S1*SITH)
        Z1R =   DBLE(Z1)
        Z1I =  DIMAG(Z1)
        Z2 = R*(COTH + S2*SITH)
        Z2R =   DBLE(Z2)
        Z2I =  DIMAG(Z2)
C
        IF  (Z1R .GE. ZER) THEN
          FZ1 = FC*(Z1 - CDSQRT(Z1**2 - CHL**2)) + GF1*Z1
          ELSE
          FZ1 = FC*(Z1 + CDSQRT(Z1**2 - CHL**2)) + GF1*Z1
        END IF
C
        IF  (Z2R .GE. ZER) THEN
          PZ2 = PC*(Z2 - CDSQRT(Z2**2 - CHL**2)) + GF2*Z2
          ELSE
          PZ2 = PC*(Z2 + CDSQRT(Z2**2 - CHL**2)) + GF2*Z2
        END IF
C
        U = 2.D0*DBLE(P1*FZ1 + P2*PZ2)
        V = 2.D0*DBLE(Q1*FZ1 + Q2*PZ2)
C
        RRUN(I,1) = U
        RRUN(I,2) = V
C
        RRPT(I,1) = RRP(I,1) + RRUN(I,1)
        RRPT(I,2) = RRP(I,2) + RRUN(I,2)
C
      END DO
C
      RRDX = RRP(2,1) - RRP(1,1)
      RRDY = RRP(3,2) - RRP(1,2)
C
      RRU  = RRPT(1,1) - RRP(1,1)
      RRV  = RRPT(1,2) - RRP(1,2)
C
      RRDUDX = (RRPT(2,1) - RRP(2,1) - RRU)/RRDX
      RRDVDX = (RRPT(2,2) - RRP(2,2) - RRV)/RRDX
      RRDUDY = (RRPT(3,1) - RRP(3,1) - RRU)/RRDY
      RRDVDY = (RRPT(3,2) - RRP(3,2) - RRV)/RRDY
C
      WXY = 0.5D0*(RRDUDY - RRDVDX)
      PRINT *,'WXY =',WXY
C
```

```
      DO I = 1, IM
C
C       Position with referece the crack center
C
        X = XP(I,1) - SHX
        Y = XP(I,2) - SHY
        R = DSQRT(X**2 + Y**2)
C
        CALL DATG(1.D0,X,Y,TH)
        COTH  = DCOS(TH)
        SITH  = DSIN(TH)
C
        Z1 = R*(COTH + S1*SITH)
        Z1R =   DBLE(Z1)
        Z1I =  DIMAG(Z1)
        Z2 = R*(COTH + S2*SITH)
        Z2R =   DBLE(Z2)
        Z2I =  DIMAG(Z2)
C
        IF  (Z1R .GE. ZER) THEN
          FZ1 = FC*(Z1 - CDSQRT(Z1**2 - CHL**2)) + GF1*Z1
          ELSE
          FZ1 = FC*(Z1 + CDSQRT(Z1**2 - CHL**2)) + GF1*Z1
        END IF
C
        IF  (Z2R .GE. ZER) THEN
          PZ2 = PC*(Z2 - CDSQRT(Z2**2 - CHL**2)) + GF2*Z2
          ELSE
          PZ2 = PC*(Z2 + CDSQRT(Z2**2 - CHL**2)) + GF2*Z2
        END IF
C
        U = 2.D0*DBLE(P1*FZ1 + P2*PZ2) - WXY*Y
        V = 2.D0*DBLE(Q1*FZ1 + Q2*PZ2) + WXY*X
C
        UN(I,1) = U
        UN(I,2) = V
C
      END DO
C
      RETURN
      END
C     ----------------------------------------------------------------
      SUBROUTINE DATG(RA,X,Y,TH)
C     ----------------------------------------------------------------
      IMPLICIT DOUBLE PRECISION (A-H,O-Z)
      COMMON/C1/PI,TPI,RSQ2,RSQ3,RSQ6
C
       TH = DATAN2(Y,RA*X)
C
      RETURN
      END
C     ----------------------------------------------------------------
      SUBROUTINE C_INIT
C     Subroutine of constants (numerical,material,crack)
C     ----------------------------------------------------------------
      IMPLICIT DOUBLE PRECISION (A-H,O-Z)
      COMMON/C1/PI,TPI,RSQ2,RSQ3,RSQ6
      COMMON/C2/A11,A12,A16,A26,A22,A66,AS,FK,CHL
C
C     NUMERICAL CONSTANTS
C
      PI   = 4.D0*DATAN(1.D0)
      TPI  = 2.D0*PI
      USTPI= 1.D0/TPI
      RSQ2 = DSQRT(2.D0)
      RSQ3 = DSQRT(3.D0)
      RSQ6 = DSQRT(6.D0)
C
C     MATERIAL CONSTANTS
C     Elastic stiffness constants (units:GPa)
C     Al Elastic moduli computed with AP potential
      C11 = 116.63D0
      C12 = 61.028D0
      C44 = 29.618D0
C     Elastic compliance constants (units:1/GPa)
      S11 =  (C11+C12)/(C11**2 + C11*C12 - 2.D0*C12**2)
      S12 = -C12/(C11**2 + C11*C12 - 2.D0*C12**2)
```

```
      S44 =  1.D0/(C44)
C     Plane-strain elastic compliances (units:1/GPa)
      A11 = S11 - (S12*S12)/S11
      A12 = S12 - (S12*S12)/S11
      A16 = 0.D0
      A26 = 0.D0
      A22 = S11 - (S12*S12)/S11
      A66 = S44
C     Coefficient of energy release rate (units:1/GPa)
      CG1 = (A11*A22)/2.D0
      CG2 = DSQRT(A22/A11)+(2.D0*A12 + A66)/(2.D0*A11)
      CG  = DSQRT(CG1*CG2)
C     Surface excess energy (100) (units:GPa*A)
      GS  = 7.9D0
C     Griffith's criterion (units:GPa*A**0.5)
      SIFG =  DSQRT((2.D0*GS)/CG)
C
      PRINT *,'MATERIAL CONSTANTS'
      PRINT *,'C11 = ',C11,'[GPa]'
      PRINT *,'C12 = ',C12,'[GPa]'
      PRINT *,'C44 = ',C44,'[GPa]'
      PRINT *,'S11 = ',S11,'[1/GPa]'
      PRINT *,'S12 = ',S12,'[1/GPa]'
      PRINT *,'S44 = ',S44,'[1/GPa]'
      PRINT *,'Plane-strain deformation'
      PRINT *,'A11 = ',A11,'[1/GPa]'
      PRINT *,'A12 = ',A12,'[1/GPa]'
      PRINT *,'A16 = ',A16,'[1/GPa]'
      PRINT *,'A26 = ',A26,'[1/GPa]'
      PRINT *,'A22 = ',A22,'[1/GPa]'
      PRINT *,'A66 = ',A66,'[1/GPa]'
      PRINT *,'CG  = ',CG,'[1/GPa]'
      PRINT *,'GS  = ',GS,'[GPa*A]'
      PRINT *,'SIFG  = ',SIFG,'[GPa*A**0.5]'
      PRINT *,' '
C
C     CRACK CONSTANTS
C
      PRINT *,'CRACK CONSTANTS'
      PRINT *,'Enter value for:'
      PRINT *,'EXTERNAL APPLIED STRESS (units:GPa)'
      PRINT *,'along [010]-direction'
      READ  *,AS
      PRINT *,'Enter value for:'
      PRINT *,'CRACKS HALF LENGHT (units:a0)'
      READ  *,CHL
C
      AS  =  DBLE(AS)
      FK  =  0.D0
      ASX =  AS*FK
      ASY =  AS
      CHL =  DBLE(CHL)
C
      PRINT *, 'UNIAXIAL/BIAXIAL LOADING CONDITIONS'
      PRINT *, 'APPLIED STRESS along X//[100] to infinity', ASX,'[GPa]'
      PRINT *, 'APPLIED STRESS along Y//[010] to infinity', ASY,'[GPa]'
      PRINT *, 'CRACK LENGTH 2a where,', 'a =',CHL,'[a0]'
C
      RETURN
      END
C     ---------------------------------------------------------------
      SUBROUTINE FIXORD(NP,XPD,IP,L,M)
C     Subroutine that arrange the FIX/DYN atoms of the configuration
C     ---------------------------------------------------------------
      IMPLICIT DOUBLE PRECISION (A-H,O-Z)
C
      DIMENSION XPD(NP,3)
      DIMENSION IP(NP,3),L(NP),M(NP)
C
      WRITE(*,FMT='(/)')
      PRINT *,'SUBROUTINE FIXORD ACTIVATE'
      PRINT *,'NP = ',NP,'atoms found'
C
      MFA = 0
C
      DO I = 1, NP
        IF (L(I) .EQ. 1) THEN
```

```
          MFA = MFA + 1
          WRITE (90,FMT='(I6,3(2X,F22.15),2X,5I5)')
     $    MFA,(XPD(I,IC),IC=1,3),(IP(I,IC),IC=1,3),L(I),M(I)
        ENDIF
       END DO
C
       MDA = MFA
C
       DO  I = 1, NP
         IF (L(I) .EQ. 0) THEN
          MDA = MDA + 1
          WRITE (90,FMT='(I6,3(2X,F22.15),2X,5I5)')
     $    MDA,(XPD(I,IC),IC=1,3),(IP(I,IC),IC=1,3),L(I),M(I)
         END IF
       END DO
C
       NFA = MFA
       NDA = MDA-MFA
C
       PRINT *,NFA,'FIXED atoms found'
       PRINT *,NDA,'DYNAMIC atoms found'
       PRINT *,'total atoms',MDA,'atoms found'
       PRINT *,'of initial',NP,'atoms'
C
       RETURN
       END
C      ---------------------------------------------------------------
```

F.2. Program bccFeaniccrack.f

```
C      ---------------------------------------------------------------
C      |     Construction of the BODY-CENTERED-CUBIC lattice of IRON      |
C      |   with a crack configuration under mode I plane-strain loading   |
C      ---------------------------------------------------------------
C      | Coordinates system: x=[ 1  0  0], y=[ 0  1  0], z=[ 0  0  1]     |
C      | Atomic positions - normalized units: divided by lattice constant |
C      | Crack geometry (010)[001] - FULL ELASTIC DISPLACEMENT FIELD      |
C      | ANISOTROPIC MEDIA APPROACH = Complex variable approach           |
C      | Fixed boundary conditions: xy  Periodic boundary conditions: z   |
C      ---------------------------------------------------------------
C      | Program: bccFeaniccrack.f          M. Zacharopoulos - 11/07/2014 |
C      ---------------------------------------------------------------
       IMPLICIT DOUBLE PRECISION (A-H,O-Z)
       PARAMETER (LA=200,LB=160,LC=6,NP=2*LA*LB*LC)
       PARAMETER (ND=1)
C
       COMMON/C1/PI,TPI,RSQ2,RSQ3,RSQ6
C
       DIMENSION ZL(3),ZLS2(3),TR(3),RCM(3),RRCM(3),SX(ND),SY(ND)
       DIMENSION XP(NP,3),IP(NP,3),XPD(NP,3),UN(NP,3),UNT(NP,3),L(NP)
       DIMENSION M(NP)
C
       CALL C_INIT1BCC
C
C      Construction of perfect crystal lattice
C      (coordinares system : x=[ 1  0  0], y=[ 0  1  0], z=[ 0  0  1])
C
       ZL(1) = DBLE(LA)*1.D0            ![ 1  0  0] LA*Identity period
       ZL(2) = DBLE(LB)*1.D0            ![ 0  1  0] LB*Identity period
       ZL(3) = DBLE(LC)*1.D0            ![ 0  0  1] LC*Identity period
       ZLS2  = 0.5D0*ZL
C
       CALL BES100(NP,LA,LB,LC,ZLS2,TR,XP,IP,L,M)
C
       EN = DBLE(NP)
       PRINT *,'EN',EN
C
C      Position of (mode I) the crack's center (center of the ellipse)
C
       SX(1) =  0.D0
       SY(1) =  0.D0
C
C      Displacement field calculation
C
       UNT = 0.D0
```

```
      UN  = 0.D0
      CALL  DIS_FL(NP,XP,SX(1),SY(1),UN)
      UNT = UNT + UN
C
      XPD = XP + UNT
C
C     Writing transformed positions
C
      DO I = 1, NP
        WRITE(30,FMT='(I6,9(2X,F15.8),2X,3I5)')
     $           I, (XPD(I,IC),IC=1,3), (UNT(I,IC),IC=1,3),
     $          (XP(I,IC),IC=1,3), (IP(I,IC),IC=1,3)
      END DO
C
C     Centering the system
C
      DO IC = 1, 3
        RCM(IC) = SUM(XPD(1:NP,IC))/EN
        XPD(1:NP,IC) = XPD(1:NP,IC) - RCM(IC)
      END DO
      PRINT *,'Center of mass: defore centering the system'
      PRINT *,'[ 1  0  0]', RCM(1)
      PRINT *,'[ 0  1  0]', RCM(2)
      PRINT *,'[ 0  0  1]', RCM(3)
C
      DO IC = 1, 3
        RRCM(IC) = SUM(XPD(1:NP,IC))/EN
      END DO
      PRINT *,'Center of mass: after centering the system'
      PRINT *,'[ 1  0  0]', RRCM(1)
      PRINT *,'[ 0  1  0]', RRCM(2)
      PRINT *,'[ 0  0  1]', RRCM(3)
C
C     Writing transformed positions with centered atoms
C
      DO I = 1, NP
       WRITE(60,FMT='(I6,3(2X,F22.15),2X,5I5)')
     $   I,(XPD(I,IC),IC=1,3),(IP(I,IC),IC=1,3),L(I),M(I)
      END DO
C
C     Fixed/Criterion atoms CONTROL
C
      DO I=1,NP
        IF (L(I) .EQ. 1) THEN
!       IF (M(I) .EQ. 1) THEN
          WRITE(61,FMT='(I6,2X,3(F22.15,1X),5I5)')
     $        I,(XPD(I,J),J=1,3),(IP(I,IC),IC=1,3),L(I),M(I)
        END IF
      END DO
C
      CALL FIXORD(NP,XPD,IP,L,M)
C
      WRITE(*,FMT='(/,A,/)') '  PROGRAM FINISHED   '
C
      END
C     ------------------------------------------------------------------
      SUBROUTINE DIS_FL(IM,XP,SHX,SHY,UN)
C     Displacement field calculation
C     ------------------------------------------------------------------
      IMPLICIT DOUBLE PRECISION (A-H,O-Z)
C
      COMPLEX(KIND(1.D0))  YY,Y1,Y2,R1,R2,R3,R4
      COMPLEX(KIND(1.D0))  S1,S2,P1,P2,Q1,Q2,Z1,Z2
      COMPLEX(KIND(1.D0))  GF1,GF2,FC,PC,FZ1,PZ2
C
      COMMON/C1/PI,TPI,RSQ2,RSQ3,RSQ6
      COMMON/C2/A11,A12,A16,A26,A22,A66,AS,FK,CHL
C
      DIMENSION XP(IM,3),UN(IM,3),RRP(3,2),RRUN(3,2),RRPT(3,2)
C     XP perfect crystal position, UV displacements
C
C     complex roots calculation (S1,S2)
C
      AA = (0.5D0*A66+A12)/A11
      BB = DSQRT(A22/A11)
C
      PRINT *,'A=',AA
```

```
      PRINT *,'B=',BB
      PRINT *,'A**2 - B**2 = ',AA**2 - BB**2,' CASE I/III'
!     (positive=caseI/negative=caseIII)
C
      YY  =  CDSQRT(DCMPLX(AA**2 - BB**2,0.D0))
      Y1 = -AA + YY
      Y2 = -AA - YY
      R1 =  CDSQRT(Y1)
      R2 =  CDSQRT(Y2)
      R3 = -CDSQRT(Y1)
      R4 = -CDSQRT(Y2)
C
      PRINT *,'CMPLX ROOT R1',R1
      PRINT *,'CMPLX ROOT R2',R2
      PRINT *,'CMPLX ROOT R3',R3
      PRINT *,'CMPLX ROOT R4',R4
C
      S1 =  R1
      A1 =  DBLE(S1)
      B1 =  DIMAG(S1)
      S2 =  R4
      A2 =  DBLE(S2)
      B2 =  DIMAG(S2)
C
      PRINT *,'CMPLX ROOT S1',S1
      PRINT *,'Re part',A1
      PRINT *,'Im part',B1
      PRINT *,'CMPLX ROOT S2',S2
      PRINT *,'Re part',A2
      PRINT *,'Im part',B2
C
C     Stress function constants
C
      DOM     = 2.D0*((A2 - A1)**2 + (B2**2 - B1**2))
      BSCNUM  = AS*FK + AS*(A2**2 + B2**2)
      BSCDOM  = DOM
      BSC     = BSCNUM/BSCDOM
      BTSCNUM = ((A1**2 - B1**2) - 2.D0*A1*A2)*AS - FK*AS
      BTSCDOM = DOM
      BTSC    = BTSCNUM/BTSCDOM
      CTSCNUM = (A1-A2)*FK*AS+(A2*(A1**2-B1**2)-A1*(A2**2-B2**2))*AS
      CTSCDOM = DOM*B2
      CTSC    = CTSCNUM/CTSCDOM
C
      GF1 = DCMPLX(BSC,0.D0)
      GF2 = DCMPLX(BTSC,CTSC)
C
      FC  =  AS*S2/(2.D0*(S1 - S2))
      PC  = -AS*S1/(2.D0*(S1 - S2))
C
      PRINT *,'B*',BSC
      PRINT *,'B"*',BTSC
      PRINT *,'C"*',CTSC
      PRINT *,'FC',FC
      PRINT *,'PC',PC
      PRINT *,'GAMMA 1',GF1
      PRINT *,'GAMMA 2',GF2
C
C     Displacement function constants
C
      P1 = A11*S1**2 + A12 - A16*S1
      P2 = A11*S2**2 + A12 - A16*S2
C
      Q1 = (A12*S1**2 + A22 - A26*S1)/S1
      Q2 = (A12*S2**2 + A22 - A26*S2)/S2
C
      ZER = 0.D0
C
      PRINT *,'P1',P1
      PRINT *,'P2',P2
      PRINT *,'Q1',Q1
      PRINT *,'Q2',Q2
C
C       Calculate rigid rotation
C
C      Point P
       RRP (1,1) = -10000000000.D0
```

```
       RRP (1,2) = -10000000000.D0
C      Point R1
       RRP (2,1) =  10000000000.D0
       RRP (2,2) = -10000000000.D0
C      Point R2
       RRP (3,1) = -10000000000.D0
       RRP (3,2) =  10000000000.D0
C
      DO I = 1, 3
C
C       Position with referece the crack center
C
        X = RRP(I,1) - SHX
        Y = RRP(I,2) - SHY
        R = DSQRT(X**2 + Y**2)
C
        CALL DATG(1.D0,X,Y,TH)
        COTH  = DCOS(TH)
        SITH  = DSIN(TH)
C
        Z1 = R*(COTH + S1*SITH)
        Z1R =   DBLE(Z1)
        Z1I =  DIMAG(Z1)
        Z2 = R*(COTH + S2*SITH)
        Z2R =   DBLE(Z2)
        Z2I =  DIMAG(Z2)
C
        IF  (Z1R .GE. ZER) THEN
          FZ1 = FC*(Z1 - CDSQRT(Z1**2 - CHL**2)) + GF1*Z1
          ELSE
          FZ1 = FC*(Z1 + CDSQRT(Z1**2 - CHL**2)) + GF1*Z1
        END IF
C
        IF  (Z2R .GE. ZER) THEN
          PZ2 = PC*(Z2 - CDSQRT(Z2**2 - CHL**2)) + GF2*Z2
          ELSE
          PZ2 = PC*(Z2 + CDSQRT(Z2**2 - CHL**2)) + GF2*Z2
        END IF
C
        U = 2.D0*DBLE(P1*FZ1 + P2*PZ2)
        V = 2.D0*DBLE(Q1*FZ1 + Q2*PZ2)
C
        RRUN(I,1) = U
        RRUN(I,2) = V
C
        RRPT(I,1) = RRP(I,1) + RRUN(I,1)
        RRPT(I,2) = RRP(I,2) + RRUN(I,2)
C
      END DO
C
      RRDX = RRP(2,1) - RRP(1,1)
      RRDY = RRP(3,2) - RRP(1,2)
C
      RRU  = RRPT(1,1) - RRP(1,1)
      RRV  = RRPT(1,2) - RRP(1,2)
C
      RRDUDX = (RRPT(2,1) - RRP(2,1) - RRU)/RRDX
      RRDVDX = (RRPT(2,2) - RRP(2,2) - RRV)/RRDX
      RRDUDY = (RRPT(3,1) - RRP(3,1) - RRU)/RRDY
      RRDVDY = (RRPT(3,2) - RRP(3,2) - RRV)/RRDY
C
      WXY = 0.5D0*(RRDUDY - RRDVDX)
      PRINT *,'WXY =',WXY
C
      DO I = 1, IM
C
C       Position with referece the crack center
C
        X = XP(I,1) - SHX
        Y = XP(I,2) - SHY
        R = DSQRT(X**2 + Y**2)
C
        CALL DATG(1.D0,X,Y,TH)
        COTH  = DCOS(TH)
        SITH  = DSIN(TH)
C
        Z1 = R*(COTH + S1*SITH)
```

```
        Z1R =   DBLE(Z1)
        Z1I =  DIMAG(Z1)
        Z2 = R*(COTH + S2*SITH)
        Z2R =   DBLE(Z2)
        Z2I =  DIMAG(Z2)
C
        IF  (Z1R .GE. ZER) THEN
          FZ1 = FC*(Z1 - CDSQRT(Z1**2 - CHL**2)) + GF1*Z1
          ELSE
          FZ1 = FC*(Z1 + CDSQRT(Z1**2 - CHL**2)) + GF1*Z1
        END IF
C
        IF  (Z2R .GE. ZER) THEN
          PZ2 = PC*(Z2 - CDSQRT(Z2**2 - CHL**2)) + GF2*Z2
          ELSE
          PZ2 = PC*(Z2 + CDSQRT(Z2**2 - CHL**2)) + GF2*Z2
        END IF
C
        U = 2.D0*DBLE(P1*FZ1 + P2*PZ2) - WXY*Y
        V = 2.D0*DBLE(Q1*FZ1 + Q2*PZ2) + WXY*X
C
        UN(I,1) = U
        UN(I,2) = V
C
      END DO
C
      RETURN
      END
C     ------------------------------------------------------------------
      SUBROUTINE DATG(RA,X,Y,TH)
C     ------------------------------------------------------------------
      IMPLICIT DOUBLE PRECISION (A-H,O-Z)
      COMMON/C1/PI,TPI,RSQ2,RSQ3,RSQ6
C
       TH = DATAN2(Y,RA*X)
C
      RETURN
      END
C     ------------------------------------------------------------------
      SUBROUTINE C_INIT1BCC !for BES100 crystal structure of IRON
C     Subroutine of constants (numerical,material,crack)
C     ------------------------------------------------------------------
      IMPLICIT DOUBLE PRECISION (A-H,O-Z)
      COMMON/C1/PI,TPI,RSQ2,RSQ3,RSQ6
      COMMON/C2/A11,A12,A16,A26,A22,A66,AS,FK,CHL
C
C     NUMERICAL CONSTANTS
C
      PI   = 4.D0*DATAN(1.D0)
      TPI  = 2.D0*PI
      USTPI= 1.D0/TPI
      RSQ2 = DSQRT(2.D0)
      RSQ3 = DSQRT(3.D0)
      RSQ6 = DSQRT(6.D0)
C
C     MATERIAL CONSTANTS
C     Elastic stiffness constants [units:GPa]
C     Fe Elastic moduli computed with VP potential
C     (...and the program matrot.f)
      C11 = 243.1D0
      C12 = 137.5D0
      C13 = 137.5D0
      C22 = 243.1D0
      C23 = 137.5D0
      C33 = 243.1D0
      C44 = 121.8D0
      C55 = 121.8D0
      C66 = 121.8D0
C
C     Elastic compliance constants [units:1/GPa]
C     (...computed by www.bluebit.gr)
      S11 =  (C11+C12)/(C11**2 + C11*C12 - 2.D0*C12**2)
      S12 = -C12/(C11**2 + C11*C12 - 2.D0*C12**2)
      S13 = -C12/(C11**2 + C11*C12 - 2.D0*C12**2)
      S22 =  (C11+C12)/(C11**2 + C11*C12 - 2.D0*C12**2)
      S23 = -C12/(C11**2 + C11*C12 - 2.D0*C12**2)
      S33 =  (C11+C12)/(C11**2 + C11*C12 - 2.D0*C12**2)
```

```
      S44 =  1.D0/(C44)
      S55 =  1.D0/(C44)
      S66 =  1.D0/(C44)
C
C     Plane-strain elastic compliances [units:1/GPa]
      A11 = S11 - (S13*S13)/S33
      A12 = S12 - (S13*S23)/S33
      A16 = 0.D0
      A22 = S22 - (S23*S23)/S33
      A26 = 0.D0
      A66 = S66
C
C     Coefficient of energy release rate [units:1/GPa]
      CG1 = (A11*A22)/2.D0
      CG2 = DSQRT(A22/A11)+(2.D0*A12 + A66)/(2.D0*A11)
      CG  = DSQRT(CG1*CG2)
C
C     Surface excess energy (100) [units:GPa*A]
      GS  = 18.6779D0
C
C     Griffith's criterion [units:GPa*A**0.5]
      SIFG =  DSQRT((2.D0*GS)/CG)
C
      PRINT *,'MATERIAL CONSTANTS'
      PRINT *,' '
      PRINT *,'stiffness elastic constants'
      PRINT *,'C11 = ',C11 ,'[GPa]'
      PRINT *,'C12 = ',C12 ,'[GPa]'
      PRINT *,'C13 = ',C13 ,'[GPa]'
      PRINT *,'C22 = ',C22 ,'[GPa]'
      PRINT *,'C23 = ',C23 ,'[GPa]'
      PRINT *,'C33 = ',C33 ,'[GPa]'
      PRINT *,'C44 = ',C44 ,'[GPa]'
      PRINT *,'C55 = ',C55 ,'[GPa]'
      PRINT *,'C66 = ',C66 ,'[GPa]'
      PRINT *,' '
C
      PRINT *,'compliance elastic constants'
      PRINT *,'S11 = ',S11 ,'[1/GPa]'
      PRINT *,'S12 = ',S12 ,'[1/GPa]'
      PRINT *,'S13 = ',S13 ,'[1/GPa]'
      PRINT *,'S22 = ',S22 ,'[1/GPa]'
      PRINT *,'S23 = ',S23 ,'[1/GPa]'
      PRINT *,'S33 = ',S33 ,'[1/GPa]'
      PRINT *,'S44 = ',S44 ,'[1/GPa]'
      PRINT *,'S55 = ',S55 ,'[1/GPa]'
      PRINT *,'S66 = ',S66 ,'[1/GPa]'
      PRINT *,' '
C
      PRINT *,'plane-strain COMPLIANCE elastic constants'
      PRINT *,'A11 = ',A11,'[1/GPa]'
      PRINT *,'A12 = ',A12,'[1/GPa]'
      PRINT *,'A16 = ',A16,'[1/GPa]'
      PRINT *,'A22 = ',A22,'[1/GPa]'
      PRINT *,'A26 = ',A26,'[1/GPa]'
      PRINT *,'A66 = ',A66,'[1/GPa]'
      PRINT *,' '
C
      PRINT *,'stress intensity factor (critical)'
      PRINT *,'CG  = ',CG,'[1/GPa]'
      PRINT *,'GS  = ',GS,'[GPa*A]'
      PRINT *,'SIFG  = ',SIFG,'[GPa*A**0.5]'
      PRINT *,' '
C
C     CRACK CONSTANTS
C
      PRINT *,'CRACK CONSTANTS'
      PRINT *,'Enter value for:'
      PRINT *,'EXTERNAL APPLIED STRESS [units:GPa]'
      PRINT *,'along [010]-direction'
      READ  *,AS
      PRINT *,'Enter value for:'
      PRINT *,'CRACKS HALF LENGHT'
      PRINT *,'[units:a0]'
      PRINT *,'identity period along x=[ 1  0  0] direction'
      READ  *,CHL
C
```

```
      AS  =  DBLE(AS)
      FK  =  0.D0
      ASX =  AS*FK
      ASY =  AS
      CHL =  DBLE(CHL)*(1.D0)
C
      PRINT *, 'UNIAXIAL/BIAXIAL LOADING CONDITIONS'
      PRINT *, 'APPLIED EXTERNAL STRESSES'
C
      PRINT *, 'along x=[ 1  0  0] to infinity', ASX,'[GPa]'
      PRINT *, 'along y=[ 0  1  0] to infinity', ASY,'[GPa]'
      PRINT *, 'CRACK LENGTH 2a where,', 'a =',CHL,'[a0]'
C
      RETURN
      END
C     ------------------------------------------------------------------
      SUBROUTINE FIXORD(NP,XPD,IP,L,M)
C     Subroutine that arrange the FIX/DYN atoms of the configuration
C     ------------------------------------------------------------------
      IMPLICIT DOUBLE PRECISION (A-H,O-Z)
C
      DIMENSION XPD(NP,3)
      DIMENSION IP(NP,3),L(NP),M(NP)
C
      WRITE(*,FMT='(/)')
      PRINT *,'SUBROUTINE FIXORD ACTIVATE'
      PRINT *,'NP = ',NP,'atoms found'
C
      MFA = 0
C
      DO I = 1, NP
        IF (L(I) .EQ. 1) THEN
          MFA = MFA + 1
          WRITE (90,FMT='(I6,3(2X,F22.15),2X,5I5)')
     $    MFA,(XPD(I,IC),IC=1,3),(IP(I,IC),IC=1,3),L(I),M(I)
        ENDIF
      END DO
C
      MDA = MFA
C
      DO  I = 1, NP
        IF (L(I) .EQ. 0) THEN
          MDA = MDA + 1
          WRITE (90,FMT='(I6,3(2X,F22.15),2X,5I5)')
     $    MDA,(XPD(I,IC),IC=1,3),(IP(I,IC),IC=1,3),L(I),M(I)
        END IF
      END DO
C
      NFA = MFA
      NDA = MDA-MFA
C
      PRINT *,NFA,'FIXED atoms found'
      PRINT *,NDA,'DYNAMIC atoms found'
      PRINT *,'total atoms',MDA,'atoms found'
      PRINT *,'of initial',NP,'atoms'
C
      RETURN
      END
C     ------------------------------------------------------------------
      SUBROUTINE BES100(NP,LA,LB,LC,ZLS2,TR,XP,IP,L,M)
C     Construction of perfect crystal lattice
C     (coordinares system : x=[ 1  0  0], y=[ 0  1  0], z=[ 0  0  1])
C     ------------------------------------------------------------------
      IMPLICIT DOUBLE PRECISION (A-H,O-Z)
      COMMON/C1/PI,TPI,RSQ2,RSQ3,RSQ6
      COMMON/C2/A11,A12,A16,A26,A22,A66,AS,FK,CHL
C
      DIMENSION BZ(3),TR(3),U(2,3),ZLS2(3)
      DIMENSION XP(NP,3),IP(NP,3)
      DIMENSION L(NP),M(NP)
C
      DATA U/0.D0,1.D0,               !x=[ 1  0  0]
     $       0.D0,1.D0,               !y=[ 0  1  0]
     $       0.D0,1.D0/               !z=[ 0  0  1]
C            at1, at2
C
      WRITE(*,FMT='(/,A,/,2(3F5.0,/))')
```

```
     $             '  MATRICE U(2,3)   ',((U(I,J), J = 1, 3),I = 1, 2)
C
      TR(1) = ZLS2(1) - 0.5D0*0.5D0    !x=[ 1  0  0]
      TR(2) = ZLS2(2) - 0.5D0*0.5D0    !y=[ 0  1  0]
      TR(3) = ZLS2(3) - 0.5D0*0.5D0    !z=[ 0  0  1]
C
C     Fixed boundary conditions
C     (along x=[ 1  0  0] and y=[ 0  1  0] directions)
C
      XMAX =   ZLS2(1) - 7.D0
      XMIN = -(ZLS2(1) - 7.D0)
      YMAX =   ZLS2(2) - 7.D0
      YMIN = -(ZLS2(2) - 7.D0)
C
C     Minimization criterion
C     (along x=[ 1  0  0] and y=[ 0  1  0] directions)
C
      YCH =   1.5D0
      YCL =  -1.5D0
      XCH =   CHL + 10.D0
      XCL = -(CHL + 10.D0)
C
      I = 0
      DO JA = 1, LA
        BZ(1) = DBLE(JA)
        DO JB = 1, LB
          BZ(2) = DBLE(JB)
          DO JC = 1, LC
            BZ(3) = DBLE(JC)
            DO JD = 1, 2
              I = I + 1
C
              XP(I,1) = U(JD,1)*0.5D0 + (BZ(1)-1.D0)*1.D0 - TR(1)
              XP(I,2) = U(JD,2)*0.5D0 + (BZ(2)-1.D0)*1.D0 - TR(2)
              XP(I,3) = U(JD,3)*0.5D0 + (BZ(3)-1.D0)*1.D0 - TR(3)
              PX = 1.D0 + U(JD,1) + (BZ(1) - 1.D0)*2.D0
              PY = 1.D0 + U(JD,2) + (BZ(2) - 1.D0)*2.D0
              PZ = 1.D0 + U(JD,3) + (BZ(3) - 1.D0)*2.D0
              IP(I,1) = IDNINT(PX)
              IP(I,2) = IDNINT(PY)
              IP(I,3) = IDNINT(PZ)
C
C             Fixed boundary conditions
C
              IF (XP(I,1) .GE. XMAX .OR. XP(I,1) .LE. XMIN) THEN
                L(I) = 1
           ELSE IF (XP(I,2) .GE. YMAX .OR. XP(I,2) .LE. YMIN) THEN
                L(I) = 1
              ELSE
                L(I) = 0
              END IF
C
C             Minimization criterion
C
              IF (XP(I,1) .LE. XCH .AND. XP(I,1) .GE. XCL  .AND.
     $            XP(I,2) .LE. YCH .AND. XP(I,2) .GE. YCL) THEN
                M(I) = 1
              ELSE
                M(I) = 0
              END IF
C
              WRITE(20,FMT='(I5,2X,6(F22.15,1X),4I5)')
     $             I,(XP(I,J),J=1,3),
     $             PX,PY,PZ,(IP(I,IC),IC=1,3),L(I)
C
            END DO
          END DO
        END DO
      END DO
C
      WRITE(*,*) 'BES100 : Lattice construction OK IM =',I,' atoms'
C
C     Fixed/Criterion atoms CONTROL
C
      DO I=1,NP
        IF (L(I) .EQ. 1) THEN
!       IF (M(I) .EQ. 1) THEN
```

```
          WRITE(21,FMT='(I5,2X,6(F22.15,1X),5I5)')
     $              I,(XP(I,J),J=1,3),
     $              PX,PY,PZ,(IP(I,IC),IC=1,3),L(I),M(I)
        END IF
       END DO
C
       RETURN
       END
C      ---------------------------------------------------------------
```

Appendix G: N-body character

The present appendix aims to demonstrate the N-body character of the inter-atomic potential of aluminium [ZAC2017] used in our work. To this end, the analytic expression of the resultant force should be determined. According to the equation III.9, the acting force on the atom k (figure G.1), due to the interaction with the neighbouring atoms, is given by:

$$\vec{F}_k = -\vec{\nabla}_k U_{Al} = \frac{\partial}{\partial \vec{r}_k} U_{Al} = \left(\frac{\partial}{\partial x_k}\vec{e}_1 + \frac{\partial}{\partial y_k}\vec{e}_2 + \frac{\partial}{\partial z_k}\vec{e}_3\right) U_{Al} \qquad (G.1)$$

By substituting the potential energy (equations III.11 and III.12) into the above equation,

$$\vec{F}_k = -\vec{\nabla}_k \sum_i^{r<r_c} \sum_{j\neq i}^{r<r_c} \Phi_r(r_{ij}) + \vec{\nabla}_k \sum_i^{r<r_c} \sqrt{\sum_{j\neq i}^{r<r_c} \Phi_a(r_{ij})} - \vec{\nabla}_k \sum_i^{r<r_c} \sum_{j\neq i}^{r<r_c} \Phi_o(r_{ij})$$

$$\vec{F}_k = \vec{F}_k^r + \vec{F}_k^a + \vec{F}_k^o \qquad (G.2)$$

The first term is equal to

$$\vec{F}_k^r = -\sum_i^{r<r_c} \sum_{j\neq i}^{r<r_c} \vec{\nabla}_k \Phi_r(r_{ij}) = -\sum_i^{r<r_c} \sum_{j\neq i}^{r<r_c} \left[\left(\frac{\partial}{\partial x_k}\vec{e}_1 + \frac{\partial}{\partial y_k}\vec{e}_2 + \frac{\partial}{\partial z_k}\vec{e}_3\right) \Phi_r(|\vec{r}_j - \vec{r}_i|)\right]$$

$$\vec{F}_k^r = -\sum_i^{r<r_c} \sum_{j\neq i}^{r<r_c} \left\{\frac{\partial \Phi_r(r_{ij})}{\partial r_{ij}} \left(\frac{\partial}{\partial x_k}\vec{e}_1 + \frac{\partial}{\partial y_k}\vec{e}_2 + \frac{\partial}{\partial z_k}\vec{e}_3\right) \left[(x_j - x_i)^2 + (y_j - y_i)^2 + (z_j - z_i)^2\right]^{\frac{1}{2}}\right\}$$

Since, only the terms $k = i$ and $j \neq i$ (i.e. $j \neq k$) are non-zero,

$$\vec{F}_k^r = -\sum_{j\neq k}^{r<r_c} \left\{2\frac{\partial \Phi_r(r_{kj})}{\partial r_{kj}} \frac{1}{|\vec{r}_{kj}|}\left[(x_j - x_k)\vec{e}_1 + (y_j - y_k)\vec{e}_2 + (z_j - z_k)\vec{e}_3\right]\right\}$$

$$\vec{F}_k^r = -2\sum_{k\neq i}^{r<r_c} \left(\frac{\partial \Phi_r(r_{kj})}{\partial r_{kj}} \frac{\vec{r}_{kj}}{|\vec{r}_{kj}|}\right) \qquad (G.3)$$

Similarly, the second and third term of the equation G.2 are respectively equal to

$$\vec{F}_k^a = \sum_i^{r<r_c} \vec{\nabla}_k \sqrt{\sum_{j\neq i}^{r<r_c} \Phi_a(r_{ij})} = \sum_i^{r<r_c} \frac{r_{ij}}{\partial r_k} \frac{\partial \Phi_a(r_{ij})}{\partial r_{ij}} \frac{\partial}{\partial \Phi_a} \left[\sqrt{\sum_{j\neq i}^{r<r_c} \Phi_a(r_{ij})} \right]$$

$$\vec{F}_k^a = \frac{\sum_{j\neq k}^{r<r_c} \left(\frac{\partial \Phi_a(r_{kj})}{\partial r_{kj}} \frac{\vec{r}_{kj}}{|\vec{r}_{kj}|} \right)}{2\sqrt{\sum_{j\neq k}^{r<r_c} \Phi_a(r_{kj})}} + \sum_{i\neq k}^{r<2r_c} \frac{\frac{\partial \Phi_a(r_{ik})}{\partial r_{ik}} \frac{\vec{r}_{ik}}{|\vec{r}_{ik}|}}{2\sqrt{\sum_{\substack{j\neq i \\ i\neq k}}^{r<2r_c} \Phi_a(r_{ij})}} \qquad (G.4)$$

and,

$$\vec{F}_k^o = -\sum_i^{r<r_c} \sum_{j\neq i}^{r<r_c} \vec{\nabla}_k \Phi_o(r_{ij}) = -2 \sum_{k\neq i}^{r<r_c} \left(\frac{\partial \Phi_o(r_{kj})}{\partial r_{kj}} \frac{\vec{r}_{kj}}{|\vec{r}_{kj}|} \right) \qquad (G.5)$$

Therefore, the analytic expression of the total force on the atom k is equal to:

$$(G.2) \Rightarrow \vec{F}_k = -2 \sum_{k\neq i}^{r<r_c} \left(\frac{\partial \Phi_r(r_{kj})}{\partial r_{kj}} \frac{\vec{r}_{kj}}{|\vec{r}_{kj}|} \right) + \frac{\sum_{j\neq k}^{r<r_c} \left(\frac{\partial \Phi_a(r_{kj})}{\partial r_{kj}} \frac{\vec{r}_{kj}}{|\vec{r}_{kj}|} \right)}{2\sqrt{\sum_{j\neq k}^{r<r_c} \Phi_a(r_{kj})}}$$

$$+ \sum_{i\neq k}^{r<2r_c} \frac{\frac{\partial \Phi_a(r_{ik})}{\partial r_{ik}} \frac{\vec{r}_{ik}}{|\vec{r}_{ik}|}}{2\sqrt{\sum_{\substack{j\neq i \\ i\neq k}}^{r<2r_c} \Phi_a(r_{ij})}} - 2 \sum_{k\neq i}^{r<r_c} \left(\frac{\partial \Phi_o(r_{kj})}{\partial r_{kj}} \frac{\vec{r}_{kj}}{|\vec{r}_{kj}|} \right) \qquad (G.6)$$

It should be noted that the range of the third term in the above equation is doubled compared to the other terms, because the sum of the dominator runs over $j \neq i \neq k$. The figure below illustrates this point: in order to calculate the force acting on the atom k, the contributions from all of its neighbours, identified as j, should be first computed within the cut-off sphere (with radius r_c) and contributions from the i-atoms, the neighbouring atoms of j, should be also considered. Consequently, the range of interactions contributing to the calculation of the acting force ($2r_c$) amounts on the atom k has double the length compared to the range of interactions required to determine its potential energy (r_c).

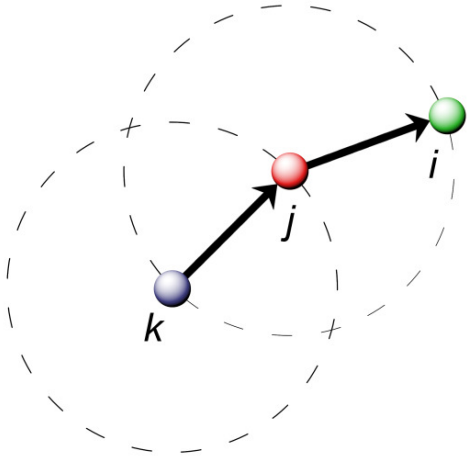

Figure G.1: Force calculation. The spheres of interactions are defined by the cut-off radius, r_c.

Appendix H: Crystal structure

To construct the atomic model of a crack configuration inside a material system it is necessary initially to form its ground state structure at the atomic scale, the perfect crystalline lattice. The ground state atomic structure describes the manner in which the atoms are spatially arranged inside a defect-free solid corresponding to the lowest potential energy. The type of the perfect crystalline lattice can be conveniently defined by describing the arrangement of the Bravais unit cell. This unit cell contains all the symmetry information of the lattice, and thus by replicating it in space along the directions of its reference coordinate system, perfect crystals at any size are formed. This study focuses on two metals corresponding to different types of crystal structures:

(1) aluminium with face-centered cubic (fcc), and

(2) alpha iron with body-centered cubic (bcc) structure.

The Bravais unit cells of both the fcc and bcc structures have been constructed with orientation along the cubic axes (i.e. the $x = [100]$, $y = [010]$ and $z = [001]$ crystallographic direction), as illustrated in figure H.1.

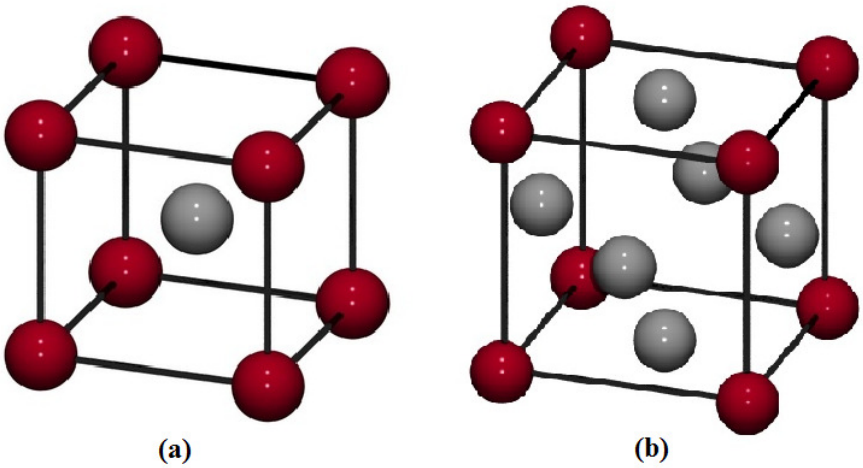

Figure H.1: Unit cells of (a) body-centered cubic and (b) face-centered cubic types of crystal lattices.

The orientation of the unit cells has been chosen compatible with the crystallographic orientation of the crack configuration (Chapter III). Crystallographic features (Appendix E) of both the fcc and bcc units cells, referring to the cubic coordinate system, are given respectively in the tables H.1 and H.2. The two types of crystals have been developed in orthogonal shape models. The model for fcc aluminium consisted of 400 planes in x,

160 planes in y and 12 planes in the z direction while for bcc iron the number of planes in the y direction is twice larger. These models of $N = 384000$ atoms were computationally constructed using the FORTRAN programming language (Appendix F).

Table H.1: Crystallographic features of the fcc unit cell oriented along the cubic axes.

Crystallographic orientation	**Cubic axes coordinate system**		
	$\boldsymbol{x = [100]}$	$\boldsymbol{y = [010]}$	$\boldsymbol{z = [001]}$
identity period along $[hkl]$ direction	a_{fcc}	a_{fcc}	a_{fcc}
spacing between planes (hkl) planes	$a_{fcc}/2$	$a_{fcc}/2$	$a_{fcc}/2$
plane number within unit cell	2	2	2
atoms number per (hkl) plane	2	2	2
Unit cell matrix of atomic position coordinates			
Atoms number	$\boldsymbol{x = [100]}$	$\boldsymbol{y = [010]}$	$\boldsymbol{z = [001]}$
1	0	0	0
2	$a_{fcc}/2$	$a_{fcc}/2$	0
3	$a_{fcc}/2$	0	$a_{fcc}/2$
4	0	$a_{fcc}/2$	$a_{fcc}/2$

Table H.2: Crystallographic features of the bcc unit cell oriented along the cubic axes.

Crystallographic orientation	**Cubic axes coordinate system**		
	$\boldsymbol{x = [100]}$	$\boldsymbol{y = [010]}$	$\boldsymbol{z = [001]}$
identity period along $[hkl]$ direction	a_{bcc}	a_{bcc}	a_{bcc}
spacing between planes (hkl) planes	$a_{bcc}/2$	$a_{bcc}/2$	$a_{bcc}/2$
plane number within unit cell	2	2	2
atoms number per (hkl) plane	1	1	1
Unit cell matrix of atomic position coordinates			
Atoms number	$\boldsymbol{x = [100]}$	$\boldsymbol{y = [010]}$	$\boldsymbol{z = [001]}$
1	0	0	0
2	$a_{bcc}/2$	$a_{bcc}/2$	0

Appendix I: Molecular Dynamics

In the current appendix the key ingredients of the molecular dynamics (MD) method are presented. In addition, we describe the way in which a program of MD can be modified in order to perform energy minimization (EM) of an atomic system. Both MD and EM simulations in our study were performed on the cluster units of the ''Service de Recherches Métallurgiques Appliquées'' of CEA Saclay using the LFNPT, a simulation FORTRAN code package developed by V. Pontikis [ASL1998a, ASL1998b, ASL2000]. The general structure of the MD technique consists in the following four main steps:

(1) **Initialization**: the definition of the initial conditions of the atomic configuration, i.e. the atomic positions and velocities at the time $t = 0$, and the implementation of the boundary conditions.

(2) **Interactions - Forces calculation**: the atoms interact through the inter-atomic potential, which provides the potential energy and force for each atom within the system.

(3) **Integration**: The atomic system evolves in time through the Newton's equations of motion (Classical Mechanics). The solution of these equations is performed numerically by the using an appropriate integration algorithm.

(4) **Interpretation - Analysis**: Periodic collection and storage of atomic positions, momenta, forces and energies, allow obtaining thermodynamic properties expressed as time averages of microscopic observables (Statistical Mechanics).

I.1. Equations of motion

In a classical system of N interacting atoms, the time-evolution of the system is determined by the Newton's equations of motion:

$$\vec{F}_i(t) = m_i \frac{d^2\vec{r}_i(t)}{dt^2} \ (i = 1, \dots, N) \qquad (I.1)$$

where m_i, $\vec{r}_i(t) = \{r_{xi}(t), r_{yi}(t), r_{zi}(t)\}$ and $\vec{F}_i(t) = \{F_{xi}(t), F_{yi}(t), F_{zi}(t)\}$ are the mass, the position and the acting force of each atom i at time t. The relation I.1 constitutes a set of $3N$ coupled second order differential equations, whose solution start requires the

knowledge of the system's initial conditions, i.e. the positions $\left(\vec{r}_1(0), \ldots, \vec{r}_N(0)\right)$ and velocities $\left(\vec{v}_1(0), \ldots, \vec{v}_N(0)\right)$ of the atoms at the initial moment $(t = 0)$. The forces calculation is performed by assuming that the system is conservative [YOU1999]. Under this hypothesis, the force acting on each atom depends only from the position coordinates of the system's other atoms; hence, can be expressed and determined as the gradient of an analytic potential energy function U_{pot},

$$\vec{F}_i(\vec{r}_1, \ldots, \vec{r}_N) = -\nabla_i U_{pot}(\vec{r}_1, \ldots, \vec{r}_N) \;\; (i = 1, \ldots, N) \qquad (I.2)$$

where ∇_i is the derivative operation for each atom i:

$$\nabla_i \equiv \frac{\partial}{\partial \vec{r}_i} = \frac{\partial}{\partial_{xi}}\vec{\imath} + \frac{\partial}{\partial_{yi}}\vec{\jmath} + \frac{\partial}{\partial_{zi}}\vec{k}$$

Thus, by combining the equations I.1 and I.2 one gets the expression:

$$m_i \frac{d^2\vec{r}_i(t)}{dt^2} = \vec{F}_i(t) = -\nabla_i U_{pot}\left(\vec{r}_1(t), \ldots, \vec{r}_N(t)\right), \qquad (i = 1, \ldots, N) \qquad (I.3)$$

which is the base of the classical molecular dynamics method [GOU2006, GRI2007]. Equations I.3 satisfy time reversibility and conservation of the total energy [GOL2002].

I.2. Integration Algorithm

For atomic systems containing a large number of particles, the analytic solution of the equations I.3 is practically difficult. Thus, MD programs solve Newton's equations numerically by using integration algorithms. All integration algorithms determine the positions ($\vec{r}$), velocities ($\vec{v}$) and accelerations ($\vec{a}$) of the system's particles for a specific time using finite difference methods based on Taylor series expansion [ALL1987, CHA2006]. However, the choice of an algorithm appropriate to MD method complies with specific requirements, such as [ALL1987, GUN1990]:

(a) to satisfy the energy and momentum conservation

(b) to be time-reversible

(c) to preserve volume in the phase-space

Additional requirements are about performance:

(d) to be fast and with low computational cost

(e) to be accurate

I.2.1. Verlet algorithm

In 1967, Loup Verlet has proposed a time-integration algorithm to numerically solve the Newton's equations of motion, based on the central difference approach [VER1967]. The algorithm is derived from a Taylor expansion of the positions, forward and backward in time:

$$\vec{r}(t+\delta t) = \vec{r}(t) + \vec{v}(t)\delta t + \frac{1}{2!}\vec{\alpha}(t)\delta t^2 + \frac{1}{3!}\vec{b}(t)\delta t^3 + \mathcal{O}(\delta t^4) \qquad (I.4)$$

$$\vec{r}(t-\delta t) = \vec{r}(t) - \vec{v}(t)\delta t + \frac{1}{2!}\vec{\alpha}(t)\delta t^2 - \frac{1}{3!}\vec{b}(t)\delta t^3 + \mathcal{O}(\delta t^4) \qquad (I.5)$$

where $\vec{v} = d\vec{r}/dt$, $\vec{\alpha} = d^2\vec{r}/dt^2 = \vec{F}/m$ and $\vec{b} = d^3\vec{r}/dt^3$ for every atom and δt is the time step of the numerical scheme. The sum of the equations I.4 and I.5 gives the Verlet algorithm:

$$\vec{r}(t+\delta t) = 2\vec{r}(t) - \vec{r}(t-\delta t) + \vec{\alpha}(t)\delta t^2 + \mathcal{O}(\delta t^4) \qquad (I.6)$$

By essence, the positions in equation I.6, $\vec{r}(t+\delta t)$ and $\vec{r}(t-\delta t)$, are symmetrical in respect to time thus making the Verlet algorithm time-reversible. Moreover, the Verlet algorithm satisfies the conservation of energy since the forces ($\vec{F} = m \cdot \vec{\alpha}$) depends only on the position coordinates in the framework of a conservative system. Finally, as can be seen in equation I.6 numerical errors are of the order of δt^4. Atomic velocities are be obtained by subtracting equation I.4 and I.5.

$$\vec{r}(t+\delta t) - \vec{r}(t-\delta t) = 2\vec{v}(t)\delta t + \mathcal{O}(\delta t^3)$$

or

$$\vec{v}(t) = \frac{\vec{r}(t+\delta t) - \vec{r}(t-\delta t)}{2\delta t} + \mathcal{O}(\delta t^2) \qquad (I.7)$$

As a result, the numerical error in velocities per simulation time step is of the order of δt^2; hence larger than that committed when counting atomic positions. The algorithm is not ''self-starting'' since additional the initial values $\vec{r}(0)$ the equation I.6 requires the previous

position $\vec{r}(0-\delta t)$ to tackle the first time step. However, in a typical initial value problem the quantities $\vec{r}(0)$ and $\vec{v}(0)$ are given instead. By estimating some suitable $\vec{r}(0-\delta t)$ in order to start a Verlet calculation one solve not the given initial values problem but a very similar one. Despite its imperfections, the Verlet algorithm has been widely used in MD simulations since is simple to applied, numerically stable and sufficient accurate.

I.2.2. Accuracy and time step

Equations I.6 and I.7 constitute approximation of the analytic solution and therefore are characterized by accuracy errors. These errors are divided into two categories: the ''truncation errors'' [STO2002] that related to the truncation of the Taylor's expansion in equations I.4 and I.5, and the ''round-off errors'' [WIL1994] that relate to the discrete representation of numbers in digital computers. Truncation errors are decreasing with decreasing the time step; hence a relatively small δt generates results accurate trajectories in phase-space. On the other hand, the δt should be relatively large in order to sample wide the phase space and the time evolution of the system. Moreover, the increase of δt is accompanied by a reduction of the computational cost [SCH2001]. Therefore, the optimum value of δt is a compromise between numerical and statistical accuracy and computational cost. The regular size of δt for a crystalline system in atomic level is equal to $1-10$ femto-seconds (where $fsec = 10^{-15} sec$). The time step size is determined by testing the energy conservation with the time evolution of the system. Experience has shown that Verlet algorithm presents in general moderate short time energy conservation but negligible energy drift over long times, even with relatively large δt. Therefore, is considered as the best choice for the present study.

I.3. Statistical averaging

I.3.1. Ergodic Hypothesis

In MD technique, the system evolves in time by passing through different microscopic states Ω in phase-space Γ; consequently, the MD method generates information at the microscopic level, atomic positions and momenta, as function of time. The collective contribution of the atoms in the properties of the system can be expressed on the macro-scale using averaging approaches. This is the field of Statistical Mechanics [MA1985,

PAT2011]. Suppose that A is a macroscopic equilibrium property of the system under study, such as the temperature, stress, pressure etc. Consider that is possible to determine its instantaneous value $\mathcal{A}$ for each microstate Ω along the generated trajectory in phase-space. To obtain the macroscopic observable quantity of A the average value of $\mathcal{A}$ is required. The approach used in the MD method to evaluate average quantities is based on time averaging. The time-average of a property is defined according to:

$$A_{time} = \langle \mathcal{A} \rangle_{time} = \lim_{T \to \infty} \frac{1}{T} \int_0^T \mathcal{A}\big(\Gamma(t)\big) dt \qquad (I.8)$$

where $\mathcal{A}$ is a function of the phase-space $\Gamma(t)$ and the observation time T goes to infinity. However, the averaging approaches used in Statistical Mechanics are not based on time like the MD method. In particular, Gibbs developed a more analytical averaging approach by introducing the concept of the ensemble. An ensemble can be regarded as a collection of a very large number of systems corresponding in different microstates but sharing a common set of macroscopic properties. Each miscrostate Ω can be found in the place-space Γ with a probability density ρ, which is unique for every ensemble ($\rho \equiv \rho_{ens}$). Hence, the macroscopic observable quantity of A is defined through the ensemble-average:

$$A_{ensemble} = \langle \mathcal{A} \rangle_{ens} = \int \mathcal{A}(\Omega) \rho_{ens}(\Omega)\, d\Omega \qquad (I.9)$$

where $\langle \mathcal{A} \rangle_{ens}$ is taken over a large number of replicas of the system. At a first glance, one can say that $\langle \mathcal{A} \rangle_{ens}$ and $\langle \mathcal{A} \rangle_{time}$ are not equal. Nevertheless, by allowing the system to evolve for infinite amount of time, it will be able to pass through all the possible microscopic states in phase-space. Such a system is called ergodic and establishes equality between the time-average and the ensemble-average:

$$\langle \mathcal{A} \rangle_{ens} = \langle \mathcal{A} \rangle_{time} \qquad (I.10)$$

a relation also known as the ergodic hypothesis [BON2007]. This suggests that if a MD system samples a sufficient amount of the phase-space then the simulation can generates enough information to satisfy the ergodic hypothesis, and therefore to provide reliable information regarding the properties of the system.

I.3.2. Statistical Ensembles

In Statistical Mechanics, the statistical ensembles can be classified according to its conservative-constant macroscopic quantities [GIB1902]:

Micro-canonical ensemble (NVE): It represents the collection of possible microscopic states of a mechanical system which is characterized by a fixed number of atoms (symbol: N), in a fixed volume (symbol: V) and with an exactly specified and constant total energy (symbol: E). An ensemble as such corresponds to an isolated system which cannot exchange energy or particles with its environment. The NVE-ensemble constitutes the most fundamental ensemble of molecular dynamics simulation. In a simulation of an isolated system where the total energy is conserved, the temperature is fluctuated.

Canonical ensemble (NVT): It can be regarded as the collection of all thermodynamic states of a closed system which is characterized by a fixed number of atoms (symbol: N), in a fixed volume (symbol: V) at a fixed temperature (symbol: T). The NVT-ensemble maintain its temperature through the use a thermostat. In particular, the thermostat, acting as a ''heat bath'', supplies or removes ''heat'' in the form of energy from the system whenever is required. As a result, in a simulation of a canonical system at a fixed temperature, the total energy is not a constant macroscopic observable.

Isothermal-isobaric ensemble (NPT): It is a mechanical ensemble characterized by a fixed number of atoms (symbol: N) and maintains constant pressure (symbol: P) and constant temperature (symbol: T) applied. To maintain a constant temperature and pressure in a NPT system requires the use of a thermostat and a barometer, respectively. Specifically, the barostat fixes the pressure of the system by altering its volume whenever is necessary.

Other categories of statistical ensembles are the grand canonical (μVT), the isoenthalpic-isobaric (NPH) and the open statistical (μVT) ensembles. It is worth mentioning that by increasing the number of the atoms, the behaviour of the different types of ensembles converges. Ensembles available in the LFNPT molecular dynamic code are the NVE, NVT, NPT and NPH.

I.3.3. Average properties

The determination of the average value of a system property in MD simulation is performed over a finite period of time T_{av}. However, the proper performance of the averaging procedure requires satisfaction of the following two conditions: Firstly, it is crucial to ensure that the actual averaging is performed after the system reaches its thermodynamic equilibrium states. Consequently, an equilibration period T_{eq} must be preceded before the averaging calculation. Secondly, the period that the averaging, T_{av}, is conducted should be long enough to satisfy the ergodic hypothesis. As a result, the average property of a system provided by the MD simulation can be expressed as:

$$A \approx \langle \mathcal{A} \rangle_{MD} = \frac{1}{T_{av}} \int_{T_{eq}}^{T_{eq}+T_{av}} \mathcal{A}(t) dt \qquad (I.11)$$

Since the time-integration of equations of motion is performed by a discrete manner, with time-spacing δt, it produces a sequence of instantaneous values of the property of interest $\{A_i\}$. Consequently, the integral of the equation I.11 turns into a summation:

$$A \approx \langle \mathcal{A} \rangle_{MD} = \frac{1}{m} \sum_{i=1}^{m} \mathcal{A}_i \qquad (I.12)$$

where $\mathcal{A}_i = \mathcal{A}\left(T_{eq} + i\delta t\right)$ are the instantaneous values of A for each simulation time step i and $m = T_{av}/\delta t$ is the total number of time-steps during averaging procedure. The macroscopic observable A value obtained from a MD study usually contains systematic and statistical errors. Systematic errors in MD usually come from the model size limitations or poor equilibration of the system before averaging procedure. Such errors should be reduced as much as possible. On the other hand, the statistical errors are caused by the fact that the averaging measurements are performed for a finite period of time. This leads to statistical imprecision of the obtained mean value, A, as disputes the validity of the ergodic hypothesis. The statistical error can be estimated by the variance of the mean value through the use of Gaussian statistics. According to this, the variance of the mean value can then be expressed as:

$$\sigma^2(\langle \mathcal{A} \rangle_{MD}) = \frac{\sigma^2(\mathcal{A})}{m} \qquad (I.13)$$

with

$$\sigma^2(\mathcal{A}) = \langle \delta\mathcal{A}^2 \rangle_{MD} = \frac{1}{m}\sum_{i=1}^{m}(\mathcal{A}_i - \langle \mathcal{A} \rangle_{MD})^2 = \langle \mathcal{A}^2 \rangle_{MD} - \langle \mathcal{A} \rangle_{MD}^2 \qquad (I.14)$$

Thus, the final result of the average property is given by:

$$A = \langle \mathcal{A} \rangle_{MD} \pm \frac{\sigma(\mathcal{A})}{\sqrt{m}} \qquad (I.15)$$

I.4. **Damping method** [BEE1972, GEH1972, EVA1974, BEN1975, BEE1983]

A MD program can be amended to compute the static equilibrium configuration of an atomic system containing a structural defect, which corresponds to a local (or global) minimum of the potential energy function, $U_{pot}(\vec{r}_1, \ldots, \vec{r}_N)$. This can be done, by artificially damping the motion of the atoms at appropriate times and hence draw out progressively all the kinetic energy of the system. Consequently, in a static equilibrium calculation the system can characterized only at zero temperature. This computational approach based on the assumption that every atom can be treated as an individual oscillating mass point in a simple harmonic motion. According to the classical mechanics, when a one-dimensional harmonic oscillator is moving towards its equilibrium position, its velocity and acceleration have the same sign while when the oscillator moves away from its equilibrium position then its velocity and acceleration have opposite signs (figure I.1). In addition, according to the Newton's second law of motion, the acceleration and the restoring force of the oscillator are characterized by the same direction. Based on these, Evans and Beeler [EVA1974, BEE1972] introduced the idea of setting individually the velocity of any atom i to zero whenever the dot product between its velocity $\vec{v}_i$ and its net acting force $\vec{F}_i$ becomes negative, i.e.,

$$\text{If } \vec{v}_i \cdot \vec{F}_i \leq 0 \text{ then } \vec{v}_i = 0 \qquad (I.16)$$

Evans [EVA1974] called this approach as the ''micro-convergence'' method, which is also known in the literature as the ''localized damping'' (LD) method. The LD scheme prevents movement away from the equilibrium position but allows motion toward the equilibrium position for each atom on an individual basis.

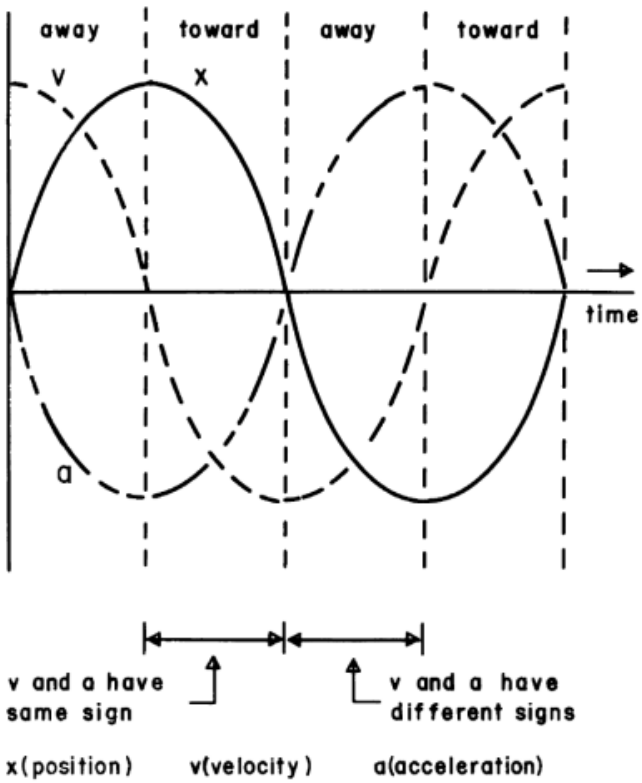

Figure I.1: As a mass point, in single harmonic motion, passes through the equilibrium position, the acceleration changes sign. This behaviour consist the basis for the local (micro-convergence) damping method [BEE1983].

Considering the fact the motion of atoms is three-dimensional, the damping criterion is applied independently to each Cartesian coordinate (x, y and z) of velocity and force vectors, i.e.,

$$\text{If } v_{i,x} \cdot F_{i,x} \leq 0 \text{ then } v_{i,x} = 0 \qquad (I.17a)$$

$$\text{If } v_{i,y} \cdot F_{i,y} \leq 0 \text{ then } v_{i,y} = 0 \qquad (I.17b)$$

$$\text{If } v_{i,z} \cdot F_{i,z} \leq 0 \text{ then } v_{i,z} = 0 \qquad (I.17c)$$

Thus, damping occurs only for those individual velocity components of an individual atom that are tending to cause a deviation from its static equilibrium position. The LD method is performed iteratively in finite time intervals, δt, and leads to the relaxation of the atomic configuration. This process constitutes the discrete time evolution of the atomic model in order to obtain its optimal static form. It is important to emphasize that only the static equilibrium configuration has physical significance, since the atomic trajectories generated by the relaxation process do not maintain thermodynamic quantities, as happen for the MD ensembles. Therefore, it is crucial to ensure that the atomic configuration has reached its

ground or equilibrium static state before the simulation completion. To this end, a relaxation criterion should be defined. The most commonly used relaxation criterion is the stabilization of the system's instantaneous value of the total potential energy in respect to the simulation time ($U_{tot} = f(t)$). A more precise one, is the stabilization of the variance of the mean value of the total potential energy, $\sigma^2(\langle U_{tot} \rangle)$, calculated over finite time intervals. Finally, it is worth mentioning that the sensitivity of the relaxation criterion can be improved if these studies are performed not globally but locally inside the system. For example, atomic regions close to structural defect are much more influenced by relaxation process.

Bibliography

1. [ABR1997] F.F. Abraham, D. Schneider, B. Land, D. Lifka, J. Skovira, J. Gerner and M. Rosenkrantz, Instability dynamics in three-dimensional fracture: An atomistic simulation, Journal of the Mechanics and Physics of Solids, Volume 45, Issue 9, (1997), pages 1461-1471.

2. [ALL1956] N.P. Allen, B.E. Hopkins and J.E. McLennan, The Tensile Properties of Single Crystals of High-Purity Iron at Temperatures from 100 to -253 degrees C, Proceedings A, The Royal Society, Volume 234, Issue 1197, (1956), pages 221-246.

3. [ALL1987] M.P. Allen and D.J. Tildesley, Computer Simulation of Liquids, Oxford University Press: Oxford, (1987).

4. [ARG2001] A.S. Argon, Mechanics and Physics of Brittle to Transitions in Fracture, Journal of Engineering Material and Technology, Volume 123, Issue 1, (2001), pages 1-11.

5. [ASL1998a] A. Aslanides and V. Pontikis, Atomistic calculation of the interaction between an edge dislocation and a free surface, Philosophical Magazine Letters, Volume 78, Issue 5, (1998), pages 377-383.

6. [ASL1998b] A. Aslanides and V. Pontikis, Atomistic study of dislocation cores in aluminium and copper, Computational Materials Science, Volume 10, Issues 1-4, (1998), pages 401-405.

7. [ASL2000] A. Aslanides and V. Pontikis, Numerical study of the athermal annihilation of edge-dislocation dipoles, Philosophical Magazine A, Volume 80, Issue 10, (2000), pages 2337-2353.

8. [BAR1965] T.H.K. Barron and M.L. Klein, Second-order elastic constants of a solid under stress, Proceedings of Physical Society of London, Volume 85, Issue 3, (1965), pages 523-532.

9. [BAS1955] Z.S. Basinski, W. Hume-Rothery and A.L. Sutton, Proceedings A, The Royal Society, Volume 229, Issue 1179, (1955), pages 459-467.

10. [BEA1968] C.D. Beacham and D.A. Meyn, Electron Fractography, American Society for Testing and Materials STP 436, Philadelphia, (1968), page 76.

11. [BEE1972] From J.R. Beeler Jr. and G.L. Kulcinski, Agenda discussion: computer techniques, In: J.R. Beeler Jr., P.C. Gehlen and R.I. Jaffe, editors , Interatomic Potentials and Simulation of Lattice Defects, Plenum Press, (1972), pages 735-751.

12. [BEE1983] J.R. Beerler, Radiation Effects Computer Experiments, 1st Edition, Defects in Solids, Volume 13, (1983), Elsevier.

13. [BEL1999] G.E. Beltz, D.M. Lipkin and L.L. Fisher, Role of Crack blunting in ductile versus brittle response of crystalline materials, Physical Review Letters, Volume 82, Issue 22, (1999), pages 4468-4471.

14. [BEL2004] G.E. Beltz and A. Machová, Effect of T-stress on dislocation emission in iron, Scripta Materialia, Volume 50, Issue 4, (2004), pages 483-487.

15. [BEL2007] G.E. Beltz and A. Machová, Reconciliation of continuum and atomistic models for the ductile versus brittle response of iron, Modeling and Simulation in Materials Science and Engineering, Volume 15, Issue 2, (2007), pages 65-83.

16. [BEN1975] C.H. Bennett, Exact Defects Calculations in Model Substances, in Diffusion in Solids: Recent Developments, A.S. Nowick and J.J. Button Eds., Academic Press NY, (1975), pages 73-113.

17. [BEN1982] W. Bendick and W. Pepperhoff, On the α/γ phase stability of iron, Acta Metallurgica, Volume 30, Issue 3, (1982), pages 679-684.

18. [BIL1968] H. Bilger, V. Hivert, J. Verdone, J.L. Leveque and J.C. Soulie, in: International Conference on vacancies and interstitials in metals, Kernforshungsanlage Juelich, (1968), page 751.

19. [BOH1988] K.-P. Bohnen and K.-M. Ho, First principles calculation of lattice relaxation and surface phonons on Al(100), Surface Science, Volume 207, Issue 1, (1988), pages 105-117.

20. [BON2007] S.D. Bond and B.J. Leimkuhler, Molecular dynamics and the accuracy of numerically computed average, Acta Numerica, Volume 16, (2007), pages 1-65.

21. [BOO1997] A.S. Booth and S.G. Roberts, The brittle-ductile transition in γ-TiAl single crystals, Acta Materialia, Volume 45, Issue 3, (1997), pages 1045-1053.

22. [BOR1927] M. Born and J.R. Oppenheimer, Zur Quantentheorie der Molekeln (On the Quantum Theory of Molecules), Annelen der Physik, Volume 389, Issue 20, (1927), pages 457-484.

23. [BOU2005] C. Bouchet, B. Tanguy, J. Besson and S. Bugat, Prediction of the effects of neutron irradiation on the Charpy ductile to brittle transition curve of an A508 pressure vessel steel, Computational Materials Science, Volume 32, Issues 3-4, (2005), pages 294-300.

24. [BRE1988] M. Brede and P. Haasen, The brittle-to-ductile transition in doped silicon as a model substance, Acta Metallurgica, Volume 36, Issue 8, (1988), pages 2003-2018.

25. [BRE2000] D.W. Brenner, The Art and Science of an Analytic Potential, Physica Status Solidi (b), Volume 217, Issue 1, (2000), pages 23-40.

26. [BRO1999] J.Q. Broughton, F.F. Abraham, N. Bernstein and E. Kaxiras, Concurrent coupling of length scales: Methodology and application, Physical Review B, Volume 60, Issue 4, (1999), pages 2391-2403.

27. [CAG1988] T. Cagin and J.R. Ray, Elastic constants of sodium from molecular dynamics, Physical Review B, Volume 37, Issue 2, (1988), pages 699-705.

28. [CAO2006] L.-X. Cao, C.-Y. Wang, Atomistic simulation for configuration evolution and energetic calculation of crack in body-centered-cubic iron, Journal of Material Research, Volume 21, Issue 10, (2006), pages 2542-2549.

29. [CHA2002] M. Chang, Multi-Scale Multi-Plane Model for Stacking Fault and Twinning Formation in bcc Iron, PhD Thesis, University of California, Santa Barbara, (2002).

30. [CHA2006] X. Chang, Y. Wang and L. Hu, An implicit Taylor series numerical calculation method for power system transient simulation, The Guide to Computing Literature, (2006), pages 82-85.

31. [CHA2010] J. Chaussidon, C. Robertson, M. Fivel and B. Marini, Internal stress evolution in Fe laths deformed at low temperature analysed by dislocation dynamics simulations, Modelling and Simulation in Materials Science and Engineering, Volume 18, Issue 2, (2010), pages 025003.

32. [CHE1990] K.S. Cheung and S. Yip, Brittle-Ductile Transition in Intrinsic Fracture Behavior of Crystals, Physical Review Letters, Volume 65, Issue 22, (1990), pages 2804-2807.

33. [CUR1990] W.A. Curtin, On lattice trapping of cracks, Journal of Materials Research, Volume 5, Issue 7, (1990), pages 1549-1560.

34. [DEC1983] B. deCelis, A.S. Argon and S. Yip, Molecular dynamics simulation of crack tip processes in alpha-iron and copper, Journal of Applied Physics, Volume 54, Issue 9, (1983), pages 4864-4878.

35. [DOM2001] C. Domain and C.S. Becquart, Ab initio calculations of defects in Fe and dilute Fe-Cu alloys, Physical Review B, Volume 65, Issue 2, (2001), pages 024103-17.

36. [EVA1974] R.H. Evans, PhD Thesis, Department of Electrical Engineering, North Carolina States University, (1974).

37. [EVA1987] G.A. Evangelakis, J.P. Rizos, I.E. Lagaris and I.N. Demetropoulos, Merlin - a portable system for multidimensional minimization, Computer Physics Communications, Volume 46, Issue 3, (1987), pages 401-415.

38. [FIS2001] L.L. Fisher and G.E. Beltz, The effect of crack blunting on the competition between dislocation nucleation and cleavage, Journal of the Mechanics and Physics of Solids, Volume 49, Issue 3, (2001), pages 635-654.

39. [FLU1978] M.J. Fluss, L.C. Smedskjaer, M.K. Chason, D.G. Legnini and R.W. Siegel, Measurements of the vacancy formation enthalpy in aluminum using positron annihilation spectroscopy, Physical Review B, Volume 17, Issue 9, (1978), pages 3444-3455.

40. [FRA2002] D. Francois and A. Pineau, From Charpy to Present Impact Testing, Elsevier Science, European Structural Integrity Society, Volume 30, (2002), pages 3-486.

41. [FU2004] C.-C. Fu, F. Willaime and P. Ordejón, Stability and Mobility of Mono- and Di-Interstitials in α-Fe, Physical Review Letters, Volume 92, Issue 17, (2004), pages 175503-7.

42. [GEH1972] P.C. Gehlen, J.R. Beeler Jr. and R.I. Jaffee, Interatomic potentials and simulations of lattice defects, Plenum Press, (1972).

43. [GEO1979] A. George and G. Champier, Velocities of screw and 60° dislocations in n- and p-type silicon, Physica status solidi (a), applications and materials science, Volume 53, Issue 2, (1979), pages 529-540.

44. [GIA2007] A. Giannattasio and S.G. Roberts, Strain-rate dependence of the brittle-to-ductile transition temperature in tungsten, Philosophical Magazine, Volume 87, Issue 17, (2007), pages 2589-2598.

45. [GIB1902] J.W. Gibbs, Elementary Principles in Statistical Mechanics, New York: Charles Scribner's Sons, (1902).

46. [GIL1959] J.J. Gilman, Cleavage, Ductility, and Tenacity in Crystals, Fracture, M.I.T. Technology Press, Cambridge, Mass., (1959), pages 193-224.

47. [GIL1989] M.J. Gillan, Calculation of the vacancy formation energy in aluminium, Journal of Physics: Condensed Matter, Volume 1, Issue 4, (1989), pages 689-711.

48. [GOL2002] H. Goldstein, C.P. Poole Jr. and J. Safko, Classical Mechanics, 3rd edition, Addison Wesley, (2002).

49. [GOU2006] H. Gould, J. Tobochnik and W. Christian, An Introduction to Computer Simulation Methods: Application to Physical Systems, 3rd edition, Addison-Wesley, (2006).

50. [GRI1920] A.A. Griffith, The phenomena of rupture and flow in solids, Philosophical Transactions of the Royal Society of London A, Volume 221, Issues 582-593, (1920), pages 163-197.

51. [GRI2007] M. Griebel, S. Knapek and G. Zumbusch, Numerical Simulation in Molecular Dynamics: Numerics, Algorithms, Parallelization, Applications, Springer, (2007).

52. [GUM1995] P. Gumbsch, An atomistic study of brittle fracture: Toward explicit failure criteria from atomistic modeling, Journal of Material Research, Volume 10, Issue 11, (1995), pages 2897-2907.

53. [GUM1998] P. Gumbsch, J. Riedle, A. Hartmaier and H.F. Fischmeister, Controlling factors for the brittle-to-ductile transition in tungsten single crystals, Science, Volume 282, Issue 5392, (1998), pages 1293-1295.

54. [GUN1990] W.F. van Gunsteren and H.J.C. Berendsen, Computer Simulation of Molecular Dynamics: Methodology, Applications, and Perspectives in Chemistry, Angewandte Chemie International Edition in English, Volume 29, Issue 9, (1990), pages 992-1023.

55. [GUO2003] Y.-F. Guo, C.-Y. Wang and D.-L. Zhao, Atomistic simulation of crack cleavage and blunting in bcc-Fe, Materials Science and Engineering: A, Volume 349, Issues 1-2, (2003), pages 29-35.

56. [GUO2006] Y.-F.Guo and Y.-C. Gao, Combined atomistic simulation and continuum mechanics: Size-dependent behavior of atomistic simulation for brittle fracture in bcc-iron, Computational Materials Science, Volume 36, Issue 4, (2006), pages 432-439.

57. [GUO2007a] Y.-F. Guo and D.-L. Zhao, Atomistic simulation of structure evolution at a crack tip in bcc-iron, Materials Science and Engineering: A, Volume 448, Issues 1-2, (2007), pages 281-286.

58. [GUO2007b] Y.-F. Guo, Y.-S. Wang and D.-L. Zhao, Atomistic simulation of stress-induced phase transformation and recrystallization at the crack tip in bcc iron, Acta Materialia, Volume 55, Issue 1, (2007), pages 401-407.

59. [HA1994] K.F. Ha, C. Yang and J.S. Bao, Effect of dislocation density on the ductile-brittle transition in bulk Fe - 3%Si single crystals, Scripta Metallurgica et Materialia, Volume 30, Issue 8,(1994), pages 1065-1070.

60. [HAH1984] G.T. Hahn, The Influence of Microstructure on Brittle Fracture Toughness, Metallurgical and Materials Transactions A, Volume 15, Issue 6, (1984), pages 947-959.

61. [HAI1997] J.M. Haile, Molecular Dynamics Simulation: Elementary Methods, Wiley Professional Paperback Edition ed. Wiley Professional Paperback Series, ed. I. John Wiley & Sons, (1997), New York: A Wiley-Interscience Publication.

62. [HAM1992] B. Hammer, K.W. Jacobsen, V. Milman and M.C. Payne, Stacking fault energies in aluminium, Journal of Physics: Condensed Matter, Volume 4, Number 50, (1992), pages 10453-10460.

63. [HAR1997] A. Hartmaier and P. Gumbsch, On the activation energy for the brittle/ductile transition, Physica Status Solidi B-Basic solid state physics, Volume 202, Issue 2, (1997), pages R1-R2.

64. [HIR1982] J.P. Hirth and J. Lothe, Theory of dislocations, 2nd edition, John Wiley & Sons, New York, (1982).

65. [HIR1989] P.B. Hirsch, S.G. Roberts and J. Samuels, The brittle-ductile transition in silicon. II. Interpretation, Proceedings of the Royal Society of London. Series A, Mathematical and Physical Sciences, Volume 421, Issue 1860, (1989), pages 25-53.

66. [HIR1996] P.B. Hirsch and S.G. Roberts, Comment on the brittle-to ductile transition: A cooperative dislocation generation instability; dislocation dynamics and the strain-rate dependence of the transition temperature, Acta Materialia, Volume 44, Issue 6, (1996), pages 2361-2371.

67. [HIR1997] P.B. Hirsch and S.G. Roberts, Modelling plastic zones and the brittle-ductile transition, Philosophical Transactions of the Royal Society of London. Series A, Volume 355, Issue 1731, (1997), pages 1991-2001.

68. [HO1985] K.M. Ho and K.P. Bohnen, Investigation of multilayer relaxation on Al(110) with the use of self-consistent total-energy calculations, Physical Review B, Volume 32, Issue 6, (1985), pages 3446-3450.

69. [HOW1961] S. Howe, B. Liebmann and K. Lücke, High temperature deformation of aluminum single crystals, Acta Metallurgica, Volume 9, Issue 7, (1961), pages 625-631.

70. [HUG1923] M.L. Huggins, Crystal cleavage and crystal structure, American Journal of Science, Series 5, Volume 5, (1923) pages 303-313.

71. [HUL1958] D. Hull, Nucleation of cracks by the intersection of twins in a-iron, Philosophical Magazine, Volume 3, Issue 36, (1958), pages 1468-1469.

72. [HUL1963] D. Hull, Orientation and Temperature Dependence of Plastic Deformation Processes in 3.25% Silicon Iron, Proceedings of the Royal Society A, Volume 274, Issue 1356, (1963), pages 5-20.

73. [ING1913] C.E. Inglis, Stresses in a plate due to the presence of cracks and sharp corners, Transactions of the Institute of Naval Architects, Volume 55, (1913), pages 219-242.

74. [INT1] http://www.personal.soton.ac.uk/jav/soton/HELM/workbooks/workbook_31/31_3_num_diff.pdf

75. [INT2] https://en.wikipedia.org/wiki/Taylor_series

76. [INT3] https://en.wikipedia.org/wiki/Aluminium

77. [INT4] https://www.oxford-instruments.com/getmedia/83622c16-8dca-4c76-923e-2c1f0aa9fe18/determining-the-fcc-bcc-orientation-relationship-in-plessite-regions-of-iron-meteoites

78. [INT5] https://www.doitpoms.ac.uk/tlplib/slip/slip_geometry.php

79. [IWA1985] T. Iwadate, Y. Tanaka. H. Takemata and T. Kabutomori, Elastic-plastic fracture toughness behaviour of heavy section steels for nuclear pressure vessels, Nuclear Engineering and Desing, Volume 87, (1985), pages 89-99.

80. [JAM2014] M. Jamal, S. Jalali Asadabadi, Iftikhar Ahmad and H.A. Rahnamaye Aliabad, Elastic constants of cubic crystal, Computational Materials Science, Volume 95, (2014), pages 592-599.

81. [JAO1965] B. Jaoul, Étude de Plasticité et Application aux Métaux, (1965) Dunod.

82. [JOH1975] C. St. John, The brittle-to-ductile transition in pre-cleaved silicon single crystal, Philosophical Magazine, Volume 32, Issue 6, (1975), pages 1193-1212.

83. [KAS2012] K.T. Kashyap, A. Bhat, P.G. Koppad and K.B. Puneeth, On Peierls Nabarro stress in Iron, Computational Materials Science, Volume 56, (2012), pages 172-173.

84. [KEL1967] A. Kelly, W.R. Tyson and A.H. Cottrell, Ductile and brittle crystals, Philosophical Magazine, Volume 15, Issue 135, (1967), pages 567-586.

85. [KHA1994] M. Khantha, D.P. Pope and V. Vitek, Dislocation Screening and the Brittle-to-Ductile Transition: A Kosterlitz-Thouless Type Instability, Volume 73, Issue 5, (1994), pages 684-687.

86. [KIM1994] H.-S. Kim and S. Roberts, Brittle-Ductile Transition and Dislocation Mobility in Sapphire, Journal of the American Ceramic Society, Volume 77, Issue 12, (1994), pages 3099-3104.

87. [KIT1976] C. Kittel, Introduction to Solid State Physics, 5th edition, New York: John Wiley, (1976).

88. [KIT2004] C. Kittel, Introduction to Solid State Physics, 8th edition, New York, John Wiley, (2004).

89. [KOH1991] S. Kohlhoff, P. Gumbsch and H.F. Fischmeister, Crack propagation in b.c.c. crystals studied with a combined finite-element and atomistic model, Philosophical Magazine A-Physics of condensed matter structure defects and mechanical properties, Volume 64, Issue 4, (1991), pages 851-878.

90. [KOI2000] H. Koizumi, T. Koizumi and T. Kosugi, Determination of the pre-exponential factor and the activation energy for the low-temperature dislocation relaxation in aluminum, Journal of Alloys and Compounds, Volume 310, Issues 1-2, (2000), pages 107-110.

91. [KUR1930] G. Kurdjumov and G. Sachs, Over the mechanisms of steel hardening, Zeitschrift für Physik, Volume 64, Issue 5, (1930), pages 325-343.

92. [KUR1979] E. Kuramoto, Y. Aono and K. Kitajima, Thermally activated slip deformation of high purity iron single crystals between 4.2 K and 300 K, Scripta Metallurgica, Volume 13, Issue 11, (1979), pages 1039-1042.

93. [LAN2002] M. Landa, J. Cerv, A. Machová and Z. Rosecky, Acoustic Emission Sources by Atomistic Simulations, Journal of Acoustic Emission, Volume 20, (2002), pages 25-38.

94. [LAT2003] A. Latapie and D. Farkas, Molecular dynamics simulations of stress-induced phase transformations and grain nucleation at the crack tips in Fe, Modelling and Simulation in Materials Science and Engineering, Volume 11, Issue 5, (2003), pages 745-753.

95. [LEK1963] S.G. Lekhnitskii, Theory of elasticity of an anisotropy elastic body, San Francisco: Holden-Day, (1963).

96. [LEK1968] S.G. Lekhnitskii, Anisotropic plates. New York: Gordon and Breach Science Publishers, (1968).

97. [LIM2001] W.-K. Lim, S.-Y. Choi and B.V. Sankar, Biaxial load effects on crack extension in anisotropic solids, Engineering Fracture Mechanics, Volume 68, Issue 4, (2001), pages 403-16.

98. [LOV1944] A.E.H. Love, A treatise on the mathematical theory of elasticity, 4th Edition, Dover Publications, New York, (1944).

99. [MA1985] S.-K. Ma, Statistical Mechanics, World Scientific, (1985).

100. [MAC1998] A. Machová and G.E. Beltz, Stability of crack tip in terms of molecular dynamics, Kovoné Materiály, Volume 36, Issue 3, (1998), pages 135-144.

101. [MAC1999] A. Machová, G.E. Beltz and M. Chang, M, Atomistic simulation of stacking failt formation in bcc iron, Modelling and Simulation in Materials Science and Engineering, Volume 7, Issue 6, (1999), pages 949-974.

102. [MAC2004] A. Machová and G.E. Beltz, Ductile-brittle behavior of (001)[110] nano-cracks in bcc iron, Materials Science and Engineering: A, Volumes 387-389, (2004), pages 414-418.

103. [MÄN1999] M. Mäntylä, A Rossoll, I Nedbal, C. Prioul and B. Marini, Fractographic observations of cleavage fracture initiation in bainitic A508 steel, Journal of Nuclear Materials, Volume 264, Issue 3, (1999), pages 257-262.

104. [MAS1980] K. Masubuchi, Analysis of Welded Structures: Residual Stresses, Distortion, and their Consequences, International Series on Materials Science and Technology, Volume 33, Massachusetts Institute of Technology, USA, Pergamon Press, (1980).

105. [MIC1994] G. Michot, M.A.L. de Oliveria and A. George, Dislocation loops at the crack tips: control and analysis of sources in silicon, Material Science and Engineering: A, Volume 176, Issues 1-2, (1994), pages 99-109.

106. [MIL1989] M.J. Mills and P. Stadelmann, A study of the structure of Lomer and 60° dislocations in aluminium using high-resolution transmission electron microscopy, Philosophical Magazine A, Volume 60, Issue 3, (1989), pages 355-384.

107. [MOS1966] P. Moser, Mémoire Scientifique de la Revue de Métallurgie, 63, (1966), pages 431-462.

108. [MOU2009] C.M. Moura, J.J. Vilela, E.G. Rabello, G. de P. Martins and J.R.G. Carneiro, Evaluation of the Ductile-to-Brittle temperature in Steel low carbon, 2009 International Nuclear Atlantic Conference (INAC 2009), Rio de Janeiro, Brazil, (2009).

109. [MUR1975] L.E. Murr, Interfacial Phenomena in Metals and Alloys, Addison-Wesley Publishing Company, (1975).

110. [NEE1987] J. Needs, Calculations of the Surface Stress Tensor at Aluminum (111) and (110), Physical Review Letters, Volume 58, Issue 1, (1987), pages 53-56.

111. [NIS1934] Z. Nishiyama, X-ray investigation of the mechanism of the transformation from face-centered cubic to body-centered cubic, Science Reports of the Tohoku Imperial University, Volume 23, (1934), pages 637-664.

112. [NIS2004] K. Nishimura and N. Miyazaki, Molecular dynamics simulation of crack growth under cyclic loading, Computational Materials Science, Volume 31, Issues 3-4, (2004), pages 269-278.

113. [OBR2005] K. Obrtlik, C.F. Robertson and B. Marini, Dislocation structures in 16MND5 pressure vessel steel strained in uniaxial tension, Journal of Nuclear of Materials, Volume 342, Issues 1-30, (2005), pages 35-41.

114. [OHR1985] S.M. Ohr, An electron microscope study of crack tip deformation and its impact on the dislocation theory of fracture, Materials Science and Engineering, Volume 72, Issue 1, (1985), pages 1-35.

115. [PAN1998] J. Panova and D. Farkas, Atomistic simulation of fracture in TiAl, Metallurgical and Materials Transactions A, Volume 29, Issue 13, (1998), pages 951-955.

116. [PAT2011] R.K. Pathria and P.D. Beale, Statistical Mechanics, 3rd edition, Academic Press, (2011).

117. [PÉN1979] J.M. Pénisson and A. Bourret, High resolution study of [011] low-angle tilt boundaries in aluminium, Philosophical Magazine A, Volume 40, Issue 6, (1979), pages 811-824.

118. [PON2007] V. Pontikis, V. Russier and J. Wallenius, An analytic n-body potential for bcc Iron, Nuclear Instruments and Methods in Physics Research Section B: Beam Interactions with Materials and Atoms, Volume 255, Issue 1, (2007), pages 37-40.

119. [POP1974] Z.D. Popovic, J.P. Carbotte and G.R. Piercy, On the vacancy formation energy and volume of simple cubic metals, Journal of Physics F: Metal Physics, Volume 4, Issue 3, Number 3, (1974), pages 351-360.

120. [PUL1981] M.P. Puls, Atomic Models of single dislocations, Dislocation Modeling of Physical Systems, Proceedings of the International Conference (Gainasville, Florida, USA, 1980), Pergamon, Oxford, (1981) pages 249-268.

121. [QIA2003] Y. Qiao and A.S. Argon, Brittle-to-ductile fracture transition in Fe-3wt.%Si single crystals by thermal crack arrest, Mechanics of Materials, Volume 35, Issue 9, (2003), pages 903-912.

122. [RAF1998] H. Rafii-Tabar, L. Hua and M. Cross, A multi-scale atomic-continuum modelling of crack propagation in a two-dimensional macroscopic plane, Journal of Physics Condensed Matter, Volume 10, Issue 11, (1998), pages 2375-2387.

123. [RAP2004] D.C. Rapaport, The Art of the Molecular Dynamics Simulation, Cambridge University Press, (2004).

124. [REN1996] S. Renevey, S. Carassou, M. Marini, C. Eripret and A. Pineau, Ductile-Brittle Transition of Ferritic Steels Modelled by the Local Approach to Fracture, Journal de Phisique IV, Colloque C6, supplément au Journal de Physique III, Volume 6, (1996), pages 343-352.

125. [RIC1974] J.R. Rice and R. Thomson, Ductile versus brittle behaviour of crystals, Philosophical Magazine, Volume 29, Issue 1, (1974), pages 73-97.

126. [RIC1992] J.R. Rice, Dislocation nucleation from a crack tip: An analysis based on the Peierls concept, Journal of the mechanics and Physics of Solids, Volume 40, Issue 2, (1992), pages 239-271.

127. [RIC1994] J.R. Rice and G.E. Beltz, The activation energy for dislocation nucleation at a crack, Journal of the mechanics and physics of solids, Volume 42, Issue 2, (1994), pages 333-360.

128. [RIE1996] J. Riedle, P. Gumbsch and H.F. Fischmeister, Cleavage Anisotropy in Tungsten Single Crystals, Physical Review Letters, Volume 76, Issue 19, (1996), pages 3594-3597.

129. [ROB1993] S.G. Roberts, M. Ellis and P.B. Hirsch, Dislocation dynamics and brittle-to-ductile transitions, Materials Science and Engineering: A, Volume 164, Issues 1-2, (1993), pages 135-140.

130. [ROB1996] S.G. Roberts, Modelling the brittle to ductile transition in single crystals, In H.O. Kirchner, L.P. Kubin and V. Pontikis, editors, Computer Simulations in Material Science, Volume 308, Series E: Applied Sciences, pages 409-433. Kluwer Academic Publishers, Dordrecht, Netherlands, (1996).

131. [ROS1996] A. Rossoll, M. Tahar, C. Berdin, R. Piques, P. Forget, C. Prioul and B. Marini, Local Approach of the Charpy Test at Low Temperature, Journal de Phisique IV, Colloque C6, supplément au Journal de Physique III, Volume 6 (1996), pages 279-286.

132. [SAM1989] J. Samuels, S.G. Roberts, The Brittle-Ductile Transition in Silicon. I. Experiments, Proceeding of the Royal Society of London A, Volume 421, Issue 1860, (1989), pages 1-23.

133. [SAV1961] G.N. Savin, Stress concentration around holes, Oxford, Pergamon Press, (1961).

134. [SCH1983] L.D. Schepper, D. Segers, L. Dorikens-Vanpraet, M. Dorikens, G. Knuyt, L.M. Stals and P. Moser, Positron annihilation on pure and carbon-doped α-iron in thermal equilibrium, Physical Review B, Volume 27, Issue 9, (1983), pages 5257-5269.

135. [SCH1995] J. Schöchlin, K.P. Bohnen and K.M. Ho, Surface and dynamics at the Al(111)-surface, Surface Science, Volume 324, Issues 2-3, (1995), pages 113-121.

136. [SCH1996] G. Schoeck, The formation of dislocation rings on a crack front, Philosophical Magazine A, Volume 74, Issue 2, (1996), pages 419-430.

137. [SCH1997] J. Schiøtz, L.M. Canel and A.E. Carlsson, Effects of crack tip geometry on dislocation emission and cleavage: A possible path to enhanced ductility, Physical Review B, Volume 55, Issue 10, (1997), pages 6211-6221.

138. [SCH2001] T. Schlick, Time-trimming tricks for dynamic simulations: Splitting force updates to reduce computational work, Structure, Volume 9, Issue 4, (2001), pages R45-R53.

139. [SEE1976] A. Seeger and C. Wüthrich, Dislocation relaxation processes in body-centered cubic metals, Il Nuovo Cimento B (1971-1996), Volume 33, Issue 1, (1979), pages 38-75.

140. [SER1994] F.C. Serbena and S.G. Roberts, The brittle-to ductile transition in germanium, Acta Metallurgica et Materialia, Volume 42, Issue 7, (1994), pages 2505-2510.

141. [SER1995] F.C. Serbena, The brittle-ductile transition in NiAl, Doctor of Philosophy thesis, (1995), University of Oxford.

142. [SHA1936] M.D. Shappell, Cleavage of ionic minerals, The American Mineralogist, Journal of the Mineralogical Society of America, Volume 21, Issue 2, (1936), pages 75-102.

143. [SHA1996] V. Shastry and D. Farkas, Modelling statics simulation of fracture in α-iron, Modelling and Simulation in Materials Science and Engineering, Volume 4, Issue 5, (1996), pages 473-492.

144. [SHI2013] I. Shin and E.A. Carter, Possible origin of the discrepancy in Peierls stresses of fcc metals: First-principles simulations of dislocation mobility in aluminum, Physical Review B, Volume 88, Issue 6, (2013), pages 064106-16.

145. [SIH1968] G.C. Sih and H. Liebowitz, In : Liebowitz H, editor, Mathematical theories of brittle fracture, in fracture mechanics, Vol. II, Academic Press, New York, (1968).

146. [SIM1960] R.O. Simmons and R.W. Balluffi, Measurements of Equilibrium Vacancy Concentrations in Aluminum, Physical Review, Volume 117, Issue 1, (1960), pages 52-61.

147. [SIM1971] G. Simmons and H. Wang, Single Crystal Elastic Constants and Calculated Aggregate Properties: A HANDBOOK, 2nd Edition, (Cambridge: M.I.T. Press), (1971).

148. [SIN1972] J.E. Sinclair and B.R. Lawn, An Atomistic Study of Cracks in Diamond-Structure Crystals, Proceedings of The Royal Society of London Series A-Mathematical and Physical Science, Volume 329, Issue 1576, (1972), pages 83-103.

149. [SIN1975] J.E. Sinclair, The influence of the interatomic force law and of kinks on the propagation on the propagation of brittle cracks, Philosophical Magazine, Volume 31, Issue 3, (1975), pages 647-671.

150. [SMA1970] R.E. Smallmann and P.S. Dobson, Stacking fault energy measurement from diffusion, Metallurgical Transaction, Volume 1, Issue 9, (1970), pages 2383-2389.

151. [SMI2014] T. Smida and V. Magula, Brittle to ductile - An engineer's point of view, Materials and Design (1980-2015), Volume 54, (2014), pages 582-586.

152. [SPI2007] A. Spielmannova, M. Landa, A. Machova, P. Hausild and P. Lejcek, Influence of crack orientation on the ductile-brittle behavior in Fe-3wt.%Si single crystals, Materials Characterization, Volume 58, Issue 10, (2007), pages 892-900.

153. [STA1996] R. Stadler, W. Wolf, R. Podloucky, G. Kresse, J. Furthmüller and J. Hafner, Ab initio calculations of the cohesive, elastic, and dynamical properties of $CoSi_2$ by pseudopotential and all-electron techniques, Physical Review B, Volume 54, Issue 3, (1996), page 1729-1734.

154. [STE1949] A.V. Stepanov, J. Tech. Phys. (U.S.S.R.), Volume 19, (1949), 492.

155. [STO2002] J. Stoer and R. Bulirsch, Introduction to Numerical Analysis, 3rd edition, Berlin, Springer-Verlag New York, (2002).

156. [STU2010] A. Stukowski and K. Albe, Extracting dislocations and non-dislocation crystal defects from atomistic simulation data, Modelling and Simulation in Material Science and Engineering, Volume 18, Issue 8, (2010), pages 085001.

157. [STU2012] A. Stukowski, V.V. Bulatov and A. Arsenlis, Automated identification and indexing of dislocations in crystal interfaces, Modelling and Simulation in Material Science and Engineering, Volume 20, Issue 8, (2012), pages 085007.

158. [SUN2003] H. Sun, Fractal Finite Element Method for Anisotropic Crack Problems, Master Thesis, The University of Hong Kong, Pokfulam, Hong Kong, (2003).

159. [SUZ1988] T. Suzuki and S. Takeuchi, in: T. Suzuki, S. Takeuchi (Eds.), Lattice Defects in Ceramics, Publication Office of Japan Journal of Applied Physics, Tokyo, (1988), page 9.

160. [SUZ1999] T. Suzuki, Y. Kamimura and O.K. Kirchner, Plastic homology of bcc metals, Philosophical Magazine A, Volume 79, Issue 7, (1999), pages 1629-1642.

161. [TAD2000] H. Tada, P.C. Paris and G.R. Irwin, The Stress Analysis of Cracks Handbook, Third edition, The American Society of Mechanical Engineers, New York, (2000), Appendix D, pages 513-514.

162. [TAK1982] S. Takeuchi, T. Hashimoto and K. Maeda, Plastic Deformation of bcc Metal Single Crystals at Very Low Temperatures, Transactions of the Japan Institute of Metals, Volume 23, Issue 2, (1982), pages 60-69.

163. [TAM2002] Y. Tamarin, Atlas of Stress-Strain Curves, 2nd edition, ASM International, (2002).

164. [TAN2005a] B. Tanguy, J. Besson, R. Piques and A. Pineau, Ductile to brittle transition of an A508 steel characterized by the Charpy impact test: Part I: experimental results, Engineering Fracture Mechanics, Volume 72, Issue 1, (2005), pages 49-72.

165. [TAN2005b] B. Tanguy, J. Besson, R. Piques and A. Pineau, Ductile to brittle transition of an A508 steel characterized by the Charpy impact test: Part II: modeling of the Charpy transition curve, Engineering Fracture Mechanics, Volume 72, Issue 3, (2005), pages 413-434.

166. [TAN2008] M. Tanaka, E. Tarleton and S.G. Roberts, The brittle-ductile transition in single-crystal iron, Acta Materialia, Volume 56, Issue 18, (2008), pages 5123-5129.

167. [THO1971] R. Thomson, C. Hsieh and V. Rana, Lattice Trapping of Fracture Cracks, Journal of Applied Physics, Volume 42, Issue 8, (1971), pages 3154-3160.

168. [TRI1975] W. Triftshäuser, Positron trapping in solid and liquid metals, Physical Review B, Volume 12, Issue 11, (1975), pages 4634-4639.

169. [TSA1979] D.H. Tsai, The virial theorem and stress calculation in molecular dynamics, Journal of Chemical Physics, Volume 70, Issue 3, (1979), pages 1375-1382.

170. [TYS1973] W.R. Tyson, R.A. Ayres and D.F. Stein, Anisotropy of cleavage in b.c.c. transition metals, Acta Metallurgica, Volume 21, Issue 5, (1973), pages 621-627.

171. [TYS1977a] W.R. Tyson and W.A. Miller, Surface free energies of solid metals: Estimation from liquid surface tension measurements, Surface Science, Volume 62, Issue 1, (1977), pages 267-276.

172. [TYS1977b] W.R. Tyson, Atomistic simulation of the ductile/brittle transition, International Conference on Fracture, Volume 2, ICF4, Waterloo (Canada), (1977), pages 159-164.

173. [VER1967] L. Verlet, Computer ''Experiments'' on Classical Fluids. I. Thermodynamical Properties of Lennard-Jones Molecules, Physical Review, Volume 159, Issue 1, (1967), pages 98-103.

174. [VIT1974] V. Vitek, Theory of the core structures of dislocations in body-centered cubic metals, Crystal Lattice Defects, Volume 5, Issue 1, (1974), pages 1-34.

175. [VOI1966] W. Voigt, Lehrbuch der Kristallphysik, Johnson Reprint Corporation, Reprint of 1928 edition, New York, (1966).

176. [WAL1967] D.C. Wallace, Thermoelasticity of Stressed Materials and Comparison of Various Elastic Constants, Physical Review, Volume 162, Issue 3, (1967), pages 776-789.

177. [WAL2005] J. Wallenius, P. Olsson and C. Lagerstedt, Relation between thermal expansion coefficient and interstitials formation energy in Fe and Cr, Nuclear Instruments and Methods in Physics Research B, Volume 228, (2005), pages 122-125.

178. [WAN1996] J.N. Wang, Prediction of Peierls stress for different crystals, Materials Science and Engineering: A, Volume 206, Issue 2, (1996), pages 259-269.

179. [WAN2014] S.J. Wang, H. Wang, K. Du, W. Zhang, M.L. Sui and S.X. Mao, Deformation-induced structural transition in body-centred cubic molybdenum, Nature Communications, Volume 5, Issue 3433, (2014), pages 1-9.

180. [WAR1989] P.D. Warren, The brittle-ductile transition in silicon: The influence of the pre-existing dislocation arrangements, Scripta Metallurgica, Volume 23, Issue 5, (1989), pages 637-642.

181. [WAW1975] H. Wawra, Numerical Comparison of the Values for Temperature Dependence of the Surface Free Energy of Solids Determined by Ultrasonic and Other

Conventional Testing Methods - 1, Zeitschrift fuer Metallkunde (Materials Research and Advanced Techniques), Volume 66, Issue 7, (1975), pages 395-401.

182. [WEE1997] J. Weertman, The Paris exponent and dislocation crack tip shielding, in High Cycle Fatigue of Structure Materials, The Paul Paris Symposium, edited by T.S. Srivatsan and Wolé Sobojeyro. Minerals, Metals & Materials Society (TMS) of the AIME, Warrendale, PA, (1997), pages 41-48.

183. [WEE2008] J. Weertman, Dislocation Based Fracture Mechanics, Singapore, Reprint of 1996 edition, World Scientific, (2008).

184. [WES1939] H.M. Westergaard, Bearing Pressures and Cracks, Journal of Applied Mechanics, Volume 6, (1939), pages A49-53.

185. [WIL1994] J.H. Wilkinson, Rounding Errors in Algebraic Processes, New York, NY Doven, (1994).

186. [WIL1997] R.E. Wilde and S. Singh, Statistical Mechanics: Fundamentals and Modern Applications, 1st edition, John Wiley & Sons - Interscience Publication, (1997).

187. [WOO1932] N. Wooster, The correlation of cleavage and structure, Science Progress in the Twentieth Century (1919-1933), Volume 26, Issue 103, (1932), pages 462-473.

188. [XU1997] G. Xu, A.S. Argon and M. Ortiz, Critical configurations for dislocation nucleation from crack tips, Philosophical Magazine A, Volume 75, Issue 2, (1997), pages 341-367.

189. [YOU1999] H.D. Young, R.A. Freedman, T.R. Sandin and A.L. Ford, Sears and Zemansky's University Physics, 10th edition, Addison Wesley Longman, (1999).

190. [ZAC2017] M. Zacharopoulos and V. Pontikis, Assessment of a phenomenological n-body potential for Aluminum (2017 - in preparation).

191. [ZIE1992] W. Zielinski, M.J. Lii and W.W. Gerberich, Crack-tip dislocation emission arrangements for equilibrium - I. *In situ* TEM observations of Fe-2wt%Si, Acta Metallurgica et Materialia, Volume 40, Issue 11, (1992), pages 2861-2871.